Gas-Phase Cleaning of Silicon Wafer Surfaces

by

Andrew Scott Lawing

B.S., Chemical Engineering
University of Rhode Island, 1985

M.S., Chemical Engineering
University of Rhode Island, 1992

Submitted to the Department of Chemical Engineering
in partial fulfillment of the requirements for the Degree of

Doctor of Philosophy
in
Chemical Engineering

at the
Massachusetts Institute of Technology
September, 1997

Signature of Author_____
Department of Chemical Engineering

Certified by_____
Professor Herbert H. Sawin
Department of Chemical Engineering and
Electrical Engineering and Computer Science

Accepted by_____
Professor Robert E. Cohen
Chairman, Committee for Graduate Students

Gas-Phase Cleaning of Silicon Wafer Surfaces

by

Andrew Scott Lawing

Submitted to the Department of Chemical Engineering
on August 11, 1997 in partial fulfillment of the
requirements for the Degree of Doctor of Philosophy in
Chemical Engineering

Abstract

Gas-phase cleaning of silicon wafer surfaces was investigated. Two distinct applications of gas-phase wafer cleaning were explored; 1) the mechanism of transition metal removal in UV excited chlorine and, 2) surface residue characterization and removal after oxide plasma etching in fluorocarbon gases. With regard to 1), it was found that the UV/Cl_2 metals removal process is driven by photon stimulated surface reduction and desorption processes, and that efficient metal removal is realized when the chlorine flux to the surface is balanced with the reducing tendency of the UV flux such that a high concentration of the volatile monovalent transition metal chloride is maintained on the surface. With regard to 2), it was found that the residue remaining on a wafer surface after an oxide etch process can be effectively removed with a combination of UV excited processes for organic contamination removal and vapor phase HF for oxide removal.

Gas-phase cleaning processes are of interest in the semiconductor industry for various reasons. They are a potential replacement for wet cleaning systems which have historically dominated the industry. Wet cleaning processes generate large amounts7 of waste, are incompatible with the vacuum environment in which most wafer etching and deposition processes are performed and may not be capable of cleaning the small high aspect ratio features in future generations of devices. Gas phase cleaning processes can potentially provide an answer to these shortcomings of wet processes, but the mechanisms by which gas phase processes work are not well understood and their applications have so far been limited. This thesis was intended to further the mechanistic understanding and applications of gas phase cleaning processes.

In the UV/Cl_2 process, two dominant phenomena take place; 1) chlorine absorbs UV in the gas phase in the wavelength range 250-400 nm to form reactive chlorine radicals and, 2) surface photolytic processes are enhanced due to the bombardment of the wafer surface with energetic photons. In the literature, the mechanism of transition metal removal in the UV/Cl_2 process has been attributed to silicon etching due to the formation of reactive chlorine radicals, and the formation of $Si_XCl_YM_Z$ complexes which should be more volatile than metal chlorides, whose equilibrium vapor pressures are generally too low to account for the observed removal rates.

In this work, the mechanism of copper removal in the UV/Cl_2 system was investigated with a series of wavelength dependent experiments, in order to separate the effects of gas phase and surface photolysis. It was found that the dominant effect in the UV/Cl_2 copper removal process is the photon stimulated reduction of higher chlorides (i.e. $CuCl_2$), which are not volatile, to lower chlorides (i.e. CuCl) which are the volatile products. Gas-phase chlorine radical production is in fact detrimental to the metals removal process since it pushes the equilibrium towards the formation of non-volatile

products. Efficient copper removal is realized by balancing these effects to maintain a high concentration of CuCl on the surface. CuCl is removed from the wafer surface through a photon stimulated desorption process at a rate much higher than would be predicted from equilibrium considerations. Nickel and iron are removed through a similar mechanism. On an oxide surface, the removal of transition metals is complicated by spontaneous and UV enhanced oxidation processes. These oxidation processes impose an additional bond-breaking constraint on the removal mechanism (i.e. the breaking of the metal-oxygen bond). These processes due not significantly affect the efficiency of the copper removal process. In the case of iron, the oxidizing tendency is overcome at elevated temperature. Nickel has not been successfully removed from an oxide surface in the temperature range achievable in these experiments (<140°C).

In the plasma etching of oxide films in fluorocarbon gases, selectivity is achieved through the deposition of an etch inhibiting polymer film on the silicon surface. At the proper process conditions, this polymer does not deposit on the oxide surface due to the presence of oxygen and the formation of volatile etch products. This process is typically followed with exposure to an oxygen plasma. The oxygen plasma removes much of the bulk fluorocarbon polymer but results in a silicon surface covered with a polymer-bearing native oxide. This contamination must be removed before proper electrical contact can be made to the underlying active device region.

We have characterized and developed integrated gas-phase cleaning methodologies for two separate plasma oxide etching systems. In the first investigation, wafers were etched in a conventional parallel plate Reactive Ion Etcher (RIE) and exposed to oxygen plasma in a barrel asher. The etch and ash portion of this process were performed outside of the vacuum system. The samples were then transferred to our vacuum system were the wafer surface was characterized with *in situ* XPS, and a sequential UV/Cl_2-HF/Vapor-UV/Cl_2 process was performed to remove polymer and oxide contamination. This process sequence resulted in a wafer surface which was largely free of carbon and oxygen contamination. In the second investigation wafers were etched in a high density Inductively Coupled Plasma (ICP) reactor. An *in situ* oxygen plasma Post Etch Treatment (PET) was performed in the same reactor. Various combinations of gas-phase cleaning processes were then applied to the wafers. In this system, the entire process sequence was performed on both blanket and patterned oxide films without removal of the samples from the integrated processing apparatus in our laboratory. In this manner, extraneous effects due to ambient contamination were entirely avoided. Due to the efficiency of the high density PET, it was found that (as opposed to the RIE system studied in the first investigation) a UV/Cl_2 pre-clean for polymer removal was unnecessary prior to the HF/Vapor native oxide strip. Two types of contamination were observed on patterned wafers. The first is due to incorporated carbon and is analogous to the incorporated contamination observed on blanket wafers in both the high density and RIE systems. The second has not been observed on blanket wafers, and is due to polymeric contamination which is chemically bonded to the oxide. This second type of contamination may be related to critical dimension control, but its' origin and significance are in question.

Thesis Supervisor: Professor Herbert H. Sawin
MIT Professor of Chemical Engineering and
Electrical Engineering and Computer Science

Acknowledgments

I would like to thank all of the people who have made the last five years of my life bearable, and who contributed to making this thesis a success.

First of all I would like to thank Herb for giving me a long leash (but not quite long enough to hang myself with), and letting me run with things when I needed to. I would like to thank FSI International, who funded most of this work, and especially Jeff Butterbaugh and Ty Fayfield who made valuable contributions both directly and indirectly. To all the members of the Sawin Group who made the lab experience more enjoyable, and who put up with my constant horseplay; Andrew, Arpan, Brett ("You're a zero-man"), Brian, Colin, Dave (for getting me started), Frank, Gavin, Gib, Gil, Han, Heeyeop, Ohseung (good luck), Jane (thanks for the tie), John (for helping to get me a job!), Jun, Minh, Steve, Tim (for dubbing the tapes), Tony, Troy, Vivek!, Young Frank and Zhe. Quite a list, I hope I didn't forget anyone! I would especially like to thank Yong-Pil Han ("little buddy") and Anthony Muscat, who both contributed directly and invaluably to this work. Thanks also to Peter and Glori for the support and understanding when I misplaced my yellow slips.

Thanks for the love and support of my family and friends; Mom, Dad, Bill & Annette and the Kids, Bruce & Julie, Jon, Lars, Janice, Michela, Matt & Jeanne, Krissy, the Tallmans, the list goes on and on, so I'll stop there so as not to upset anyone. I would like to acknowledge the contributions of Dave Hayes, who kept my stomach full on a regular basis, went to many Sox games, and helped me to maintain my sanity (mebs). Thanks to the members of Gloryhound, Danny and Chris, for providing me with an outlet for my creative juices, and thanks to everyone who came out to see us. Thanks to Brian Phenix for tolerating my guitar playing and nasty habits. Finally, I need to thank Jane Ciebien, for being "low maintenance" and helping to restore my peace of mind at a time when I needed it. It would have been a lot more difficult and considerably less enjoyable getting through this without you.

Scott Lawing
Cambridge MA
August 9, 1997

Table of Contents

List of Figures

List of Tables

Chapter 1

Introduction and Background

1.1 Motivation

As critical dimensions decrease and the performance of devices becomes sensitive to lower levels of contamination, wafer cleaning has become much more important in semiconductor manufacturing. Part of this renewed interest in wafer cleaning has been an interest in gas-phase or "dry" wafer cleaning processes. Much of the work in this area has been phenomenological in nature, with little emphasis placed on understanding the science underlying the cleaning process. This thesis is intended to further the mechanistic understanding of gas phase cleaning processes.

1.2 Contamination and Wafer Cleaning in Microelectronics Manufacturing

Wafer cleaning processes are required to remove the damage and contamination introduced on the wafer surface as a result of etching, deposition, implantation, patterning and polishing processes. On the order of one third of the process steps involved in the manufacture of a chip are cleaning processes. The types and extent of the contamination are fairly specific to the processes which cause them. For instance, plasma etching processes introduce contaminating films on wafer structures. Generally the deposition of these films is crucial to the maintenance of etch anisotropy and/or selectivity, as they tend to passivate the surface on which they are deposited and so inhibit etching. For instance, in the selective etching of SiO_2 over silicon, a fluorocarbon film is deposited on the silicon surface during the

etch. In polysilicon etching in halocarbon gases, a passivating film deposits on the sidewalls, inhibiting lateral etching. These films must be removed prior to subsequent processing. The fluorocarbon film remaining after oxide etching contributes to increasing the resistance of electrical contacts made to the substrate. Residual halogens in the sidewall films after polysilicon etching contribute to the corrosion of metal lines which connect devices together. Some cleaning processes actually introduce contaminants while they are removing others. Oxygen plasmas are used to remove photoresist residues and organic materials from the wafer surface, but result in the growth of a thin oxide on silicon surface. This oxide increases contact resistance and can inhibit the growth of epitaxial layers. Hydrofluoric acid solutions are used to remove oxides from wafer surfaces, but it has been shown that metals (especially copper) will deposit on the wafer surface (even in very low concentrations) from these solutions. Other wet cleaning solutions can also cause metallic contamination or native oxide growth. Metals must be removed from the wafer surface before the growth of a gate oxide. This is an especially critical application since low quantities of metals can cause the degradation of electrical performance in the extremely thin gate oxides used in the current generation of devices.

Even from this cursory coverage of wafer cleaning, it is obvious that it involves a very demanding and complicated set of problems. These problems will become larger in magnitude and even more convoluted as device dimensions decrease and the processing sequence becomes more complicated in future generations of devices. A complete coverage of wafer cleaning issues is beyond the scope of this thesis. We have limited our studies to two specific cases, cleanup of trace metals with ultraviolet excited chlorine and the development of a dry cleaning sequence for cleanup after oxide etching processes in fluorocarbon gas

mixtures. In the following sections, some general background, and more specific information on the particular wafer cleaning problems of interest here, will be presented.

1.3 Wet Wafer Cleaning Processes

"Wet Cleaning" refers to wafer cleaning processes based on liquid phase chemistry. Most wet cleaning processes are based on the "RCA" cleaning sequence developed by Kern[1] in the 1960's. This sequence consists of an "SC1" ($H_2O/H_2O_2/NH_4OH$) and an "SC2" ($H_2O/H_2O_2/HCl$) clean, and is designed to remove metals and organic contamination. Other widely used chemistries include dilute HF for the removal of oxide films and "piranha" (H_2O_2/H_2SO_4) for the removal of heavy organic contamination. With the realization that trace chemical contamination can have a disastrous effect on yield and device performance in IC's with ever shrinking dimensions and the development of analytical techniques which make it possible to identify contaminants at the level of 10^{10} atoms/cm^2 and below, there has been renewed interest in understanding the mechanisms involved in wet chemical cleaning, and in modifying the wet chemical "recipes" in order to minimize surface roughening. There has also been interest in correlating device performance with levels of chemical contamination.

While wet chemical cleaning has served the industry's needs for a number of years, it has inherent limitations which make it unattractive for the production of future generations of devices. Foremost among these are its incompatibility with clustered processing (wafers must be removed from the vacuum environment to undergo a wet clean) and the difficulty in completely removing wet chemicals from high aspect ratio features. The environmental, safety and cost issues associated with handling large quantities of high purity wet chemicals make alternative cleaning strategies attractive.

1.4 Gas-Phase ("Dry") Wafer Cleaning Processes

Dry wafer cleaning covers a broad range of processes and process chemistries. Dry wafer cleaning processes can be classified as excited or non-excited processes. Excited processes refer to cleaning strategies in which energy must be added to the system in order to stimulate the cleaning reaction or mechanism. The class of excited processes can be further broken down into: thermally excited processes (rapid thermal processing), plasma excited processes (sputter cleaning, remote plasma processing), photo-excited processes (UV enhanced processing) and particle beam processes. Non-excited processes require little or no external energy input to initiate the cleaning reaction and operate through a chemical (vapor phase HF cleaning for oxide removal) or physical (CO_2 or cryogenic argon "snow" for particle removal) mechanism.

Many in the semiconductor industry believe that dry cleaning processes will supplant wet chemical cleaning for future device processing. Dry processes have the potential to be more easily controlled and inherently cleaner than their wet chemical counterparts[2]. Dry processes can be easily incorporated into a clustered processing environment. Dry processes also have the benefit of reduced chemical consumption and reduced operator exposure to the (usually toxic) chemicals utilized in cleaning processes. Werner Kern[3] is quoted as follows:

> "There is no doubt that silicon wafer cleaning will be based on dry processes or applications to advanced submicron featured ICs (1 Gbit DRAMS) ... The entire cleaning process will be incorporated in an integrated single-wafer system and be part of a process sequence"

Whether this vision will be fulfilled or not, it is fairly obvious that dry processes will have to replace wet chemical cleans to a large extent if the ambitious goals of the semiconductor industry are to be met. Yet there are large gaps in the current menu of dry cleaning processes. These gaps require that research be performed to develop new dry cleaning processes and understand existing processes so that they can be successfully incorporated into semiconductor manufacturing.

The two dry cleaning processes that were utilized in this research are ultra-violet excited chlorine (UV/Cl_2) and vapor phase hydrofluoric acid (HF/Vapor). The prior art regarding these two processes will be reviewed in the next two sections and a few other dry cleaning technologies of interest will also be discussed.

1.4.1 Ultra-violet Excited Chlorine

Silicon etching using chlorine gas coupled with UV exposure has been demonstrated as a potential process to remove trace metal contamination[4,5,6]. In the UV/Cl_2 process photons in the wavelength range of 250-400 nm cause the gas phase dissociation of molecular chlorine to create reactive atomic chlorine. It has also been shown that silicon etching is accelerated in the UV/Cl_2 process through a combination of gas phase and surface photolysis. Various mechanisms for trace metal removal in the UV/Cl_2 system have been proposed. These include; volatilization of metal chlorides[6,7,8], formation of volatile M-Si-Cl complexes[6,7], "lift-off"[6,8], where metals or metal chlorides are carried away with silicon etch products, or the simultaneous desorption of metal chlorides with silicon etch products[7]. Etching of silicon through a chemically grown native oxide has been demonstrated, and a metal removal

mechanism where metals are removed through the native oxide has been proposed[9]. Figure 1.1 schematically illustrates some of the proposed mechanisms for metal removal with UV/Cl_2. Metal removal of two orders of magnitude (in terms of atoms/cm^2) has been reported[6,10]. Figure 1.2 illustrates the results of Butterbaugh *et al.* for metal removal with several dry processes.

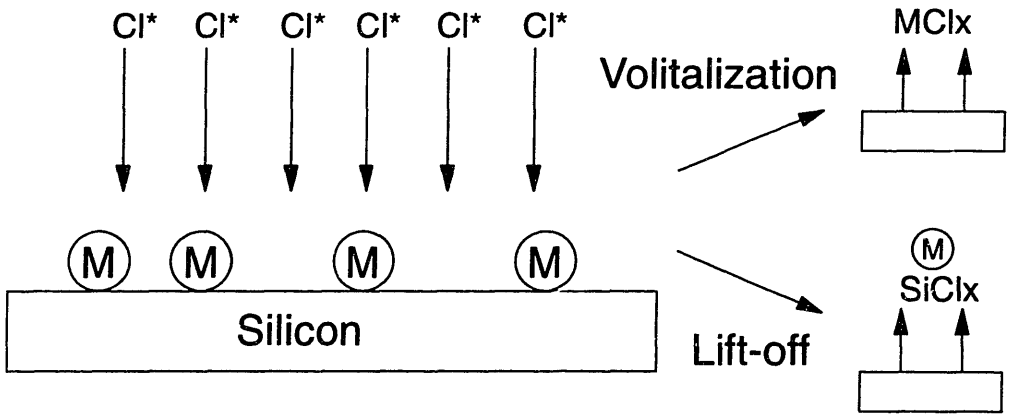

Figure 1.1-Schematic representation of some of the proposed metal removal mechanisms in the UV/Cl_2 process.

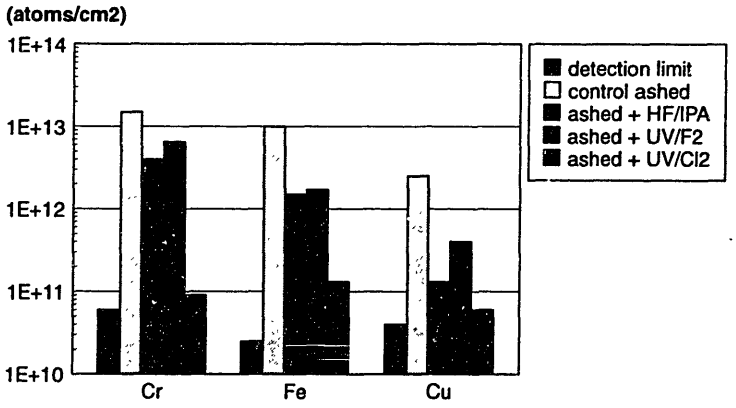

Figure 1.2-Metal removal results with several dry processes. Data from Butterbaugh[10].

The substrate temperature during the process is extremely important, and the efficiency of removal of Fe has been reported to increase by 2 orders of magnitude when the substrate temperature is increased from 140 to 170 °C[5,6]. The electrical properties of gate oxides grown on UV/Cl_2 are improved relative to control samples[6]. Epitaxial films have also been successfully grown on UV/Cl_2 cleaned surfaces[6].

One of the major goals of this thesis has been to investigate and clarify the mechanism by which metals are removed in the UV/Cl_2 process. We have found that the process can be performed in a low pressure/low temperature regime where the mechanism of metal removal is quite different from what has previously been reported in the literature. These results are discussed in Chapter 4. Silicon etching and surface roughening in the UV/Cl_2 process are discussed in Chapter 3. We have also used the UV/Cl_2 process to remove polymeric contamination resulting from oxide etching in fluorocarbon gases in both conventional RIE and high density plasma systems. These results are discussed in Chapters 6 and 7.

1.4.2 Vapor Phase Hydrofluoric Acid (HF/Vapor)

Vapor phase HF has been investigated as a replacement for liquid phase HF oxide stripping[11,12,13,14,15,16,17,18,19]. Ruzyllo *et al.*[19] have demonstrated controlled vapor-phase etching of thermal oxides at rates up to 200 Å/min and BPSG/thermal oxide selectivity in excess of 6000/1 with vapor phase HF/CH_3OH mixtures. Helms and Deal[15] express the need for a condensed layer or film on the oxide surface for etching to take place. They proposed a model based on vapor-liquid equilibrium calculations which describes the parameter space where condensation will occur in the system HF/H_2O. Deal *et al.*[12] have also demonstrated oxide etching in vapor-phase HF/H_2O mixtures. They reported BPSG/thermal oxide

selectivity of 2/1. They noted that thermal oxide etching exhibits an incubation period of 20 seconds while BPSG exhibits a 3 second incubation period under identical process conditions. Wong *et al.*[13] used HCl additions and a hot H_3PO_4 pretreatment to adjust oxide etch rates and the incubation period before etching ensues. They reported superior electrical properties with gate oxides grown on vapor-phase HF/H_2O cleaned surfaces.

The role of water vapor in the vapor-phase HF etching of oxides has been clarified during the time period over which this thesis was performed. Some investigators have postulated that water must be present as a condensed layer on the surface of the oxide for the reaction to proceed[13,15]. Others claim to have obtained etching in an anhydrous system[19]. In our laboratory, A.J. Muscat and Y-P. Han have made great strides toward clarifying the role of water and condensation in the vapor phase HF etching process. Muscat[20] found that in a truly anhydrous process, oxide etching only proceeds on the order of 30 Å and then terminates. Presumably this is due to adsorbed water on the wafer surface (from ambient exposure prior to insertion into the vacuum system) allowing the etching reaction to proceed initially, but when this water is consumed no additional etching takes place. This effect was observed in both HF-water and HF alcohol systems. Muscat *et al.*[20] proposed that etching occurs by a Langmuir-Henshelwood mechanism in a sub-monolayer coverage regime. This hypothesis was supported by showing that the fraction of the saturation vapor pressure for water and HF was the correct metric to use to scale the surface coverage of adsorbed species in a series of response surface experiments. Chamber pump-down times and in situ ellipsometric film thickness measurements also supported the postulation of a sub-monolayer etching regime. Y-P. Han[21] has taken this a step further and has been able to track growth of a monolayer film on an oxide wafer surface by monitoring the ellipsometric parameter ψ as a function of exposure

time. At the saturation vapor pressure, in both water and alcohol systems, the parameter ψ increased slightly initially, corresponding to initial monolayer growth, then leveled off and increased asymptotically when the saturation vapor pressure was reached. We interpret this signal response as the initial sticking of water molecules on the surface (where ψ increases slightly) followed by the growth of a monolayer film (where ψ is relatively constant) and condensation or multilayer film growth (where ψ increases asymptotically as the condensed film is formed). Below the saturation vapor pressure, the parameter ψ never increases significantly above the initial value, even after long times, indicating that multilayer film formation does not take place. These results are illustrated in Figure 1.3. It should be noted that no HF was present in these experiments, but we do not expect that the condensation behavior will be different in an etching regime. What these results tell us is that the HF/Vapor process can be thought of as a truly dry process. It is not necessary to have condensation occurring to etch oxide at a significant and reproducible rate. Surface water can be removed and samples can be transferred to other processing chambers at reasonable rates without concern for water transport via condensation on the wafer surface.

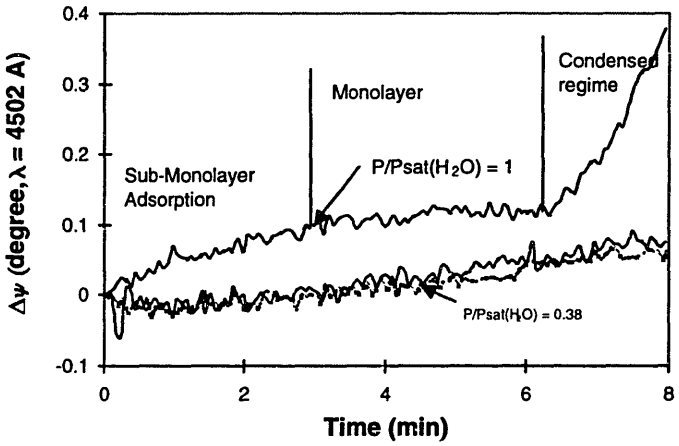

Figure 1.3-Ellipsometric data from condensation experiments illustrating three distinct adsorption regimes at the saturation pressure, and only sub-monolayer adsorption below the saturation pressure. Data from Han[21].

Since impurities whose oxides are thermodynamically favored to form relative to silicon (such as Al, Fe and C) are believed to be incorporated in the oxide grown on a contaminated silicon layer[22], it may be possible to remove these impurities through the growth of a sacrificial oxide layer and its' removal with a vapor-phase HF process. The potential of this process has not been explored in this thesis, but it is an interesting topic for future work.

Vapor phase HF has been used to remove the native oxide due to an oxygen ash (in conventional RIE) or oxygen post-etch treatment (in a high density plasma reactor) in conjunction with oxide etching. These results are discussed in Chapters 6 and 7. We have also performed some preliminary work on combined HF/Vapor-UV/Cl_2 metals removal which is reported in Chapter 4. These results are interesting and indicate that the combination of these processes provides an alternate chemical pathway for removing metals from a wafer surface.

1.4.3 Other Dry Cleaning Processes

UV/ozone has recently been investigated for bulk photoresist removal[23,24,25]. Stripping rates greater than 1 μm/min can be obtained in these systems at process temperatures of 250-350 °C. Addition of N_2O to UV/ozone systems enhances the etch rate but can result in increased levels of trace metal contamination[23].

Remote plasma processes have been demonstrated to be effective in wafer cleaning. Thomas *et al.*[26] have used a remote H_2 plasma to remove carbon contamination. Zhou *et al.*[27] have shown that hydrocarbon contamination can be removed at room temperature using atomic H generated in a remote plasma. Pre-epitaxial hydrogen plasma cleaning has also been shown to allow for the growth of epitaxial films at reduced temperatures[28,29]. Nishino *et al.*[30] used remote plasma generation of reactive species in NH_3/NF_3 and SF_6/H_2O mixtures to

selectively etch native oxides. They stress that the formation of a condensed film on the wafer containing active ionic species is necessary to initiate reaction. In a separate study they demonstrated "surface smoothing" using CF_4/O_2 gas mixtures[31]. Fujimura *et al.*[32] have used an O_2/H_2O plasma for resist stripping.

Chang *et al.*[33] in our group have demonstrated trace metals removal with various thermal beam chemistries, the most successful of which was a combination of SiH_2Cl_2 and F_2. In this process a beam of gas molecules is pyrolized at 1000 °C and is directed at a wafer which is maintained at room temperature. Monolayer quantities of Cu, Ni, Fe, were removed with a 1:4 SiH_2Cl_2+F_2 beam composition in a five second process. Although this chemistry has a strong tendency to deposit a layer of $SiCl_X$ on the sample surface, deposition can be minimized by controlling the gas ratio and process duration. In the thermal beam process, the mechanism appears to involve the formation of a volatile M_YSiCl_X ("M" represents a metal atom) complex. An attempt was made to extrapolate this gas phase chemistry to a UV activated process using a mixture of SiH_2Cl_2 and halogens to remove metals from a wafer surface. These experiments yielded limited success, and are discussed in Chapter 5.

1.5 Reactive Ion Etching

Reactive ion etching is a plasma assisted etching process where the removal of material occurs by a combination of physical and chemical processes. In reactive ion etching, the wafer to be etched is placed on the smaller electrode (cathode) where it is subjected to bombardment by energetic ions as well as chemical attack by reactive radicals produced in the plasma.

Reactive ion etching is widely used in semiconductor processing because of its selectivity and ability to yield an anisotropic etch profile. Selectivity in reactive ion etching is largely controlled by the gas phase chemistry employed. For instance, the selective etching of SiO_2 films over silicon is often performed in CF_4/H_2 gas mixtures where the selectivity arises from the formation of an etch inhibiting polymer film when the silicon surface is reached. This etch inhibiting polymer does not form on the SiO_2 etching surface. Anisotropy in reactive ion etching results from two main factors; (1) the directionality of ion bombardment and (2) the formation of sidewall passivation films that inhibit lateral etch rates. The consequences of the mechanisms that lead to the desired properties of selectivity and anisotropy in RIE are contamination and damage.

Contamination and damage in reactive ion etching have been characterized for a number of RIE processes. Contamination in RIE occurs in the form of polymer surface films which form in the selective etching of SiO_2 over silicon, polymer or oxide sidewall films which contribute to etch anisotropy in silicon trench etching and trace metal contamination, either from metal surfaces in the chamber or from contaminants present in the photoresist. Damage from RIE is primarily in the form of lattice damage and impurity incorporation due to ion bombardment.

Most of the literature relating to dry etching induced damage and contamination relates to conventional diode configurations. The damage induced in an inductively coupled system (or any other high efficiency plasma source) should be qualitatively similar. Therefore a review of the literature relating to contamination in conventional systems will enhance the understanding of contamination in high density systems.

1.5.1 Contamination from Selective RIE of SiO_2 Over Silicon

In the etching of SiO_2 over silicon with chloro-fluorocarbon/H_2 gas mixtures, much work has been focused on compositional analysis of the fluorocarbon film which forms on the silicon surface upon clearing of the oxide film. A schematic diagram of the contamination and damage observed after a typical process is shown in Figure 1.4. Coburn and Winters[34] originally

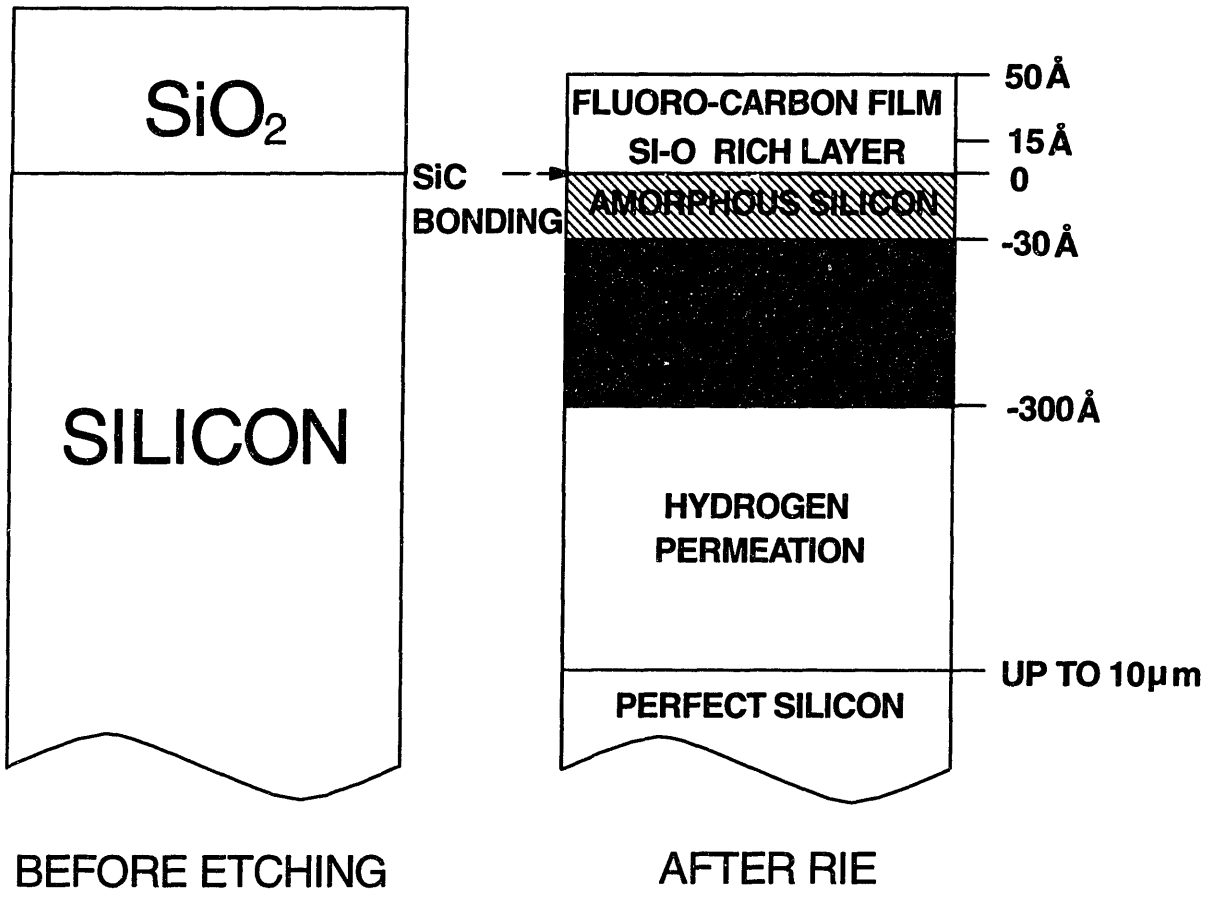

Figure 1.4-Schematic diagram of the contamination and damage after a typical RIE process. After Oehrlein[35].

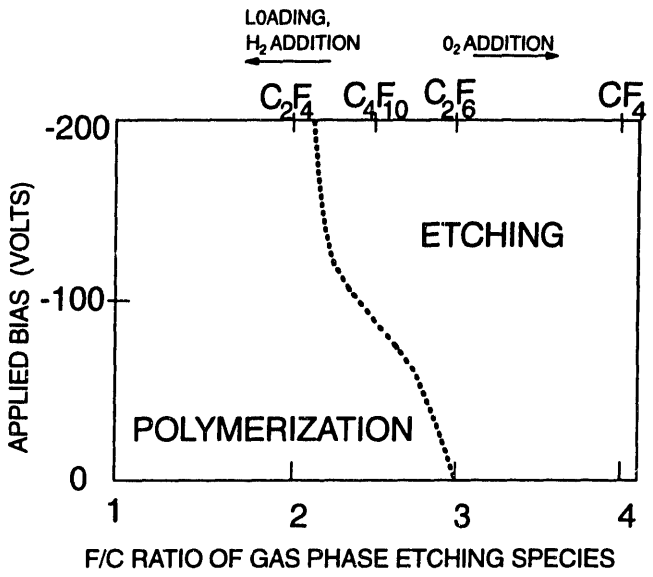

Figure 1.5-Qualitative representation of the etching and deposition regimes in oxide etching and the effect of gas additions. After Coburn and Winters[34].

hypothesized that the composition of the polymer film formed in this RIE chemistry would be "teflon-like". In their investigation, the parameter space in which etching and deposition would take place (Figure 1.5) was defined based on the fluorine to carbon ratio of gas phase etching species. This plot provides a qualitative description of the formation of polymer films on silicon surfaces during RIE and the effect of gas additions. Oehrlein *et al.*[35] have characterized the surface contamination layer after RIE of SiO_2 over silicon in CF_4/40%H_2 gas mixtures. In this system the etch rate of SiO_2 ≈400 Å/min while the etch rate of silicon was ≈ 15-20 Å/min. They found that a carbon and fluorine containing polymer was present on the silicon surface after overetch, and that the thickness of the layer was limited to less than 50 Å. After one minute of overetching the nominal composition of the polymer (determined by XPS) was 15 atomic% F, 14.8% O, 63.4% C and 6.8% Si. They reported that the thickness of the polymer layer decreased slightly after about three minutes and reached a steady state thickness after about ten minutes of overetching, at which time the nominal composition was

35.4% F, 11.3% O, 40.8% C and 12.5% Si. They also reported the presence of an O rich transition layer located at the film/silicon interface. They hypothesized that the O rich layer formed on exposure to air. In related work, Coyle and Oehrlein[36] identified a Si-C layer located at the film/silicon interface. The formation of the carbide layer was independent of H_2 concentration in the gas mixture from 0-40% H_2. Thomas *et al.*[37] studied the formation of RIE residue in a CF_4/50% H_2 gas mixture. They also noted the presence of a "teflon-like" polymer and detected CF_2, CHF and CH/C-C groups by XPS. A SiO_2 layer ≈8-10 Å thick was detected at the film/silicon interface. The carbide film detected by Oehrlein was not detected, and this was attributed partially to the gas composition. A layer of graphitic carbon was detected on the surface of the polymer film and the thickness of this layer was "dependent on the plasma conditions". Oehrlein *et al.*[38] as well as Potter *et al.*[39] have reported the dependence of the steady-state fluorocarbon film thickness in CF_4/H_2 gas mixtures on the percentage of H_2 in the gas mixture. Both show the thickness of the polymer film increasing with increasing H_2 concentration. Both also report that the silicon etch rate drops to ≈0 at a polymer film thickness of ≈50 Å, corresponding to ≈40% H_2 in the gas mixture. Figure 1.6 illustrates these results. Potter *et al.* report that the polymer film thickness reaches a steady-state thickness after about five minutes for low H_2 concentrations but above about 40% H_2, "catastrophic" deposition of polymer occurs with the polymer thickness increasing linearly with time. Potter *et al.* also report that etching in pure CHF_3 yields a steady state film thickness. Oehrlein *et al.* conclude that the silicon etching reaction stops because the fluorocarbon film limits the transport of fluorine to the silicon surface. Oehrlein *et al.*[40] have studied the surface films formed in a $CClF_3/H_2$ gas mixture and the results are "qualitatively similar" to those obtained in CF_4, although the polymer does contain Cl at a ratio of ≈3F/1Cl.

In a related study, Mu *et al.*[41] report detecting ≈25 atomic% H in the polymer layer deposited in a $CClF_3/H_2$ gas mixture.

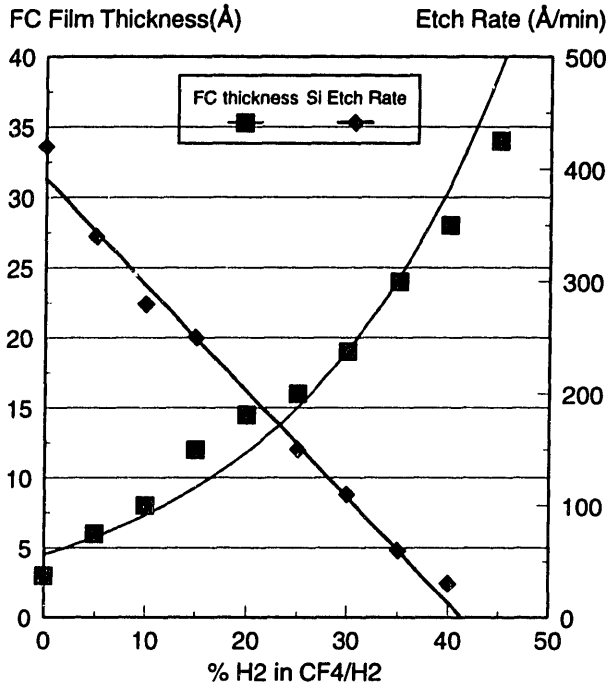

Figure 1.6-Relationship between fluorocarbon film thickness, silicon etch rate and % H_2 in CF_4 etching of SiO_2. Data from Oehrlein[38] and Potter[39].

1.5.2 Trace Metal Contamination in RIE

Trace metal contamination in RIE has been reported to occur from two primary sources, metal atoms sputtered from chamber surfaces or other metal objects in the RIE chamber[42] and metal contaminants in the photoresist which are driven into the silicon during plasma exposure[43]. Anzai *et al.*[44] report Fe contamination on the order of 10^{12} atoms/cm^2 and Cu and Ni contamination on the order of 10^{11} atoms/cm^2 measured with TXRF resulting from dry etching processes. Figure 1.7 illustrates Anzai's reported levels of trace metallic contamination for several dry processes. Gambino *et al.*[45] report Fe contamination levels of 4 x 10^{10} atoms/cm^2 and Ni levels of $8x10^{11}$ atoms/cm^2 detected with SIMS after CF_4 RIE. High leakage currents were reported for shallow n^+-p junctions fabricated on CF_4 reactive ion

etched surfaces. The authors attributed the presence of stacking faults which were nucleated and made electrically active by the metallic contaminants as the cause of the high leakage currents.

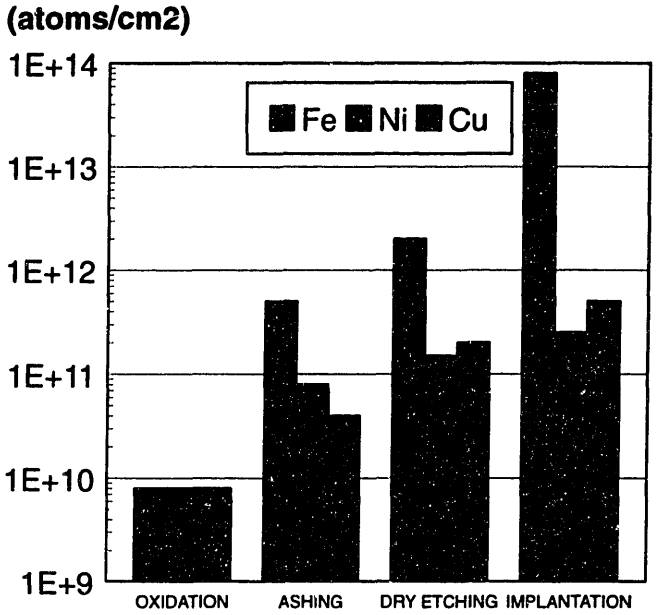

Figure 1.7-Trace metal contamination from several dry processes. Data from Anzai[44].

1.5.3 Contamination from Resist Stripping

Photoresist stripping, although not part of the dry etching process itself, is an essential process step and is usually performed immediately after a dry etching process. Fujimura and Yano[43] report that heavy metals contained in photoresist at levels < 0.5 ppm can cause contamination during resist stripping. In their experiments the major contaminant observed was Fe. Joubert *et al.*[46,47] used deep level transient spectroscopy (DLTS) to identify metallic contamination from plasma stripping. They report that the resist is a source of Fe and C contamination. They conclude that metallic impurities are implanted due to the impact of energetic ions during the ashing process and then thermally diffuse into the substrate. Olness

et al.[23] have reported that ozone ashing of photoresist can result in metallic contamination. They surmise that most of the contamination came from the chamber walls.

Hashimoto *et al.*[48] have reported that the organic contamination which remains after a H_2O_2/H_2SO_4 wet resist strip causes a deterioration of gate oxide performance. A thorough literature search has not revealed any reported studies on the combined effects of RIE plasma exposure and resist stripping on wafer contamination. RIE exposure is known to modify the resist, but the effect on subsequent resist removal efficiency and related contamination problems due to resist residues have not been reported. Resist residues after ion implantation processes have been reported in the literature[24,49,50]. Ion implantation processes are known to harden photoresist and leave a surface film which can be difficult to remove. While this process is somewhat more severe than a RIE process, the types of contamination observed should be qualitatively similar, and similar contamination would be expected (although to a lesser extent) in a RIE process. Modifications to the photoresist have not been well characterized in high density systems.

1.5.4 Substrate Damage from RIE

Damage resulting from RIE processes has been extensively characterized and the results of the investigations are qualitatively similar[51,52,53,54,55]. The type of damage observed as a result of CF_4/H_2 etching of SiO_2 over silicon is illustrated in Figure 1.4. The first 30 Å of the silicon surface is heavily damaged and probably in an amorphous state. The silicon substrate is lightly damaged to a depth of ≈30 nm. This region contains point defects and incorporated impurity atoms such as hydrogen, carbon and fluorine. Simko *et al.*[56] report that hydrogen can penetrate the surface to a depth of 10 μm. Lee *et al.*[57] conclude that at least 50

nm of the silicon substrate must be removed or recovered to fabricate a "good quality" device. The extent of subsurface damage is dependent on the overetch time[35,53,57]. Since silicon is not etched significantly due to the formation of the inhibiting polymer film, damage due to ion bombardment tends to accumulate with increasing overetch times. Damage in silicon trench etching is not as severe since the damaged silicon layer is being continuously removed during the etching process.

1.5.5 Surface Cleaning and Damage Removal After RIE

Various cleaning procedures have been attempted to remove the damage and contamination resulting from RIE processes. Oehrlein *et al.*[58] report the use of a low temperature (400 °C) O_2 annealing process that removed most of the polymer film after CH_4/H_2 RIE. The cleaning process was reported to yield "greatly improved electrical characteristics" although it resulted in the presence of a thin (≈ 30 Å) oxide layer and failed to remove a thin layer of the polymer film. Oehrlein *et al.*[59] investigated the use of O_2 plasma cleaning coupled with an HF dip for post CHF_3/CO_2 RIE cleaning. This cleaning process was ineffective in removing the polymer film and the damaged silicon layer. The efficiency of the clean was shown to depend greatly on the pressure in the primary RIE environment. In $CClF_3/H_2$ RIE, O_2 RIE or O_2 ashing coupled with an HF dip[40,41] has been shown to improve contact behavior. Simko *et al.*[56] report that a hydrogen discharge can reduce a 50 Å fluorocarbon film deposited during CF_4/H_2 RIE to a 10 Å carbon film that contains little fluorine, without the side-effect of a residual oxide film. They note that the cleanliness of the process is limited by previously deposited RIE residues in the chamber. Cerva *et al.*[53] report that a NF_3/Ar plasma resulted in the complete removal of the polymer film and lattice damage

resulting from CHF_3/O_2 RIE, although this process resulted in surface roughening on the order of 5 nm. Sidewall films present after trench etching have been removed in BHF solutions[60,61] and phosphoric acid solutions[62].

Wet chemical methods have been reported for removing trace metal impurities from post-RIE surfaces. Hosoya *et al.*[42] report that chromium could be removed by a combination of a Piranha clean followed by an RCA clean, iron could be removed by the same clean coupled with the removal of 200 Å of silicon in a wet etch and nickel was not removed despite the application of multiple cleaning procedures. Gambino *et al.*[45] have reported that a plasma oxidation followed by an HF dip and an RCA clean can be effective in removing trace metals if enough contaminated silicon is consumed in the oxidation process.

While some significant research has been performed relating to post-RIE cleaning, none of the methods developed to date are totally satisfactory. Most of the methods involve one or more wet cleaning steps and are not compatible with integrated processing. In Chapter 6, our integrated dry cleaning process to remove both the polymer and oxide contamination from a RIE oxide etch coupled with an O_2 ash is discussed. Since an O_2 ashing process for photoresist removal is generally coupled with an oxide etch, we considered realistic to study this sequence. In the integrated dry clean, we use UV/Cl_2 to remove polymeric contamination and HF/Vapor to remove oxide residues. The cleaning process is monitored with in situ XPS, and all of the cleaning steps (including the analysis) were performed sequentially under vacuum. In this way we can avoid cross contamination due to ambient exposure, and obtained a more accurate picture of the evolution of the wafer surface during the cleaning sequence. We also compare our dry sequence to a typical wet sequence, consisting of a "Piranha" etch (H_2SO_4/H_2O_2) followed by a wet HF dip.

1.6 High Density Plasma Etching

In conventional RIE, the process is carried out in a diode configuration where the power is capacitively coupled to the plasma. In this configuration, the ion bombardment energy and ion flux to the wafer surface cannot be varied independently, and their magnitudes are determined by parameters such as the process pressure and power input to the plasma. As critical device dimensions decrease, the inherent limitations of conventional RIE processing make it less able to yield the desired anisotropic profile. High etching rates and anisotropy in RIE are accomplished by increasing the energy and directionality of the ions incident on the wafer surface. Unfortunately this results in more physical or "sputter-like" etching and decreases the chemical nature of the etch, resulting in a loss of selectivity (which is generally dependent on the chemistry employed) and a loss of critical dimension control (due to etching of the photoresist)[63]. Because of these problems it is difficult to fabricate high aspect ratio sub-micron features with conventional RIE.

Recently, alternative high density plasma sources have been investigated for applications to plasma processing[63,64]. These include electron cyclotron resonance (ECR), helicon, and inductively coupled sources. These sources have the advantage of higher plasma density than conventional RIE, creating electron densities that are typically two orders of magnitude higher than diode systems. In addition, since the power is not capacitively coupled into the plasma, sheath voltages are much lower than in an analogous diode system. Because of this, the substrate can be independently biased through low power rf capacitive coupling, yielding more independent control of the plasma density and ion flux to the surface (through control of the source power) and the ion energy incident on the sample (through control of the substrate bias voltage).

1.6.1 Contamination and Damage in High Density Plasma Etching

Oehrlein *et al.*[65,66] have investigated fluorocarbon film deposition and etching characteristics in ECR-RIE of SiO_2 over silicon in CF_4 and CHF_3 gas. This system is characterized by a threshold voltage, below which fluorocarbon film deposition occurs on all surfaces. They report that three regimes occur in this process: 1) at low rf substrate bias fluorocarbon film deposition occurs on all surfaces and SiO_2 etching does not occur, 2) at rf voltages greater than the threshold voltage, fluorocarbon suppression occurs and oxide etching commences although the oxide is still covered with a fluorocarbon film, 3) at higher rf voltages oxide etching occurs and scales linearly with the ion flux to the substrate surface. Regime 3 represents the parameter space where selective etching of SiO_2 to Si occurs. Fluorocarbon film thicknesses of ≈5.5 nm in CHF_3 and ≈2.5 nm in CF_4 are reported at an rf bias of 100 V.

Yapsir *et al.*[67] have reported that the level of damage and electrical degradation of silicon surfaces is lower in an ECR plasma than a conventional RIE plasma during silicon etching with CF_4. They attribute this to the low dc self-bias potential across the plasma sheath. They report that the application of an rf bias to the substrate results in reduced damage to the surface because of an increase in the etch rate. This is most likely due to higher ion bombardment energies resulting in a reduction of the fluorocarbon film thickness on the silicon surface and increasing the etch rate (fluorocarbon films are not discussed in this article). High concentrations of Fe ($10^{13}/cm^2$), C ($10^{12}/cm^2$), Ni ($10^{12}cm^2$), and Cu ($10^{12}/cm^2$) were observed to occur from this process. This metallic contamination was attributed to reaction of the high density plasma with the chamber walls.

Oehrlein[68] has reported that the depth of the damaged layer is much lower in low energy ion etching of silicon in CF_4 and SF_6. He reports that the fluorinated silicon layer and the associated lattice damage due to ion bombardment penetrates on the order of 1 nm in low energy etching, while in high energy etching the depth of this damaged layer is≈40 nm.

It is expected that the passivating polymer films which form on silicon surfaces in high density plasma etching will be similar in composition to those formed in conventional RIE. This assumption is supported by the initial work of Oehrlein. It is also expected that the damage resulting from high density plasma etching will be less than that observed in conventional RIE this assumption is supported by the initial work of Yapsir and Oehrlein. Trace metal contamination will remain a problem due to the high density of reactive species in the plasma.

1.7 X-ray Photoelectron Spectroscopy (XPS)

Since XPS (or ESCA) is the primary analytical tool utilized in this thesis, it is pertinent to include some background on the technique and specifically the aspects of spectrum analysis which apply to this work. XPS has its' origins in studies of the photoelectric effect, where X-rays were used to excite a substrate and cause the emission of photoelectrons[69]. Kai Sieghban and his group in Uppsala where the first to observe the chemical shift and in effect developed the field of modern electron spectroscopy over the period 1950-1970. This group coined the term Electron Spectroscopy for Chemical Analysis (ESCA) to highlight the fact that both photoelectron peaks and Auger transitions appear in the 'XPS' spectrum, and published a seminal book on the subject[70].

The defining equation of XPS can be represented in simplified form as:

$$E_{KE} = h\upsilon - E_{BE} \quad (1)$$

where hν is the energy of the incident X-ray (1254 eV in the case of the Mg K_α radiation used in these experiments) and E_K and E_{BE} are the kinetic and binding energies of the emitted photoelectron. To a first approximation, the XPS process results in the ejection of an electron of a characteristic kinetic energy due to the absorption of an X-ray of fixed energy hν. The energy lost is the binding energy, or the energy with which the emitted electron was bound to the nucleus. Electron spectrometers measure the kinetic energy of the emitted electrons, but XPS spectra are typically represented in terms of the binding energy. The photoelectron spectrum of any particular element or compound yields a "fingerprint", since the characteristic photoelectron energies emitted by substances are particular to their electronic structure.

Various aspects of the XPS spectrum can be used for chemical analysis. In this work, we are primarily interested in core-level chemical shifts, satellite structures, and signal attenuation due to the presence of an overlayer. Although the absolute binding energy of a given core electron level in a given element is fixed, small shifts in the electron energy are observed depending on differences in the local electronic environment. This phenomena is dubbed the "chemical shift" in an analogy to the chemical shift observed in NMR spectroscopy. For instance, silicon metal exhibits a binding energy of 99.75 eV, while silicon dioxide typically exhibits a binding energy of 103.6 eV[71]. This binding energy difference is due to the difference in the electronic environment of the electrons bound to silicon in the respective substances. The use of chemical shifts for chemical identification is well established. The use of chemical shifts in this work is prevalent in the identification of silicon, carbon, oxygen, halogen and metallic bonding states.

Satellite structures are also useful in the identification of chemical compounds. In this work we are primarily interested in "shake-up" satellites. The "shake-up" process involves the perturbation of the valence electrons upon the ejection of a core electron through photoemission. The subsequent reorganization of the valence electrons can involve excitation to a higher unfilled orbital. The energy required for this process is then not available to the primary photoelectron, and results in a discrete "satellite structure" on the low kinetic energy (high binding energy) side of the main peak. These transitions are not allowed in all compounds, but are particularly prevalent in the 2p spectra of divalent transition metals. They are extremely useful for identification and in fact one can discern, for instance, NiO from $NiCl_2$ from NiF_2 by the satellite structure alone (see Chapter 4).

The attenuation of the substrate due to the presence of overlayers is another aspect of XPS is that is exploited extensively in this work. This topic is handled specifically in Section 2.1.4 dealing with the calibration of the sputter source. This topic is also covered by Briggs and Riviére[72] and Dilks[73]. In this work, the substrate-overlayer model presented in Chapter 2 is used to calculate the thickness of contamination films (polymer and oxides) based on the attenuation of the substrate silicon peak intensity. A related topic deals with the sampling depth of XPS. Generally it is accepted that 95% of the photoelectron signal is derived from a depth of 3 λ (λ = the mean free path of a photoelectron) within the substrate. This depth is represented by:

$$d = 3\lambda \sin\theta \qquad (2)$$

where d is the sampled depth and θ is the angle between the sample and the spectrometer. Obviously the sampled depth is dependent on the angle θ. This angle resolved capability is exploited in Chapter 7.

A word should be said about binding energy referencing. A problem in the analysis of XPS spectra is the phenomenon of charging. Especially on insulating surfaces, charging can induce large shifts in the observed binding energies due to the build-up of positive charge on the sample surface. Fortunately, in this system we have a built-in reference peak. The silicon substrate peak, the binding energy of which is known, is clearly distinguishable in all of the XPS spectra presented in this work. Because of this, binding energy shifts due to charging can be removed with a high degree of confidence.

1.8 Goals of this Thesis

The specific goals of this thesis are; 1) to investigate trace metals removal with ultraviolet excited chlorine and to clarify the mechanism by which metals are removed in the UV/Cl_2 process, and 2) to develop and evaluate a gas phase cleaning procedure to remove the contamination resulting from an oxide etching process.

With regard to the first point, the mechanism of UV/Cl_2 metals removal is discussed in detail in Chapter 4. Preliminary studies of metals removal in combined UV/Cl_2-HF/Vapor and in ultraviolet excited dichlorosilane are also discussed. In order to evaluate the feasibility of using the UV/Cl_2 process in manufacturing, the etching of silicon in UV/Cl_2 was also studied and these results are described in Chapter 3.

With regard to the second point, a gas phase cleaning process using UV/Cl_2 and HF/Vapor in combination to remove both the polymer and oxide contamination resulting from RIE of blanket oxide films is discussed in Chapter 6. This same process sequence was applied to the etching of patterned wafers in an Inductively Coupled Plasma (ICP) reactor. This work is described in Chapter 7.

1.9 References

[1] W. Kern and D.A. Puotinen, *RCA Review*, vol. 31, 187 (1970).

[2] R.A. Bowling, S.C. O'Brien, L.M.Lowenstein, M.H. Bennett, and B.K. Bohanon, *Solid State Technology*, vol. 37, no. 1, 61-65 (1994).

[3] W. Kern, *Handbook of Semiconductor Wafer Cleaning Technology: Science, Technology, and Applications*, W. Kern, ed., 595-610, Park Ridge N.J.: Noyes Publications (1993).

[4] R. Sugino, Y. Nara, T. Yamakazi, S. Watanabe, and T. Ito, from *Extended Abstracts of the 19th Conference on Solid State Devices and Materials*, 207-210 (1987).

[5] S. Watanabe, R. Sugino, T. Yamakazi, Y. Nara, and T. Ito, *Jpn. J. Appl. Phys.*, vol. 28, no. 10, 2167-2171 (1989).

[6] Y. Sato, R. Sugino, and T. Ito, *Fujitsu Sci. Tech. J.*, vol. 24, no. 4, 317-328 (1991).

[7] B.E. Deal and C.R. Helms, in *Handbook of Semiconductor Wafer Cleaning Technology: Science, Technology, and Applications*, W. Kern, ed., p. 316, Park Ridge N.J.: Noyes Publications (1993).

[8] J. Ruzyllo, in *Handbook of Semiconductor Wafer Cleaning Technology: Science, Technology, and Applications*, W. Kern, ed., p. 208, Park Ridge N.J.: Noyes Publications (1993).

[9] R. Sugino, Y. Nara, H. Horie, T. Ito, J. Appl. Phys., 76 (9), 5498-5502 (1994).

[10] J.W. Butterbaugh, D.C. Gray, C.Fred Hiatt, H.H. Sawin, and A.S. Lawing, Submitted to *Second International Symposium on Ultra Clean Processing of Silicon Surfaces*, (1994).

[11] R.L. Bersin and R.F. Reichelderfer, *Solid State Technology*, vol. 20, no. 5, 78-80 (1977).

[12] B.E. Deal, M.A. McNeilley, D.B. Kao, and J.M. deLarios, *Proceedings of the First International Symposium on Cleaning Technology in Semiconductor Device Manufacturing*, 1-8 (1989).

[13] M. Wong, M.M. Moslehi, and D.W. Reed, *J. Electrochem. Soc.*, vol. 138, no. 6, 1799-1802 (1991).

[14] B.J. Jurcik, Jr., J.R. Brock, and Isaac Trachtenberg, *J. Electrochem Soc.*, vol. 138, no. 7, 2141-2145 (1991).

[15] C.R. Helms and B.E. Deal, *J. Vac. Sci. Technol. A*, vol. 10, no. 4, 806- 811 (1992).

[16] A.E.T. Kuiper and E.G.C. Lathouwers, *J. Electrochem. Soc.*, vol 139., no. 9, 2594-2599 (1992).

[17] M. Wong, M.M. Moslehi, and R.A. Bowling, *J. Electrochem. Soc.*, vol. 140, no. 1, 205-208 (1993).

[18] M. Wong and R.A. Bowling, *J. Electrochem. Soc.*, vol. 140, no. 2, 567-570 (1993).

[19] J. Ruzyllo, K. Torek, C. Daffron, R. Grant, and R. Novak, *J. Electrochem. Soc.*, vol.140, no.4, L64-L66 (1993).

[20] A.J. Muscat, A.S. Lawing, H.H. Sawin, J.W. Butterbaugh, D. Syverson and C.F. Hiatt, Proceedings of the Fourth International Symposium on Cleaning Technology in Semiconductor Device Manufacturing, PV 95-20, J. Ruzyllo and R.E. Novak eds., p. 371, The Electrochemical Society, Pennington, N.J. (1996).

[21] Y-P. Han, H.H. Sawin, Unpublished Data.

[22] T. Ohmi, T. Imaoka, I. Sugiyama, and T. Kezuka, *J. Electrochem. Soc.*, vol. 139, no. 11, 3317-3335 (1992).

[23] G. Olness, S. Bernasek, M. Gordon, B. Chung, and C. Draper, *Proceedings of the Symposium on Surface Chemical Cleaning and Passivation for Semiconductor Processing*, G.S. Higashi, E.A. Irene, and T. Ohmi, eds., 261-266 (1993).

[24] D.L. Flamm, *Solid State Technology*, vol. 35, no. 9, 43-48 (1992).

[25] C.K. Huynh, J.C. Mitchener, *J. Vac. Sci. Technol. B*, vol. 9, no. 2, 353-356 (1991).

[26] R.E. Thomas, M.J. Martini, R.A. Rudder, D.P. Malta, S.V. Hattangady, and R.J. Markunas, *J. Vac. Sci. Technol. A*, vol. 10, no. 4, 817-822 (1992).

[27] Z.-H. Zhou, E.S. Aydil, R.A. Gottscho, Y.J. Chabal, and R. Reif, *J. Electrochem. Soc.*, vol. 140, no. 11, 3316-3321 (1993).

[28] J. Ramm, E. Beck, I. Eisele, W. Hansch, B.-U. Klepser, and H. Senn, *Proceedings of the Symposium on Surface Chemical Cleaning and Passivation for Semiconductor Processing*, G.S. Higashi, E.A. Irene, and T. Ohmi, eds., 91-96 (1993).

[29] T. Hsu, B. Anthony, R. Qian, J. Irby, S. Banerjee, A. Tasch, S. Lin, H. Marcus, and C. Magee, *Journal of Electronic Materials*, vol. 20, no. 3, 279-287 (1991).

[30] H. Nishino, N. Hayasaka, and H, Okano, *J. Appl. Phys.*, vol. 74, no. 2, 1345-1348 (1993).

[31] H. Nishino, N. Hayasaka, K. Horioka, J. Shiozawa, S. Nadahara, N. Shooda, Y. Akama, A. Sakai, and H. Okano, *J. Appl. Phys.*, vol. 74, no. 2, 1349-1353 (1993).

[32] S. Fujimura, K. Shinagawa, M.T. Suzuki, and M. Nakamura, *J. Vac. Sci. Technol. B*, vol. 9, no. 2, 357-361 (1991).

[33] J.T-P. Chang, Z. Zhang, H. Xu, H.H. Sawin, and J.W. Butterbaugh, Submitted to J. Vac. Sci. Technol.

[34] J.W. Coburn and H.F. Winters, *J. Vac. Sci. Technol.*, vol. 16, no. 2, 391-403 (1979).

[35] G.S. Oehrlein, R.M. Tromp, J.C. Tsang, Y.H. Lee, and E.J. Petrillo, *J. Electrochem. Soc.*, vol. 132, no.6, 1441-1447 (1985).

[36] G.J. Coyle and G.S. Oehrlein, *Appl. Phys. Lett.*, vol. 47, no. 6, 604-606 (1985).

[37] J.H. Thomas, X.C. Mu, and S.J. Fonash, *J. Electrochem. Soc.*, vol. 134, no. 12, 3122-3125 (1987).

[38] G.S. Oehrlein, S.W. Robey, J.L. Lindstrom, K.K. Chan, M.A. Jaso, and G.J. Scilla, *J. Electrochem. Soc.*, vol. 136, no. 7, 2050-2057 (1989).

[39] G.E. Potter, G.H. Morrison, P.K. Charvat, and A.L. Ruoff, *J. Vac. Sci. Technol. B*, vol. 10, no. 6, 2398-2406 (1992).

[40] G.S. Oehrlein, C.M. Ransom, S.N. Chakravarti, and Y.H. Lee, *Appl. Phys. Lett.*,vol. 46, no. 7, 686-688 (1985).

[41] X.C. Mu, S.J. Fonash, G.S. Oehrlein, S.N. Chakravati, C. Parks, and J. Keller, *J. Appl. Phys.*, vol. 59, no. 8, 2958-2967 (1986).

[42] T. Hosoya, Y. Ozaki, and Hirata, *J. Electrochem. Soc.*, vol. 132, no. 10, 2436-2439 (1985).

[43] S. Fujimura and H. Yano, *J. Electrochem. Soc.*, vol. 135, no. 5, 1195-1201 (1988).

[44] N. Anzai, Y. Kureishi, S. Shimizu, and T. Nitta, in *Proceedings of 8th Workshop on ULSI Ultra Clean Technology*, 75 (1989).

[45] J.P. Gambino, M.D. Monkowski, J.F. Shepard, and C.C. Parks, *J. Electrochem. Soc.*, vol. 137, no. 3, 976-979 (1990).

[46] O. Joubert, D. Mathiot, and J. Pelletier, *Appl. Phys. Lett.*, vol. 54, no. 22, 2241-2243 (1989).

[47] O. Joubert, D. Mathiot, and J. Pelletier, *Mat. Sci. Eng. B*, vol. B4, no. 1-4, 467-470 (1989).

[48] K. Hashimoto, K. Egashira, M. Suzuki, D. Matsunaga, *Extended Abstracts of the 1991 International Conference on Solid State Devices and Materials*, 243-245 (1991).

[49] K. Hiroshi, H. Shimada, S. Shimomura, M. Onodera, and T. Ohmi, *J. Electrochem. Soc.*, vol. 141, no. 1, 192-205 (1994).

[50] S. Yegnasubramanian, C.W. Draper, and C.W. Pearce, *Proceedings of the Symposium on Materials Reliability in Microelectronics II*, C.V. Thompson and J.R. Lloyd, eds., 295-300 (1992).

[51] S.J. Fonash, *Solid State Tech.*, vol. 28, no. 4, 201-205 (1985).

[52] G.S. Oehrlein, J.G. Clabes,G.J. Coyle, J.C. Tsang, and Y.H. Lee, *J. Vac. Sci. Technol.*, vol. 4, no. 3, 750-751 (1986).

[53] H. Cerva, E.-G. Mohr, and H. Oppolzer, *J. Vac. Sci. Technol. B*, vol. 5, no. 2, 590-593 (1987).

[54] Ch. Cardinaud, G. Turban, B. Grolleau, J.P. Grandchamp, C. Lejeune, P. Scheiblin, and E. Collard, *Appl. Surf. Sci.*, vol. 36, 322-331 (1989).

[55] S.J. Yun, S.-J. Park, M.-C. Paek, and J.Y. Lee, *J. Electrochem. Soc.*, vol. 137, no. 8, 2634-2639 (1990).

[56] J.P. Simko, G.S. Oehrlein, and T.M. Mayer, *J. Electrochem. Soc.*, vol. 138, no. 1, 277-284 (1991).

[57] Y.H. Lee, G.S. Oehrlein, and C. Ransom, *Radiation Effects and Defects in Solids*, vol. 111&112, 221-232 (1989).

[58] G.S. Oehrlein, J.G. Clabes, and P. Spirito, *J. Electrochem Soc.*, vol. 133, no. 5, 1002-1008 (1986).

[59] G.S. Oehrlein, G.J. Scilla, and S.-J. Jeng, *Appl. Phys. Lett.*, vol. 52, no. 11, 907-909 (1988).

[60] M. Sato and Y. Arita, *J. Electrochem. Soc.*, vol. 134, no. 11, 2856-2862 (1987).

[61] D. Allred, S. Jackel, C. Mazure, H.J. Barth, H. Cerva, and W. Hosler, *J. Vac. Sci. Technol. B*, vol. 7, no. 3, 505-511 (1989).

[62] K. Hirobe, K. Kawamura, and K. Nojiri, *J. Vac. Sci. Technol. B*, vol. 5, no. 2, 594-600 (1987).

[53] H.H. Sawin, *Microelectronic Engineering*, vol. 23, 15-21 (1994).

[64] M. Lieberman and R. Gottscho, "Design of High Density Plasma Sources for Materials Processing", *Phys. of Thin Films: Advances in Res. and Dev.*, vol. 17, J. Vossen ed., Academic Press, Orlando, Florida (1993).

[65] G.S. Oehrlein, Y. Zhang, D. Vender, and M. Haverlag, *J.Vac. Sci. Technol. A*, vol. 12, no. 2, 323-332 (1994).

[66] G.S. Oehrlein, Y. Zhang, D. Vender, and O. Joubert, *J. Vac. Sci. Technol. A*, vol. 12, no 2, 333-344 (1994).

[67] A.S. Yapsir, G. Fortuno-Wiltshire, J.P. Gambino, R.H. Kastl, and C.C. Parks, *J. Vac. Sci. Technol. A*, vol. 8, no. 3, 2939-2944 (1990).

[68] G.S. Oehrlein, *J. Vac. Sci. Technol. A*, vol. 11, no. 1, 34-46 (1993).

[69] M.P. Seah and D. Briggs, Practical Surface Analysis, D. Briggs and M.P. Seah, eds., 2nd ed, p.7, John Wiley & Sons, New York (1990).

[70] K. Seighban, et al, ESCA: Atomic, Molecular and Solid State Structure Studied by Means of Electron Spectroscopy, Almqvist and Wiksells, Uppsala (1967).

[71] C.D. Wagner, Practical Surface Analysis, D. Briggs and M.P. Seah, eds., 2nd ed, p.602, John Wiley & Sons, New York (1990).

[72] D. Briggs and J.C. Riviére, ibid p. 134-136.

[73] A. Dilks, Electron Spectroscopy: Theory, Techniques and Applications, Vol.4, C.R. Brundle and A.D. Baker, p. 301-305, Academic Press, London (1981).

Chapter 2

Experimental

2.1 First Experimental Set-up

The apparatus used in these experiments consisted of two "clustered" systems, in which multiple vacuum chambers were connected under vacuum via a system of transfer rods. The advantage of this type of system is that it allows one to perform multiple, sequential processes and the associated surface analysis without exposing the sample to ambient, thus avoiding extraneous effects due to exposure of the sample to air or other contaminating conditions.

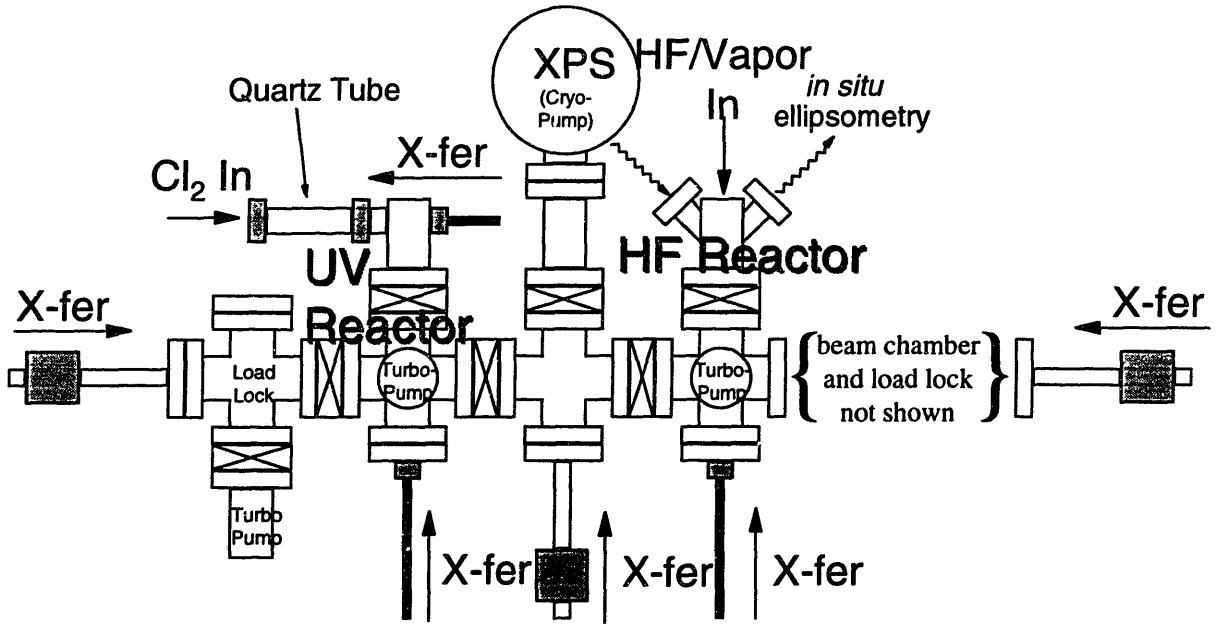

Figure 2.1-Schematic diagram of first experimental apparatus.

The first experimental set-up, fondly referred to as the "old surface table", is schematically illustrated in Figure 2.1. This apparatus consisted of two load lock chambers,

an analytical chamber which also had metal sputtering capability (section 2.1.3), A UV/Cl_2 reactor (section 2.1.1), an HF/Vapor reactor (section 2.1.2) and a molecular beam chamber which was not utilized in this work and will not be discussed in this thesis. This apparatus was dismantled in August 1996 to make room for the apparatus which is described in section 2.2.

A typical experimental sequence in the above apparatus would be as follows: 1) a sample is introduced into the load lock chamber, 2) the load lock chamber is pumped to vacuum, 3) the sample is transferred to the analytical chamber where XPS is performed, 4) trace metal is sputter deposited on the sample, 5) XPS is performed to determine the trace metal contamination level, 6) the sample is transferred to the UV/Cl_2 chamber where a UV/Cl_2 process is performed, 7) the sample is transferred back to the analytical chamber where XPS is performed to determine the post-process contamination level and chemical state

2.1.1 UV/Cl_2 Reactor

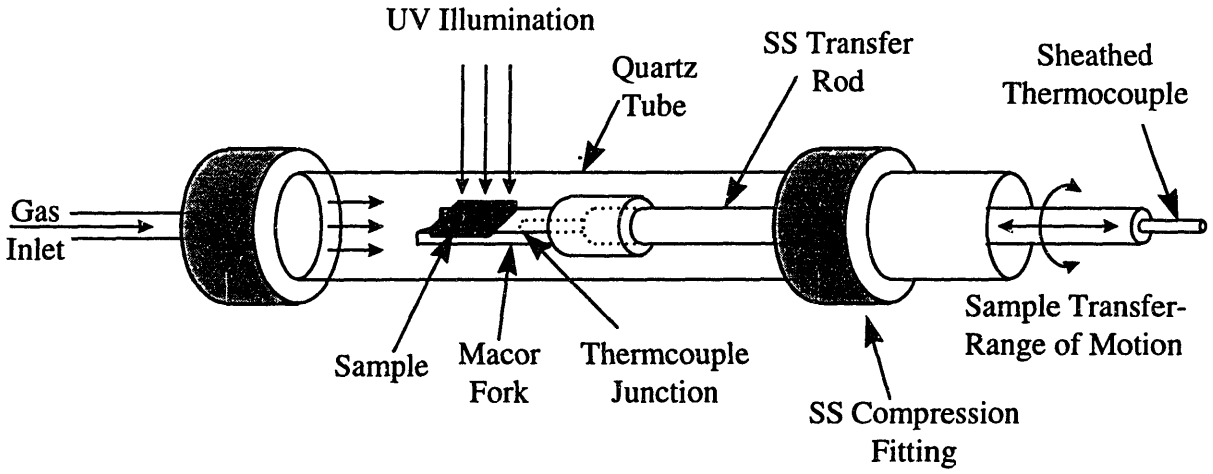

Figure 2.2-Schematic diagram of UV/Cl_2 reactor (first experimental apparatus)

The UV/Cl_2 reactor system consists of a cleaning chamber and a UV illumination system. The system is illustrated in Figure 2.2. The UV cleaning chamber consists of a 1 inch outer diameter quartz or sapphire tube. A quartz tube was used for most of the experiments described herein. UV grade quartz (equivalent to GE type 214) with a cut-off of 160 nm, ~66% transmittance at 185 nm, ~85% transmittance at 245 nm, and > 90% transmittance between 270 nm and 3.5μm, was obtained from Finkenbeiner (Waltham, MA). Sapphire tube was used in the case of ClF_3 etching experiments, where superior chemical resistance was required. Detailed transmittance specifications were unavailable for the sapphire tube, but it is generally superior to the quartz described above. Single crystal sapphire tubing was obtained from Saphikon (Milford, NH). Gas is introduced via a VCR® to compression seal transition at the inlet and flows axially down the tube. The outside of the tube was wrapped with heating tape to provide sample heating above ambient temperatures. The sample is introduced via a stainless steel transfer rod, with a stainless steel sheathed thermocouple mounted annularly in the rod such that the junction is within 1 cm of the sample surface. The sample holder and sample transfer fork were fabricated from Macor® (a machinable ceramic) in an attempt to limit sample contamination due to chemical vapor transport of metals by the chlorine radicals. It should be noted that several different materials were tested for the transfer fork. 316 stainless steel as well as anodized aluminum proved unsatisfactory in terms of their chemical resistance in this system. Stainless steel became discolored after several runs, indicating chemical attack. Anodized aluminum was stable for a short time, but suffered catastrophic failure on the sharp leading edge of the fork, where the anodized coating failed, resulting in copius amounts of aluminum chloride deposited inside the chamber. Samples were fixed to an alumina mounting stub with Torr-seal®, a vacuum compatible adhesive. The

mounting system allows for the sample to be rotated with respect to the incident UV light. The Cl_2 gas used was 99.998 % purity (Matheson ULSI grade). Pressure was controlled via a throttle valve and capacitance manometer with a PID controller. Process gas was evacuated through a 18 cfm mechanical pump. Chamber base pressure was maintained with a 240 l/s turbo pump (Balzers TPU 240).

The illumination system consisted of a Spectral Energy model LH 151N lamp housing with a 1000 watt high pressure Hg-Xe arc lamp (Hanovia #977B0010/Oriel #6293 ozone producing) and model LPS 255HR power supply. This system provides on the order of 1 Watt/cm^2 in the wavelength range of 235-400 nm. Both the full lamp spectrum and monochromated light were used at various points in this work. Two different monochromators were used in these experiments. A Spectral Energy model GM-100-1 with a 240 nm blaze was used for the 245 nm experiments. A model GM-100-3 with a 300 nm blaze was used for the 367 nm experiments. A 2.0 mm slit was used in both systems to provide an effective 8 nm full-width-at-half-maximum peak. With this arrangement, ~1.5 mWatts/cm^2 and 3 mWatts/cm^2 were obtained for the 245 and 367 nm wavelengths, respectively. The full spectrum output of the illumination system is illustrated in Figure 4.3. An in-line IR filter (Spectral Energy model LHA 162/1) was utilized to reduce the heat load on the monochromator.

2.1.2 HF/Vapor Reactor

The first HF/vapor reactor was designed by Anthony Muscat (1993). The HF/vapor reactor was constructed from stainless steel. Metered amounts of anhydrous HF, isopropyl alcohol (IPA) vapor using a nitrogen carrier, and dry nitrogen were introduced into the reactor

via a temperature controlled gas handling system. The IPA contactor was maintained at room temperature and is designed such that the vapor exiting the contactor was in equilibrium with the liquid. The gas handling line leading to the reactor was maintained at the nominal reactor processing temperature of 49°C. The remaining gas handling lines and mass flow controllers were kept at a fixed temperature of 65°C to prevent condensation. The total pressure in the reactor was measured using a heated capacitance manometer and was maintained at 250 Torr via a throttle valve using feedback control. The reactor was pressurized with a mixture of 90 sccm of dry N_2 and 100 sccm of N_2/IPA vapor. HF flow was introduced at 40 sccm to initiate etching and maintained for 30 seconds. These conditions provide an HF partial pressure of 43.5 torr, and an IPA partial pressure of 23.6 torr during the reaction. The exhaust gases were pumped with a mechanical pump downstream from a liquid nitrogen trap to remove condensables. The chamber is equipped with a J.A. Woollam & Co. model M-44 ellipsometer. This instrument is a spectroscopic ellipsometer which collects data at 44 discrete wavelengths. Although we have the capability of performing ellipsometric measurements *in situ*, these measurements were made *ex situ.*

2.1.3 Analytical Chamber

The analytical chamber is illustrated in Figure 2.3. This chamber was originally described in the thesis of Igor Tepermeister. Some modifications were made to the original design, and are described in this section. In the configuration used in this work, the analytical chamber consisted of the following; a sample manipulator system as described in the thesis of Tepermeister, a Kratos Mini Beam II ion gun, an X-ray Photoelectron Spectroscopy (XPS) system consisting of; 1) a VG Instruments Mark II dual anode (Mg and Al Kα) X-ray source

and 2) a VG Instruments 100AX electron energy analyzer, a Kimball Physics model FRA-2X1-2 low energy electron flood gun, and a metal target carousel for trace metal sputtering. This arrangement differs from the original design in the following respects; 1) the electron energy analyzer designed and built by Tepermeister was used in initial experiments but was replaced by the analyzer described above, and all of the results reported here are with the new analyzer, 2) a rotary flange was added to the sample transfer arm to allow for transfer of a sample from the UV/Cl_2 chamber to the analytical chamber, and 3) the metal target carousel was added. The carousel of five $\approx$ 1 cm square metal targets was located adjacent to the sample. To deposit trace metals on the sample, an argon ion beam was directed at the target of choice, which was biased at 1200 V, reducing the potential for sputtering unwanted metal contaminants from the adjacent targets. Generally, metal was deposited at an argon pressure of 4×10^{-7} torr and a beam energy of 1.7 kV, resulting in a current of 1.8 $\mu A/ cm^2$ to the selected sputtering target. In this manner, contamination rates on the order of 1 Å/min could be reproducibly obtained. For XPS, the take-off angle was fixed at 90°. Mg Kα radiation at an energy of 1254 eV was used in all of the results presented here. This system yielded a resolution of ~ 1.2 eV and 1.8 eV (full-width at half-maximum) for the Si 2p (½ & 3/2) peak(s) at a pass energy of 20 eV and 50 eV respectively. (Note: the Si 2p peak is composed of the ½ and 3/2 components which generally cannot be resolved without monochromatic radiation).

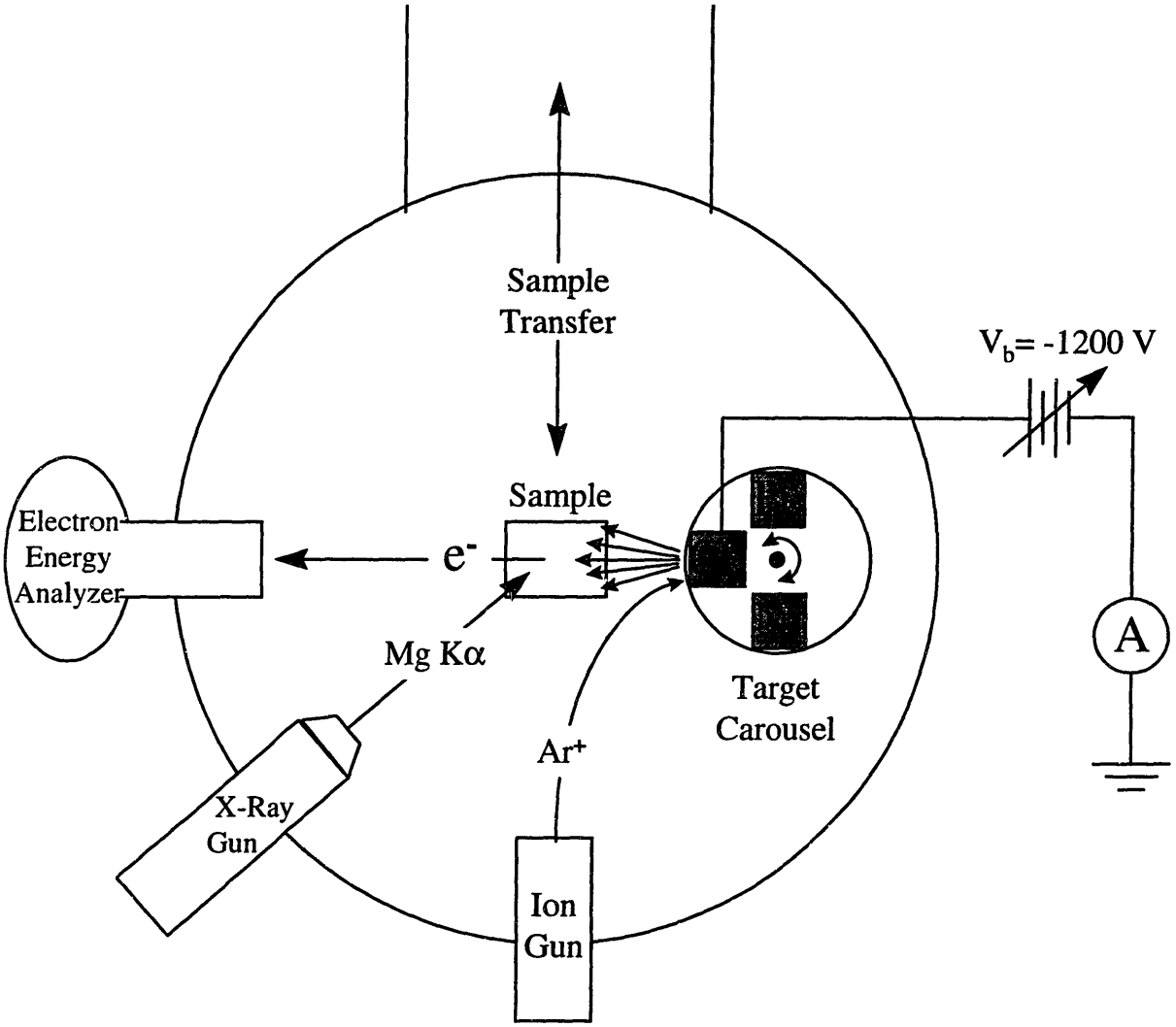

Figure 2.3-Schematic diagram of the analytical chamber (first experimental apparatus).

2.1.4 Trace Metal Sputtering System Calibration

The sputter deposition system was calibrated by a carefully controlled sequential deposition of copper on a SiO_2 substrate and measuring the copper, oxygen, and silicon XPS signals after each deposition interval. The XPS peak intensities plotted versus time are shown in Figure 2.4. In the calibration experiment, the sputter conditions were controlled so as to maintain

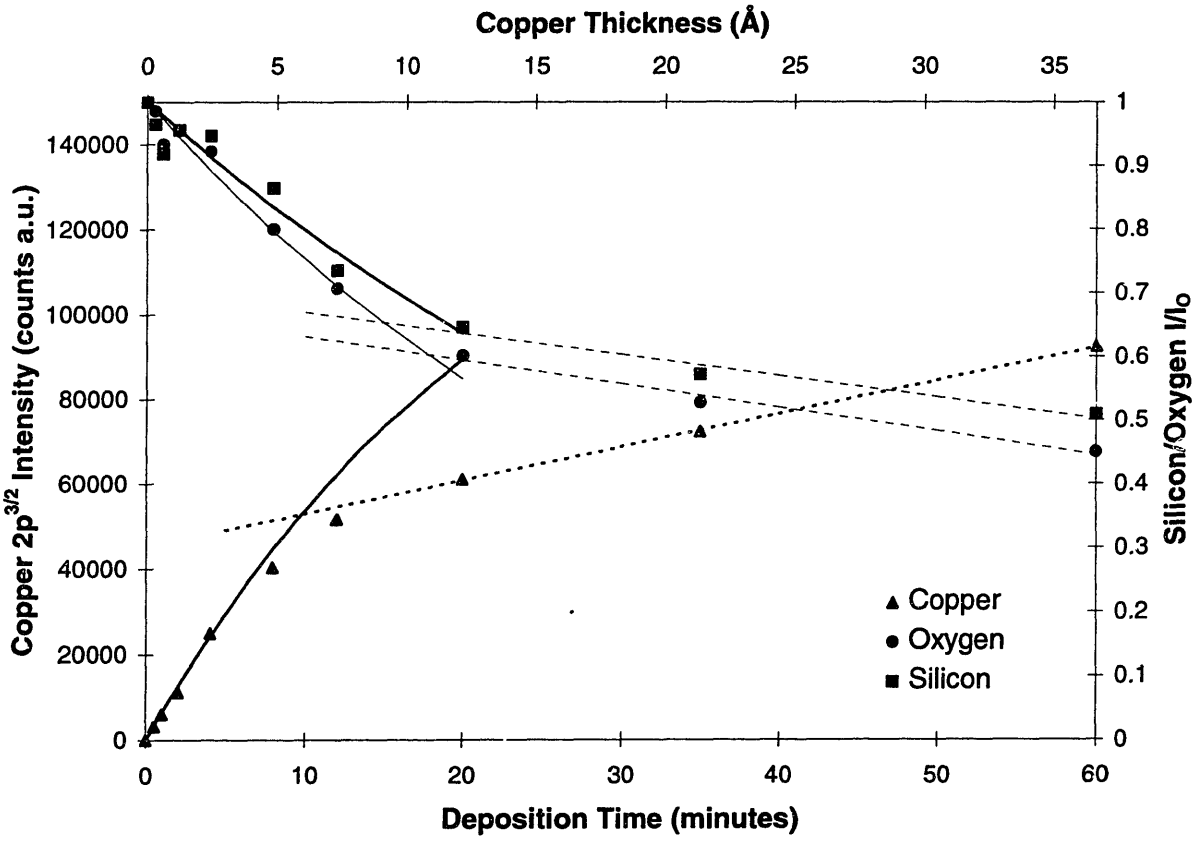

Figure 2.4-Data from copper sputter calibration.

a constant deposition rate of copper on the silicon dioxide sample. The copper target bias was set at 1200 V. The ion gun was set at 1700 V and the argon pressure was maintained at 4.4 x 10^{-7} torr with the ion gun leak valve. These parameters were maintained constant throughout the experiment. The deposition was interrupted periodically to measure the surface concentrations of copper, silicon and oxygen with XPS.

The silicon and oxygen signals are due to the substrate and decay from their initial maximum value, I_O. The copper signal is initially zero, and increases as the sputtered layer thickness increases. The XPS data shows an initial exponential response versus sputter time (exponential decay for the substrate peaks, and exponential growth for the copper overlayer) and then a linear response in all of the elemental signals. This behavior is indicative of an initial 2-dimensional layer-by-layer coverage of copper (exponential regime) which then switches to an 3-dimensional island growth mode (linear regime) as the coverage increases.

The deposition rate of copper can be determined from this data. The exponential portion of the substrate data can be fit to the following equation:

$$I = I_0 \exp\left(\frac{-d}{\lambda \sin\theta}\right) \qquad 2.1$$

where I_O is the intensity of the substrate peak with no overlayer, d is the thickness of the overlayer, λ is mean free path of the photoelectron through the overlayer and θ is the "take-off angle" or the angle between the substrate and the electron energy analyzer, which in this case is 90^O. Initially, the values "d" and "λ" will be expressed in units of deposition time. If the silicon and oxygen data are fit to an exponential (solid lines in Figure 2.4), values of λ_{Si}=44.25 minutes, and λ_O=35.68 minutes are obtained. The accepted value of λ_{Si}= 27 Å is divided by the value of λ_{Si} in minutes to yield a deposition rate of 0.61 Å/min. The values of

the upper (secondary) X-axis in Figure 2.4 are based on this value for the deposition rate. This deposition rate yields a value of λ_O=21.77 Å which compares well to the accepted value of 21.4 Å (based on the value of 27 Å for silicon and the relation $\lambda \alpha E^{1/2}$). The exponential portion of the copper data is fit to the relation:

$$I = I_o\left(1 - \exp\left(\frac{-d}{\lambda \sin\theta}\right)\right) \qquad 2.2$$

with the accepted value of λ_{Cu}=15 Å and I_O=160680 counts. The origin of this value for I_O will be discussed in the next paragraph.

The linear portion of the substrate data can be modeled by the following relation:

$$\dot{I} = \dot{J}\exp\left(\frac{-d_{ISLAND}}{\lambda \sin\theta}\right) \qquad 2.3$$

This model assumes coverage of the surface by islands of constant thickness "d_{ISLAND}" which are covering the surface at a constant rate, "$\dot{J}$", thus yielding the (constant) rate of change of the intensity, "$\dot{I}$". Figure 2.5 illustrates this growth mode schematically.

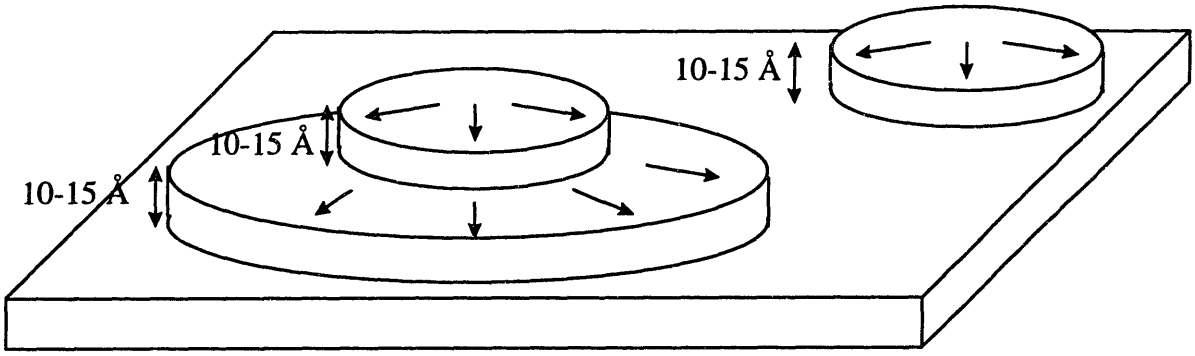

Figure 2.5-Schematic representation of islands growing in sheets of constant thickness.

If two signals are compared, the following relation is obtained:

$$\ln\left(\frac{\dot{I}_1}{\dot{I}_2}\right) = d_{ISLAND}\frac{(\lambda_1 - \lambda_2)}{\lambda_1\lambda_2} \qquad 2.4$$

and, since the mean free paths of the electrons are known, and $\dot{I}$ is just the slope of the linear portion of the curve, the thickness of the islands can be obtained. Comparing the slope of the linear fits of the silicon and oxygen data (dashed lines in Figure 2.4) yields a value of $11.2\text{Å} < d_{ISLAND} < 12.2$ Å, depending on whether the literature value or the fit value for λ_O is used. Note that the linear break point in the silicon and oxygen curves occurs at ~12 Å. Similarly, the absolute value of I_O for copper can be obtained by "backing out" the normalized value of $\dot{I}$ for copper using equation 2.4 and the value of d_{ISLAND} calculated above. This analysis yields a value of I_O for copper of between 166838 and 160680 counts, which compares well with the value of 174731 counts obtained by multiplying I_O for silicon by the appropriate atomic sensitivity factors. The data is generally self-consistent except for the fact that the deviation from exponential growth in the copper data seems to appear much earlier than the linear break in the silicon and oxygen data. There are two possible reasons for this phenomenon. The first is that the photoelectron cross-section of copper is much greater than that of either silicon or oxygen. This would make trends in the copper data (such as a transition between uniform coverage and island growth) easier to resolve. The second is that there may be another growth mode of copper which is active in the deposition range of ~8-20 minutes which does not significantly effect the intensity of the substrate signal(s) but does effect the overlayer signal.

Figure 2.6 shows AFM images of the surface of the sample after 60 minutes of deposition. Islands are clearly visible on the surface. Line scans of isolated islands indicate an island thickness on the order of 10-15 Å, which agrees well with the calculated value.

One point that should be emphasized is that in all of the copper removal results presented in this thesis, the initial copper coverage is « 1 Å (and generally on the order of 0.1 ML or less), such that the initial copper coverage can be characterized as more or less uniform, and the presence of "large" islands of copper should have no influence on the copper removal mechanism.

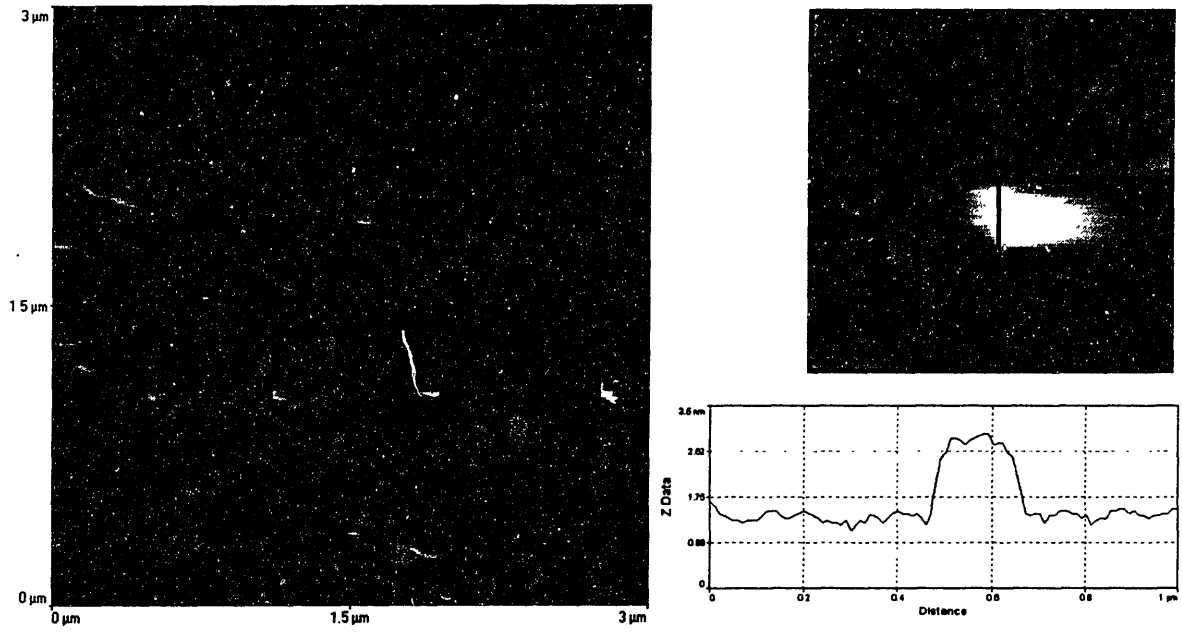

Figure 2.6-AFM scans illustrating islands on the sample surface after 60 minutes of copper deposition. The height data for the vertical line through the small scan at the upper right is illustrated in the lower right corner.

2.2 Second Experimental Setup

2.2.1 Integrated Processing Apparatus

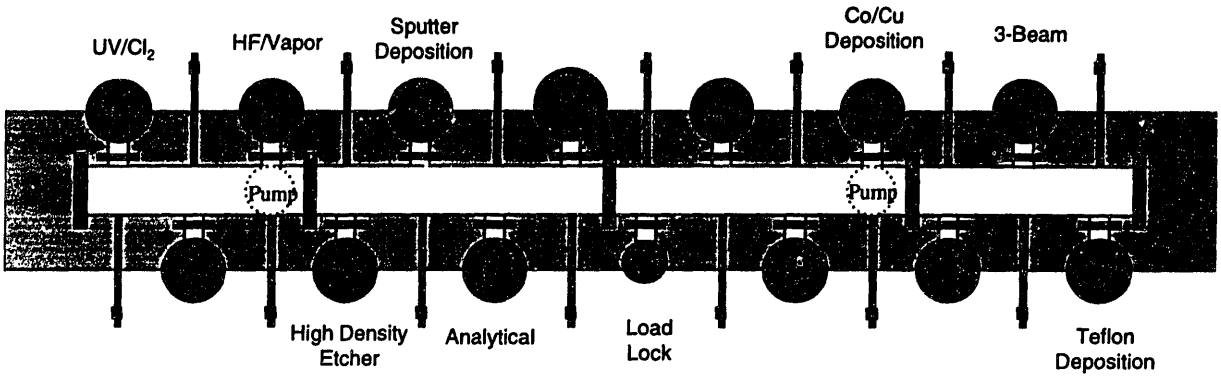

Figure 2.7-Schematic diagram of the Integrated Processing Apparatus.

The apparatus described in Section 2.1 was dismantled in August 1996. In its' place, a large clustered system, illustrated in Figure 2.6, was constructed. This system consists of 13 chambers, most of which are configured to process 4" silicon wafers, connected to a central transfer tube. A sample transfer system, consisting of a cart running on rails down the length of the tube, allows samples to be moved along the length of the tube. In addition each chamber has a transfer rod associated with it, allowing wafers to be moved from the cart into/out of the individual chambers. This system allows for wafer transfer between any chamber connected to the apparatus, while maintaining vacuum integrity. The base pressure of the transfer tube is in the low 10^{-8}-mid 10^{-9} Torr range.

At the time of this writing, the chambers labeled in Figure 2.7 were operational. Only the chambers used in the work discussed here will be described in this section, and these are; the UV/Cl_2 chamber, the HF/Vapor chamber, the High Density Etcher, The Analytical Chamber and the Sputter Deposition Chamber.

2.2.2 UV/Cl_2 Chamber

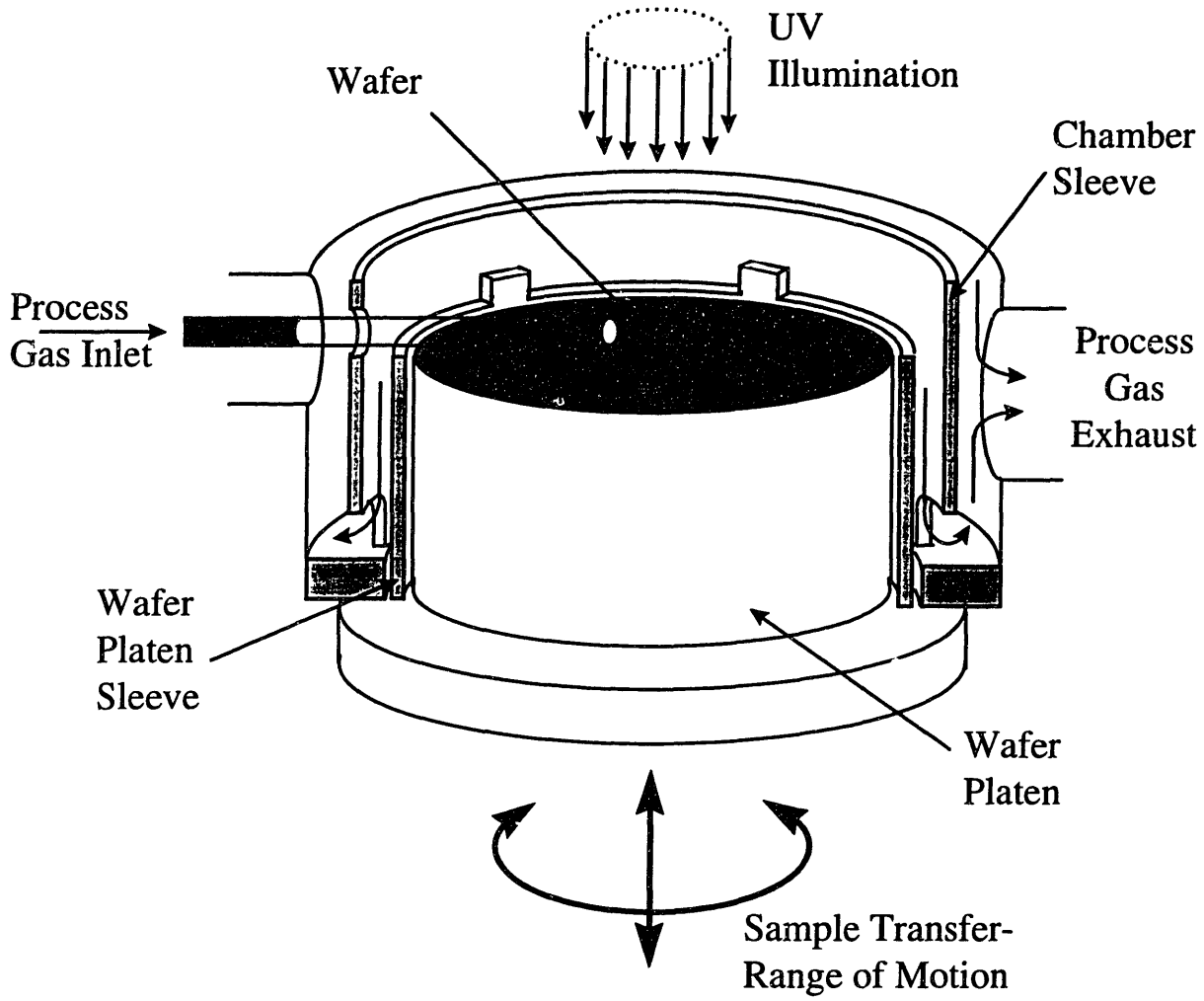

Figure 2.8-Schematic diagram of UV/Cl_2 chamber (second experimental apparatus).

The UV/Cl_2 reactor is schematically illustrated in Figure 2.8. The 4" wafer rests on a anodized aluminum platen which can be raised or lowered from the reaction position and rotated through 360°. The chamber itself is fabricated from stainless steel. The exposed surfaces of the wafer platen are protected with a pyrex sleeve (shown in cut-away in figure 2.8). Four tabs in the pyrex sleeve hold the wafer in position. Another pyrex sleeve shields the chamber walls. Process gas is introduced through a ¼" stainless steel tube which

transitions to pyrex in the reactor itself. The gas outlet is located ≈ ½" from the center of the wafer. Gas flows over the reactor and through the annular gap between the pyrex sleeves and is exhausted through slots in the bottom of the chamber sleeve, as illustrated in Figure 2.8. UV illumination is introduced thorough a quartz window (not shown in Figure 2.8) at the top of the reactor. The UV illumination system is the described in Section 2.1.1. A aluminum mirror in line with the UV optics allows the light flux to be directed in a perpendicular direction. The illuminated area of the wafer is ≈1" in diameter. This area provides ample area for XPS analysis. The pressure control system is the same as for the reactor described in Section 2.1.1. Base pressure on the chamber is maintained with the same turbo pump described in Section 2.1.1, and the typical base pressure in the chamber is in the mid 10^{-8} Torr range.

2.2.3 High Density (ICP) Etcher

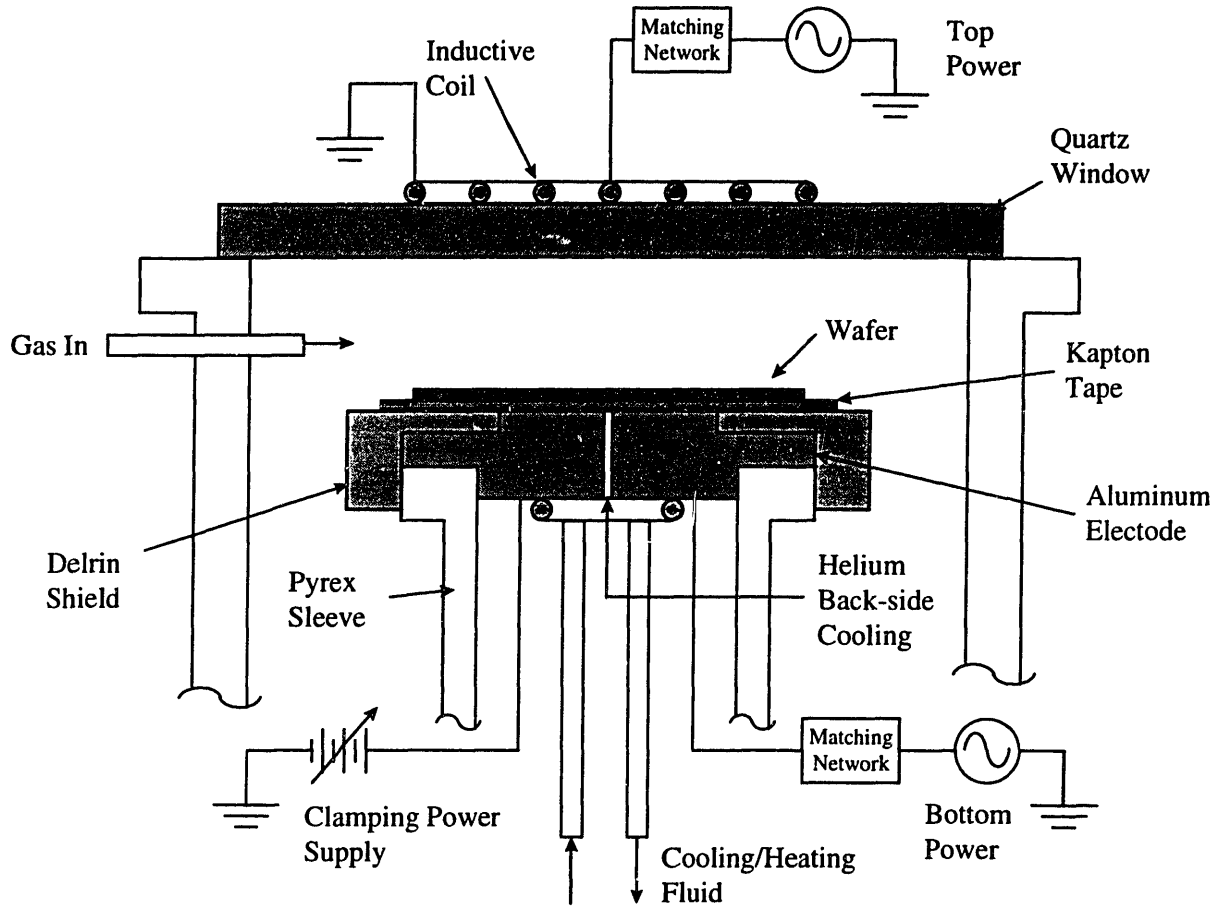

Figure 2.9-Schematic diagram of high density etcher.

The high density etcher is schematically illustrated in Figure 2.9. In this reactor, the plasma is generated via an inductive coil which sits on top of the quartz window. A separate power supply provides "bottom power" to the wafer electrode. In this configuration, somewhat separate control of the plasma density and the ion energy striking the wafer are maintained through manipulation of the top power and bottom power respectively. Generally, the top and bottom power supplies are operated at different frequencies. This minimizes

interference between the power supplies which can manifest itself as a "beat frequency" or oscillation of the plasma when two power supplies of similar but slightly different frequencies are used. The wafer electrode is temperature controlled with a cooling/heating coil which is attached to the bottom surface of the electrode. A water/glycol solution is circulated through the coil, and the temperature of the solution is maintained with a VWR model 1162 refrigerated circulating bath. Typically, the pressure of the chamber is on the order of 10 mTorr during an etching run. At 10 mtorr the heat transfer between the wafer and the electrode would be very slow, making the thermal stability of the wafer poor. In order to increase the heat transfer coefficient between the wafer and the electrode, helium is introduced to the back-side of the wafer. This technique is known as "helium back-side cooling". The wafer must be clamped to the electrode in some fashion to maintain the pressure differential between the back-side of the wafer and the chamber, and to prevent the wafer from shifting position when the back-side helium is applied. Another feature of this reactor is the ability to electrostatically clamp the wafer. The wafer electrode is covered with a sheet of Kapton tape, which acts as an insulator between the electrode itself and the wafer. When a DC voltage is applied to the electrode, and the plasma is struck, a capacitor is formed with the plasma acting as the ground. The aluminum electrode and the wafer act as the capacitor plates and the Kapton sheet forms the insulator in this unipolar configuration. The build-up of charge between the capacitor plates creates an electrostatic force of attraction which acts to pull the wafer down to the electrode surface. Electrical isolation between the aluminum electrode and the plasma is critical to maintaining the integrity of the circuit, as the shortest path to ground between the electrode and the plasma will inevitably be found. To successfully implement this technique, it was found to be necessary to cover any and all exposed surfaces of the

electrode with an insulator. Even very small gaps, such as the space around quartz pins (used to maintain the wafer in position on the electrode-not shown) press fit in the Delrin shield would provide a short circuit path to ground. A potential of 1000 V applied to the wafer electrode was sufficient to maintain adequate clamping force at a back-side helium pressure of 5 Torr.

2.2.4 Analytical Chamber

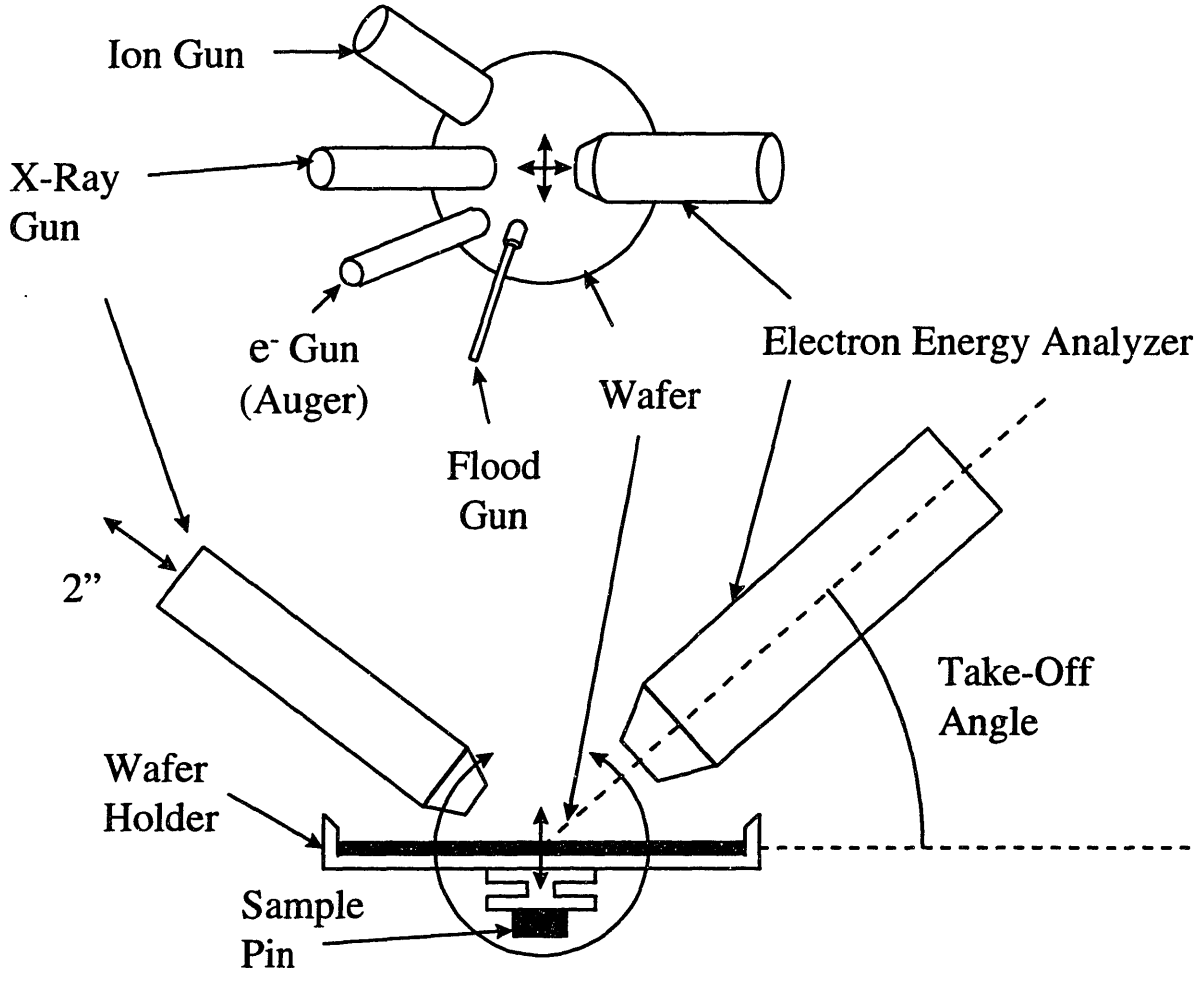

Figure 2.10-Schematic diagram of the Analytical Chamber (second experimental apparatus).

The analytical chamber is schematically illustrated in Figure 2.10. The top view in the figure shows the overall analytical capability in the chamber while the side view illustrates sample rotation for angle resolved surface analysis. Double-headed arrows in the figure illustrate the range of motion of the sample. Also note that the X-ray gun can be retracted up to 2" for sample transfer. Most of the equipment in the chamber was transferred from the analytical chamber described in Section 2.1.3. The addition of a Kimball Physics EMG-12 electron gun allows Auger Electron Spectroscopy as well as XPS to be performed in this chamber. The ability to rotate the sample gives us the capability to perform angle resolved surface analysis in this chamber. While the angle between the X-ray gun and the electron energy analyzer is fixed at ≈67°, the angle between the sample and the analyzer can be adjusted by rotating the sample, and with proper sample positioning, the same spot on the sample will be analyzed. The take-off angle (see Figure 2.10) can be adjusted in this manner from a maximum of ≈ 90° to a minimum of ≈ 20°. This ability can advantageous in that the sensitivity to surface species can be enhanced relative to the bulk (note the sin(θ) dependence of photoelectron escape depth in equations 2.1-2.3). While X-rays penetrate on the order of μm's into the sample, photoelectrons can only escape from a depth on the order of 50 Å. As the angle between the sample and the analyzer is reduced, the "line of sight" into the sample will be titled such that the effective analyzed depth becomes sin(take-off angle). Figure 2.11 shows silicon 2p and oxygen 1s XPS spectra of a native oxide on a single crystal silicon substrate taken at various take-off angles.

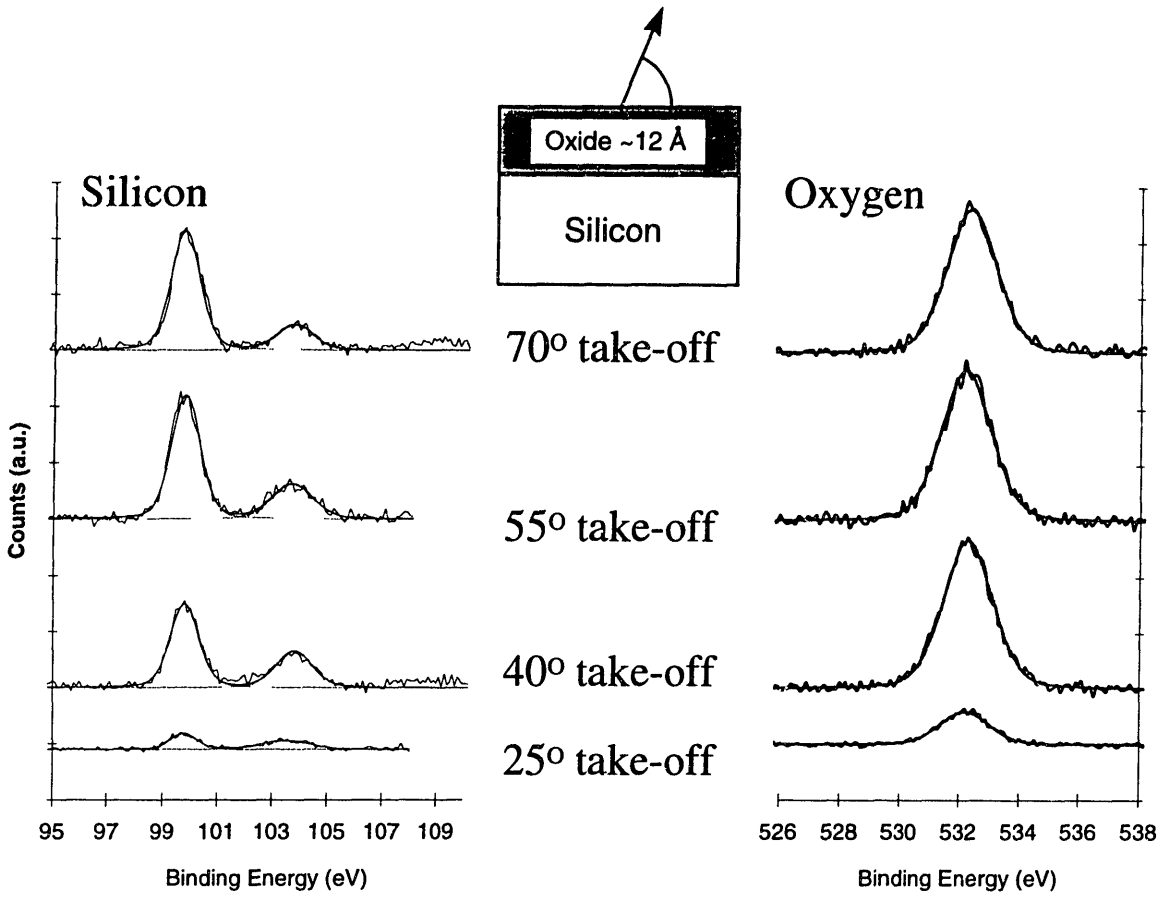

Figure 2.11-Silicon 2p and oxygen 1s XPS spectra of a 12 Å native oxide on a silicon substrate taken at various take-off angles at a pass energy of 20 eV.

The overall signal strength is relatively insensitive to take-off angle over a wide range. Note that the oxygen signal strength does not change significantly between 70 and 40°. What does change is the relative ratios of the substrate (99.75 eV) and oxide (103.6 eV) peaks in the silicon spectrum. This is a manifestation of the increased surface sensitivity as the take-off angle is decreased. At 25° the signal strength has fallen off drastically. Practically, 30° is the lowest take-off angle that should be used in this chamber to maintain an acceptable signal to noise ratio. In addition, since the relationship between signal strength and take-off angle is not trivial, I_O must be ascertained separately at each take-off angle for the materials and samples of interest if accurate concentration and thickness data are to be obtained.

Application of angle resolved XPS to the analysis of chemical topography using differential charging and geometrical shading is discussed in Chapter 7.

2.2.5 HF/Vapor Chamber

The HF/Vapor chamber is configured to accept full 4" wafers or smaller samples. Generally, 4" wafers were used in the work described in this thesis. Alcohol and/or water vapor is delivered from heated stainless steel ampoules. The ampoules are maintained at > 100°C, and the vapor over the liquid is metered through mass flow controllers and delivered to the reactor through a stainless steel tubing manifold which is maintained at a higher temperature than the reactor but generally at ≈ 65°C. The idea is to maintain the gas handling system at a temperature such that the equilibrium vapor pressure of the solvent is significantly less than the saturation vapor pressure in order to prevent condensation in the gas lines. Nitrogen and anhydrous HF vapor are mixed with the solvent upstream from the reactor, to provide a total gas flow of the appropriate composition for the experiment. The difference between this system and the one described in Section 2.1.2 is that in the old system, solvent vapors were delivered via a contactor in which nitrogen vapor was passed over a stagnant reservoir of solvent and the gas mixture was assumed to be at equilibrium at the outlet of the contactor. In the new system, solvent vapors are metered in their pure form, giving more accurate control over the gas mixture composition. The gas mixture flows through a showerhead and is distributed over the wafer. Process gas is exhausted with a mechanical pump through a liquid nitrogen trap. Chamber base pressure is maintained with a Balzers TPU240 240 l/s turbo pump. The base pressure of the chamber is typically on the order of 10^{-7} Torr.

Chapter 3

Substrate Etching with UV Excited Halogen Chemistries

UV excited halogen chemistries are known to etch silicon as well as some other materials that may be exposed on a wafer surface during a cleaning operation. Before exploring the cleaning efficiency and mechanisms of UV excited processes, we expended significant effort to characterize the effect of some of these chemistries on the wafer surface. Of prime concern in this regard are the post-process surface roughness, which must be maintained below acceptable levels, and the amount of material removed during the process, which must be small enough not to effect device dimensions and performance. Most of our effort was devoted to the study of the effect of the UV/Cl_2 process on a silicon surface. We also studied the interaction of UV/ClF_3 with silicon, silicon dioxide and silicon nitride surfaces.

The major findings of these studies were that a parameter space exists, where acceptable substrate integrity can be maintained both in terms of surface roughness and the amount of silicon etched, which is of interest for application of the UV/Cl_2 process for wafer cleaning. The surface roughness increases by approximately 1 Å R_{MS} for every 100 Å etched over a broad range of conditions. We found evidence that UV/Cl_2 silicon etching is dominated primarily by surface photolytic processes under broad band UV illumination.

3.1 Substrate Etching with UV/Cl_2

Photochemical etching of silicon has been studied. Houle[1] and Chuang[2] have published reviews of photochemical etching which discuss general photochemical etching

mechanisms. Okano *et al.*[3] have studied the photo-excited etching of both poly- and single crystalline silicon in a chlorine atmosphere with a 200 W Hg-Xe lamp. Ikawa *et al.*[4] have studied silicon photo-etching in chlorine with a microwave excited mercury lamp. Sesselmann *et al.*[5] have studied ultraviolet laser induced etching mechanisms at 308 and 254nm on single crystal silicon, while Paulsen-Boaz *et al.*[6] have studied the effect of 248, 308 and 351nm radiation on the chlorination and photodesorption processes of single crystalline silicon. The pertinent aspects of the above investigations will be invoked in the discussion of the results presented here.

In general, the following phenomena should be considered in the interpretation of these experimental results. In UV/Cl_2 silicon etching, there are two primary processes which activate or enhance the etching reaction; 1) gas phase photolysis, in which molecular chlorine dissociates in the gas phase with illumination in the wavelength range 250-400nm and 2) surface photolytic processes. Surface photolytic processes can be subdivided into; 1) formation of electron-hole pairs in the substrate (through the absorption of photons with energy higher than the band gap) which diffuse to the surface and participate in the reaction, band bending, and/or desorption processes and 2) direct bond breaking. It should also be noted that at the conditions of the experiments reported here, molecular chlorine does not spontaneously etch silicon, and neither molecular or UV excited chlorine etches oxide at a detectable rate.

3.1.1 Results and Discussion

Our work involved the characterization of the UV/Cl_2 process in terms of the effect of sample temperature, process pressure and UV fluence on the silicon etch rate and post process

surface roughness. These experiments were performed (for the most part) in the reactor described in Section 2.1.1. Samples used in these experiments were 1 x 1 cm squares cleaved from a silicon wafer. Etched depths were measured with a Dektak II or Dektak 8000 profilometer. Surface roughness was measured with a Topometrix Discoverer Scanning Probe Microscope (SPM). Reported values of roughness represent the mean of at least nine 5 μm square scans spanning a representative area of the sample surface. Generally, the standard deviation of R_{MS} roughness was ≈20 % of the mean value for a given sample.

A. Designed Experiment

A designed experiment was performed in an earlier version of the UV/Cl_2 reactor in order to establish the response of surface roughness and etch rate to the input variables of chlorine pressure and UV exposure time. These experiments were performed with p-type Si <100> 5-20 Ω-cm samples which were cleaved from a 4" wafer. These samples were partially masked with photoresist such that the masked portion of the sample was not etched and the etched depth could be measured over the step. Photoresist masked samples were mounted to ceramic buttons with Torr-Seal and baked in a vacuum oven over-night at ≈120°C. Samples were dipped in HF at 40°C for 60 seconds immediately prior to introduction into the load lock in order to remove the native oxide from the silicon surface. In these experiments, pressure was varied between 1 and 99 torr. Exposure time was varied between 30 and 120 seconds. The chlorine flow rate was held constant at 10 sccm. A central composite design, consisting of 5 levels for each of the two input variables and six replicated center points for a total of 14 experimental runs, was used[7]. All runs were initiated at room temperature. A temperature rise on the order of 30 °C per minute was observed due to light exposure. The response surfaces

generated from this set of experiments, illustrating the response of surface roughness and etch depth are illustrated in Figures 3.1 & 3.2 respectively. The adjusted R^2 values of the two surfaces are 0.72 and 0.48 respectively. The high R^2 value for the etch depth response surface is mostly attributable to the difficulty in accurately measuring the step height with the masking technique which was in use at this time.

In spite of the relatively poor fits, these figures illustrate some interesting points. First is that they exhibit a similar shape. This is because the depth of silicon etched and the surface roughness are somewhat coupled, and the post process surface roughness is a function of the amount of material removed. This relationship will be further illustrated in the next section. The second point is the maximum in both surfaces with respect to pressure at about 50 Torr. This is due to the gas phase absorption of UV photons by chlorine. Ikawa *et al.*[4] witnessed a similar a similar etch rate drop in the UV/Cl_2 etching of p-type single crystal silicon which was coupled with a decrease in UV intensity at the substrate between 250-400nm, the wavelength range where chlorine absorbs strongly. Gas phase absorption of UV could potentially limit the etch rate by; 1) limiting the photon flux to the surface or 2) limiting the production of gas phase radicals in the vicinity of the sample surface, or a combination of both. The implications of these two mechanisms in terms of gas phase versus surface enhancement of the silicon etching reaction will be discussed further in the next section. The most important implications of these data is that there exists a parameter space where a UV/Cl_2 process can be performed while maintaining the integrity of the substrate surface. The data indicate that for chlorine pressures of 0-10 torr and "short" processing times (on the order of a minute), minimal substrate etching and roughening is observed.

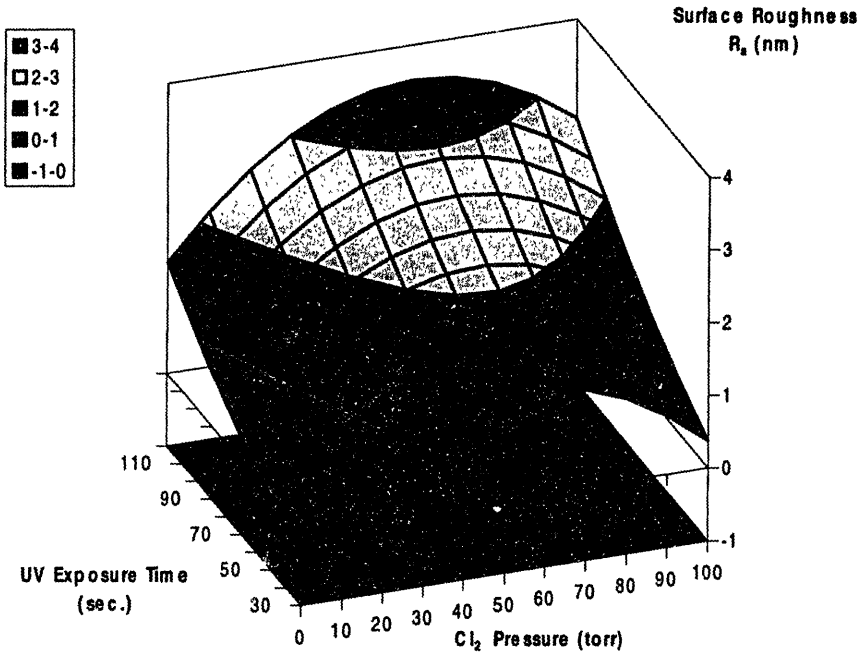

Figure 3.1-Response surface for silicon surface roughness as a function of UV exposure time and chlorine pressure.

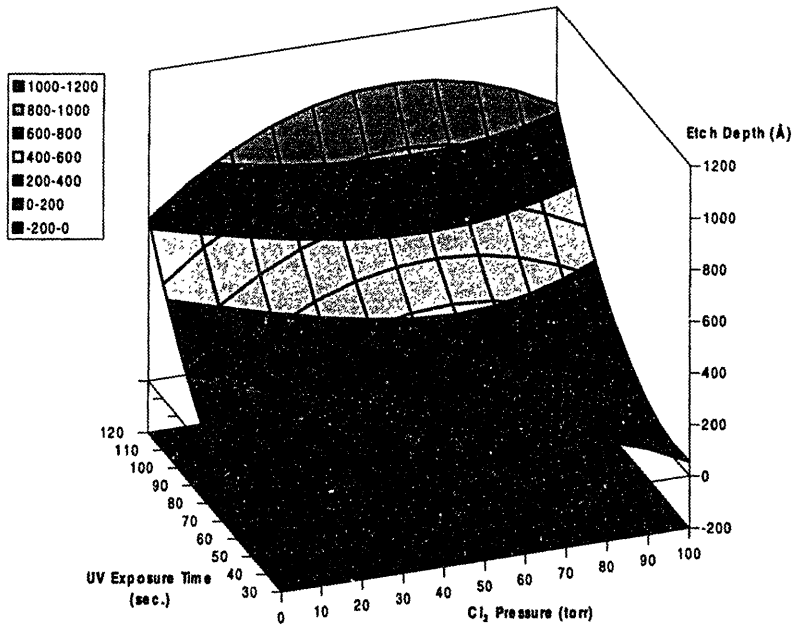

Figure 3.2-Response surface for silicon etch depth as a function of UV exposure time and chlorine pressure.

B. Other Silicon Etching Experiments

Additional silicon etching experiments were performed in the reactor described in Section 2.1.1. These experiments were performed with n-type Si <100> 1-5 Ω-cm samples which were cleaved from a 6" wafer. These samples were partially masked with oxide during the process, which was stripped after the process with aqueous HF, leaving a step for etch depth measurement. This system proved to be more reliable than the photoresist masking system. In most of these experiments, the samples were mounted on a Macor sample holder. In this holder the samples were held in place with a Macor flap fastened with an alumina screw and nut. This holder system had the benefit of being reusable and avoided the issue of cross contamination from the Torr-seal mounting compound. All samples were pre-cleaned before processing. The cleaning sequence was as follows: 1) 3/1 H_2SO_4/H_2O_2 (samples were allowed to sit in this solution until just prior to use), and 2) 10 % aqueous HF for 60 seconds immediately prior to insertion in the load lock. This cleaning sequence would result in complete removal of the native oxide on the bare silicon section of the sample, but would maintain a sufficient oxide thickness on the masked portion to totally inhibit substrate etching. All samples were rinsed in distilled H_2O before and after immersion into the cleaning solutions and blown dry with N_2 before insertion into the vacuum chamber.

Figure 3.3 illustrates the relationship between post-process surface roughness and the amount of silicon etched. The data in this figure represent a wide range of process conditions; temperature from 20-250 C°, pressure from 1-50 Torr, process times from 30-180 seconds. There is a roughly linear relationship between surface roughness and substrate etching, in agreement with the response surface data presented in the last section.

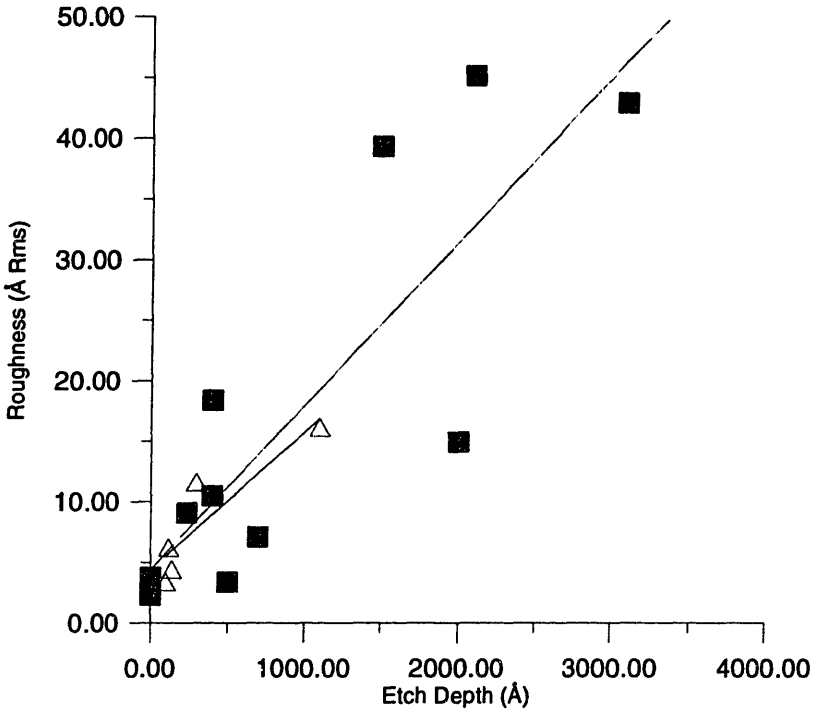

Figure 3.3-Post-process surface roughness (Å R_{MS}) versus etch depth (Å) for UV/Cl_2 silicon etching at various reaction conditions.

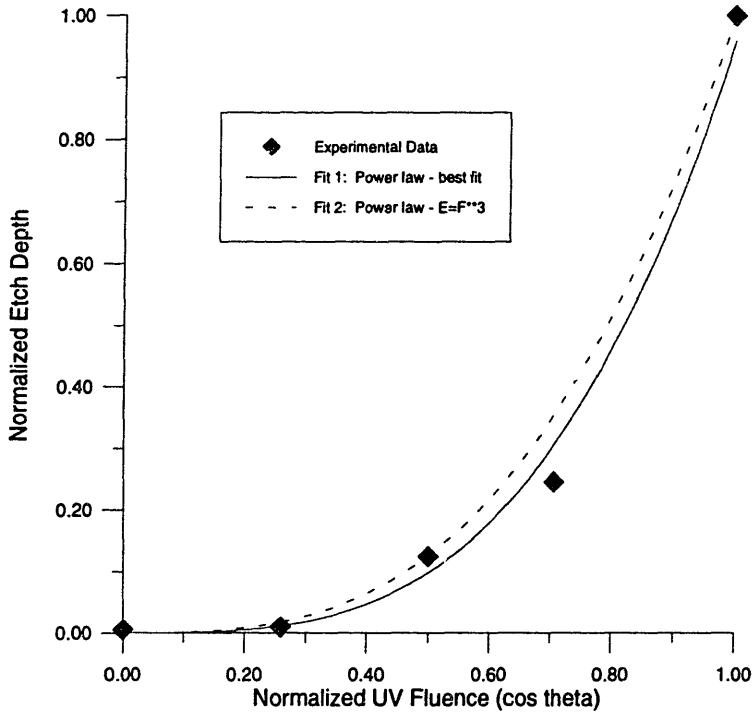

Figure 3.4-Normalized etch depth versus normalized UV fluence for UV/Cl_2 etching of silicon.

Figure 3.4 illustrates the relative effects of surface and gas phase photolysis on the silicon etching reaction. In this experiment, the UV fluence to the sample was varied by rotating the sample with respect to the light source. There is a small but measurable etch rate with zero direct UV fluence. This rate is attributable to purely chemical Cl radical etching due to gas phase dissociation of molecular chlorine. Okano *et al.*[3] also observed etching of n^+ polysilicon with parallel UV illumination, although they did not witness parallel etching of undoped polysilicon. As the UV flux to the sample is increased, the etch rate is enhanced by ≈ 2 orders of magnitude due to the contribution of surface photolysis. The etch rate does not appear to be first order in UV fluence. This is in contrast to the results of Okano *et al* who observed a first order dependence of etch rate on UV intensity. On the other hand, Ikawa *et al.*[4] observed greater than first order behavior in p-type Si<100> etching. They saw a pressure dependence of the reaction order below ~80mW/cm^2, with the order decreasing with increasing pressure. Between 80-100 mW/cm^2, the reaction order increased and the pressure dependency disappeared. Similarly, Sesselmann *et al.*[5] observed order >1 at "low" laser fluences with 248 nm radiation whereas at 308 nm the reaction was first order. At both wavelengths, as the laser fluence was increased, the apparent reaction order increased dramatically, coupled with a transition from a photon driven to a thermally driven mechanism. Additionally, they utilized remote microwave generation of chlorine radicals coupled with direct 248 nm radiation, and the reaction order in the "low" fluence regime was close to one. They attribute this difference in reaction order on a different photodesorption mechanism being active at the two wavelengths. At 308 nm, they attribute photodesorption to electron-hole pair generation contributing to enhanced desorption at the wafer surface. At 248 nm they note that the photon energy (5.0 eV) is high enough to directly break the Si-Si (4.64 eV) or Si-

Cl (4.72 eV) bond, potentially leading to a more efficient photodesorption mechanism. It should be noted that this discussion pertains to the desorption mechanism and not the overall etching mechanism. At 308nm the overall etch rate is more influenced by the gas phase production of chlorine radicals. At 248 nm the etch rate is limited by the spontaneous reaction of chlorine with silicon, and generally etching at 308nm is more efficient.

The discrepancies in the results discussed above can be reconciled by considering the illumination systems used in these experiments. Ikawa *et al.* utilized a microwave excited mercury lamp which has quite a bit of power in the high energy wavelength region (below 248 nm) where the more efficient desorption mechanism is operative. Okano *et al.* utilized a low-medium power Hg-Xe lamp which would not have high energy photon output and the desorption process would be primarily driven by electron-hole pair formation. In sum, the reaction order dependence with UV power level is most likely dependent on the energy spectrum of the illuminating radiation and not the doping level. Our results are not inconsistent with this picture since we have a significant amount of power in the high energy range below ~ 250nm, which could account for the reaction order being >1.

Figure 3.5 illustrates some additional silicon etching data which reveal an interesting effect. Figure 3.5 shows that samples reacted at an initial sample temperature of nominally 150°C etch faster than samples reacted at an initial sample temperature of nominally 200°C. Okano *et al.* also reported a maximum in the etch rate of n^+ polysilicon at 150°C, and attributed it to increased Cl desorption from the surface at higher temperature. This explanation seems unlikely, since one would expect similar desorption limited etching behavior in the etching of silicon with atomic chlorine, where a steady increase in etch rate

with temperature has been observed independent of doping level, dopant type or crystallinity between 20 and 300°C[8].

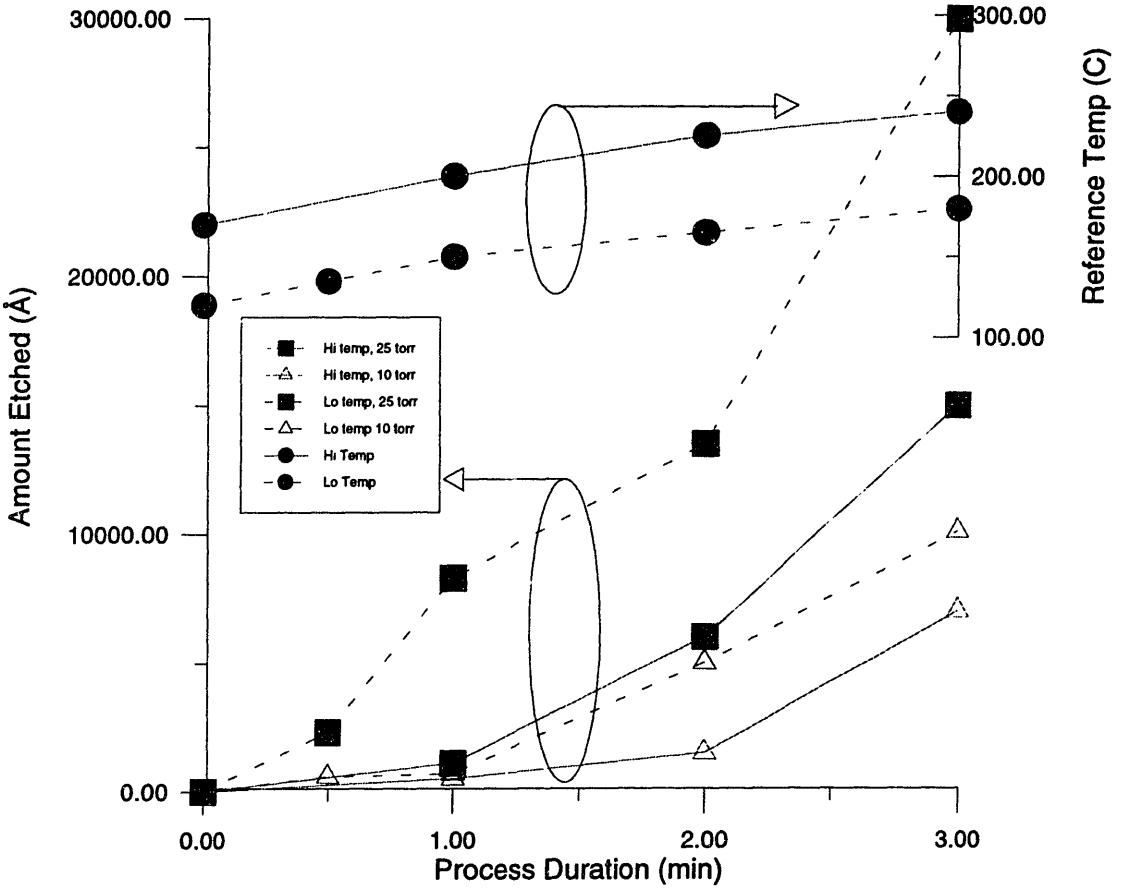

Figure 3.5-Silicon etching data. Squares represent etch depth data at 25 torr Cl_2. Triangles represent etch depth data at 10 torr Cl_2. Dotted lines represent data taken at "low" temperature. Solid lines represent data taken at "high" temperature. Circles give the sample temperature as a function of process time and are read on the upper right y-axis.

Another possible explanation lies in the proposed mechanism of photochemical reaction of semiconductors. In general, the production of electron-hole pairs due to adsorption of shorter than band gap photons is known to enhance reaction rates in semiconductors[1,2]. Electron-hole pair generation may enhance etching by enhancing adsorption, reaction or desorption. The exact mechanism of enhancement is not necessarily obvious or clear.

Ashby[9,10] has suggested a "carrier-driven" etching mechanism, and has been able to "tailor" etching rates by introducing defects into a GaAs substrate via ion implantation. These defects act as recombination centers and reduce the carrier lifetime. Etch rate was found to decrease with the decrease in carrier lifetime.

It has been suggested that the production of electron-hole pairs in the substrate near surface region due to UV absorption is a contributing effect in UV/Cl_2 silicon etching[3-6]. To explain the results in Figure 3.5 in terms of electron-hole pair generation, the drop in etch rate must be linked to some property of electron generation or transport which decreases with temperature. For the doping level of these samples, the carrier mobility drops by ≈30% between 150 and 200°C[11]. As the temperature is increased and the carrier mobility decreases, the etch rate may become limited by the transport of carriers to the wafer surface whereas at low temperature the etch rate is most likely limited by the chlorine surface coverage. This is consistent with the picture of photodesorption of $SiCl_X$ etch products from silicon surfaces put forth by Paulsen-Boaz *et al.*[6]. They propose two limiting regimes; 1) at a chlorine coverage far from saturation (high photon flux-low chlorine flux) the surface chlorine coverage is the limiting factor in the silicon etch rate and 2) on a surface saturated with chlorine (low photon flux-high chlorine pressure) the etch rate is limited by the number of charge carriers reaching the surface.

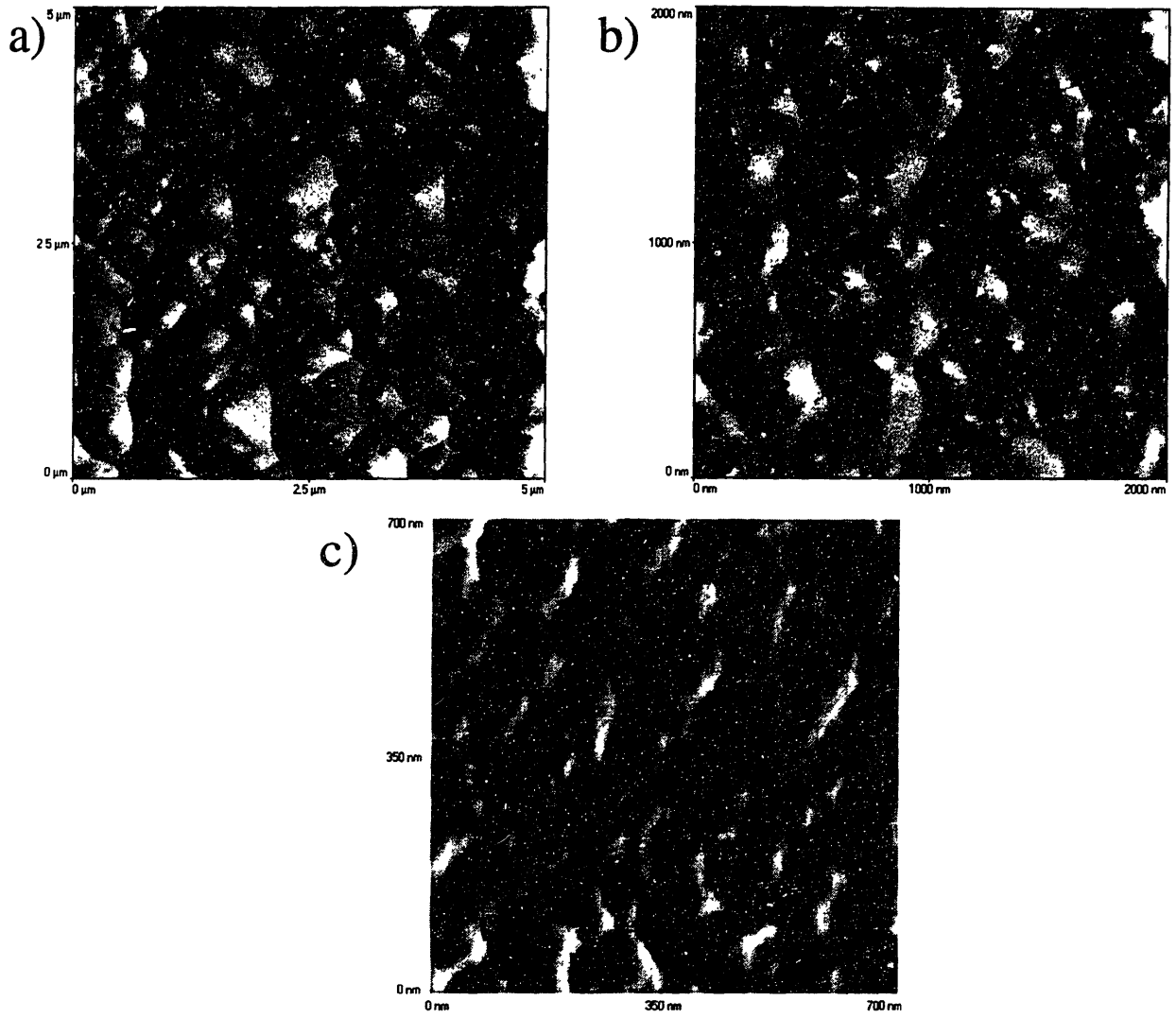

Figure 3.6-Morphology evolution in UV/Cl_2 silicon etching. All samples were etched for 3 minutes at an initial sample temperature of nominally 175°C. Samples a, b and c were etched at 25, 10 and 1 torr respectively. Note that the length scales on a, b and c are 5, 2 and 0.7 µm respectively.

Figure 3.6 illustrates the morphology evolution of the silicon surface due to UV/Cl_2 etching. The AFM images in figure 3.6 have been "shaded" to enhance the features. The images represent depressions in the surface although at first glance they may appear to be raised from the surface due to the image processing. A similar morphology is observed on all of the surfaces, although the length scale of the features is a function of reaction pressure. The scan size has been adjusted so that the features appear the same size regardless of pressure for

purposes of comparison. At 1 torr the initial stage of cell formation is observed. At 10 torr the cells are fairly well formed although the edges of the cells are somewhat smooth in appearance. At 25 torr the cells are well defined with deep pits at the center of each cell. The size of the cells increases with reaction pressure and scales roughly as $P^{1/2}$.

3.1.2 Conclusions

Although this study was by no means exhaustive and was admittedly a peripheral part of this work, it does provide some insight into the mechanisms of the UV/Cl_2 silicon etching process. At the very least, we have demonstrated that there is a parameter space where substrate etching and roughening can be minimized, a critical factor to establish UV/Cl_2 as a viable wafer cleaning process.

It is obvious from reading this work that photoetching of silicon with chlorine (and photoetching of semiconductors in general) is a complex and subtle process. Multiple effects are operative simultaneously, and the dominant mechanism is a strong function of the process conditions. Radiative enhancement of the etching process in particular is a complex process, where multiple mechanisms can be operative even at the same wavelength. This is also the case in the UV/Cl_2 copper removal process discussed in the next chapter.

Generally, our results agree well with what has been observed in the literature. We have presented evidence that the UV/Cl_2 etching of silicon is driven by both gas phase production of reactive chlorine radicals, and the production of electron-hole pairs in the substrate and possibly through direct bond breaking by energetic photons. The major discrepancy is the absence of a strong doping effect on the etching process, which has been observed by some other investigators[3]. The general mechanism elucidated by Houle[1] seems

most applicable to this process. For semiconductor surfaces without fixed surface potential (i.e. isolated substrates in contact with a gas) both charge carriers should migrate to the surface to maintain charge neutrality. In this situation, since both charge carriers are involved, the influence of doping (especially at the part per million level) may not be pronounced.

3.2 Substrate Etching with UV/ClF_3

Substrate etching with UV/ClF_3 was also studied. The etching of silicon as well as thermal and doped (BPSG) silicon oxide and silicon nitride (Si_3N_4) were investigated. Most of this work was in support of work performed by Gray *et al.*[12,13] The work will be discussed briefly here, and specifically the significant experiments that were performed in our laboratory are discussed. For more details, the interested reader is referred to the two papers by Gray *et al.* The samples and experimental methods for these experiments are as described in Section 3.2.1 B.

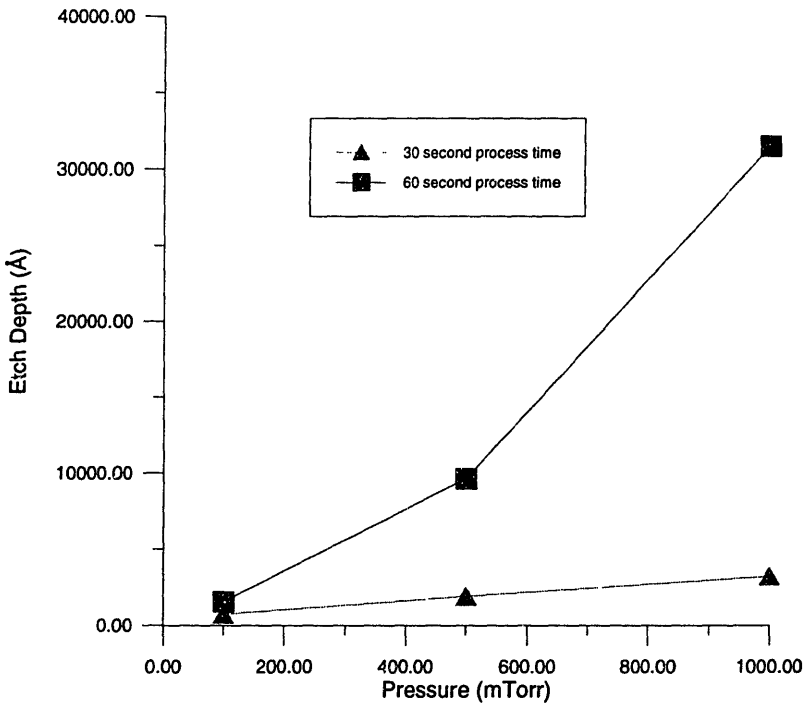

Figure 3.7-Silicon etching data for UV/ClF_3 at nominally 80°C.

Figure 3.7 illustrates some etch rate data for the reaction of silicon with UV/ClF_3. Immediately apparent is that the etch rates in this process are much higher than those observed in the UV/Cl_2 process. This is due to the fact that with UV/ClF_3, the primary etchant species is F atoms, which etch silicon more readily than Cl atoms. In fact, the spontaneous etch rate with ClF_3 is ~1/2 that of UV/ClF_3, indicating that ClF_3 dissociates readily on the silicon surface. Due to the vigorous etching behavior of UV/ClF_3, it was not considered as a viable process for trace metal removal from silicon surfaces.

The influence of UV radiation on the UV/ClF_3 etching of SiO_2, BPSG and Si_3N_4 was investigated. In the etching of thermal oxide, the spontaneous etch rate and the etch rate under parallel UV incidence (i.e. the wafer was directly exposed to UV-dissociated ClF_3 but not directly exposed to UV radiation) was not significantly different. When the wafer was exposed to direct UV, the etch rate approximately doubled. This would indicate that, as in the case of UV/ClF_3 silicon etching, ClF_3 readily dissociates on the oxide surface, and in fact, gas phase radical production is not required to maintain a significant etch rate. The etch rate increase under direct illumination indicates that, as in the case of UV/Cl_2 silicon etching, there is a UV stimulated surface process that enhances the etch rate. The picture with BPSG is not as clear, since the etch rate of BPSG is much more temperature dependent than the thermal oxide etch rate. Because of this, the temperature rise due to light exposure makes an unambiguous interpretation of the results difficult. Spontaneous etching and a significant etch rate enhancement with direct UV exposure was observed in experiments with BPSG. With Si_3N_4, the picture is quite different. Etch rate enhancement of ~ an order of magnitude was

observed between spontaneous and parallel incidence (gas phase dissociation) etching. With direct UV illumination, the etch rate approximately doubled.

3.3 References

[1] F.A. Houle, Applied Physics A 41, 315-330 (1986).

[2] T.J. Chuang, Surface Science 178, 763-786 (1986).

[3] H. Okano, Y. Horiike, and M Sekine, Jap. J. Appl. Phys., part 1, Vol. 24, No. 1, 68-74 (1985).

[4] E. Ikawa, S. Sugito, and Y. Kurogi, Surface Science, Vol. 183, 276-288 (1987).

[5] W. Sesselmann, E. Hudeczek and F. Bachmann, J. Vac. Sci. Technol. B 7 (5), 1284-1294.

[6] C.M. Paulsen-Boaz, T.N. Rhodin, and C.C. Lang, Applied Surface Science 79/80, 72-78 (1994).

[7] D.C. Montgomery, Design and Analysis of Experiments, p. 457, John Wiley and Sons, New York (1984).

[8] E.A. Ogryzlo, D.E. Ibbotson, D.L. Flamm, and J.A. Mucha, J. Appl. Phys. 67 (6), 3115-3120 (1990).

[9] C.I.H. Ashby, D.R. Myers, R.M. Biefeld, and A.K. Datye, J. Appl. Phys. 68 (5), 2406-2410 (1990).

[10] C.I.H. Ashby and D.R. Myers, Journal of Electronic Materials, Vol. 20, No. 9, 695-699 (1991).

[11] R.F. Pierret, Semiconductor Fundamentals: Volume 1, R.F. Pierret and G.W. Neudek, Eds., Addison Wesley, Reading, MA, pp. 68-69 (1988).

[12] D.C. Gray, J.W. Butterbaugh, C.F. Hiatt, A.S. Lawing, and H.H. Sawin, J. Electrochem. Soc., Vol. 142, No. 11, 3859-3863 (1995).

[13] D.C. Gray, J.W. Butterbaugh, C.F. Hiatt, A.S. Lawing, and H.H. Sawin, J. Electrochem. Soc., Vol. 142, No. 11, 3919-3923 (1995).

Chapter 4

Transition Metal Removal with UV Excited Chlorine

The mechanism of transition metal removal in the UV/Cl_2 process has been investigated. The surface mechanism which drives copper removal has been established through a series of wavelength dependent experiments. Copper removal involves the photon stimulated reduction and desorption of copper chlorides, and not silicon etching or $Si_XCl_YM_Z$ complex formation as has been postulated in the literature. By balancing the effects of chlorination (pressure) and reduction (UV flux to the surface), efficient copper removal is achieved at lower pressure and temperature than has been reported previously. We have evidence that this mechanism is generally applicable to transition metals. The removal of transition metals from a SiO_2 surface is complicated by both spontaneous and UV enhanced oxidation processes. In the case of iron the oxidizing tendency of the SiO_2 surface is overcome by elevating the process temperature. In the case of nickel, removal from an oxide surface has not been achieved in the temperature range studied here (below ~140°C).

4.1 Introduction

The removal of trace metallic contamination is an important step in the semiconductor fabrication process. Trace metals can cause degradation of device performance if not removed from the wafer surface[1,2,3,4,5]. Metallic contamination can arise from a number of sources including wet chemicals[6,7], photoresist[8,9], and redeposition of sputtered materials from chamber surfaces during plasma processing[2,10,11]. In this work, we have focused on the removal of trace amounts of transition metals form silicon and silicon dioxide surfaces.

Several methods have been investigated as potential gas phase metal removal processes. Some of these methods are summarized in Chapter 1. We have concentrated on UV excited chemistries for several reasons; 1) UV/halogen processes have been demonstrated as being effective for removing metal contaminants from wafer surfaces, 2) the combination of gas phase and surface photolytic processes yields interesting chemistry and 3) although these processes have been demonstrated as being effective, the mechanism of metal removal is not well understood.

Most of our work in this area was devoted to the mechanism of transition metal removal in the UV/Cl_2 process. Using our surface analytical tools to understand the chemistry of the process allowed us to elucidate the mechanism by which copper is removed in this process. We demonstrate that copper removal is driven not by the gas phase production of chlorine radicals and silicon etching as was previously believed, but by surface photolytic processes including photon stimulated copper chloride reduction and desorption. In fact, silicon etching is not required for copper removal and gas phase radical production generally works against efficient copper removal. Our understanding of the mechanism has allowed us to develop improved process recipes that are more efficient and less aggressive in terms of silicon etching and surface roughening. The copper removal mechanism can be applied generally to transition metals, and the removal of nickel and iron are also discussed in this chapter. The tendency of these metals to spontaneously oxidize when deposited on an oxide surface (and even a bare silicon surface with sub-monolayer oxygen coverage in the case of iron) adds additional complexity to the interpretation of the removal mechanism. Another area of limited study was combined UV/Cl_2-Vapor phase HF processing for metals removal. This work yielded some promising results and is a good candidate for further study.

4.2 The Mechanism of Copper Removal with UV/Cl_2

4.2.1 Background

Copper is known to deposit from the hydrofluoric acid solutions commonly used to strip oxides in semiconductor fabrication[12,13,14]. Aluminum alloyed with a small percentage of copper is commonly used to fabricate connecting metal lines in device fabrication. Copper is also present in small quantities in 304 and 316 stainless steels, common chamber fabrication materials. Copper is also a candidate metal for interconnects in the next generation of devices.

Particularly because of its tendency to deposit from HF solutions and therefore remain on the surface in an "HF last" cleaning sequence, copper is one of the most difficult transition metals to remove by traditional wet cleaning techniques. A dry cleaning process, ultraviolet excited chlorine (UV/Cl_2), has shown promise in removing transition metals, including copper[15,16,17,18]. UV/Cl_2 involves the simultaneous exposure of the wafer surface to chlorine gas and ultraviolet light. In addition to transition metal removal, we have successfully applied the UV/Cl_2 process to the removal of fluorocarbon polymer residue after an oxide etch in fluorocarbon gases in both conventional RIE[19] (Chapter 6) and high density systems (Chapter 7).

The mechanism by which UV/Cl_2 acts to remove transition metals from the wafer surface is poorly understood. Molecular chlorine absorbs UV radiation in the wavelength range of 250-400 nm and dissociates to form atomic chlorine[20,21]. It is well known that atomic chlorine will etch bulk silicon at conditions where molecular chlorine will not[22,23]. In Chapter 3, it was illustrated that in the UV/Cl_2 system, surface photolysis due to direct UV exposure is the dominant contributor to the observed silicon etch rate, since the etch rate

increased by two orders of magnitude with simultaneous exposure to UV radiation and atomic chlorine versus atomic chlorine alone. It is also well known that the UV/Cl_2 process does not etch silicon dioxide at the conditions typically used for a metals removal process, although substrate etching through a native oxide has been observed[18,24]. Sugino *et al.*[17,25] contend that gas phase chlorine radical generation and silicon etching are crucial to transition metal removal with UV/Cl_2. Furthermore, it has been suggested that a "lift-off" mechanism[26,27], joint evaporation of metal chlorides with $SiCl_x$ species[28], or the formation of a metal-Si-Cl complex[27,28], are potential processes by which metals with low vapor pressure chlorides are removed from the surface in the UV/Cl_2 process. All of these mechanisms, whether explicitly or implicitly, involve silicon etching.

Conversely, we have observed similar removal efficiencies from bare silicon and silicon dioxide surfaces with the UV/Cl_2 process suggesting that substrate etching is not required for metal removal. Figure 4.1 illustrates these results. In these cleaning experiments, Cl_2 gas was introduced to the chamber and the Cl_2 pressure was allowed to stabilize at 5 torr for 30 seconds prior to UV exposure. As will be discussed in the following section, the copper would be totally converted to $CuCl_2$ before UV exposure was initiated. The initial sample temperature was 50 °C for both samples. After a timed exposure to Cl_2, the chamber was evacuated and the UV exposure was maintained for 3 minutes. During this post Cl_2 exposure, the temperature rise which resulted from UV exposure at pressure was reversed, and in fact the final sample temperature was lower than the initial temperature. In these experiments, the additional UV exposure did not result in additional copper removal. An initial coverage of $\approx 7 \times 10^{13}$ copper atoms/cm^2 (0.05 ML) is removed to the detection limit from both surfaces. In none of our experiments have we observed any significant difference

between the removal efficiency of copper from oxide and silicon surfaces when the full lamp fluence was used. We contend that substrate etching is not required for copper removal with UV/Cl_2, and that copper is removed from the surface as a chloride at a rate far higher, and temperatures much lower, than would be expected from equilibrium considerations.

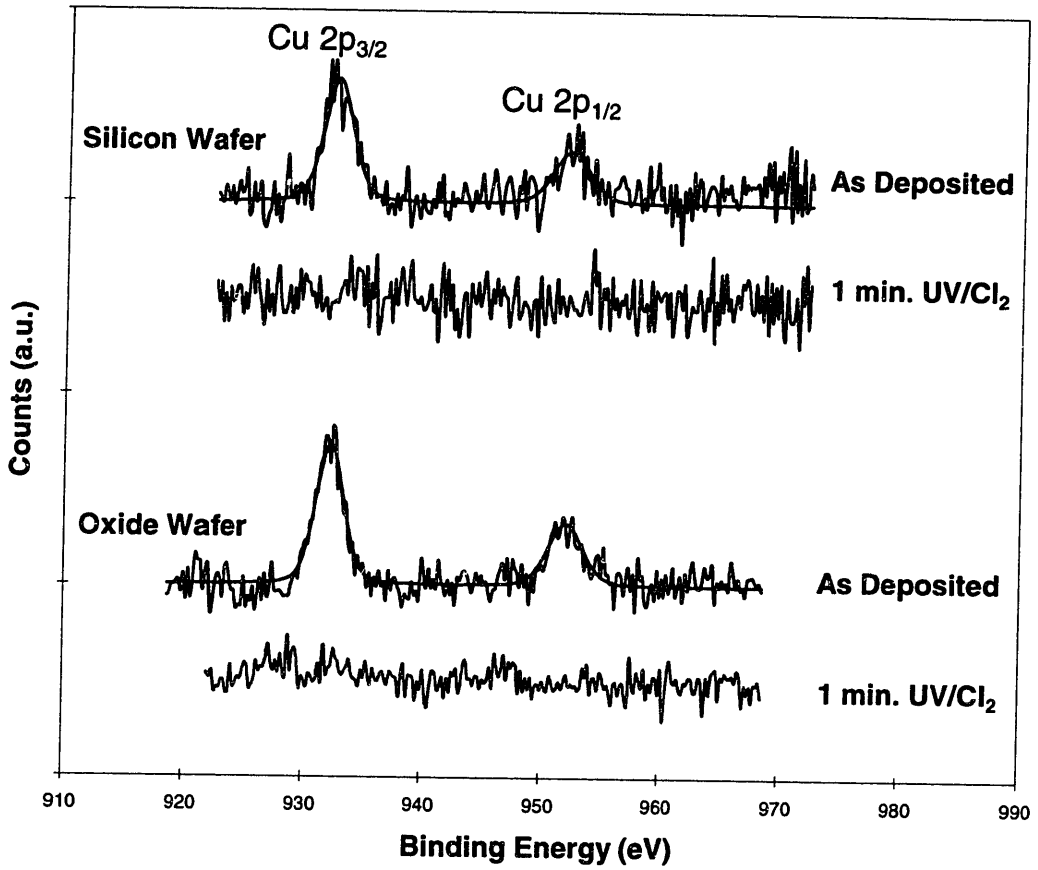

Figure 4.1-Copper 2p photoelectron emission spectra illustrating copper removal from bare silicon and silicon dioxide wafer surfaces at 5 torr Cl_2 and 50°C with a 1 minute UV/Cl_2 process.

The goal of this work was to separate the effects of gas phase (dissociation of molecular chlorine) and surface (photochemical reduction of surface chlorides) photolysis in order to obtain a clearer understanding of the mechanism by which UV/Cl_2 acts to remove copper from wafer surfaces. To accomplish this we selected two wavelengths from the output

spectrum of our illumination system, one centered at 367 nm and one centered at 245 nm. The 367 nm wavelength is contained within the region in which chlorine absorbs ultraviolet light, so we would obtain significant gas phase dissociation of molecular chlorine in this region. The 245 nm wavelength is not contained within the chlorine absorption band and is the most energetic wavelength available, so we would expect to obtain the most efficient reduction of copper chlorides while not causing significant gas phase dissociation.

The reaction of bulk copper with chlorine has been studied and we can draw some useful analogies between our system and other investigations. Sesselmann and Chuang[29] have studied the reaction of thin copper films with Cl_2 gas. They report the formation of a $CuCl_X$ ($0<X<2$) film on the surface, with X increasing in the near surface region as the film thickness is reduced, and as the chlorine pressure (or dosage) is increased. Li *et al.*[21] have studied the same reaction under illumination by synchrotron radiation between 105-400 nm. They also reported the formation of a thick $CuCl_X$ layer and observed enhanced reaction rates due to gas phase dissociation of molecular chlorine in the wavelength range 150-400 nm. Of interest here is their observation of reduced reaction efficiency when wavelengths in the range 105-150 nm where added to the 150-400 nm radiation. They attributed this reduction in $CuCl_X$ production efficiency to "destruction processes" which could potentially include enhanced desorption of Cl surface species or destruction of generated $CuCl_X$ molecules. Similar to the picture of the UV/Cl_2 process that will be presented here, they stated that; "the efficiency of light induced processes is determined in general by a balance of competing processes and this balance...is very sensitive to the exposure conditions and the spectral distribution."

Copper etching in chlorine has also been studied. Winters[30] reported that the volatile product is $(CuCl)_3$ below about 580 °C and that the activation energy for $(CuCl)_3$ desorption is

33 kcal/mol, or roughly equal to the heat of sublimation of $(CuCl)_3$. Laser stimulated etching studies have also been performed. Sesselmann, Marinero and Chuang[31,32] studied the interaction of 355 and 532 nm laser pulses on desorption from solid CuCl samples and from a chlorinated copper surface. They found that the desorption threshold behavior and mass distributions of the desorbed products were inconsistent with a thermal desorption process and suggested that photon stimulated desorption processes based on electron-hole interactions and direct bond breaking may be important mechanisms to laser induced product desorption. Van Veen *et al.* have studied laser induced etching of CuCl[33] and copper with chlorine[34] with 308 nm radiation. They reported that the major products desorbed from both surfaces were CuCl and $(CuCl)_3$. They also reported that the evaporation process differs significantly from thermally programmed desorption.

The photosensitivity of copper chlorides has been documented. Sesselmann and Chuang[29] have reported the reduction of $CuCl_2$ to CuCl due to exposure to Mg Kα radiation, and the stability of CuCl under the same exposure. In contrast, Galeotti *et al.*[35] have reported the reduction of CuCl to metallic copper under Mg Kα radiation. Taylor[36] has reported the thinning of a layer of CuCl on copper by exposure to bright sunlight for three minutes. The thinning of the CuCl layer was accompanied by the formation of tetrahedral crystals which he suspected were metallic copper. Ashkalunin and Valov[37] have reported the formation of copper particles due to the photolysis of CuCl in copper halide photochromic glasses upon exposure to UV radiation. Fleisch and Mains[38] have demonstrated that 254 nm UV radiation can reduce CuO and Cu_2O to metallic copper. In their experiment, the surface of a copper oxide pellet was reduced from an initially mixed oxide composition to metallic copper within the sampling depth of XPS ($\approx$ 50 Å) in $\approx$ 10 hours.

We have shown that the UV/Cl_2 process is capable of removing $\approx$ ½ ML of mixed Cu_2O/CuO from a silicon surface in 2 minutes. Figure 4.2 illustrates these results. In this experiment, the copper was deposited from a spiked HF solution. The initial coverage of copper oxide is converted to $CuCl_2$, after 1 minute of UV/Cl_2 exposure, and the oxygen given up by the copper reacts with silicon to form SiO_2. This can be determined by; 1) the change in the Cu 2p satellite structure (Figure 4.2a), 2) the disappearance of the Cu-O bonding contributions in the O 1s spectrum (Figure 4.2b) and 3) the growth of the Si-O contribution in both the O 1s and Si 2s (Figure 4.2c) spectra. This removal process must involve the reduction of the oxide either through a photon stimulated process, exposure to reactive chlorine, or a combination of the two. Pozanski[39] has outlined a mechanism whereby molecular chlorine attacks copper oxides to form copper chlorides.

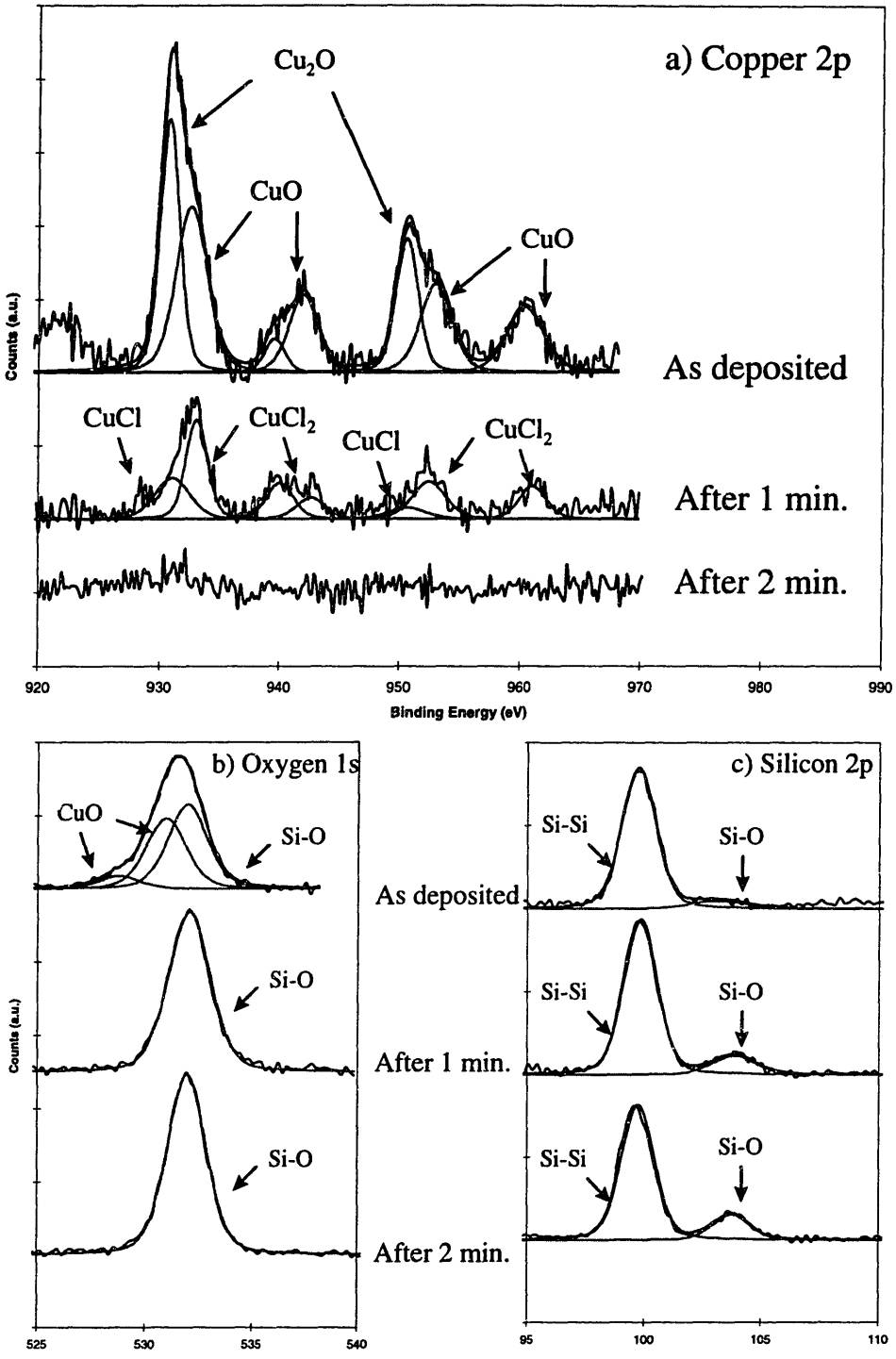

Figure 4.2-Copper 2p, oxygen 1s, and silicon 2p photoelectron emission spectra illustrating the removal of ~1/2 ML of mixed copper oxide from a silicon wafer surface. The UV/Cl_2 process was performed at 5 Torr Cl_2 and nominally 120°C. The initial mixed copper oxide is converted to $CuCl_2$ after 1 minute of UV/Cl_2 exposure. After 2 minutes, copper is removed to close to the XPS detection limit.

In this section it will be demonstrated that exposure to UV radiation can reduce $CuCl_2$ and CuCl. In addition, it will be shown that this reduction process is what drives the removal of copper from wafer surfaces in the UV/Cl_2 cleaning process. Copper desorbs from the wafer surface as CuCl, or possibly the trimer $(CuCl)_3$. Optimization of copper removal efficiency from a wafer surface involves maintaining a balance between chlorination of surface copper (which is enhanced both by gas phase dissociation of molecular chlorine in the wavelength range 250-400 nm and surface processes which may be enhanced over a broad wavelength range but are definitely operative at 245 nm) and photochemical reduction of $CuCl_2$ to the volatile product CuCl. By selecting conditions such that a dynamic equilibrium between these competing processes which results in a high surface concentration of CuCl is maintained, copper removal can be achieved at conditions which are not only more efficient, but less aggressive to a silicon wafer surface and more attractive to wafer processing than what has previously been reported.

4.2.2 Results

Samples used in these experiments were 1 cm x 1 cm n-type Si <100> 1-5 Ω-cm with a 4000 Å thermal oxide. All samples were pre-cleaned before processing. The cleaning sequence was as follows: 1) wipe and rinse with isopropyl alcohol, 2) immerse in 49 % aqueous hydrofluoric acid for 20 seconds, 3) rinse in distilled water, 4) repeat step 2, 5) repeat step 3, 6) repeat step 1. Samples were blown dry with N_2 before insertion into the vacuum chamber, and between the cleaning steps as appropriate. Samples were inserted into the vacuum chamber within 60 seconds of the completion of the cleaning sequence. This cleaning sequence resulted in a minimum amount of carbon contamination. Silicon surfaces

subjected to this sequence exhibited strongly hydrophobic character, and XPS analysis indicated oxygen coverage on the order of 1/3 monolayer.

The experiments discussed in this section were performed with the reactor and UV illumination system described in Chapter 2.1.1. The full spectrum output of the illumination system, with the chlorine absorption band and the two wavelengths chosen for these experiments superimposed for reference, is illustrated in Figure 4.3.

XPS surface analysis and trace metal deposition were achieved in the chamber described in Chapter 2.1.3. Copper sputter deposition is described in detail in section 2.1.4. The pass energy was set at 50 eV. Since the silicon metal peak arising from the substrate is easily distinguishable at all stages of these experiments, all spectra were normalized such that the silicon 2s peak was fixed at an energy of 99.75 eV in order to correct for charging effects.

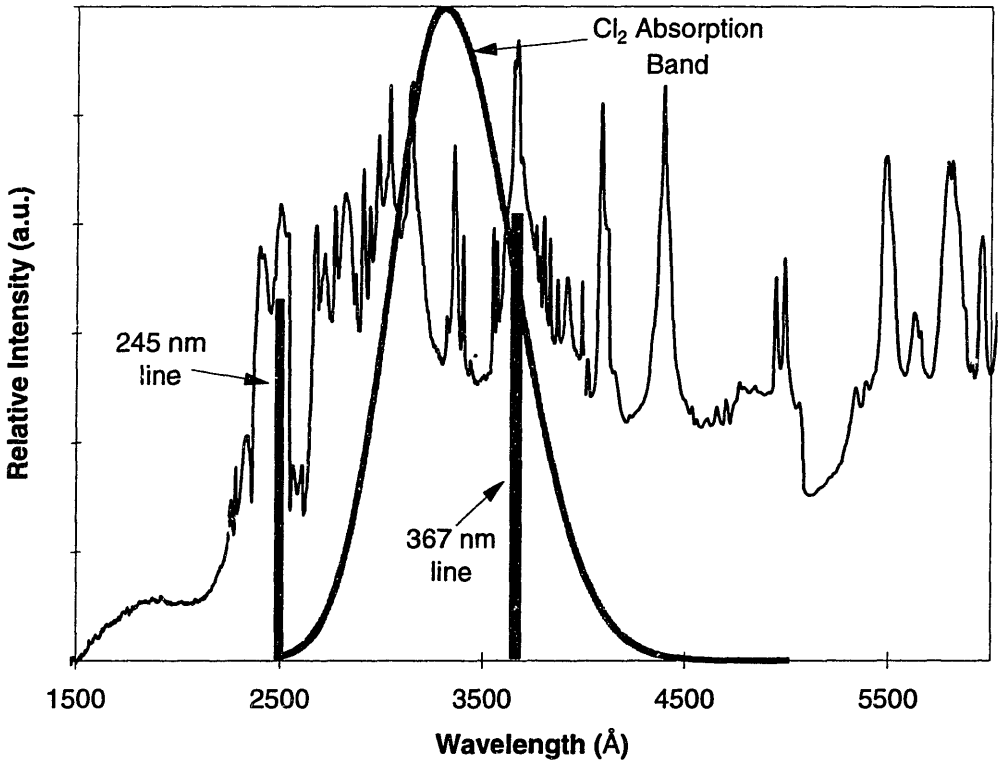

Figure 4.3-Full spectrum output of the UV illumination system used in these experiments. The chlorine absorption band and the two wavelengths chosen for these experiments are superimposed.

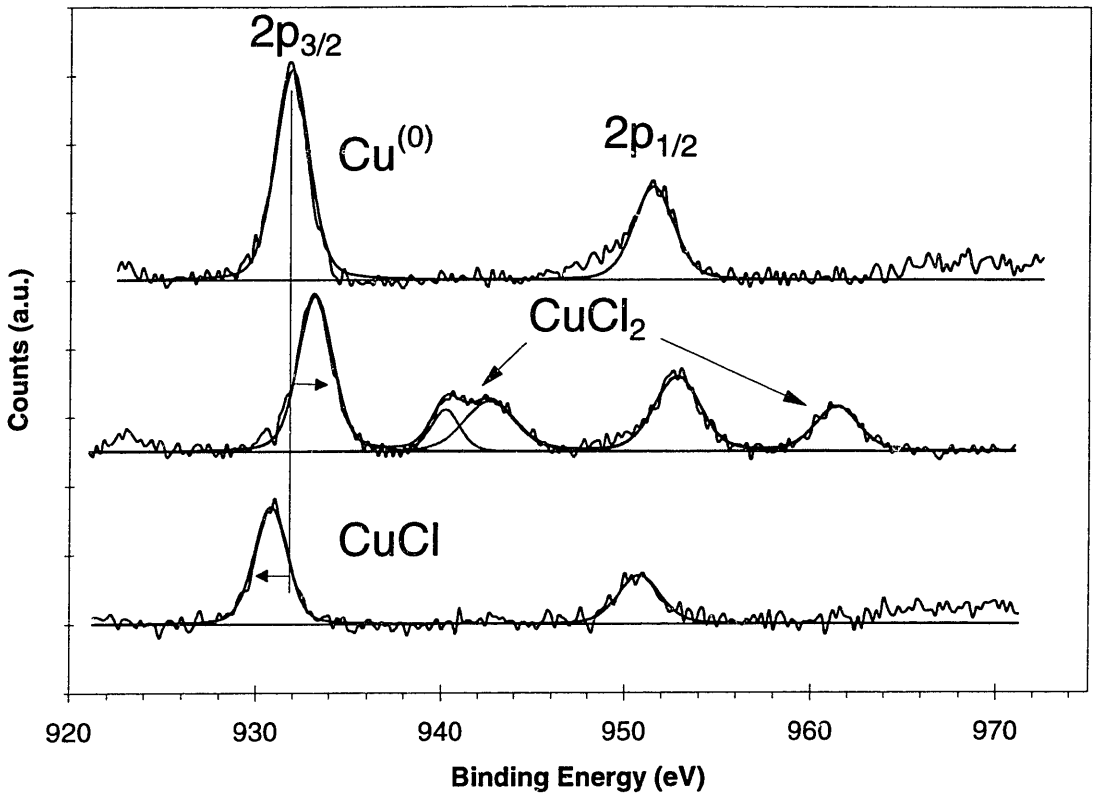

Figure 4.4-Copper 2p photoelectron emission spectra illustrating the identifying features of copper metal($Cu^{(O)}$), CuCl and $CuCl_2$.

A. Chemical State Identification

Of great importance to the analysis of our results is the ability to positively identify and distinguish the chemical states of copper and its' chlorides. Fortunately, XPS is an excellent tool to accomplish this. Figure 4.4 illustrates the 2p photoelectron spectra obtained for copper metal, copper dichloride and copper monochloride. The $2p_{3/2}$ photoemission line for metallic copper occurs at 931.9 eV. $CuCl_2$ is easily distinguished from the metal and the monochloride by the presence of characteristic "shake-up" satellites, and a positive binding energy shift with respect to the metal. The main line for $2p_{3/2}$ photoemission from $CuCl_2$ occurs at nominally 932.6 eV although there is a tendency for the main peak to shift to higher binding energy at higher coverage, and it has been observed as high as 933.2 eV in our

experiments. It is difficult to distinguish CuCl from metallic copper on the basis of peak shape alone, since CuCl does not exhibit the satellite structure observed in $CuCl_2$, although there is some broadening of the main peak of CuCl relative to the metal. We have observed a consistent downward shift in binding energy of the $2p_{3/2}$ and $2p_{1/2}$ photoemission lines which we attribute to formation of CuCl. The $2p_{3/2}$ peak for CuCl occurs at nominally 931.2 eV, but has been observed as low as 930.4 eV. Other investigators[29,40] have reported a similar, though significantly smaller in magnitude, downward shift for CuCl. The differences between the shifts observed in this work and those reported in the literature are attributable to the fact that we are working with low coverages (less than 0.125 ML) of dispersed metals on a silicon surface and the literature values are obtained on bulk materials. Copper metal and CuCl are distinguishable by comparison of the x-ray induced $L_3M_{4,5}M_{4,5}$ Auger line[29,35]The main line due to the Auger transition exhibits a shift of $\approx$ 3 eV between the two states. Because of the low coverage levels studied in these experiments, the Auger transitions were very weak in intensity and were generally not used, but in a few cases where they could be clearly distinguished, we did observe this shift. Similarly, the Cl 2p photoemission could potentially be used for identification[29], but in this case, the signal due to surface Cu-Cl bonding is obscured by the signal due to surface Si-Cl bonding.

Another point that is worth mentioning in regard to XPS of copper chlorides is the tendency of CuCl and $CuCl_2$ to reduce under x-ray exposure as discussed above. Because of this phenomenon, copper spectra were recorded immediately upon exposure of the sample to the x-ray source in all of these experiments, and the collection of the copper spectra were completed within 1 hour of initial exposure to the x-ray source. We did not observe significant reduction of copper chloride due to X-ray exposure in any of these experiments.

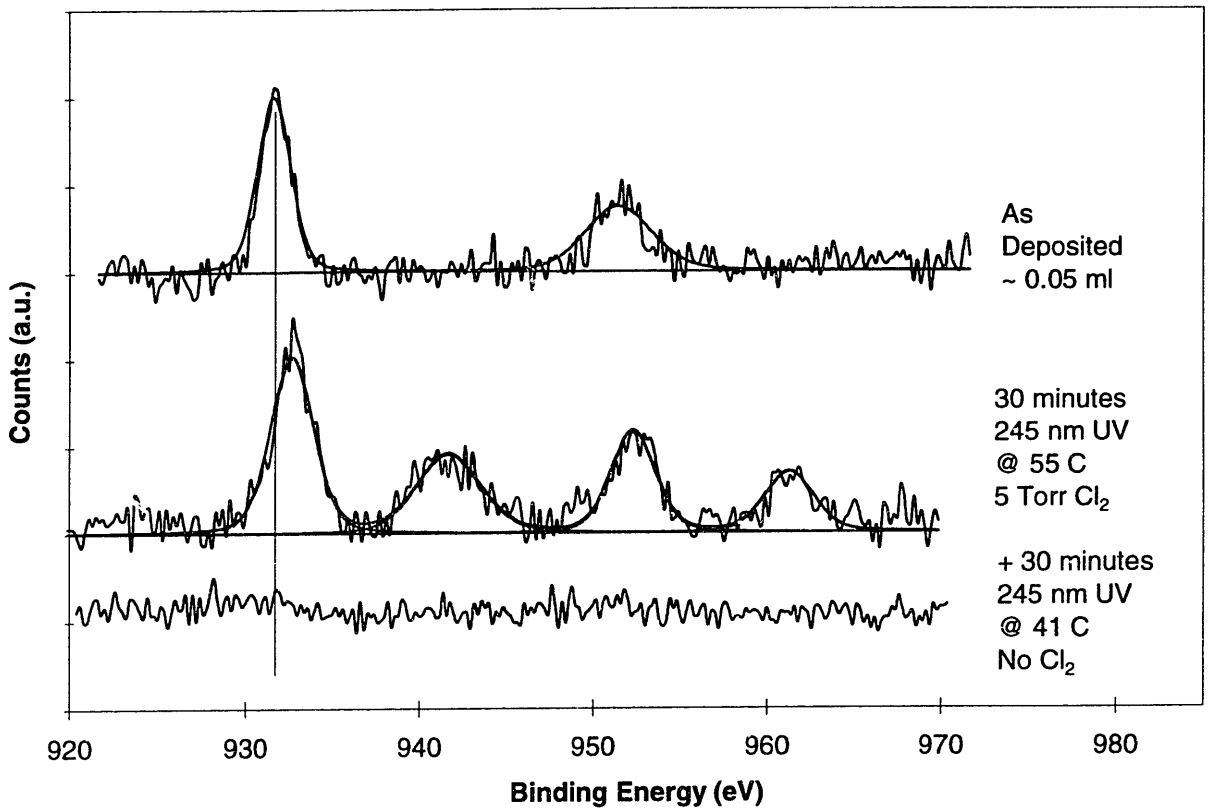

Figure 4.5- Copper 2p photoelectron emission spectra illustrating the effect of 245 nm UV on $CuCl_2$. All of the peak intensities are directly comparable. In the as deposited state at a coverage of 0.05 ML (uppermost spectrum), the copper is metallic. After 30 minutes at 5 Torr chlorine and 55 °C (middle spectrum), all of the copper is present as $CuCl_2$. After 30 minutes of 245 nm UV exposure under vacuum (bottom spectrum), all of the $CuCl_2$ has been removed form the surface.

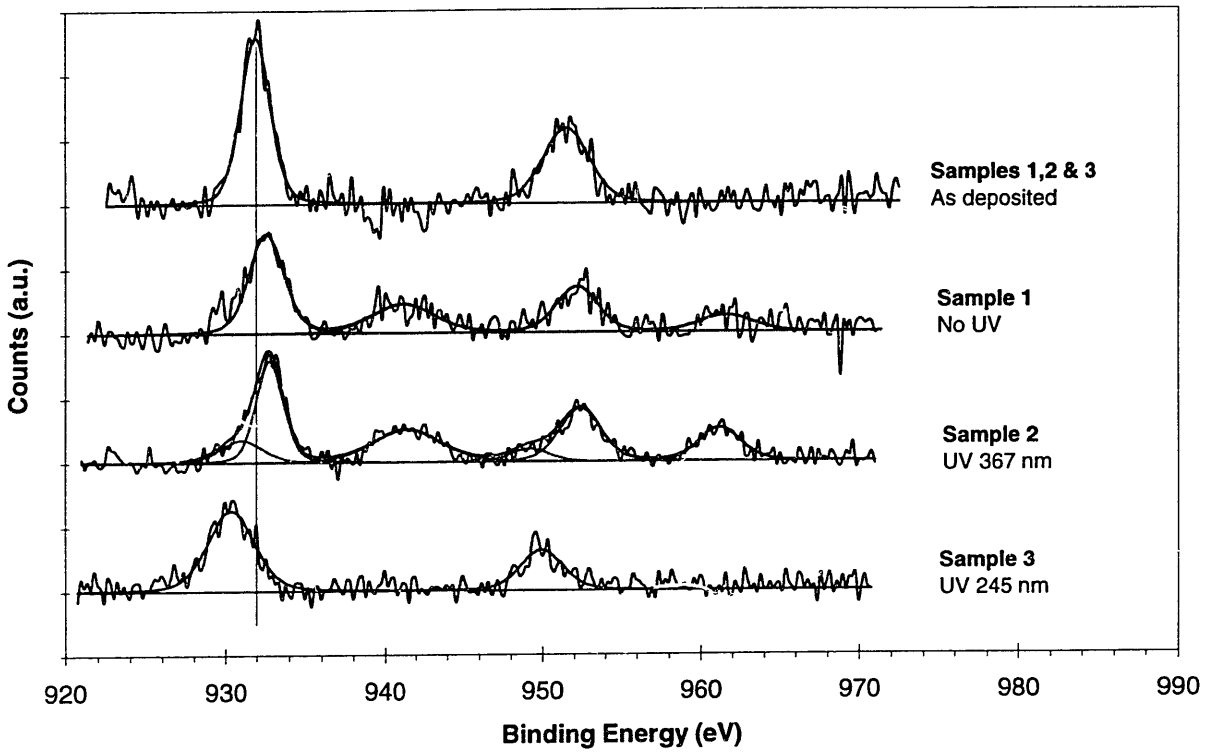

Figure 4.6-Copper 2p photoelectron emission spectra illustrating the effect of UV illumination at 20 mTorr chlorine and 65 °C. All peak intensities are directly comparable. All three samples were characterized by the initial level of metallic copper (~0.1 ML) as represented by the uppermost spectrum. Sample 1 (second spectrum from the top) was held in the dark for 60 minutes, and all of the copper on this sample is present as $CuCl_2$. Sample 2 (third spectrum from the top) was exposed to 367 nm UV for 60 minutes, and the majority of the copper on this sample is present as $CuCl_2$. Sample 3 (bottom spectrum) was exposed to 245 nm UV for 60 minutes, and all of the copper on this sample is present as CuCl. The intensity of the copper emission is slightly reduced on sample 3 relative to samples 1 & 2.

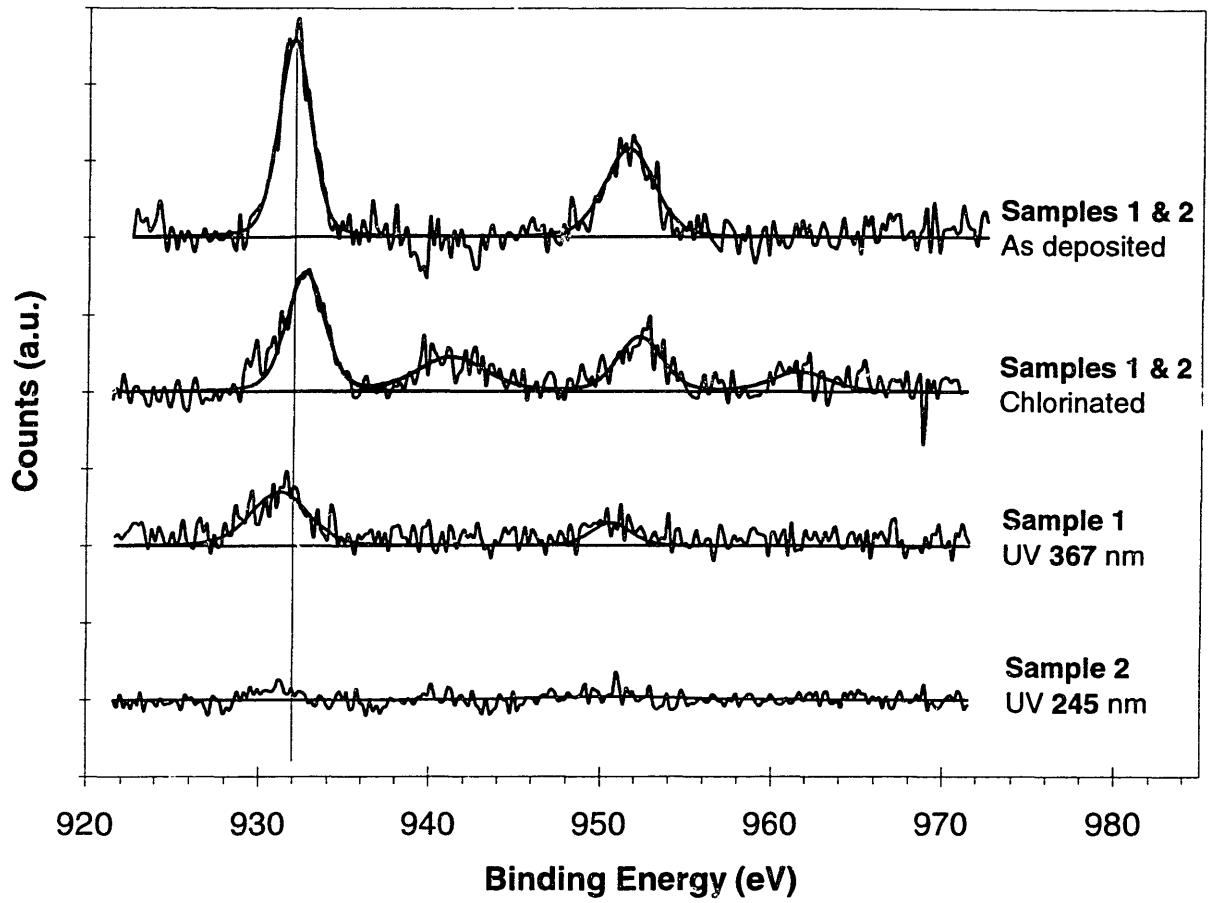

Figure 4.7- Copper 2p photoelectron emission spectra illustrating the effect of UV illumination on pre-chlorinated samples. All peak intensities are directly comparable. Both samples were characterized by the initial level of metallic copper (~0.1 ML) as represented by the uppermost spectrum and the initial level of $CuCl_2$ represented by the second spectrum from the top. Sample 1 (third spectrum from the top) was exposed to 367 nm UV for 60 minutes. Most of the copper on sample 1 is present as CuCl, and the intensity of the copper photoemission is significantly reduced. Sample 2 (bottom spectrum) was exposed to 245 nm UV and the copper has been removed almost to the detection limit.

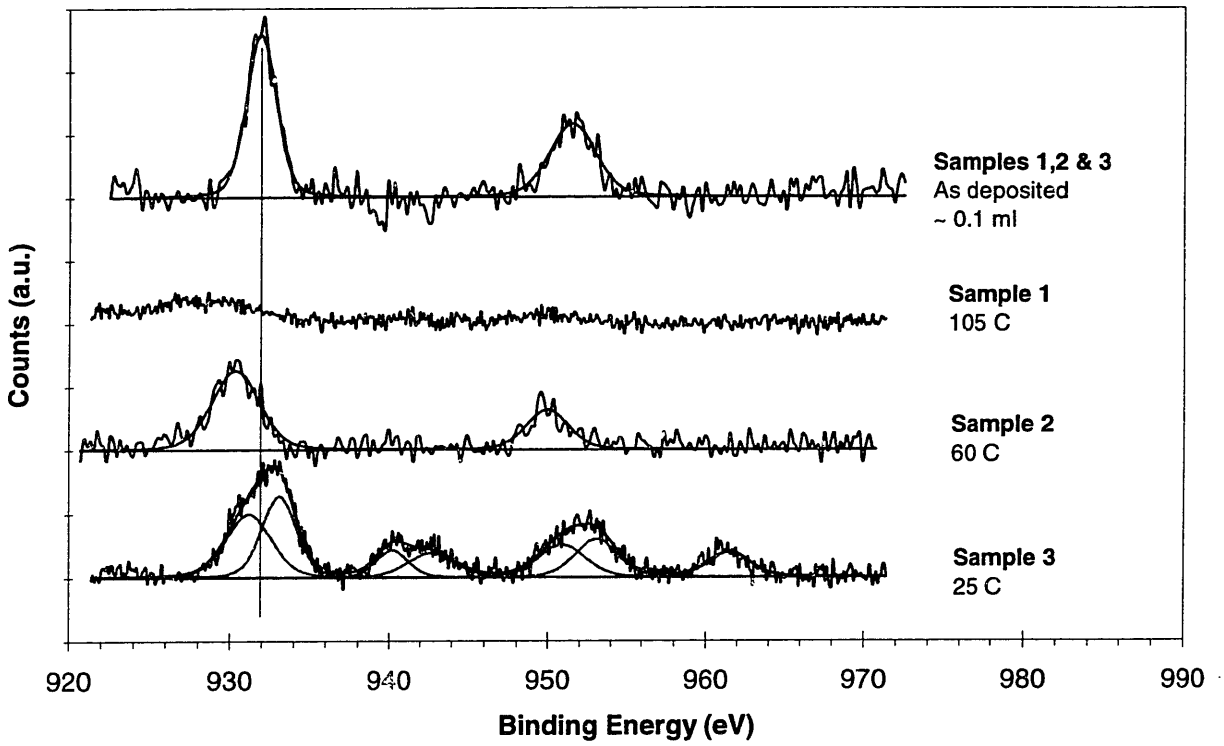

Figure 4.8- Copper 2p photoelectron emission spectra illustrating the effect of temperature on the removal process with 245 nm UV in 20 mTorr chlorine. All peak intensities are directly comparable. All three samples were characterized by the initial level of metallic copper as represented by the uppermost spectrum. Sample 1 was held at 105 °C for 60 minutes and the copper was removed to nearly the detection limit. Sample 2 was held at 60 °C for 60 minutes and all of the copper left on the surface is present as CuCl. The intensity of the copper photoemission is significantly reduced. Sample 3 was held at 25 °C for 60 minutes and the copper left on the surface is a mixed composition of CuCl and $CuCl_2$. The intensity of the copper photoemission is not significantly reduced.

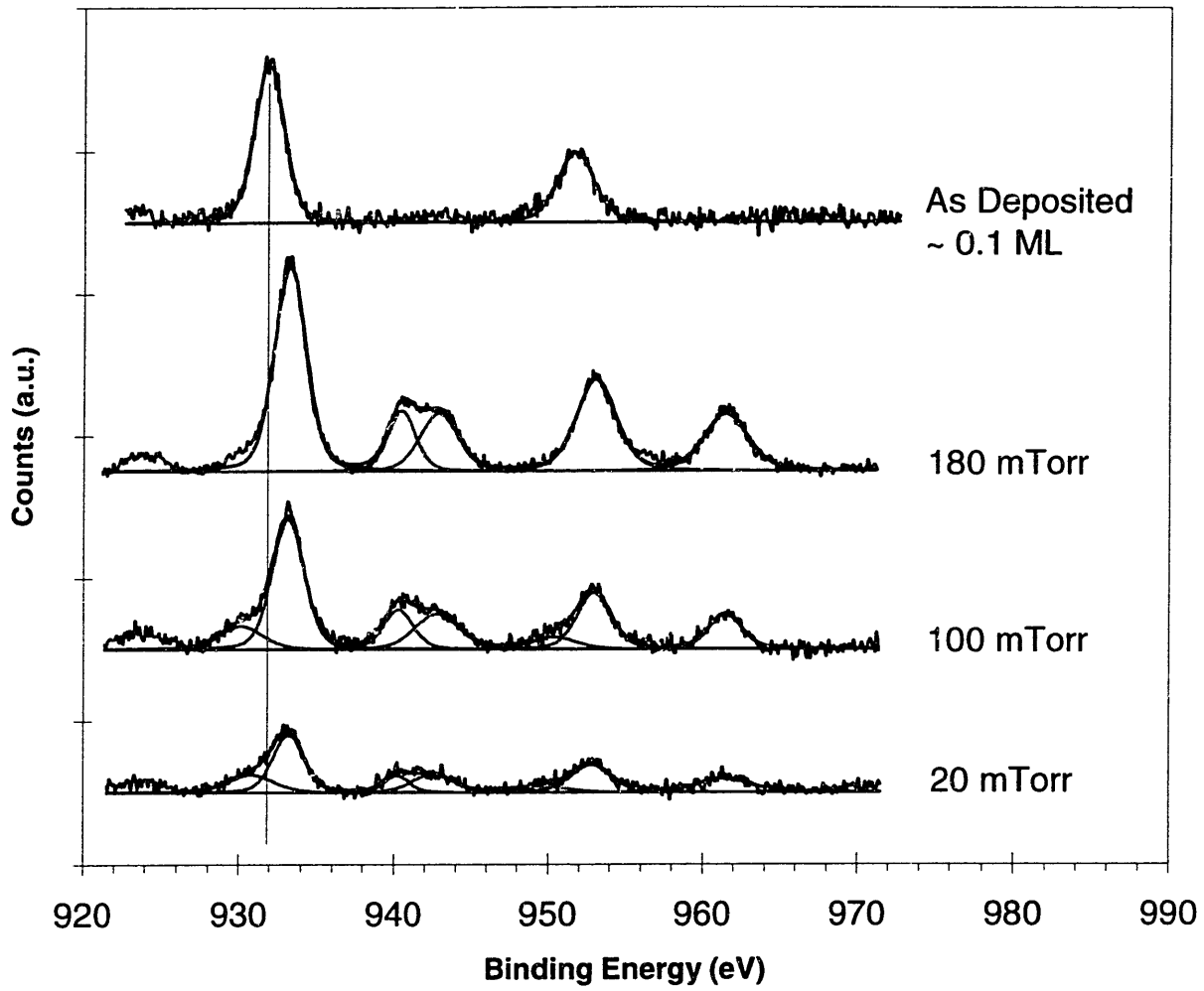

Figure 4.9- Copper 2p photoelectron emission spectra illustrating the effect of chlorine pressure on the removal process with 245 nm UV at 75 °C. All peak intensities are directly comparable. All three samples were characterized by the initial level of metallic copper as represented by the uppermost spectrum. Sample 1 was held at 180 mTorr for 60 minutes. All of the copper left on the surface is present as $CuCl_2$. The intensity of the copper photoemission is increased relative to the initial level. Sample 2 was held at 100 mTorr for 60 minutes. Most of the copper left on the surface is present as $CuCl_2$ and a small quantity of CuCl is also detected. The intensity of the copper photoemission is slightly increased relative to the initial level. Sample 3 was held at 20 mTorr for 60 minutes and the copper left on the surface is a mixed composition of CuCl and $CuCl_2$. The intensity of the copper photoemission is slightly reduced relative to the initial level.

B Wavelength Resolved Experiments

Fig. 4.5 illustrates the effect of surface photolysis on copper removal in the UV/Cl_2 process. An initial copper coverage of ≈0.05 ML is exposed to 5 Torr of chlorine for 30

minutes under 245 nm illumination. Little or no copper is removed from the surface, and further, all of the copper that remains on the surface is present as $CuCl_2$. However, when the $CuCl_2$ sample is reinserted into the reaction chamber and exposed to 245 nm illumination under vacuum, the copper is removed from the surface to the detection limit of XPS.

Fig. 4.6 illustrates the results from a similar experiment. Three different samples are represented in this figure, all of which are characterized by the initial coverage level of ≈0.1 ML as shown in the uppermost spectrum. All three samples were exposed to 20 mTorr of chlorine for 60 minutes at 65°C. Sample 1 was not illuminated. Sample 1 exhibits exclusively $CuCl_2$ with little or no copper removal. Sample 2 was illuminated with 367 nm light. Sample 2 is indistinguishable from sample 1. Most of the remaining copper is in the form of $CuCl_2$, and the level of coverage is almost identical to sample 1. Sample 3 was illuminated with 245 nm light. In contrast to samples 1 & 2, the copper on sample 3 is in the form of CuCl. Sample 3 also exhibits a lower coverage level than samples 1 & 2.

In the experiments illustrated in Fig. 4.7, both samples were pre-chlorinated by gas exposure in the dark, and then illuminated under vacuum. Both samples were characterized by an initial level of metallic copper of ≈0.1 ML as shown in the uppermost spectrum, and the level of $CuCl_2$ shown in the second spectrum after chlorination by exposure to chlorine gas in the absence of UV light. Samples 1 and 2 were then illuminated under vacuum with 367 nm and 245 nm light, respectively. Both samples 1 & 2 exhibit copper removal. The copper remaining on the surface of sample 1 is in the from of CuCl. Copper is removed to close to the XPS detection limit on sample 2 so chemical state identification is difficult although there does appear to be a slight increase in intensity in the vicinity of the CuCl line.

Fig. 4.8 illustrates the effect of temperature under 245 nm illumination. The three samples all possessed an initial coverage of ≈0.1 ML as shown in the uppermost spectrum. All three samples were illuminated with 245 nm light at a chlorine pressure of 20 mTorr for 60 minutes. Sample 1 was held at 105 °C and exhibits copper removal to nearly the XPS detection limit. Sample 2 was held at 60 °C. All of the copper remaining on sample 2 is in the form of CuCl, and about half of the initial level of copper has been removed. Sample 3 was held at 25 °C. Sample 3 exhibits a mixed composition of $CuCl_2$ and CuCl, and exhibits little or no reduction in the initial level of copper.

Fig. 4.9 illustrates the effect of chlorine pressure under 245 nm illumination. Again three samples are represented. All three samples were characterized by the initial coverage level of ≈0.1 ML as shown in the uppermost spectrum and were illuminated with 245 nm light at 75 °C for 60 minutes. A clear increase in the efficiency of copper removal is evident as the pressure is decreased from 180 mTorr to 20 mTorr. It should be mentioned that the data illustrated in Fig. 8 were obtained with a different quartz tube than the rest of the data presented in this work. A slight attenuation of the light flux to the sample surface due to the different tube would explain the qualitative difference in removal efficiency and chemical state between sample 3 in Fig. 4.9 and the data illustrated in Fig. 4.8.

4.2.3. Discussion

A. Reaction Without UV Illumination in the Sub-monolayer Coverage Regime

Before launching into an explanation of the results illustrated in Figs. 4.5-4.9, a few points need elaboration. First, $CuCl_2$ has a negligible vapor pressure in the temperature range

studied here (10^{-16} Torr at 75 °C)[41,42] and is stable in the absence of reducing UV illumination. From previous work, we know that $CuCl_2$, once formed, will remain on the surface unless it is reduced to the more volatile compound CuCl. Second, in the dark, copper exposed to chlorine exhibits a coverage dependent removal efficiency. Figure 4.10 illustrates this effect. Below ≈0.13 ML, copper is not removed from the surface upon exposure to molecular chlorine at a temperature of 45 °C, as judged by the intensity of photoemission due to the sum of the main $2p_{3/2}$ peak and the $2p_{3/2}$ satellite of $CuCl_2$. Above this coverage, and continuing to a coverage of at least 0.4 ML, about half of the initial copper on the surface is removed. We have attributed this coverage dependence to the formation of the trimer $(CuCl)_3$. Winters[30] reported that copper volatilizes in the form of the trimer $(CuCl)_3$ when the surface concentration of chlorine is greater than one monolayer, but at sub-monolayer chlorine coverage the volatile product is CuCl. By analogy, at low copper coverages, i.e. in the dispersed coverage regime, formation of the trimer would be inhibited and copper should volatilize primarily as CuCl. At greater copper coverages, where island formation was observed (see Chapter 2), the volatilization behavior would begin to resemble the bulk and copper should volatilize as $(CuCl)_3$.

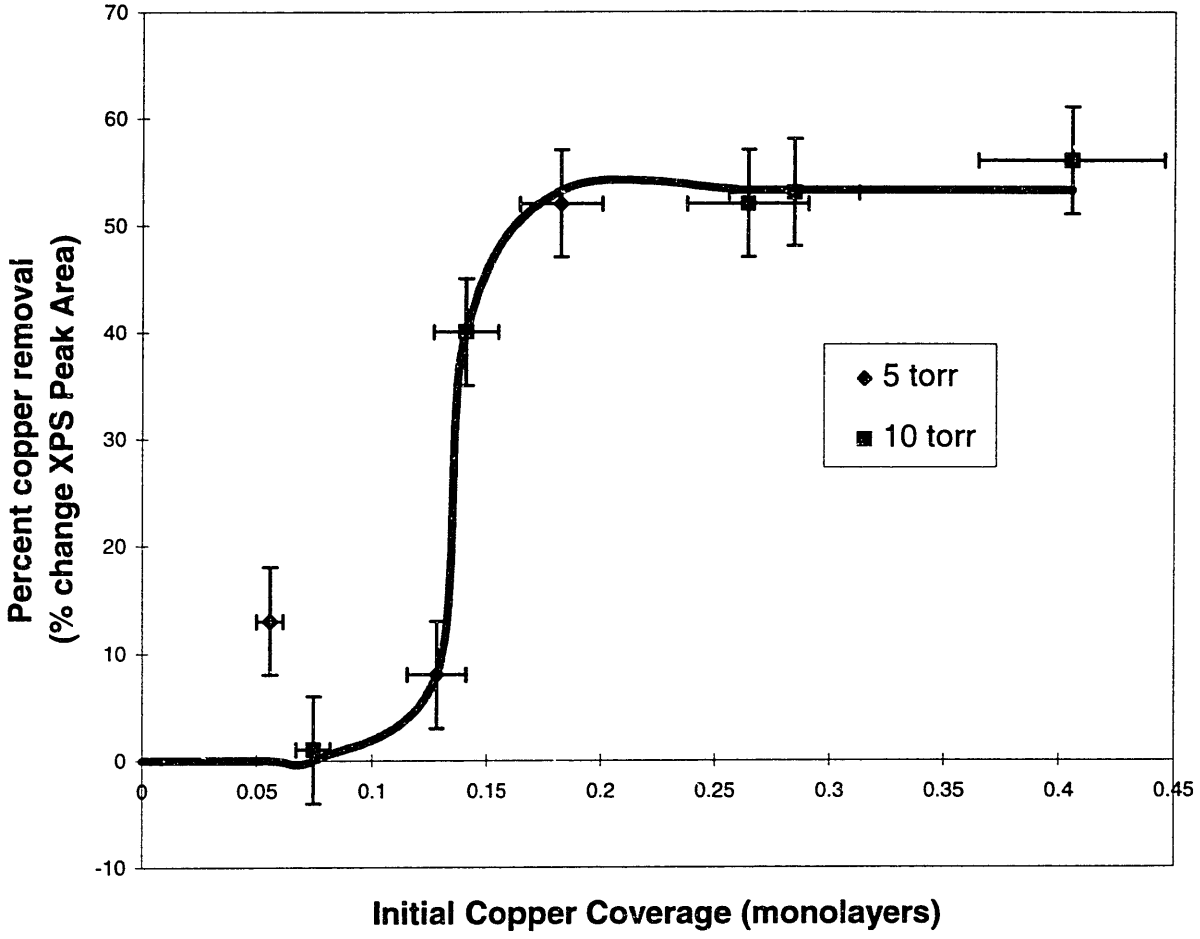

Figure 4.10-XPS data illustrating copper removal in the dark with molecular chlorine at 45°C. The copper coverage is based on a monolayer thickness of 2.55 Å and the sputter system calibration described in Chapter 2. Below ~ 0.13 ML, copper is not removed from the wafer surface. After, exposure to chlorine, all of the copper remaining on the wafer surface was present as $CuCl_2$.

B. Chloride Reduction as a Pathway to Enhanced Copper Removal

The chlorination reaction of copper proceeds according to the reactions illustrated below:

$$Cu + \tfrac{1}{2} Cl_2 \leftrightarrow CuCl \quad (1)$$

$$CuCl + \tfrac{1}{2} Cl_2 \leftrightarrow CuCl_2 \quad (2)$$

For reaction (1) $\Delta G°_f$ = -28.625 kcal/mol, and for reaction (2) $\Delta G°_f$ = -12.923 kcal/mol. Therefore, formation of $CuCl_2$ is favored thermodynamically, and as we have stated above we have observed that $CuCl_2$ is stable and involatile on the wafer surface in the absence of a reducing agent. In the bulk, where the chlorination reaction is diffusion controlled, complete reaction to $CuCl_2$ does not readily occur. But, as the results of Sesselmann and Chuang[29] show, as the film thickness is reduced or the chlorine dose to the surface is increased, the fraction of $CuCl_2$ in the reacted film increases. The formation of $CuCl_2$ in our system can be viewed as an extreme case of the experiments of Sesselmann and Chuang, i.e. an ultra-thin film coupled with a high dosage of chlorine.

In order to facilitate copper removal, the $CuCl_2$ must be reduced to form the volatile product CuCl; e.g. UV illumination can reduce $CuCl_2$ to CuCl. Fig. 4.5 illustrates this clearly. In the presence of an abundance (5 Torr) of chlorine, $CuCl_2$ is formed and remains on the wafer surface even under 245 nm illumination for 30 minutes. When the gas is evacuated, however, the situation is much different. After 30 minutes of 245 nm illumination under vacuum, all of the initial $CuCl_2$ is removed. Therefore, the UV illumination must be reducing the $CuCl_2$ to the more volatile compound CuCl. Fig. 4.6 illustrates a dynamic equilibrium situation. In the presence of 20 mTorr chlorine, an initial copper coverage of 0.1 ML (sample 1) is converted to $CuCl_2$. In the absence of any reducing radiation, this $CuCl_2$ remains on the surface, even after 60 minutes. Sample 2 was reacted under identical conditions, except that it was exposed to 367 nm radiation for the duration of the experiment. Since 367 nm radiation is efficient at dissociating molecular chlorine, and therefore, promoting chlorination of surface copper, most of the copper remaining on the surface is in the form of $CuCl_2$ and the reduction efficiency is no better than without UV exposure. There does appear to be a slight reduction

taking place at 367 nm, however in a chlorine atmosphere, any reducing tendency is overwhelmed by the chlorination due to gas phase production of atomic chlorine. Sample 3 illustrates that the photochemical reduction process dominates at low chlorine pressure in the absence of gas phase dissociation. With 245 nm exposure all of the copper remaining on the surface is in the form of CuCl. Since no significant chlorine dissociation takes place in the gas phase at 245 nm, reduction of $CuCl_2$ to CuCl dominates in the low pressure regime. Judging from the XPS intensity, there is also an increase in removal efficiency with 245 nm illumination.

Notice that the main $2p_{3/2}$ photoemission peak from $CuCl_2$ is more intense compared to the initial copper signal in Fig. 4.5 than sample 1 in Fig. 4.6. In general[43] we have observed that there is little pressure dependence on the chlorination process in the dark between 20 mTorr and 10 Torr, so the pre- and post- process XPS spectra on a sample run in the dark at 5 Torr would look like sample 1 in Fig. 5. In samples run at 5 Torr, chlorination is more efficient with 245 nm light than it is in the dark, judging from the higher relative intensity of the $2p_{3/2}$ photoemission peak which indicates a greater coverage of $CuCl_2$. It appears that there must be a promotion of chlorination due to surface processes which is promoted by 245 nm radiation and is dominant in the high pressure regime.

Fig. 4.7 illustrates further that 367 nm light is also capable of reducing $CuCl_2$. Samples 1 & 2 were chlorinated in the dark and then exposed to UV illumination under vacuum at a base pressure of $\approx 10^{-7}$ Torr. Clearly, the initial level of copper is reduced in both cases. Although 367 nm radiation is capable of $CuCl_2$ reduction, 245 nm light is much more efficient at chloride reduction and removal, removing copper almost to the detection limit of our XPS after 1 hour.

C. Temperature and Pressure Dependence of the Removal Process

Fig. 4.8 illustrates the temperature dependence of copper removal under 245 nm illumination at 20 mTorr chlorine pressure. As the temperature of the process is increased from room temperature to 105°C, the composition of the surface copper shifts from predominately $CuCl_2$ to exclusively CuCl, and the efficiency of removal increases dramatically. This behavior is attributable to three possible factors, 1) the decrease in the reaction probability of chlorine on copper as a function of temperature, 2) thermal enhancement of CuCl desorption, and 3) thermal enhancement of the photon stimulated reduction process (as will be shown in the next section, iron and nickel exhibit a temperature threshold below which the photon stimulated reduction of II states is not observed). Winters[30] reported that the reaction probability of chlorine on bulk copper decreases between 30 and 150°C, reaching a minimum at about 200 °C. Assuming that the sticking behavior on dispersed copper is similar to the bulk, then as the temperature is increased, photoreduction should begin to dominate because the surface copper is less likely to react. Or possibly, as in the case of iron and nickel, the barrier to photon stimulated reduction is lessened as the temperature is increased and the reduction process becomes more efficient. Both of these scenarios would have a similar effect to a reduction in chlorine pressure, forcing the equilibrium (as defined in equations 1 & 2) to the left. Coupled with the chlorination/reduction behavior is the enhancement of product desorption due to thermal considerations. The vapor pressure of $(CuCl)_3$ increases by ~5 orders of magnitude and the equilibrium constant for the reaction $CuCl_{(s)} \leftrightarrow CuCl_{(g)}$ increases by ~7 orders of magnitude[44] over this temperature range. So, whether the volatile product is CuCl or $(CuCl)_3$, the

thermodynamic driving force for product desorption is increasing as the temperature is increased from 25 to 105 °C.

Fig. 4.9 illustrates the pressure dependence of copper removal under 245 nm illumination. Again we see evidence of a radiation promoted surface process by which chlorination is enhanced at 245 nm. As mentioned earlier, a sample reacted in the dark will exhibit virtually no pressure dependence in regards to $CuCl_2$ formation in the pressure range 20 mTorr-10 Torr. At this initial copper coverage level and reaction temperature, the post-process $2p_{3/2}$ main peak intensity will be about half of the initial $2p_{3/2}$ intensity (similar to the relative intensity ratio illustrated by sample 1 in Fig. 5). But here we see the intensity of the main $2p_{3/2}$ peak due to $CuCl_2$ increase until at 180 mTorr, it is actually more intense than the as deposited metallic copper. (Note: this also raises the point that the photoelectron cross section for $CuCl_2$ is actually higher than that for metallic copper. We have been unable to find reliable reported data for these relative values in the literature, but we suspect that this effect may be peculiar to the low coverage regime which we are investigating). As the chlorine pressure is increased from 20 mTorr to 180 mTorr, the removal efficiency decreases and the relative proportion of $CuCl_2$ increases. This trend is purely attributable to the increased chlorine flux to the surface. As the pressure is increased, chlorination due to surface processes which are promoted by the 245 nm radiation begin to dominate over $CuCl_2$ reduction.

D. Mechanism of Product Desorption in the UV/Cl_2 Process

In addition to the chlorination/reduction of metallic copper, the desorption of the volatile product is an important aspect of the copper removal process, and this is the aspect of

the process which we least understand. But we do have evidence that the volatile species is the monomer CuCl. First of all, Figure 4.1 illustrates equal removal efficiency of copper from both oxide and bare silicon surfaces. This result implies that the product is not a silicon metal halide complex, since UV/Cl_2 does not attack oxide at these conditions and formation of the complex would be unlikely from silicon oxide etching. This result coupled with other results where we have witnessed no copper removal under conditions where 1000's of Å of silicon were etched[43] also rules out the possibility of a "lift-off" mechanism in which $CuCl_X$ species would be carried off with the silicon etch products. In addition, in none of the experiments presented in this work did we witness significant surface roughening, which we have correlated with substrate etching in this process. Especially in the case of the runs illustrated in Fig. 4.7, where the samples were pre-chlorinated in the dark (molecular chlorine does not etch silicon at these conditions) and exposed to UV under vacuum, significant substrate etching would be unlikely. Therefore we must conclude that substrate etching or the formation of silicon metal halide complexes are not necessary to remove copper from a wafer surface. The stability of $CuCl_2$ on the surface and the negligible volatility of $CuCl_2$ in this temperature range would preclude the possibility of $CuCl_2$ as a volatile product. We must conclude, as in the case of the bulk copper etching and CuCl desorption studies discussed in Section 4.2.1, that the volatile species in the UV/Cl_2 removal of copper from wafer surfaces is a form of CuCl. We do not totally discount the possibility that CuCl may desorb as the trimer $(CuCl)_3$, but our results with the coverage dependence of copper removal with chlorine in the dark illustrated in Figure 4.10 would suggest that the desorbing species is the monomer CuCl. In support of our hypothesis, Sesselmann *et al.*[31,32] and van Veen *et al.*[33,34] have studied laser induced desorption from both CuCl and chlorinated copper surfaces. The product distributions

from both surfaces contain significant quantities of the monomer CuCl, and in the case of desorption from solid CuCl, which we believe is most analogous to our system, the desorbed species is primarily CuCl. These results are significantly different than those obtained in thermal desorption experiments, where the desorbed products are almost exclusively due to the trimer $(CuCl)_3$[30].

In other discussions of the UV/Cl_2 process, including our own[15,26,27,28], the vapor pressure of the metal chloride species has been proposed as a metric for judging the potential to remove metals at a given temperature. Judging from our current results, this concept is not applicable here. Using vapor pressure as a metric implies thermodynamic equilibrium, whereas the flooding of the wafer surface with energetic photons can give rise to a fundamentally non-equilibrium process. Equilibrium considerations do not account for the observed removal rates since the equilibrium vapor pressure of the trimer is $\sim 10^{-12}$ Torr at 75 °C[41,42,45], and the concentration of the monomer is ~25 orders of magnitude less than that of the trimer in the gas phase[46]. These values correspond to an equilibrium flux of $\sim 10^{-6}$ and 10^{-31} ML/sec for the trimer and monomer respectively. This should not be interpreted as meaning that the monomer cannot desorb from the surface, only that *at equilibrium*, it does not exist in significant quantity in the gas phase. We suspect that, as has been suggested in the case of laser induced desorption from stoichiometric CuCl and chlorinated copper surfaces, there is a photon stimulated process which causes CuCl to desorb from the surface at temperatures much lower, and in quantities much higher, than would be predicted from vapor equilibrium considerations or a purely thermal process.

Another piece of evidence supporting the hypothesis of a photon induced desorption process is the power dependence of copper removal. Although we have not performed an

exhaustive study on the effect of UV fluence, we show in the next section that with the full lamp output, copper is removed from the wafer surface ~2 orders of magnitude faster than with monochromatic radiation. The full lamp fluence is also ~2 orders of magnitude more intense than the monochromatic radiation. Of course, coupled with this increase in power is the introduction of additional wavelengths, but we have already shown that the reduction process is operative over a broad wavelength range.

E. Copper Removal Processes Based on the Proposed Mechanism

Figs. 4.11 and 4.12 illustrate two different copper removal processes which we have developed based on our understanding of the mechanism. It should be noted that with these processes, the monochromator was removed from the illumination system and the full lamp fluence illuminated the sample. Under these conditions the sample receives a much higher photon flux than the experiments illustrated in Figs. 4.5-4.9 and the kinetics of the removal process are greatly accelerated.

Fig. 4.11 illustrates what we have termed a "pulsed process". In this process we expose the sample to chlorine in the dark then evacuate the chamber and expose the sample to UV illumination under vacuum at a pressure of $\approx 1 \times 10^{-7}$ Torr for 30 seconds at 40 °C. Fig. 9 shows the initial levels of metallic and chlorinated copper as well as the post process spectra for each of three UV exposure cycles. Note, the sample was exposed to chlorine before each UV cycle although only one of the chlorinated spectra is shown. After the first UV exposure cycle in Fig. 4.11, the chemical state of all the copper is metallic. With the much more intense and broad band radiation from the full lamp fluence, UV illumination is capable of completely reducing copper chlorides to metallic copper in less than thirty seconds. In fact, the efficiency

of the reduction process is such that we must repeat the chlorination/UV exposure cycle three times to remove copper to the XPS detection limit. The UV reduction kinetics are sufficiently rapid that some of the copper is reduced completely to $Cu^{(0)}$ before it can desorb from the surface as CuCl.

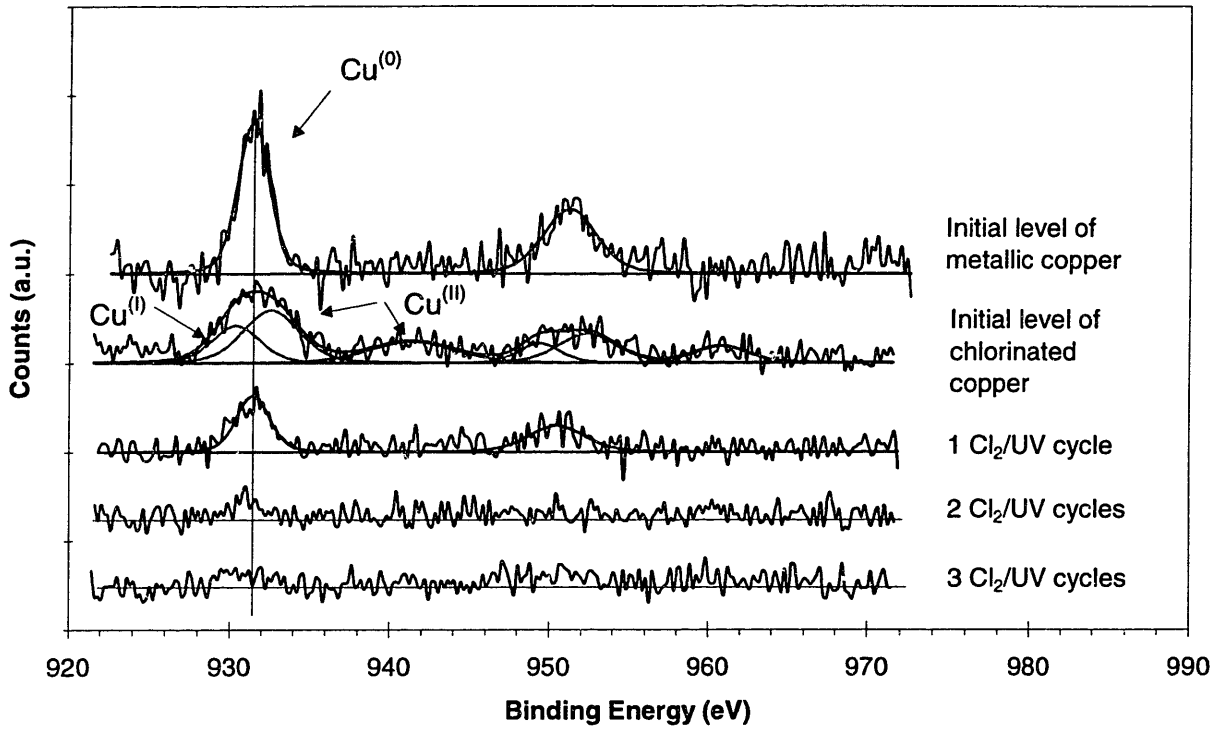

Figure 4.11-Copper 2p photoelectron emission spectra illustrating a "pulsed process". This sample was subjected to three cycles of chlorination in 5 Torr chlorine at 40 °C in the dark followed by full spectrum UV exposure under vacuum for 30 seconds at 40 °C. The initial level of metallic copper (~0.1 ML) is represented by the uppermost spectrum. The second spectrum from the top illustrates the chemical state and relative copper coverage after the first chlorination step. After three chlorination/UV exposure cycles the copper has been removed to nearly the detection limit. Note, that after a UV exposure, copper is completely reduced to the metallic state.

Fig. 4.12 illustrates a low temperature, low pressure process. In this process, the sample is exposed to UV illumination in flowing chlorine at a pressure of 50 mTorr for 60 seconds at 75 °C. Copper is removed to near the detection limit after this process. Again this

data illustrates the greatly increased reduction rate due to the exposure to the more intense broad band radiation of the full lamp fluence.

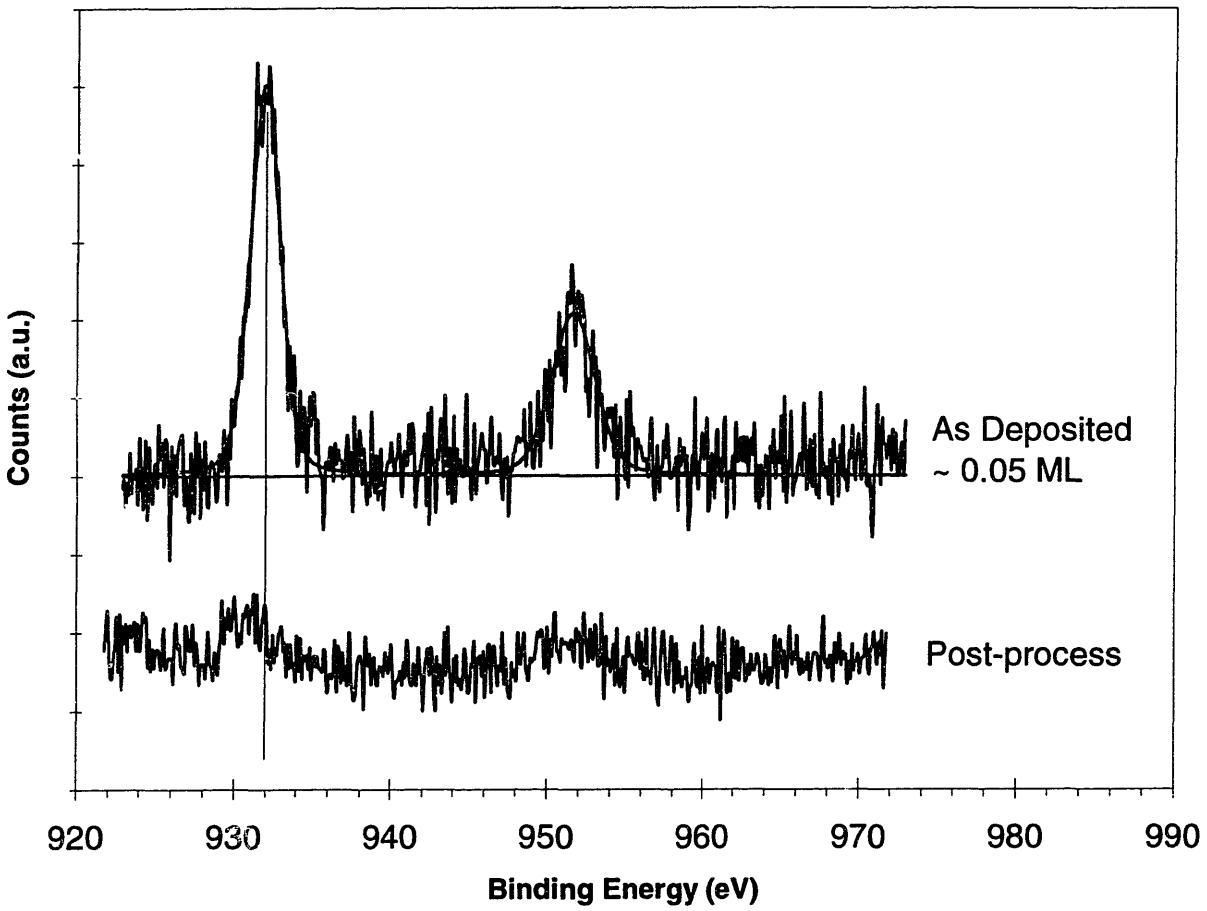

Figure 4.12-Copper 2p photoelectron emission spectra illustrating a low pressure/low temperature process. An initial copper coverage (top spectrum) of ~0.05 ML was exposed to full spectrum UV in 50 mTorr chlorine for 60 seconds at 75 °C. Copper is removed to nearly the detection limit after this process (bottom spectrum).

F. Benefits of Operating in a Reduced Pressure and Temperature Regime

UV/Cl_2 has been demonstrated to be effective in removing metals from wafer surfaces. The difficulty in implementing the process is that UV/Cl_2 can be an aggressive silicon etchant, with etch rates of 100's to 1000's of Å/min easily achievable. In addition, as was discussed in

Chapter 3, the surface of a bare silicon wafer will tend to be roughened at least on the order of 1 Å R_{ms} for every 100 Å etched[15]. For instance, Sugino *et al.*[17] have reported iron and aluminum removal at 170 °C in UV/Cl_2 at chlorine pressures of 2-20 Torr on a native oxide surface. They report silicon etch rates through the native oxide on the order of ≈ 40-670 Å/min over this pressure range. We have observed etch rates of ≈100-1000 Å/min at similar conditions on a bare silicon surface. The surfaces of these samples were roughened on the order of 10-100 Å R_{ms}. Clearly, these aggressive conditions are less than desirable for device fabrication. By lowering the temperature and pressure at which the process is performed, we can operate in a much less aggressive and more controllable process regime. Although we have not performed a detailed parametric study in the pressure range below 1 Torr, it has been well established that the etch rate in the UV/Cl_2 process is linear in pressure as long as the pressure is low enough so that gas-phase UV absorption is not significant (below ~50 Torr)[23,47,48]. Linear extrapolation of our higher pressure results (see Chapter 3)[43], would lead us to expect a silicon etch rate of less than 10 Å/min at 50 mTorr and 75 °C. In addition, lowering the chlorine pressure reduces the amount of chlorine absorbed on the surface after the process as judged by XPS. Fig. 4.13 shows the chlorine signal after a UV/Cl_2 process performed at 5 Torr for 1 minute at 75 °C compared with a process performed at 50 mTorr for 1 minute at 75 °C. The higher pressure process has a much higher chlorine signal, corresponding to the formation of a $SiCl_X$ reaction layer ~ 8 Å thick. The low pressure process corresponds to a chlorine surface coverage of ~0.9 ML.

Figs. 4.14 a & b show Atomic Force Microscopy (AFM) images of the surfaces whose chlorine signatures are illustrated in Fig. 4.13. The surface illustrated in Fig. 12a, which was

processed for 60 seconds at 75 °C and 50 mTorr, exhibits surface roughness of 1.31 Å R_A and 1.73 Å R_{MS} as measured by atomic force microscopy. The surface illustrated in Fig. 12b, which was processed for 60 seconds at 75 °C and 5 Torr, exhibits surface roughness of 4.67 Å R_A and 5.88 Å R_{MS}. By way of comparison, a "virgin" silicon surface will exhibit surface roughness on the order of 1 Å R_{MS}.

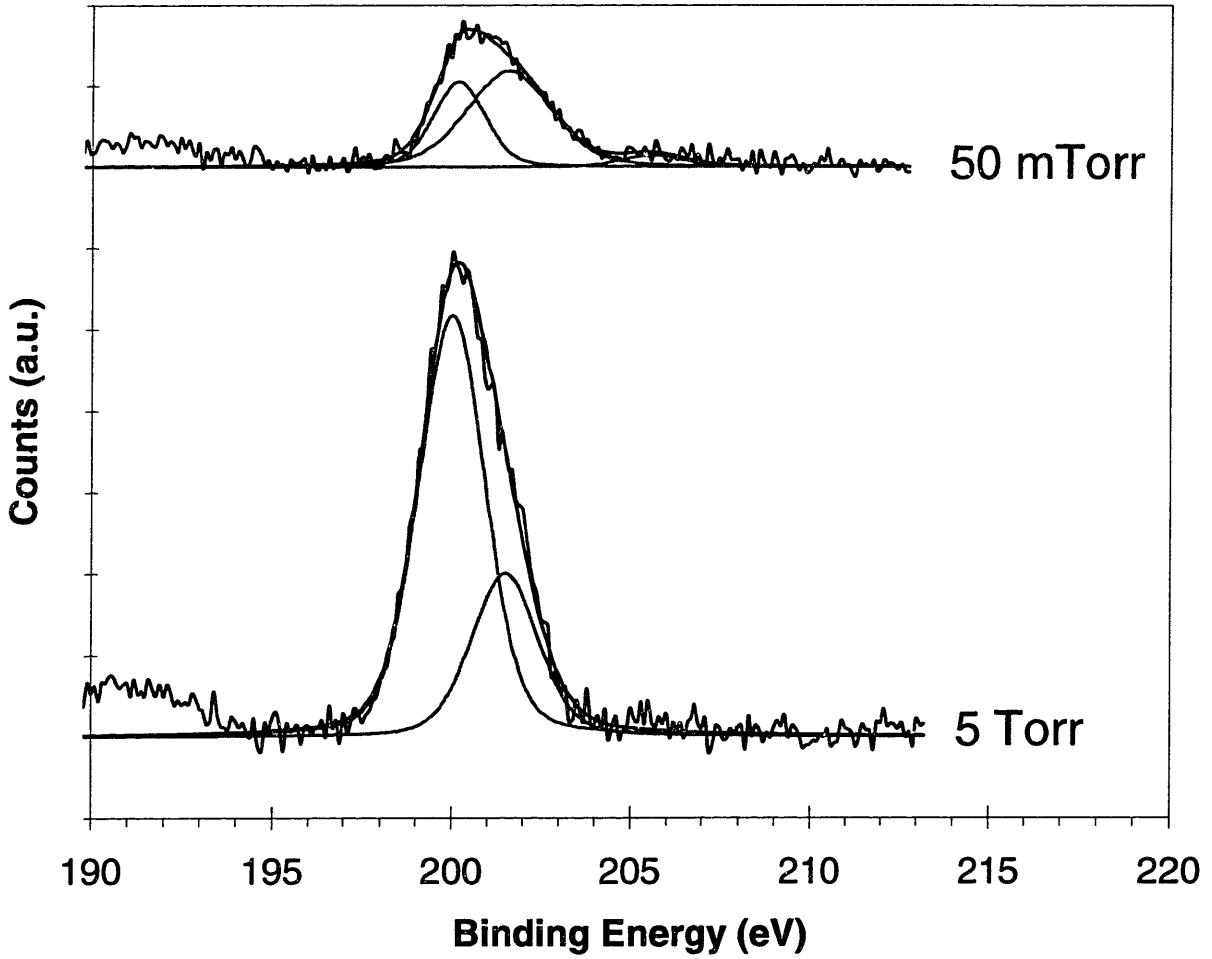

Figure 4.13-Chlorine 2p photoelectron emission spectra illustrating the effect of chlorine pressure on the residual surface chlorine after a 60 second full spectrum UV process at 75 °C. After a 50 mTorr process (top spectrum) the chlorine surface coverage is equivalent to ~ 0.9 ML. After a 5 Torr process (bottom spectrum) a $SiCl_X$ reaction layer ~ 8 Å thick is observed on the surface.

a) 50 mTorr

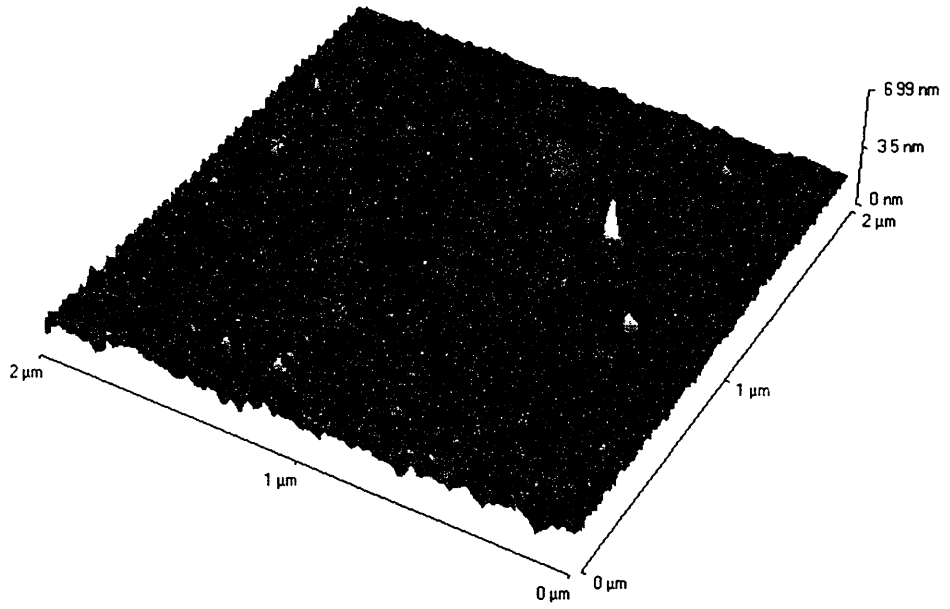

b) 5 Torr

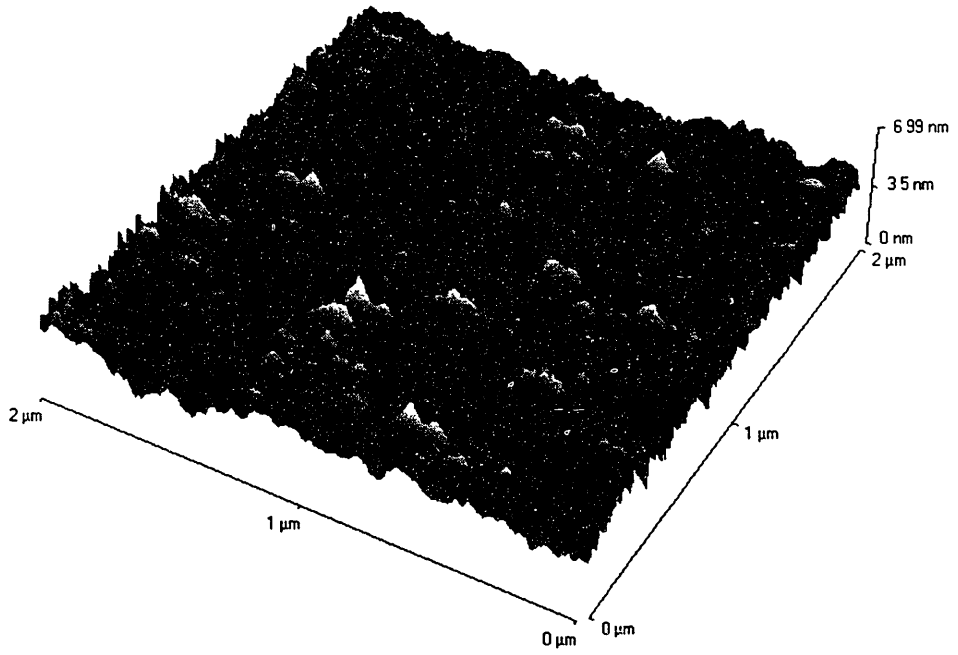

Figure 4.14-Atomic Force Microscopy images of wafer surfaces illustrating the effect of chlorine pressure on the silicon surface roughness after a 60 second full spectrum UV process at 75 °C. After a 50 mTorr process (Fig. 12a) the surface is characterized by a surface roughness of 1.73 Å R_{MS}. After a 5 Torr process (Fig. 12b) the surface is characterized by a surface roughness of 5.88 Å R_{MS}.

4.3 Removal of Nickel and Iron with UV/Cl_2

In addition to copper, we have also studied the removal of nickel and iron from both oxide and silicon surfaces. Nickel and iron are major components of stainless steels, and are also known to "plate out" of standard cleaning solutions. Nickel and iron appear to exhibit the same reduction-photodesorption behavior that we have observed in the copper-UV/Cl_2 system. We have not performed wavelength resolved experiments on the nickel and iron systems. In the case of nickel, the slower kinetics of the chlorination-reduction processes at the temperatures which we could routinely operate in the experimental system in which the wavelength resolved experiments were performed would make the experimental runs prohibitively long. In fact, we have not observed evidence of the reduction of $NiCl_2$ below about 120°C. In the case of iron, the tendency to spontaneously oxidize (even on a bare silicon surface with minimal oxygen coverage) makes interpretation of the XPS spectra difficult. We have performed experiments on these systems with the full lamp fluence on both oxide and bare silicon surfaces. These results will be presented in the following sections.

4.3.1 Removal of Metallic Nickel from a Bare Silicon Surface

Figure 4.15 illustrates two low pressure nickel removal processes. In figure 4.15a, the process was performed at nominally 70°C for a total of 7 minutes at 50 mTorr. Even after 7 minutes at this temperature, only half of the deposited nickel is removed. In figure 4.15b, the process was performed at nominally 135°C. After only two minutes, the deposited nickel is removed to nearly the detection limit of XPS. Figure 4.16 illustrates another aspect of nickel removal in UV/Cl_2. In figure 4.16a the nickel was chlorinated in the dark to form $NiCl_2$. It is important to note that we have not observed $NiCl_2$ formation below about 105°C, whereas

copper was observed to form $CuCl_2$ even at room temperature. As the figure illustrates, $NiCl_2$ is not reduced by UV exposure at 50°C. But, as figure 4.16b illustrates, $NiCl_2$ is removed from the wafer surface at 120°C. Taken together, these figures shed some light on the mechanism of metallic nickel removal. Note that with the sample that was reacted at 5 Torr illustrated in figure 4.16b, $NiCl_2$ is detected on the surface halfway through the process, whereas in the sample reacted at 50 mTorr in figure 4.15b, any remaining nickel appears to be in the metallic state. This is consistent with the pressure dependence of copper removal that was presented in the previous section, in that at reduced chlorine pressure the tendency is towards reduction and removal of nickel through the dominance of photon stimulated processes over chlorination processes. In the case of nickel however, the temperature must be increased relative to copper for efficient metal removal. As was mentioned above, the chlorination kinetics of nickel appear to be quite different from copper. The increased efficiency of nickel removal at higher temperature is therefore at least partially due to the increased efficiency of the chlorination reaction as the temperature is increased. If the nickel is not efficiently converted to a chloride, it cannot be removed from the surface.

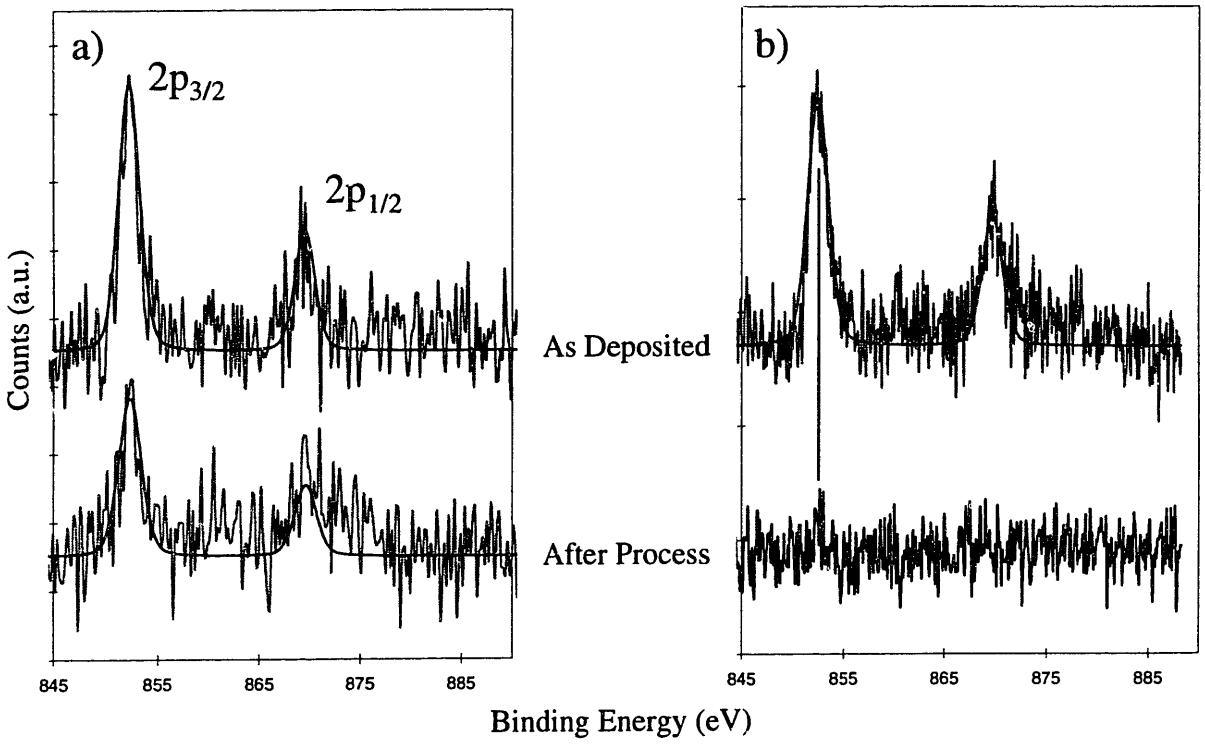

Figure 4.15-Nickel 2p photoelectron emission spectra illustrating UV/Cl_2 processing at 50 mTorr. In both a) and b), the initial coverage was ~0.02 ML. The sample in a) was processed at nominally 70°C for 7 minutes. The sample in b) was processed at nominally 135°C for 2 minutes.

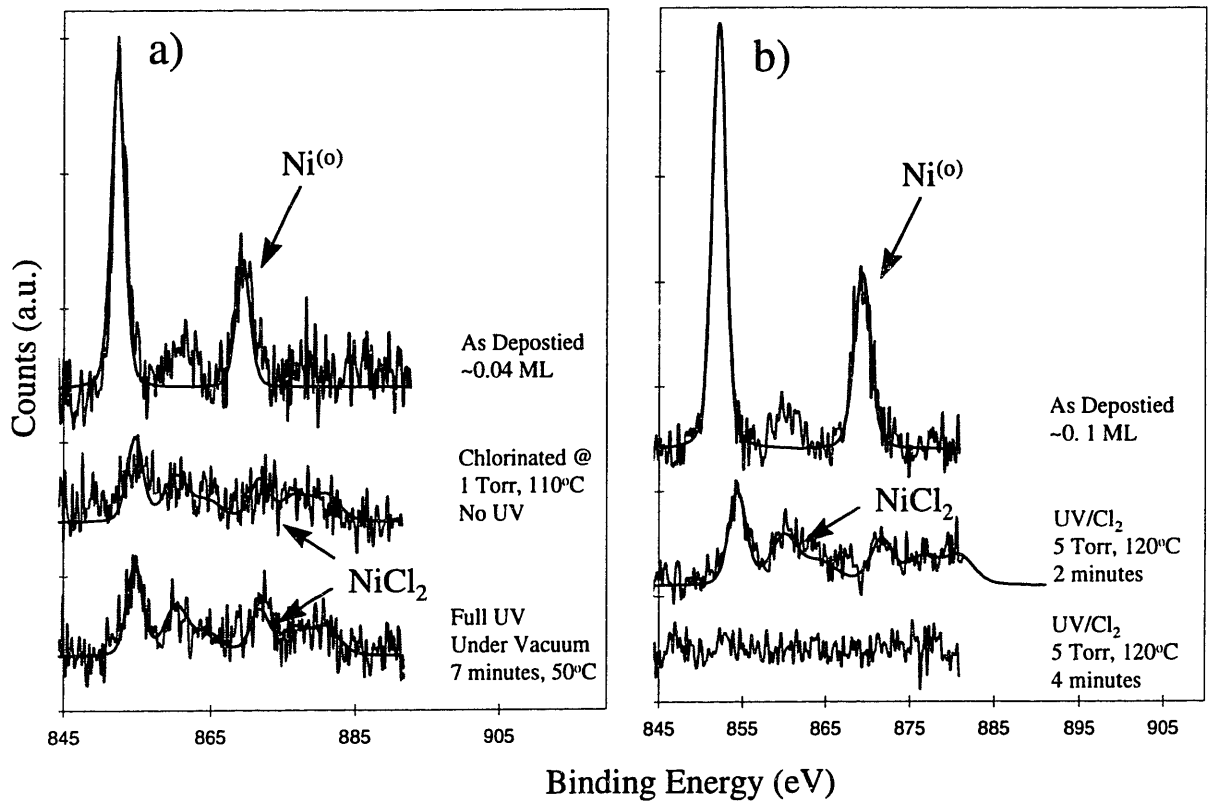

Figure 4.16- Nickel 2p photoelectron emission spectra illustrating $NiCl_2$ formation and reduction. In a) $NiCl_2$ is not reduced or removed from a silicon surface, even after extended UV exposure at 50°C. In b) the $NiCl_2$ formed after 2 minutes of UV/Cl_2 exposure at 5 Torr and 120° is removed to the XPS detection limit after 2 additional minutes of processing. It is important to note that the sample in b) was exposed to full spectrum UV under vacuum for 3 minutes at nominally 100°C after evacuation of the chlorine in the reactor after both the 2 and 4 minute reaction intervals.

4.3.2 The Influence of the Substrate on Transition Metal Removal

A. Results

A discussion of transition metal removal cannot be complete without considering the influence of the substrate on the removal process. The reason for this is the tendency of nickel and especially iron to spontaneously oxidize on a wafer surface. The XPS spectra shown in figure 4.17 illustrate this. With copper, we have witnessed no detectable tendency towards spontaneous oxidation on either silicon or oxide surfaces. With nickel, spontaneous oxidation is not detected on a (relatively oxygen free) bare silicon surface, but we do observe significant spontaneous oxidation when nickel is deposited on an oxide surface. This observation is consistent with Mukhopadhyay and Chen[49] who observed oxidation of the first 5% of a monolayer of evaporated nickel on SiO_2. Spontaneous oxidation of nickel has also been observed on alumina surfaces[49,50]. In the case of iron, spontaneous oxidation is even observed on a bare silicon surface with residual oxygen coverage on the order of 1/3 of a monolayer. On an oxide surface, all of the detectable iron is oxidized in the coverage range of interest (at least up to 0.2 ML) in these studies. This oxidation behavior is consistent with the free energy of formation of the monoxides of these elements which go as $\Delta G_{Fe} > \Delta G_{Ni} > \Delta G_{cu}$.

Not only can spontaneous oxidation occur, but we have observed enhanced oxidation due to UV exposure under vacuum. Figure 4.18 illustrates a mixed $Ni^{(o)}$/NiO sample which was exposed to UV illumination in an atmosphere of flowing nitrogen. Clearly the metallic component of the photoemission has been reduced as a result of the UV exposure while the oxidized component has increased. The total area under the 2p photoemission line is

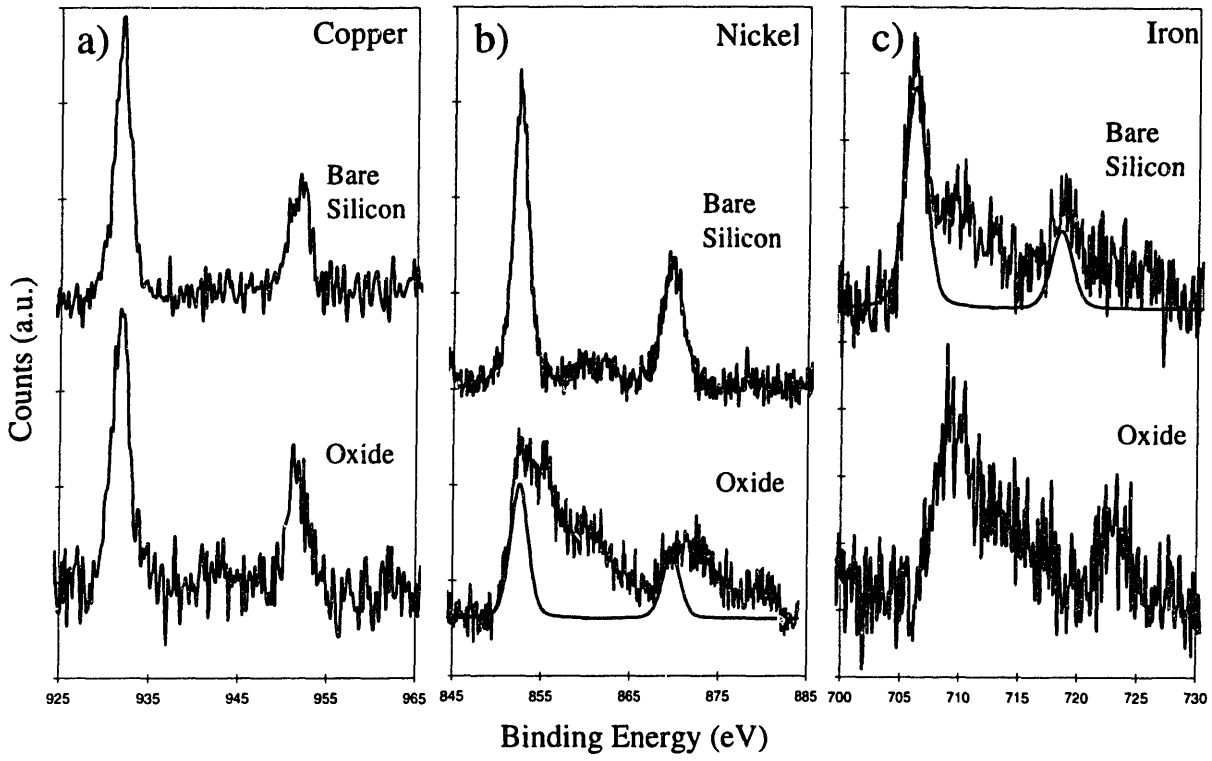

Figure 4.17- Copper (a), Nickel (b), and Iron (c) 2p photoelectron emission spectra illustrating the tendency of these metals to spontaneously oxidize on bare silicon and oxide surfaces. Where multiple chemical states are present simultaneously, the metallic state contribution to the photoemission is represented by a solid black line. Oxidized states are characterized by a broad peak which is shifted to higher binding energy relative to the metallic state. Copper exhibits no spontaneous oxidation. The first 0.05-0.1 ML of nickel is spontaneously oxidized on a SiO_2 surface. Iron is totally oxidized on a SiO_2 surface in the coverage range of interest in these experiments. Iron will even spontaneously oxidize on a bare silicon surface, the extent of which is a function of the residual oxygen coverage (which is a function of the quality of the sample preparation procedure).

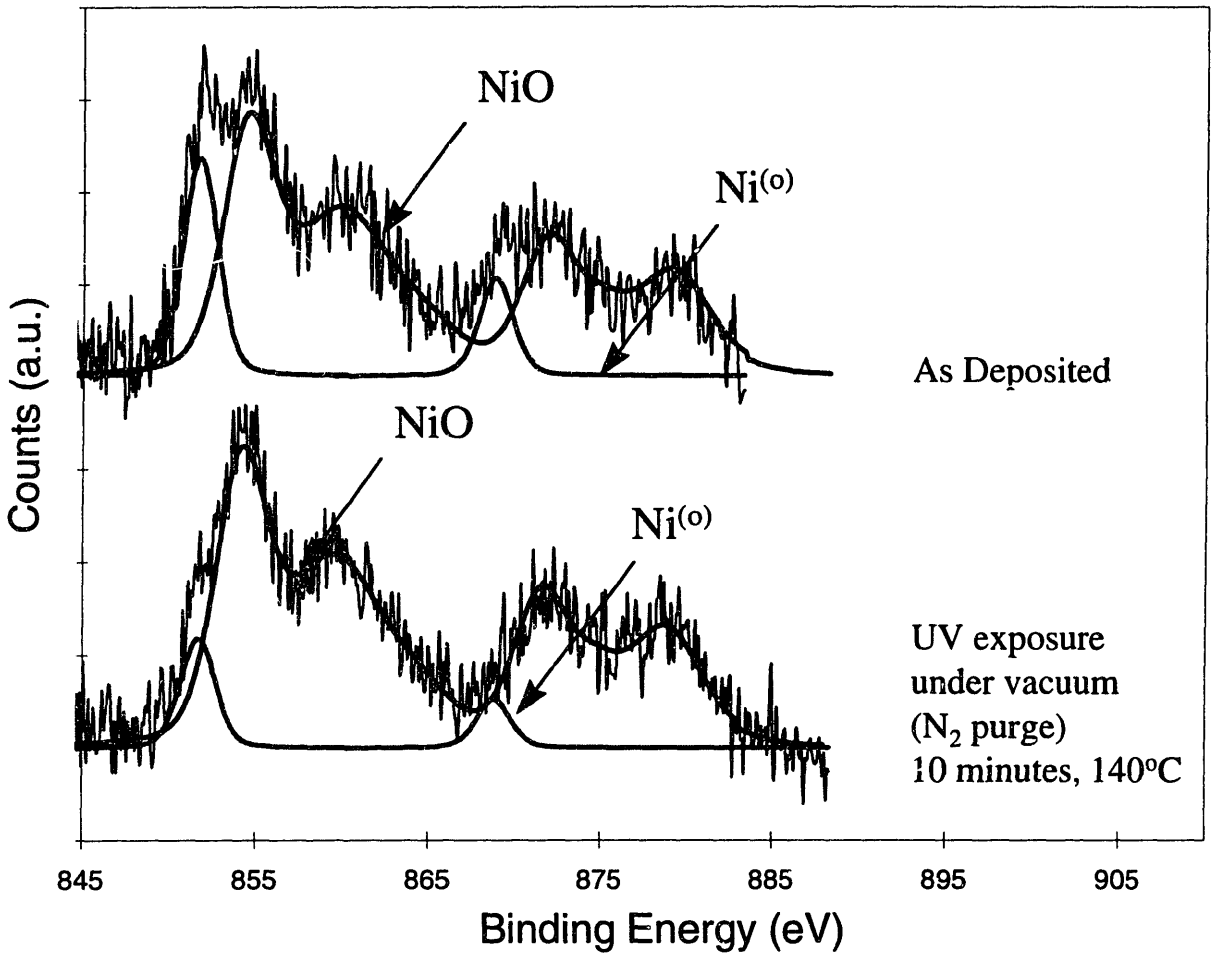

Figure 4.18- Nickel 2p photoelectron emission spectra illustrating UV stimulated oxidation of mixed $Ni^{(o)}$/NiO on a SiO_2 surface. After 10 minutes of UV exposure in 200 sccm of flowing N_2 at 350 mTorr, the $Ni^{(o)}$ component is substantially reduced while the NiO component has increased proportionally. The total photoemission is unchanged by the process.

unchanged by the process, indicating that none of the nickel was removed. While at first this phenomenon may seem counter to the mechanism that is proposed here, remember that under certain conditions we observed evidence of a UV stimulated surface chlorination process in the copper-UV/Cl_2 system. The UV stimulated surface oxidation process is directly analogous. Photo-enhanced oxidation of polycrystalline nickel in air has been reported in the literature[51].

Why is this oxidation behavior of metals on wafer surfaces important in evaluating the UV/Cl_2 cleaning process? Some investigators have reported difficulty in removing iron[52] and nickel[53] from oxide surfaces at conditions where these metals were successfully removed from bare silicon or native oxide surfaces. Generally, the lack of formation of silicon etch products and hence the elimination of a complexing or lift-off mechanism has been invoked in these cases to explain the differing removal efficiencies from bare silicon and oxide surfaces. In this section, evidence will be presented to suggest that these differences can be explained solely on the basis of the oxidation state of the metal on the wafer surface. We have not observed any evidence that would suggest that the mechanism of removal of these metals is any different on an oxide surface, only that the process becomes more complex and difficult to interpret. The oxidizing tendency of the SiO_2 surface does make metal removal more problematic, as will be discussed below.

Figure 4.19 illustrates the removal of mixed $Fe^{(o)}$/FeO from a bare silicon surface. As was discussed above, a detectable fraction of the iron is spontaneously oxidized on this surface due to the residual oxygen coverage. The metallic iron is removed with a low pressure UV/Cl_2 process. The iron which was initially present as FeO is not removed, and the total

amount of oxidized iron may even be increased by the process, although with the sensitivity of our instrumentation in this coverage range, this is difficult to determine. It is also unclear whether the oxidized iron is in the from of an oxide or a chloride. Based on the data for the nickel on SiO_2 which will be presented shortly, it is likely that the iron is present in a mixed oxide/chloride composition after the process. The inability to remove this oxidized iron at reduced temperature is consistent with other experiments for iron on a SiO_2 surface which are presented in Chapter 5 in conjunction with the UV/DCS/Halogen system.

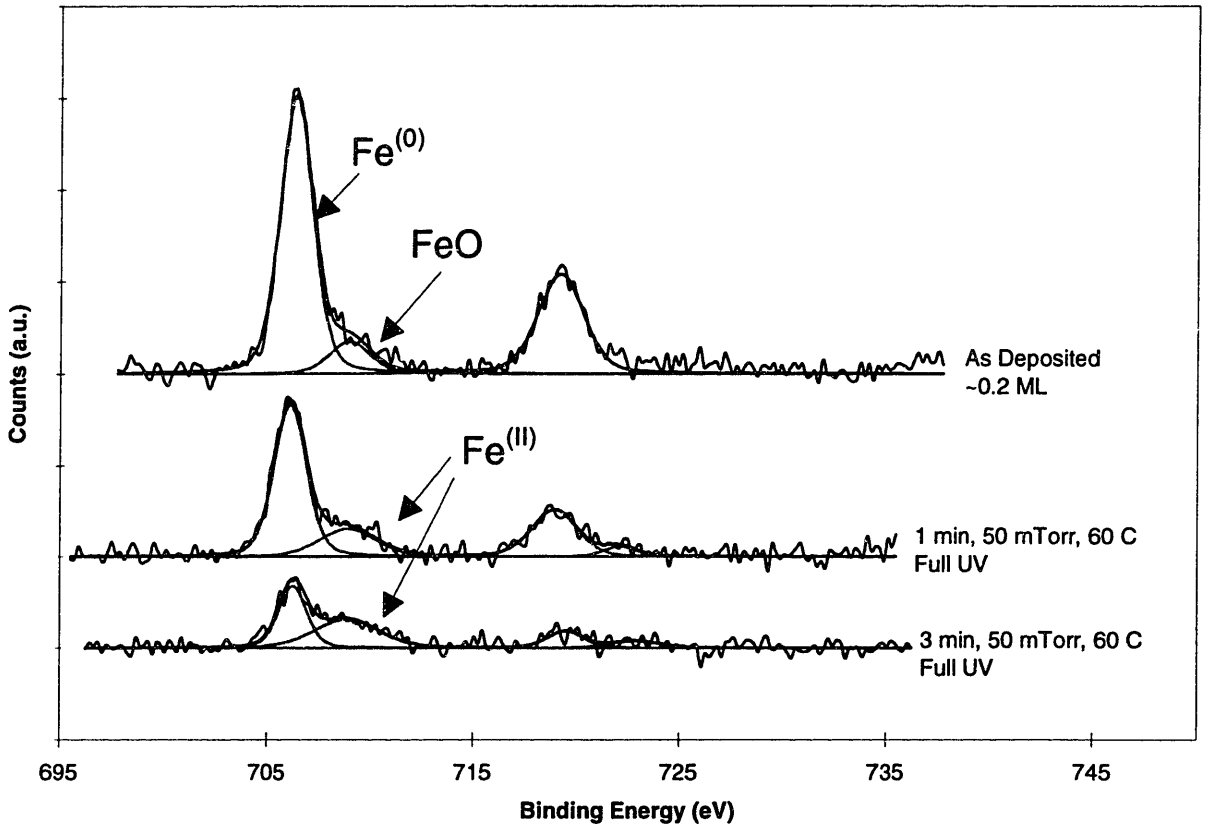

Figure 4.19- Iron 2p photoelectron emission spectra illustrating the removal of iron from a silicon surface with a low pressure-low temperature UV/Cl_2 process. The iron is initially of mixed $Fe^{(o)}$/FeO composition due to the spontaneous reaction of iron with the residual oxygen on the silicon surface. Metallic iron is effectively removed with this process while the level of oxidized iron remains unchanged and may even be increased. It is unclear whether the oxidized iron is present as an oxide or chloride after the process.

While oxidized iron is not removed at low temperature, Figure 4.20 illustrates that it is efficiently removed at a temperature of 130°C. An initial coverage of totally oxidized iron is removed to the detection limit of XPS with this process. As mentioned above, this process does not work at lower temperature. Additionally, other investigators have been unsuccessful in removing iron from an oxide surface even at temperatures as high as 500°C with a 20 Torr UV/Cl_2 process[52]. The benefit of low pressure must be to enhance the domination of the photo-reduction process over the oxidation process, as in the copper-UV/Cl_2 system. Higher temperatures are also required to make this process go, since oxidized iron is not removed at 60°C. This same behavior is observed in the nickel-UVCl_2 system where $NiCl_2$ can not be reduced or removed at 70°C but is removed at 120°C.

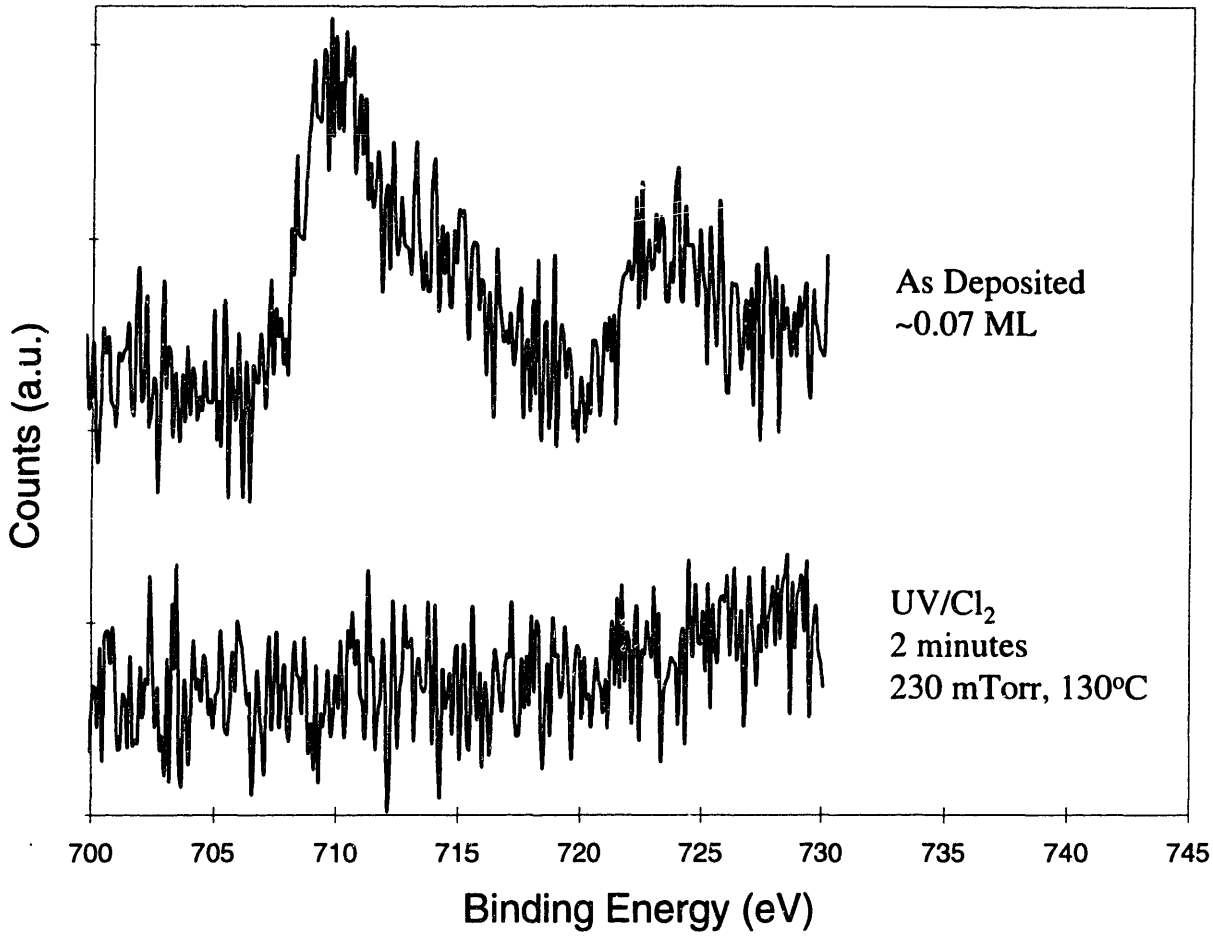

Figure 4.20-Iron 2p photoelectron emission spectra illustrating iron removal from an oxide surface with a low pressure UV/Cl_2 process. The iron is initially oxidized as discussed in the text. Iron is removed to the detection limit after a 2 minute process. The increase in the baseline beginning at ~720 eV is due to the oxygen KVV Auger photoemission.

Nickel removal from an oxide surface is somewhat more problematic. As Figure 4.21 illustrates, metallic nickel can be completely removed from a SiO_2 surface, but the initially oxidized nickel remains. The initially oxidized nickel is no longer present as pure NiO, but is converted to a mixed $NiO/NiCl_2$. The total integrated area due to the intially oxidized nickel is virtually identical with the post process level of mixed $NiO/NiCl_2$.

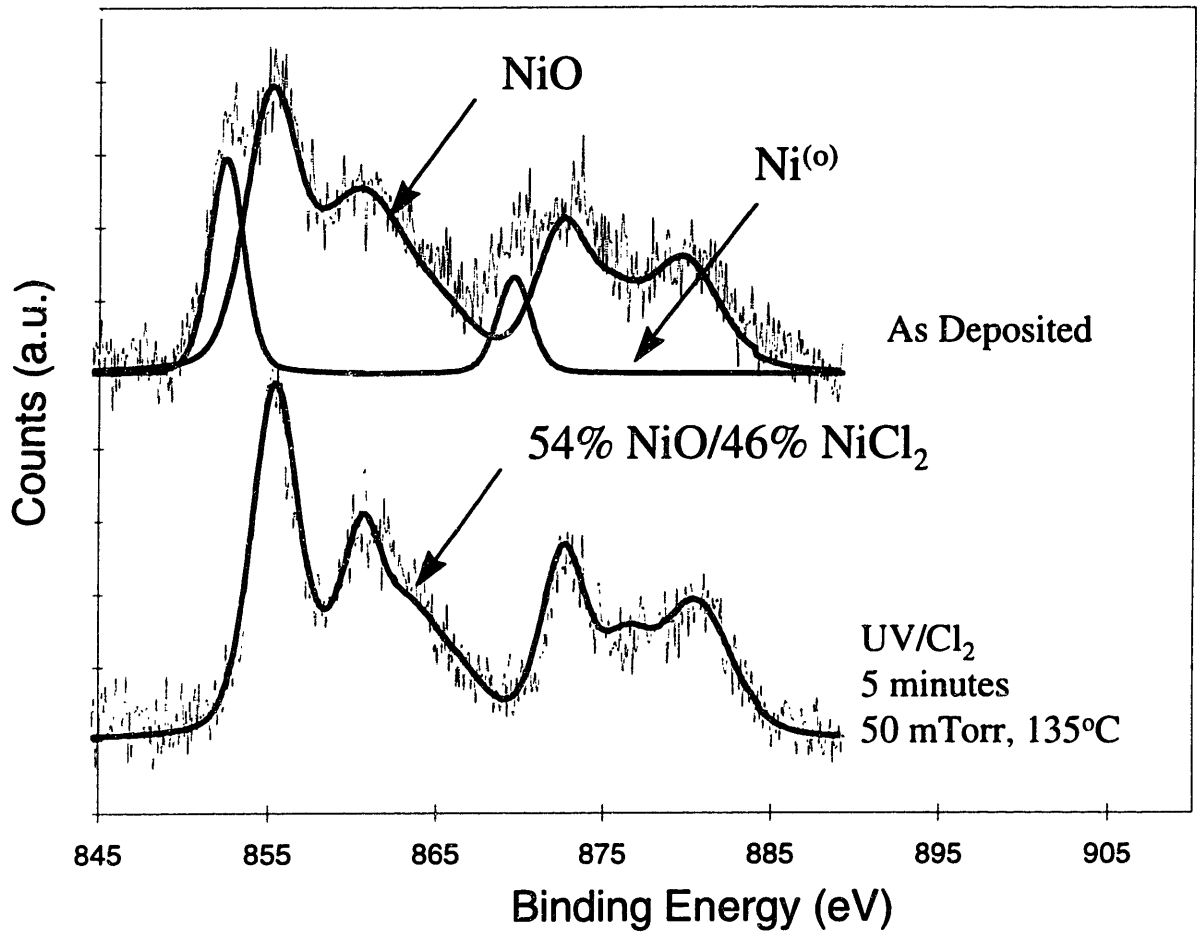

Figure 4.21-Nickel 2p photoelectron emission spectra illustrating the effect of the UV/Cl_2 process on nickel deposited on a SiO_2 surface. The as deposited nickel is present as mixed $Ni^{(o)}/NiO$. The UV/Cl_2 process completely removes the metallic nickel, and converts the initially oxidized nickel to a mixed $NiO/NiCl_2$. The total photoemission due to the initial NiO and the post-process mixed $NiO/NiCl_2$ is virtually identical, indicating that none of the initially oxidized nickel was removed by the process.

Figure 4.22 illustrates the fitting procedure used to arrive at the mixed $NiO/NiCl_2$ composition. Figure 4.22 a) represents the 2p photoemission fits used for the pure NiO and $NiCl_2$ states. The $NiCl_2$ pure state fit was obtained from the "cleanest" spectrum of chlorine reacted nickel on a silicon surface that was available in our laboratory. It is the same fit which is superimposed on the spectra in figure 4.16. The fit agrees extremely well with multiple literature sources[54,55,56] representing both experimental data and theoretical fits. The NiO pure

state fit is the average of multiple arbitrary fits on mixed $Ni^{(o)}$/NiO depositions, where the $Ni^{(o)}$ contribution is taken from a "high coverage" (i.e. good signal to noise ratio) sample of nickel deposited on a silicon surface. Although the reported experimental data for NiO is somewhat variable[49,50,57,58],

our spectra agrees qualitatively with what has been reported and especially well with an example of NiO on SiO_2[58]. The fits shown in figure 4.22a are scaled such that they have the same total integrated area. The major distinguishing feature which differentiates the two chemical states is the resolution between the main $2p_{3/2}$ peak and the $2p_{3/2}$ shake-up satellite, as indicated by the arrows in the figure. $NiCl_2$ exhibits near-baseline resolution, while the NiO emission is substantially more diffuse.

Figure 4.22b shows an example of the fitting procedure, and illustrates the fit used in figure 4.21. An arbitrary best fit to the data is first obtained. This is done to obtain a more reliable value for the total integrated area for the photoemission. This arbitrary fit is then compared to a linear combination of the fits for pure NiO and $NiCl_2$. The basis for comparison is the difference spectrum also illustrated in figure 4.22b, which simply represents a linear subtraction of the two spectra. When the deviation from zero of the difference spectrum is minimized, the best fit is obtained. As the figure shows, this fitting routine does an excellent job of capturing most of the features of the data, and especially the resolution between the main $2p_{3/2}$ peak and the satellite, as discussed above.

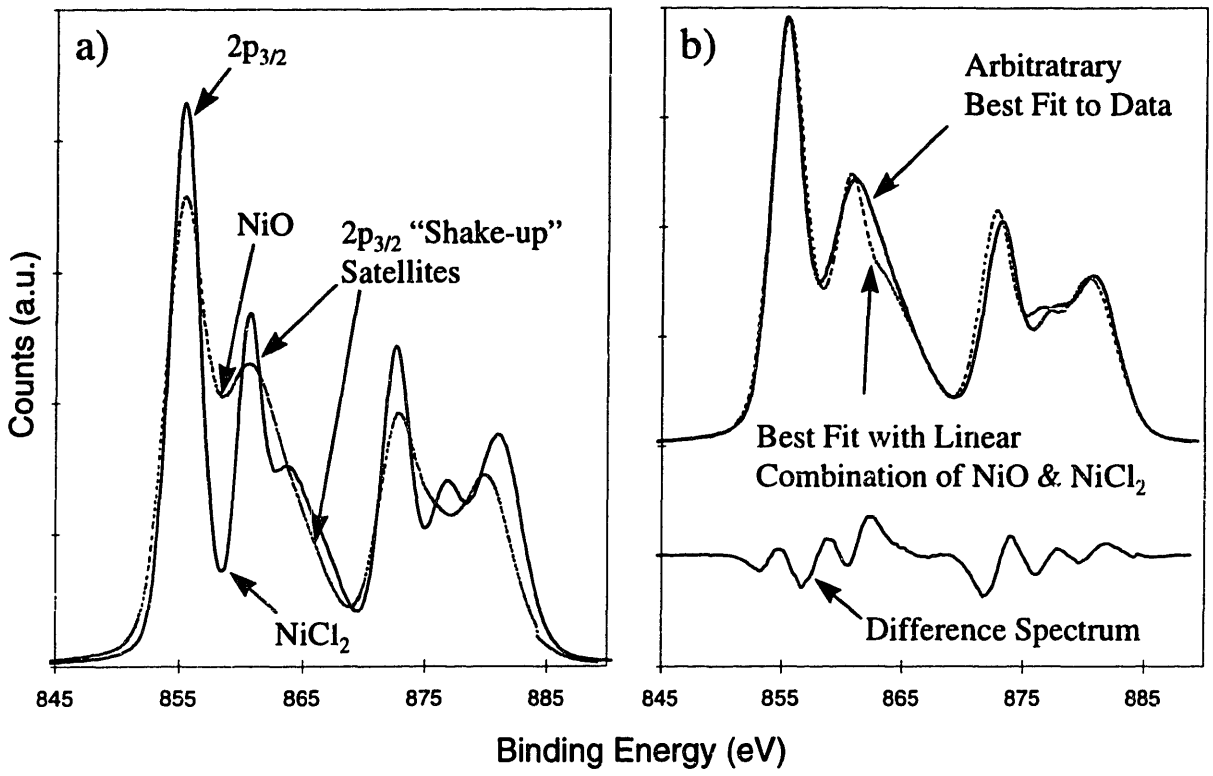

Figure 4.22-a) Fits used and, b) an example of the fitting procedure to obtain the composition of a mixed NiO/$NiCl_2$. The pure state fits for NiO (dashed line) and $NiCl_2$ (solid line) are shown in a). Note the resolution between the main $2p_{3/2}$ peak and the $2p_{3/2}$ shake-up satellite. A best fit is obtained when the difference (difference spectrum shown below in "b") between an arbitrary best fit to the data (solid line) and a linear combination of NiO and $NiCl_2$ (dashed line) is minimized. This fitting procedure succeeds in capturing most of the features in the original data.

Using this fitting procedure, we have also observed the photo-stimulated conversion of $NiCl_2$ back to NiO. Figure 4.23 illustrates this data. After UV exposure under vacuum, a higher fraction of the doubly oxidized nickel is present as NiO. Again, the total integrated area of the photoemission is unchanged by this process, indicating that no nickel was removed by this process, only converted to another chemical form. This is similar to behavior which we have observed in the copper-UV/Cl_2 system where we observed oxide to chloride conversion (Figure 4.2). It is likely that the conversion process involves the photon stimulated reduction

of $NiCl_2$. Because of the oxidizing nature of the SiO_2 surface, the nickel is not removed from the wafer but re-oxidized to form NiO. The NiO oxidation process is also enhanced by UV illumination as we have shown in Figure 4.18.

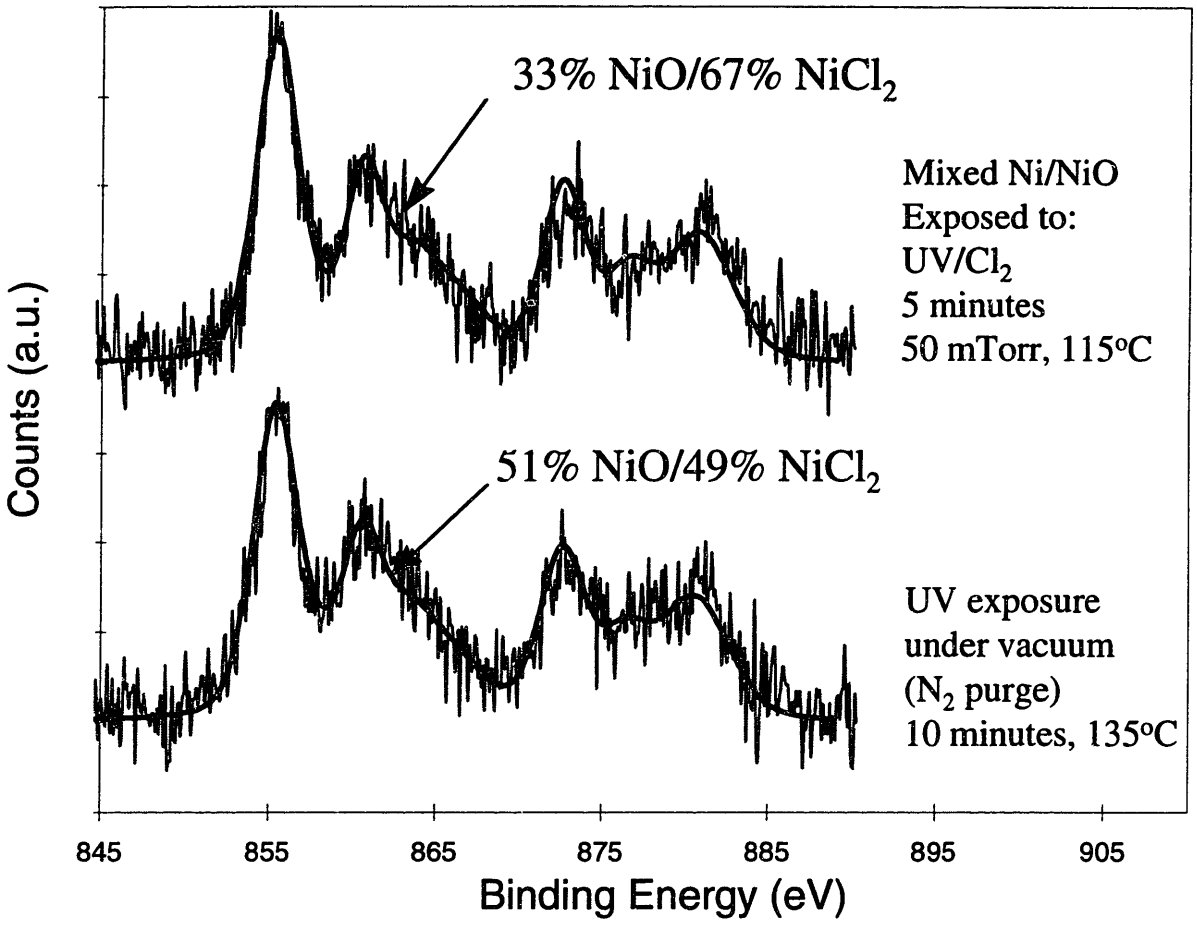

Figure 4.23-Nickel 2p photoelectron emission spectra illustrating the photo-stimulated conversion of $NiCl_2$ to NiO on an oxide surface. A 33%NiO/67%$NiCl_2$ sample which was obtained by exposing a mixed $Ni^{(o)}$/NiO to a low pressure UV/Cl_2 process (note the absence of any $Ni^{(o)}$) is converted to 51%NiO/49%$NiCl_2$ after 10 minutes of UV exposure under vacuum. The total integrated area of the photoemission is virtually identical indicating that no nickel was removed by the process.

B. Discussion

From the above results, it is apparent that the character of the wafer surface has a profound effect on the efficiency of metal removal. We have shown that metallic iron and nickel can be efficiently removed at conditions where the oxidized states of these metals are not. It is unlikely that a complexing mechanism or the lack of silicon etch products participating in the metal removal process is the cause of this behavior. More likely, it is the oxidizing nature of the SiO_2 surface which prevents the oxidized states from being removed. Consider that metallic iron is removed from a bare silicon surface when the simultaneously present oxidized component is not. The same situation occurs with nickel on a SiO_2 surface, where the metallic state is totally removed while the simultaneously present oxidized state is not.

Additional evidence for this hypothesis is illustrated in figure 4.24. The figure shows the wavelength dependence of the chemical state of copper on both oxide and silicon surfaces in the UV/Cl_2 process. As discussed in section 4.2, on a bare silicon surface (figure 4.24b) the chemical state of surface copper is dominated by the gas phase production of atomic chlorine under 367 nm illumination, and hence copper is present as $CuCl_2$. Under 245 nm illumination, in the absence of the gas phase production of atomic chlorine, the photon stimulated reduction of copper chloride is dominant, and so copper is present as CuCl. On a SiO_2 surface (figure 4.24a) the situation is much different. Under illumination by both wavelengths, copper is present as $CuCl_2$ (or possibly CuO, but definitely $Cu^{(II)}$). This can only be due to the oxidizing influence of the SiO_2 surface. In fact, on the oxide surface, removal at 245 nm appears to be

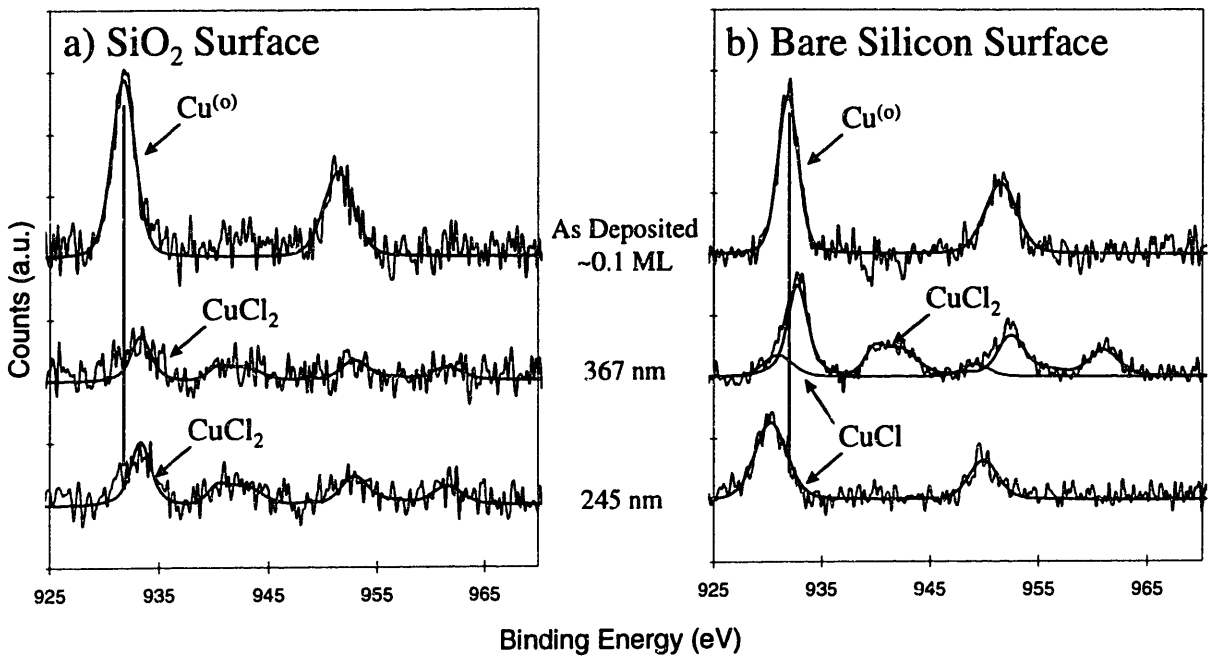

Figure 4.24-Copper 2p photoelectron emission spectra illustrating wavelength resolved copper removal with UV/Cl_2 at 20 mTorr and 60°C from a) SiO_2, and b) bare silicon surfaces. Note that in a), copper is present as $CuCl_2$ under both 367 and 245nm illumination, whereas in b) copper is present as $CuCl_2$ under 367 nm and CuCl under 245 nm illumination. This indicates that on an oxide surface the dominant effect on the chemical state of the metal is surface oxidation processes at both wavelengths, whereas on a bare silicon surface the dominant effect is gas phase production of Cl* at 367nm and photon stimulated reduction at 245nm.

less efficient than removal at 367 nm, indicating that the surface oxidation process is more efficient at 245 nm. This is consistent with the observation of a surface chlorination process on a bare silicon surface at 245 nm as the chlorine pressure was increased (see figure 4.9).

Basically, the SiO_2 surface seems to act as an oxidizing atmosphere, forcing the equilibrium towards the formation of oxidized products, much as increasing the chlorine pressure does on a bare silicon surface. Although this does not seem to affect the efficiency of copper removal (in fact copper removal appears to be more efficient on a SiO_2 surface) because of the low threshold for the photon stimulated reduction of both CuO and $CuCl_2$, it is a problem in the iron and nickel systems. In the case of iron the oxidizing tendency is overcome by simply increasing the process temperature. The process pressure is important as

well, since Sugino *et al.*[52] have not been successful in removing iron from an oxide surface at 20 Torr, even at temperatures as high as 500°C, whereas we have observed removal at 130°C at both 50 and 230 mTorr. As in the case of copper, it is likely that surface reduction processes are enhanced over chlorination processes as the chlorine pressure is reduced. In the case of nickel, we have not observed removal of $Ni^{(II)}$ from an oxide surface with the UV/Cl_2 process in the temperature range which we have studied (below 140°C). We have seen evidence of inter-conversion between NiO and $NiCl_2$, but it was not accompanied by a reduction in overall photoemission intensity, indicating that none of the material was removed. We have also observed indirect evidence that $NiCl_2$ can be reduced on a bare silicon surface at elevated temperature, and it is likely that the conversion of $NiCl_2$ to NiO also involves the photochemical reduction of $NiCl_2$. Nickel is not removed because as the $NiCl_2$ is reduced it is re-oxidized to form NiO before it can desorb from the SiO_2 surface. Based on the temperature dependence of (the reduction process in) $NiCl_2$ and $Fe^{(II)}$ removal, it is not unreasonable to predict that the barrier that prevents removal of $Ni^{(II)}$ from an oxide surface (i.e. overwhelming the tendency to form NiO) would be overcome by increasing the temperature above ~140°C.

The data presented here also suggests that the volatile products in the iron- and nickel-UV/Cl_2 systems are the monochlorides. Consider that when coexisting metallic and oxidized states are present on a wafer surface and that surface is exposed to a UV/Cl_2 process, the metallic state can be efficiently removed while the level of the II oxidation state remains unchanged. This would suggest that the metallic state is chlorinated and removed from the surface as a monochloride, while the II state is not removed (although at least in the case of nickel it is partially converted to a dichloride). Also consider that metallic nickel is removed from a silicon surface at a temperature where $NiCl_2$ exposed to UV illumination under

vacuum is stable on the surface. This would also suggest that the volatile product cannot be $NiCl_2$.

The results presented here lead to the conclusion that surface oxidation processes cause the difficulty in removing iron and nickel from oxide surfaces, but that fundamentally, the mechanism of removal is no different than that from a bare silicon surface. Surface oxidation simply adds another kinetic barrier (the breaking of the metal-oxygen bond) to the removal process. If the conditions are such that the barrier can be overcome with the available photon energies (as in the case of copper and iron) then the metal can be removed from the surface. If not, (as in the case of nickel) the metal will remain on the surface. Furthermore, it is likely that the photon stimulated reduction and desorption mechanism proposed for copper is generally applicable to iron and nickel as well, and that the volatile products in the removal of iron and nickel are monochlorides.

4.4 Combined HF/Vapor-UV/Cl_2 processing for Transition Metal Removal

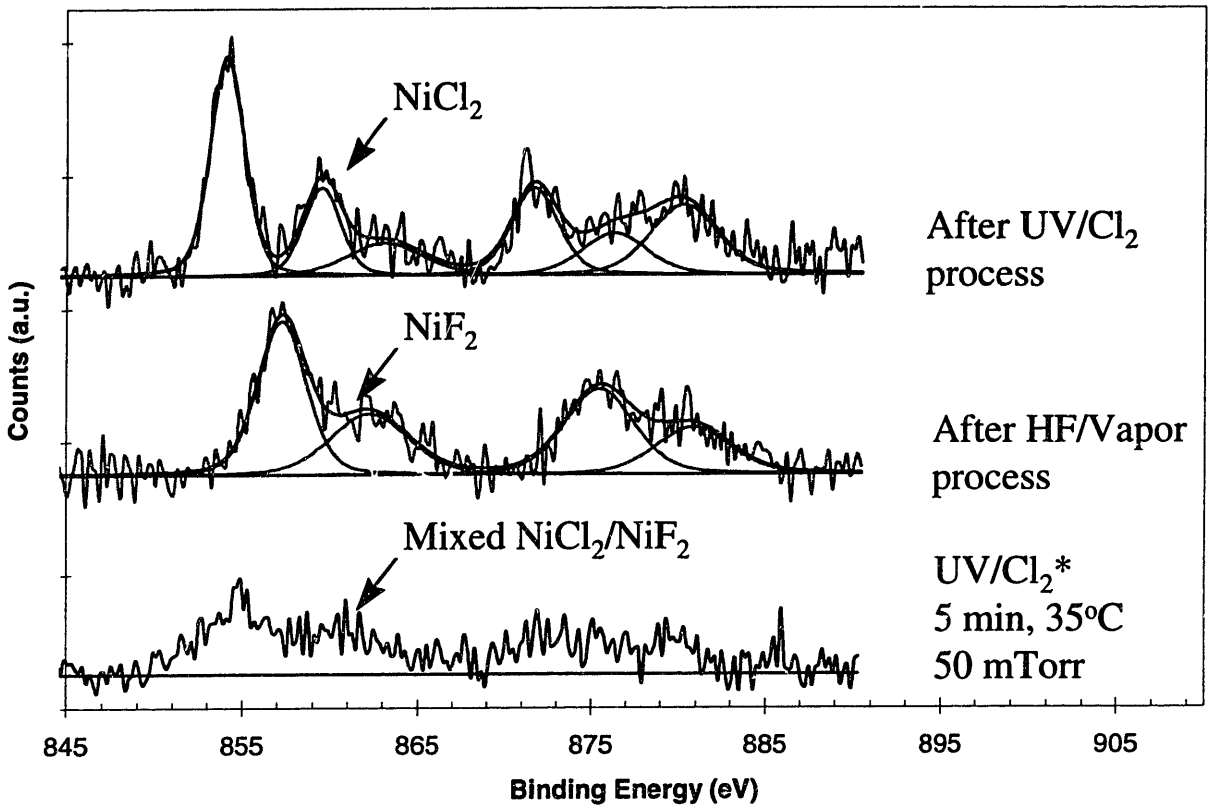

Figure 4.25-Nickel 2p photoelectron emission spectra illustrating combined UV/Cl_2-HF/Vapor processing. The uppermost spectrum shows $NiCl_2$ formed after a UV/Cl_2 process and then subjected to prolonged exposure to UV radiation under vacuum. A HF/Vapor process fully converts the $NiCl_2$ to NiF_2. Additional UV/Cl_2 processing results in partial removal and a mixed $NiCl_2/NiF_2$. This UV process was performed with a low pressure Hg lamp, which has strong emission at 185 and 254 nm, but much lower power output than the lamp used in the rest of this work.

Figure 4.25 illustrates an example of combined UV/Cl_2-HF/Vapor processing. HF/Vapor exposure converts the $NiCl_2$ formed after UV/Cl_2 processing fully to NiF_2. NiF_2 is readily identifiable and easily distinguished from $NiCl_2$ due to the binding energy shift in the main 2p peaks and the characteristic satellite structure[56]. A UV/Cl_2 process results in removal of a significant fraction of the nickel and the conversion of the NiF_2 to a mixed $NiCl_2/NiF_2$. It should be noted that this UV/Cl_2 process was performed with a low pressure Hg lamp, as was

the initial processing to form the $NiCl_2$. The low pressure Hg lamp has strong emission at 185 and 254 nm, but much lower power output than the high pressure Hg-Xe lamp used in most of this work. This lamp was used to obtain a higher photon energy than was available from the Hg-Xe system in an attempt to reduce $NiCl_2$ at low temperature with UV illumination. This aspect of the experiment was not successful. What is significant is that $NiCl_2$ was removed from the surface through an alternate chemical pathway; conversion to NiF_2 via HF/Vapor exposure and removal by exposure of the NiF_2 to UV/Cl_2. This was achieved at a temperature where UV/Cl_2 alone was not able to remove $NiCl_2$ from the wafer surface. We have also successfully applied combined processing to the removal of iron from a bare silicon surface. In this case the oxidized component of the iron was removed at conditions where UV/Cl_2 alone was unsuccessful.

We have not extensively studied the mechanism of combined UV/Cl_2-HF/Vapor processing. Our preliminary results indicate that this combination of processes provides a potential alternate chemical pathway to remove oxidized states of transition metals which cannot be removed with UV/Cl_2 processing alone. The mechanism of metal removal with these processes in combination is an area that should receive further study.

4.5 Conclusions

The removal of trace amounts of copper, iron and nickel from bare silicon and SiO_2 surfaces with the UV/Cl_2 process involves a complex interaction between photon stimulated reduction, chlorination, oxidation and desorption processes. The tendency towards spontaneous oxidation of iron and nickel further complicates the metal removal mechanism in these processes. Metal removal efficiency is maximized when the chlorination and/or

oxidation processes are balanced by the photon stimulated reduction of II oxidation states such that a high concentration of the volatile I state is maintained on the wafer surface. Specific conclusions are summarized below.

The wavelength dependence of the removal of trace amounts of copper from bare silicon surfaces with UV/Cl_2 has been established. At 245 nm competing processes take place. At low chlorine pressures, reduction of copper chlorides dominates such that a high surface concentration of CuCl is maintained. At high chlorine pressures, a surface mediated chlorination process dominates and forces the equilibrium towards the formation of $CuCl_2$. At 367 nm reduction of copper chloride takes place under vacuum. When chlorine is present, formation of $CuCl_2$ dominates due to the gas-phase dissociation of molecular chlorine. Copper is most likely removed from the surface as CuCl. The desorption of the volatile product is enhanced by a photon stimulated surface process such that CuCl can be removed from a wafer surface at temperatures lower than those predicted by equilibrium calculations. The removal rate of CuCl increases with temperature in the range 25-105 C°.

In practice, copper removal efficiency can be maximized by balancing the photon flux to the surface with the chlorine pressure such that a high surface concentration of CuCl is maintained. Based on our mechanism for the removal process, copper removal from a silicon surface has been demonstrated in both a "pulsed process" and a low pressure, low temperature process. Both of these processes represent a parameter space for operation which is far less aggressive in terms of silicon etch rate, induced surface roughness, and incorporation of chlorine in the near surface layer than what has previously been reported in the literature.

The removal of iron and nickel is complicated by the tendency of these metals to spontaneously oxidize on the wafer surface. Spontaneous oxidation behavior has not been

observed with copper. Nickel has been observed to spontaneously oxidize on a SiO_2 surface but not on a bare silicon surface. Iron will spontaneously oxidize to a small extent on a bare silicon surface and is totally oxidized in the coverage range of interest on a SiO_2 surface. UV exposure under vacuum enhances the oxidation of nickel on a SiO_2 surface.

The spontaneous oxidation behavior has implications for metal removal. The SiO_2 surface acts as an oxidizing atmosphere to push the equilibrium towards the formation of higher oxidation states. In the copper system the wavelength dependent behavior is significantly different on a SiO_2 surface, such that $CuCl_2$ is observed after both 245 and 367 nm illumination in a chlorine atmosphere. This indicates that even though spontaneous oxidation of copper is not observed, the oxidizing effect of the SiO_2 surface is in effect with UV illumination. In the copper system the reducing tendency of the UV photons overwhelms the UV enhanced oxidation such that the metal removal efficiency is not adversely affected.

With iron and nickel the situation is different. Metallic iron can be removed from a bare silicon surface at low temperature, but $Fe^{(II)}$ is not removed at these conditions. Oxidized iron is efficiently removed from a SiO_2 surface with a low pressure UV/Cl_2 process at 135°C. This indicates that the kinetic barrier that prevents the reduction and removal of $Fe^{(II)}$ at low temperature is overcome as the temperature is increased. Although metallic nickel is efficiently removed with a low pressure process at 135°C, oxidized nickel cannot be removed from a SiO_2 surface in the temperature range we have studied. This indicates that in the nickel system, the reducing potential of the UV output of our illumination system is not sufficient to overcome the oxidizing tendency of the SiO_2 surface, even at 135°C. Our results with iron and nickel indicate that these metals are removed from a wafer surface by the same mechanism as that outlined for copper.

Preliminary results with combined HF/Vapor-UV/Cl_2 cleaning indicate that this combination of processes may provide an alternate chemical pathway to overcoming some of the shortcomings of the UV/Cl_2 process.

4.6 References

[1] W. Kern, in *Handbook of Semiconductor Wafer Cleaning Technology: Science, Technology, and Applications*, W. Kern, ed., p. 9, Park Ridge N.J.: Noyes Publications (1993).

[2] J.P. Gambino, M.D. Monkowski, J.F. Shepard, and C.C. Parks, *J. Electrochem. Soc.*, vol. 137, no. 3, 976-979 (1990).

[3] H. Parks, C.R. Helms, M. Tran, and B.B. Triplett, *Proceedings of the Third International Symposium on Cleaning Technology in Semiconductor Device Manufacturing*, J. Ruzyllo and R.E. Novak, eds., pp. 50-57, (1994).

[4] B. Vermeire, A.L.P. Rotondaro, P.W. Mertens, S. Verhaverbeke, and M.M. Heyns, *Proceedings of the Third International Symposium on Cleaning Technology in Semiconductor Device Manufacturing*, J. Ruzyllo and R.E. Novak, eds., pp. 58-64, (1994).

[5] S. Naito and T. Nakashizu, Mat. Res. Soc. Symp. Proc. Vol. 262, pp. 641-651 (1992).

[6] O.J. Antilla, M.V. Tilli, M. Scaekers, and C.L. Claeys, J. Electrochem. Soc., 139 (4) 1180-1185 (1992).

[7] T. Ohmi, T. Imaoka, I. Sugiyama, and T. Kezuka, J. Electrochem. Soc., vol. 139, no.11, 3317-3335 (1992).

[8] S. Fujimura and H. Yano, J. Electrochem. Soc., vol. 135, no. 5, 1195-1201 (1988).

[9] O. Joubert, D. Mathiot, and J. Pelletier, Appl. Phys. Lett., vol. 54, no. 22, 2241-2243 (1989).

[10] T. Hosoya, Y. Ozaki, and K. Hirata, J. Electrochem. Soc., vol. 132, no. 10, 2436-2439 (1985).

[11] P. Verdonck, C.M. Hasenack, and R.D. Mansano, J. Vac. Sci. Technol. B 14 (1), 538-542 (1995).

[12] E. Hsu, H.G. Parks, R. Cragin, S. Tomooka, J.S. Ramberg, and R.K. Lowry, J. Electrochem. Soc., Vol. 139, No. 12, 3659-3664 (1992).

[13] M.L. Kniffin, T.E. Beerling, and C.R. Helms, J. Electrochem. Soc., Vol. 139, No. 4, 1195-1199 (1992).

[14] G.J. Norga, K.A. Black, H. M'saad, J. Michel, and L.C. Kimerling, *Proceedings of the Second International Symposium on Ultra Clean Processing of Silicon Surfaces*, (1994).

[15] A.S. Lawing, A.J. Muscat, H.H. Sawin and J.W. Butterbaugh, *Proceedings of the Fourth International Symposium on Cleaning Technology in Semiconductor Device Manufacturing*, PV 95-20, J. Ruzyllo and R.E. Novak eds., p. 150, The Electrochemical Society, Pennington, N.J.(1996).

[16] J. W. Butterbaugh, D. C. Gray, C. F. Hiatt, H. H. Sawin, and A.S. Lawing, *Proceedings of the Second International Symposium on Ultra Clean Processing of Silicon Surfaces*, M. Heyns, M. Meuris, and P. Mertens eds., p. 229, Acco, Leuven, Belgium (1994).

[17] R. Sugino, Y. Okui, M. Okuno, M. Shigeno, Y. Sato, A. Ohsawa, and T. Ito, IEICE Trans. Electron., Vol. E75-C, No. 7, 829-833 (1992).

[18] R. Sugino, Y. Nara, T. Yamakazi, S. Watanabe, and T. Ito, Extended Abstracts of the 19th Conference on Solid State Devices and Materials, August 25-27, 1987, Tokyo (Business Center of Academic Societies, Tokyo, 1987), pp. 207-210.

[19] A.S. Lawing, A.J. Muscat, Y-P Han, and H.H. Sawin, Submitted to J. Vac. Sci. Technol., Nov. 1996.

[20] H. Okabe, *Photochemistry of Small Molecules*, Wiley Inter-Science, N.Y., p. 185 (1978).

[21] B. Li, I. Twesten, and N. Scwentner, Appl. Phys. A, 56, 355-364 (1993).

[22] E.A. Ogryzlo, D.L. Flamm, D.E. Ibbotson, and J.A. Mucha, J. Appl. Phys. 64 (11), 6510-6514 (1988).

[23] E.A. Ogryzlo, D.E. Ibbotson, D.L. Flamm, and J.A. Mucha, J. Appl. Phys. 67 (6), 3115-3120 (1990).

[24] R. Sugino, Y. Nara, H. Horie, T. Ito, J. Appl. Phys., 76 (9), 5498-5502 (1994).

[25] R. Sugino, in U.S. Patent #5,178,721 (Fujitsu Limited, Tokyo, Japan, 1993).

[26] J. Ruzyllo, in *Handbook of Semiconductor Wafer Cleaning Technology: Science, Technology, and Applications*, W. Kern, ed., p. 208, Park Ridge N.J.: Noyes Publications (1993).

[27] Y. Sato, R. Sugino, and T. Ito, Fujitsu Sci. Tech. J., 27 (4), 317-328 (1991).

[28] B.E. Deal and C.R. Helms, in *Handbook of Semiconductor Wafer Cleaning Technology: Science, Technology, and Applications*, W. Kern, ed., p. 316, Park Ridge N.J.: Noyes Publications (1993).

[29] W. Sesselmann and T.J. Chuang, Surface Science, Vol 176, No. 1-2, 32-66 (1986).

[30] H.F. Winters, J. Vac. Sci. Technol. A, 3 (3), 786-790 (1985).

[31] W. Sesselmann, E.E. Marinero, and T.J. Chuang, Surface Science, Vol. 178, 787-797 (1986).

[32] W. Sesselmann, E.E. Marinero, and T.J. Chuang, Appl. Phys. A, Vol. 41, 209-221 (1986).

[33] G.N.A. van Veen, T. Baller, and A.E. DeVries, J. Appl. Phys., 60 (10), 3746-3749 (1986).

[34] G.N.A. van Veen, T.S. Baller, and J. Dieleman, Appl. Phys. A, Vol. 47, 183-192 (1988).

[35] M. Galeotti, B. Cortigiani, U. Bardi, B.V. Andryushechkin, A.N. Klimov, and K.N. El'tsov, J. Elec. Spec. Rel. Phenom., Vol. 76, 91-96 (1995).

[36] B.J. Taylor, J. Photographic Science, Vol. 24, 77-80 (1976).

[37] A.L. Ashkalunin and P.M. Valov, Sov. Phys. Tech. Phys., 30 (8), 974-976 (1985).

[38] T.H. Fleisch and G.J. Mains, Appl. Surf. Sci., Vol. 10, 51-62 (1982).

[39] J. Pozanski, Journal of the Less-Common Metals, 169, 181-186 (1991).

[40] C.D. Wagner, W.M. Riggs, L.E. Davis, J.F. Moulder, and G.E. Muilenberg (ed.), *Handbook of X-Ray Photoelectron Spectroscopy*, p. 171, Perkin Elmer Corp., Physical Electronics Division, Eden Prarie, MN (1979).

[41] R. Colton and J.H. Canterford, *Halides of the First Row Transition Metals*, p. 490, Wiley-Interscience, New York (1969).

[42] R.R. Hammer and N.W. Gregory, J. Phys. Chem., Vol. 68, No. 11, 3229-3233 (1964).

[43] A.S. Lawing and H.H. Sawin, Unpublished Data

[44] E.G. King, A. D. Mah, and L.B. Pankratz, *Thermodynamic Properties of Copper and its Inorganic Compounds*, The International Copper Research Association and the U.S. Department of the Interior, Bureau of Mines, p. 30, (1973).

[45] R.A.J. Shelton, Trans. Faraday Soc., Vol. 57, 2113, (1961).

[46] Ibid. p. 172.

[47] E. Ikawa, S. Sugito, and Y. Kurogi, Surface Science, Vol. 183, 276-288 (1987).

[48] H. Okano, Y. Horiike, and M Sekine, Jap. J. Appl. Phys., part 1, Vol. 24, No. 1, 68-74 (1985).

[49] S.M. Mukhopadhyay and C.S. Chen, J. Vac. Sci. Technol. A 10 (6), 3545-3549 (1992).

[50] B. Ealet, E. Gillet, V. Nehasil, and P.J. Møller, Surface Science, 318, 151-157 (1994).

[51] A Mesarwi, A. Ignatiev, and J.S. Liu, Solid State Communications, Vol. 65, No. 5, 319-322 (1988).

[52] R. Sugino, Y. Okui, M. Shigeno, S. Okubo, K. Takasaki, and T. Ito, Proceedings of the 1995 Symposium on Semiconductor Manufacturing, 262-265 (1995).

[53] Courtney and Lamb, MRS April 1997.

[54] M. Okusawa, Phys. Stat. Sol. B, 124, 673-681 (1984).

[55] J. Zaanen, C. Westra, and G.A. Sawatzky, Phys. Rev. B, 33, 8060- (1986).

[56] K. Okada and A. Kotani, J. Phys. Soc. Japan, Vol. 60, No. 3, 772-775 (1991).

[57] L. Fiermans, R. Hoogewijs, and J. Vennik, Surface Science, 47, 1-40 (1975).

[58] A.R. Gonzalez-Elipe, R. Alvarez, J.P. Holgado, J.P. Espinos, G. Munuera, and J.M. Sanz, Applied Surface Science, 51, 19-26(1991).

Chapter 5

Transition Metal Removal with a UV Excited Dichlorosilane/Halogen Process

A UV/DCS/Halogen chemistry developed in a thermal beam process in our laboratory has been transferred to a UV activated process. Iron removal and partial nickel removal has been demonstrated with the substrate held at room temperature. Metal removal has been achieved in both a downstream (no direct UV flux to the sample surface) and direct configuration. This process provides an aggressive chemical pathway to the formation of volatile metal chloride products. Some problems associated with the UV/DCS/Halogen system are excessive fluorine incorporation and $SiCl_X$ deposition.

5.1 Introduction

Previous work in our group has demonstrated the efficacy of a hot thermal beam cleaning process in removing trace metals from wafer surfaces. In this process, a directional molecular beam of dichlorosilane (SiH_2Cl_2 or DCS) is dissociated at 1000°C to create reactive $SiCl_2$ species[1]. It was shown that combining this DCS beam with a flux of pyrolized halogen atoms greatly enhanced the efficiency of the cleaning process. Copper, nickel and iron removal to the detection limit of X-ray Photoelectron Spectroscopy (XPS) was achieved with the substrate held at room temperature with a DCS/F_2 hot thermal beam process.

In this work, the DCS/halogen system is extrapolated to a UV activated process. Instead of creating the reactive species thermally, gas molecules (and in some cases the surface) are excited with UV illumination. We have explored a limited range of reaction

conditions, using *in situ* XPS to monitor contamination levels, the chemical state of the surface and the extent of film deposition from the process. In this report of preliminary findings, it is demonstrated that a UV/DCS/F_2 process can remove iron and nickel from wafer surfaces. It appears that the ability of the UV/DCS/Halogen chemistry to remove metals at reduced temperature is due at least in part to the increased reactivity of this chemistry as compared to UV/Cl_2.

5.2 Experimental

The apparatus in which these experiments were performed is as described in section 2.1.1. The SiH_2Cl_2 used in these experiments was 99.99+% pure from Aldrich Chemical. The F_2 used in these experiments was 98 % pure from Spectra Gases. The Cl_2 used in these experiments was 99.998 % pure (Matheson ULSI grade). Various lamp configurations were used in the course of this work. The high pressure mercury/xenon arc lamp described in section 2.1.1 was used to provide both direct and indirect UV flux. In the direct configuration, the UV fluence was directed at the wafer surface as illustrated in Figure 2.2. In the indirect configuration, the lamp outlet was placed upstream of the sample, and the tube area surrounding the sample was blocked with aluminum foil, such that stray light would not strike it. In the indirect configuration, the high pressure lamp was used solely to generate reactive species in the gas phase, which would then flow downstream over the wafer surface. Another lamp configuration, consisting of a medium pressure mercury lamp in a dual parabolic reflector, was used exclusively for downstream processing. This exposure system is a custom design manufactured by Uvex Inc. In this configuration the lamp was situated in one focus of the reflector, and the tube in the other, effectively "imaging" the lamp in the center of the

tube. The second downstream configuration described above is illustrated in Figure 5.1. XPS analysis and trace metal sputter contamination methods are described in Chapter 2.

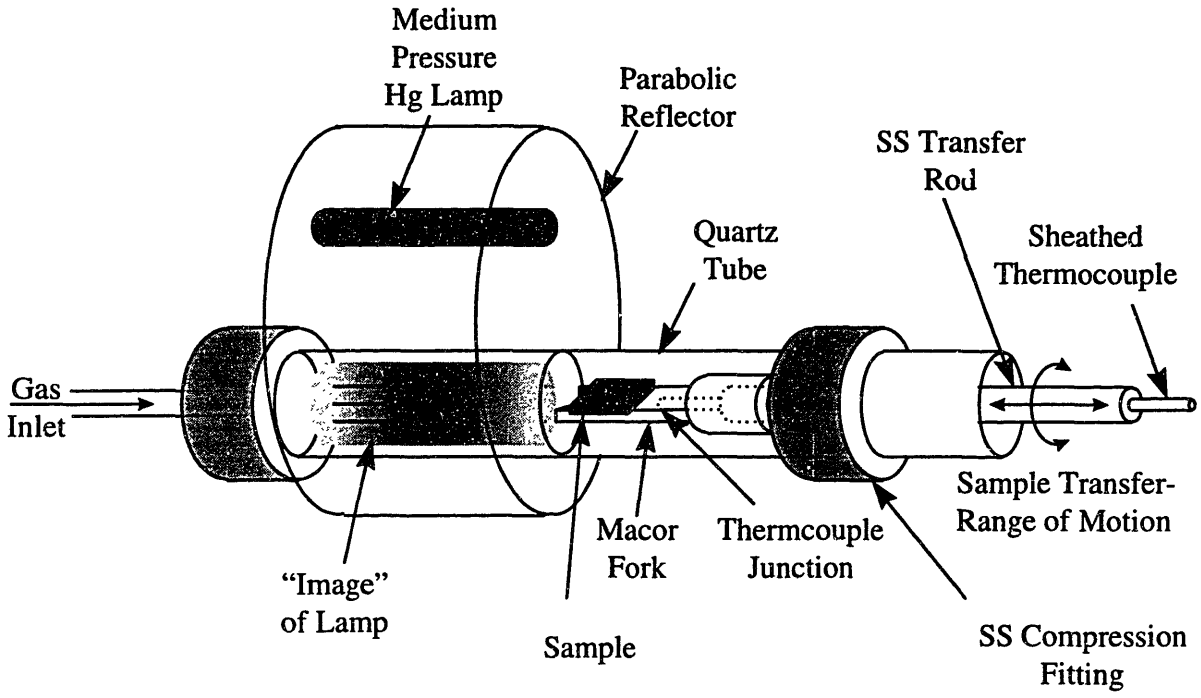

Figure 5.1-Schematic diagram of the UV reactor as configured for downstream processing with the medium pressure Hg lamp. A lamp housing with a dual parabolic reflector is located upstream from the sample. The lamp is located in one focus of the reflector and the other focus coincides with the axis of the quartz tube. The sample is positioned slightly downstream from the lamp housing so that it receives a minimum of direct UV illumination.

Samples were 1 cm square chips cut from an 8" wafer of n-type <100> silicon with a high quality thermally grown oxide of $\cong$ 3900 Å thickness. The chips were mounted on buttons fabricated of alumina for insertion into the chamber. For oxide surface experiments, the samples were wiped with IPA, rinsed in DI water and blown dry before insertion into the chamber. For bare silicon surface experiments, the samples were stripped of their oxide layer in 50 % HF, wiped with IPA and blown dry before insertion into the chamber. Care was taken to insert the bare wafers into the chamber as quickly as possible after the oxide strip to minimize oxide re-growth before the experiment could be performed.

The conditions for all of the runs made in this series of experiments is summarized in Table 1. All of the runs were made with the substrate initially at room temperature. In the case of the direct UV experiments, a temperature rise on the order of 10°C/minute was observed. In the case of the downstream experiments, where there was no direct UV fluence to the surface, little or no sample heating was observed over the course of a run. Initial metal coverage for all of the runs was ≈ 0.05-0.1 monolayer.

5.3 Results and Discussion

A. UV/DCS/Cl_2 Processing

Iron and nickel removal were attempted with a UV/DCS/Cl_2 process. A range of partial pressures (100 mTorr-10 Torr reactive gas) were explored as listed in Table 1. All of these runs were made with direct UV illumination at composition ratios in the chlorine rich regime. The UV/DCS/Cl_2 results were generally disappointing. In summary, we found no evidence that the UV/DCS/Cl_2 process was capable of removing iron with any greater efficiency than UV/Cl_2 alone. As with the UV/Cl_2 process, UV/DCS/Cl_2 removes metallic iron but is ineffective in removing oxidized iron (see Chapter 4 for a discussion of the oxidation behavior of iron on wafer surfaces). Figure 5.2 illustrates these results. Also, we found no evidence of nickel removal with the UV/DCS/Cl_2 process, although we did observe $NiCl_2$ formation at room temperature. Admittedly, this is a very limited set of experiments, and it is quite possible that there exists a parameter space where the UV/DCS/Cl_2 will remove metals effectively.

Run #	Surface	Halogen	DCS/X X=Cl_2 or F_2	Reactive Gas Pressure	Direct=X Down-stream=O	Exposure System	Metal	Run Time (sec)	Removal
1	Si	F_2	1/10	10 Torr	X	High	Iron	30	yes
2	SiO_2	F_2	1/10	10 Torr	O	High	Iron	30	yes
3	SiO_2	F_2	1/10	10 Torr	-	-	Iron	30	?
4	SiO_2	Cl_2	1/4	100 mTorr	X	High	Iron	10	no
5	SiO_2	Cl_2	1/10	500 mTorr	X	High	Iron	30	no
6	SiO_2	Cl_2	1/10	10 Torr	X	High	Iron	30	no
7	Si	Cl_2	1/10	10 Torr	X	High	Iron	30	met=yes ox=no
8	Si	Cl_2	0/1	9.09 Torr	X	High	Iron	30	as above
9	Si	Cl_2	1/10	10 Torr	X	High	Nickel	30	no
10	Si	F_2	10/1	500 mTorr	X	High	Nickel	30	yes
11	SiO_2	F_2	10/1	500 mTorr	X	High	Nickel	30	no
12	Si	F_2	10/1	500 mTorr	O	Medium	Nickel	90	yes
13	Si	F_2	0/1	45 mTorr	O	Medium	Nickel	90	no
14	Si	F_2	1/0	455 mTorr	O	Medium	Nickel	90	no
15	Si	F_2	20/1	500 mTorr	O	Medium	Nickel	90	no
16	Si	F_2	5/1	500 mTorr	O	Medium	Nickel	90	no
17	Si	F_2	10/1	500 mTorr	O	Medium	Nickel	60	yes
18	Si	F_2	1/5	500 mTorr	O	Medium	Nickel	90	yes

Table 5.1-Summary of conditions and qualitative removal evaluation of the UV/DCS/Halogen experiments. The designation "High" refers to the illumination system described in chapter 2. The designation "Medium" refers to the illumination system described in this chapter and illustrated in figure 5.1.

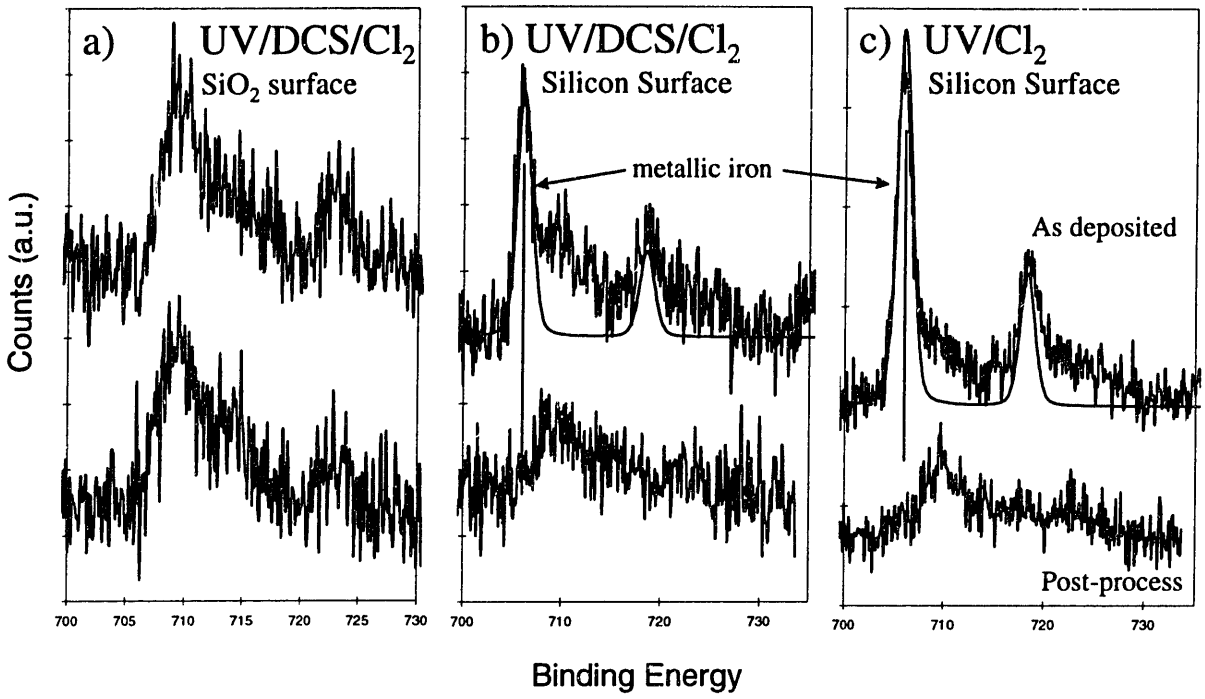

Figure 5.2-Iron 2p photoelectron emission spectra illustrating iron removal with $UV/DCS/Cl_2$ and UV/Cl_2. The uppermost spectrum is the as deposited metal signal while the lower spectrum represents the post process signal. The metallic contribution is shown as the fit superimposed on the raw data in b & c (See Chapter 4 for a discussion of the oxidation behavior of iron on wafer surfaces). Conditions for a, b & c are as listed in Table 1 for runs 6, 7 & 8 respectively. No DCS was used in the run illustrated in c. $UV/DCS/Cl_2$ is ineffective in removing oxidized iron and exhibits metallic iron removal similar to UV/Cl_2 at room temperature.

B. $UV/DCS/F_2$ Processing

Iron and nickel removal were also attempted with $UV/DCS/F_2$. As with the thermal beam process reported in Chang *et al.*[1], we achieved much better metal removal results with this chemistry.

Iron removal was achieved in both a direct and a downstream process as illustrated in Figure 5.3. There are some qualifications attached to these results, however. In both the downstream and direct process, severe fluorine incorporation was observed. As a result of the high concentration of fluorine in the near surface layer, the iron 2p photoelectron spectrum

was obscured by the plasmon loss peak due to the fluorine 1s photoemission at ~685 eV. Consequently, it is impossible to unequivocally state that the iron was totally removed by the process, although it does appear from the spectra illustrated in Figure 5.3 that the iron was removed to the detection limit. Fluorine incorporation can be minimized by lowering the reactive gas pressure. The runs illustrated in figures 5.3 were performed with 10 torr of reactive gas. Based on our results with nickel removal (discussed below) the process should work well at a pressure of 500 mTorr or less, where fluorine incorporation is reduced significantly.

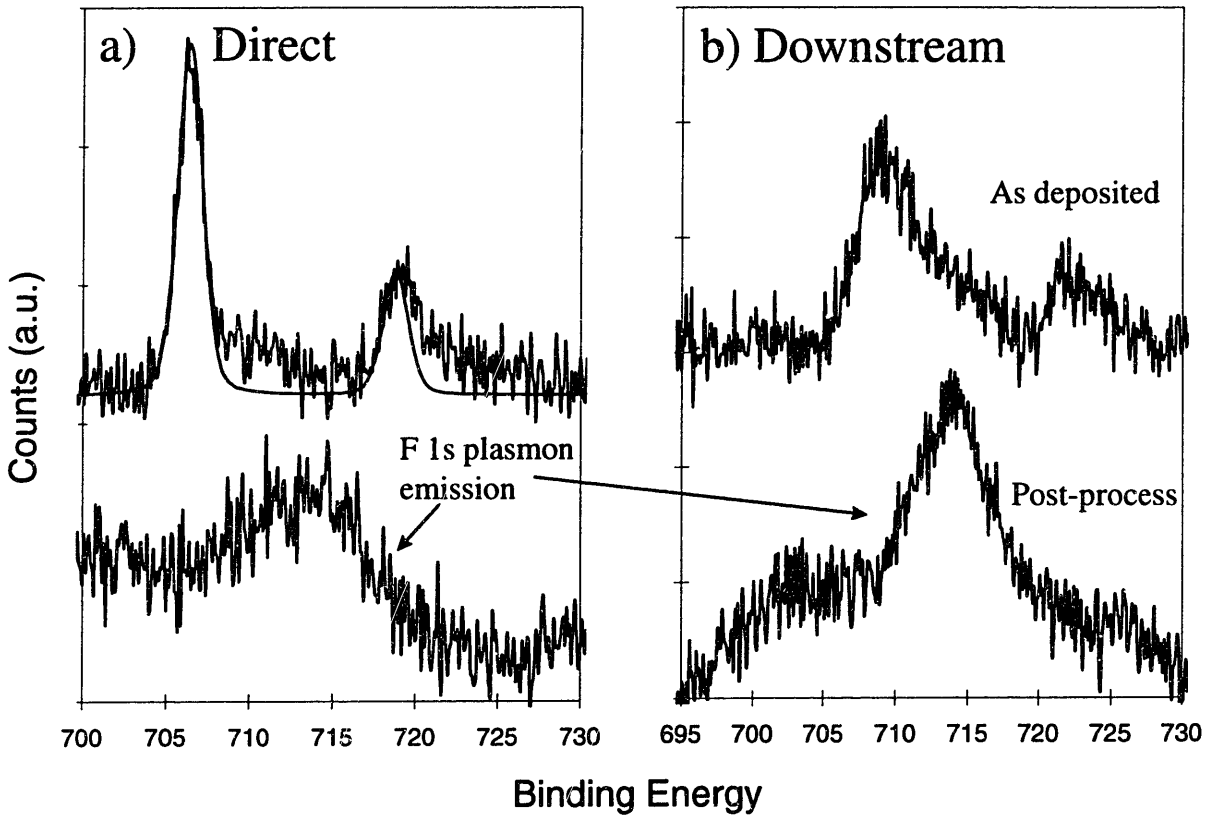

Figure 5.3-Iron 2p photoelectron emission spectra illustrating iron removal with UV/DCS/F_2 at a ratio of 1 DCS/10 F_2. Conditions for a & b are as listed in Table 1 for runs 1 & 2 respectively. Judging iron removal with XPS is difficult due to the interference from the fluorine 1s plasmon emission. UV/DCS/F_2 appears to be effective in removing oxidized iron even without the aid of direct illumination.

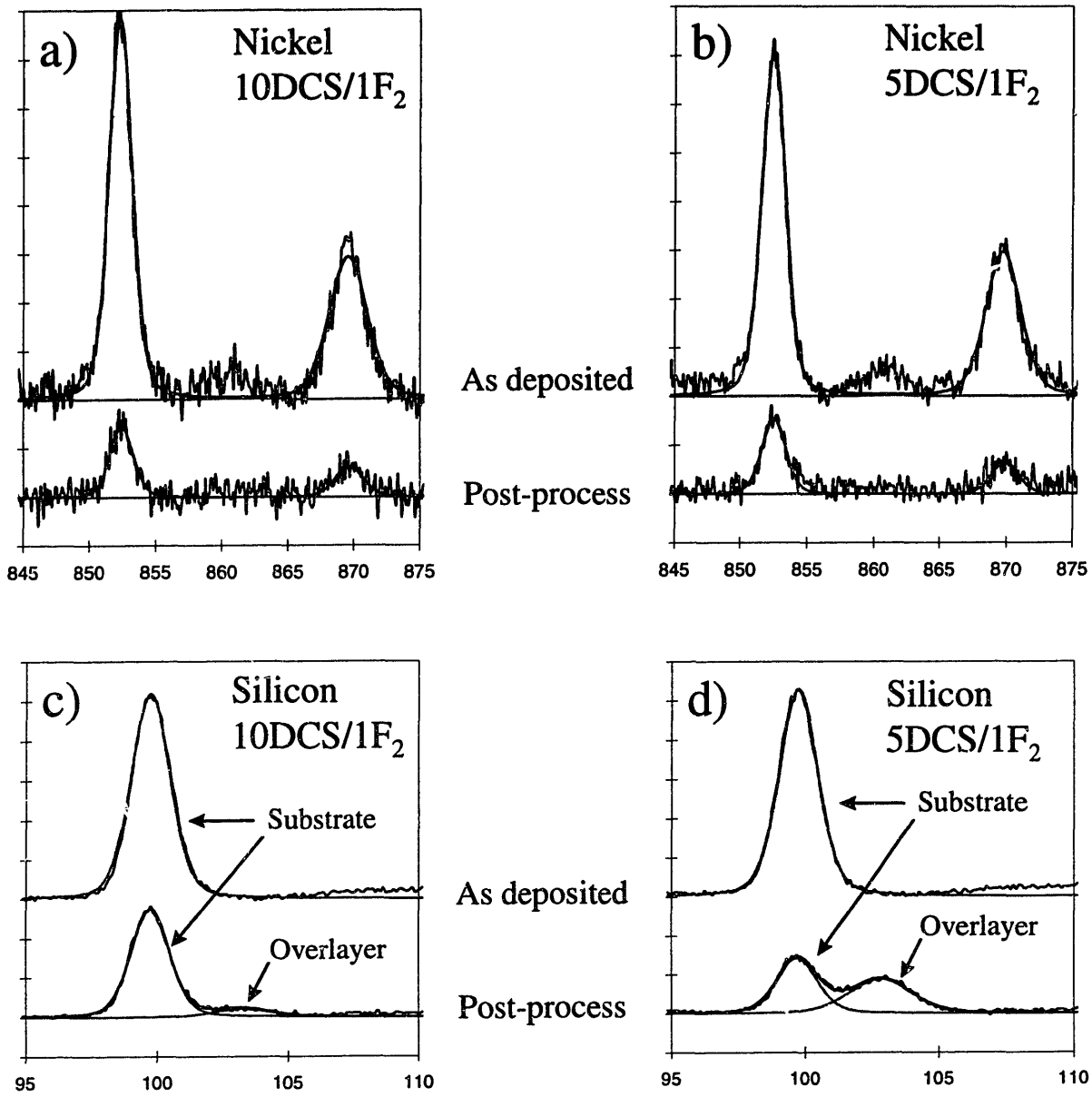

Figure 5.4-Nickel 2p (a & b) and silicon 2s (c & d) photoelectron emission spectra illustrating nickel removal with UV/DCS/F_2. The spectra in a & c represent run #12 and the spectra in b & d represent run #16 from Table 1. Although the relative removal of nickel appears to be very similar between the two runs, inspection of the silicon spectra indicates that significant deposition has occurred due to DCS/F_2 processing. The reduction in the substrate peak at 99.75 eV and the appearance of the overlayer peak at ~103 eV is evidence of this. Significantly more deposition has occurred in the 5/1 ratio experiment. Therefore substantially more nickel was removed in the 10/1 experiment and a higher percentage of the signal reduction in the 5/1 experiment is due to the presence of a thicker overlayer masking the nickel photoemmission.

Our results with nickel removal are not as clear-cut. Based on the fluorine incorporation problem discussed above, our initial approach was to attempt removal in the DCS rich regime, combined with a reduction in reactive gas pressure. In this regime, deposition from the reactive gas phase $SiCl_2$ species occurs. It becomes difficult to distinguish nickel removal from nickel signal attenuation due to the deposition of an overlayer. Figure 5.4 illustrates this problem. In these two runs, the nickel signal has been reduced by proportionally the same amount from their pre-process levels. Inspection of the nickel spectra alone would indicate that both runs show a nickel removal efficiency on the order of 75%. However, an analysis of the silicon spectra indicates that there is a difference in substrate signal attenuation between the two runs, and in fact the run illustrated in figure 5.4 a & c represents significant nickel removal while the nickel attenuation illustrated in figure 5.4 b can be entirely accounted for by the presence of an overlayer, as illustrated by the silicon spectrum in figure 5.4 d.

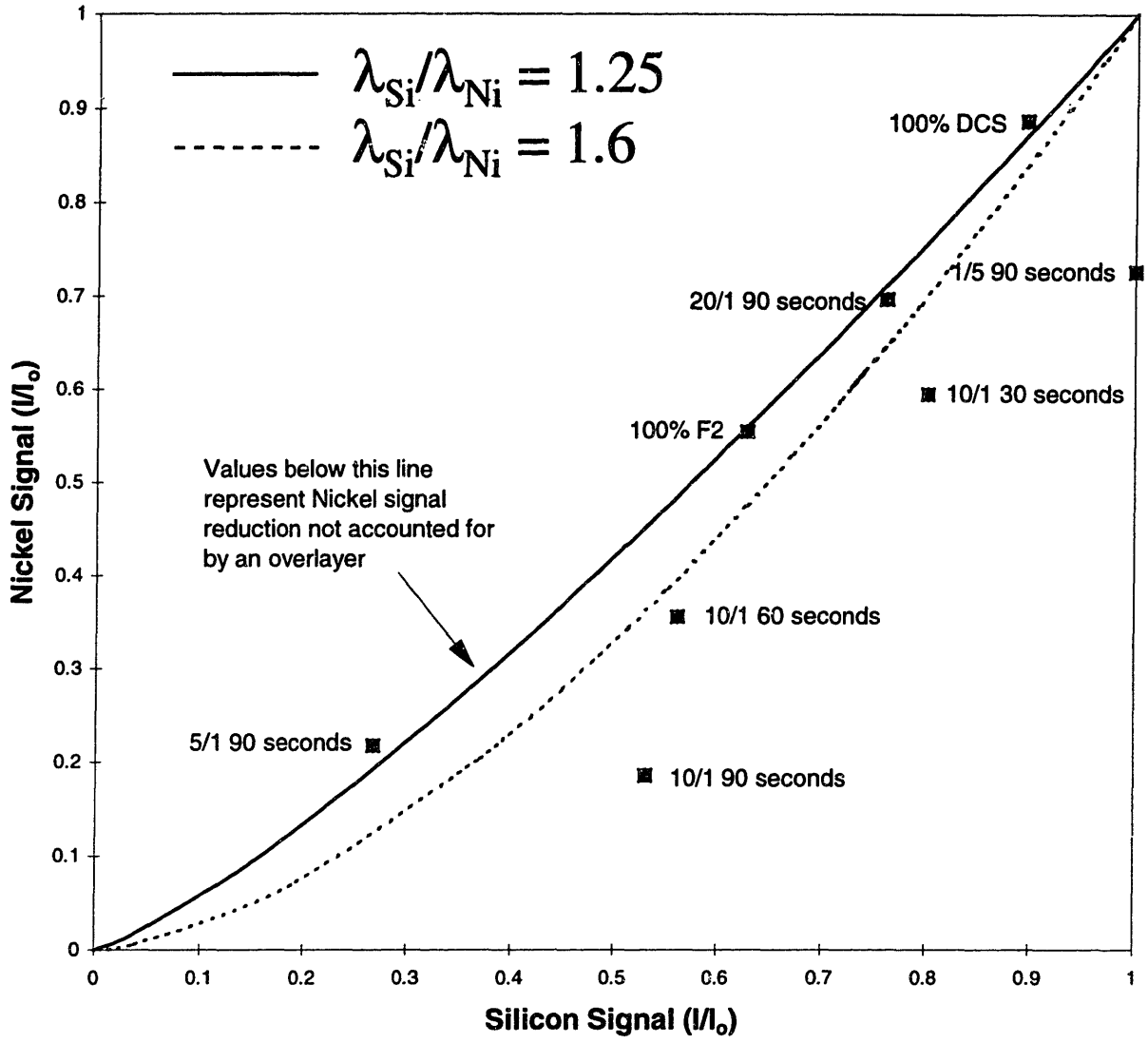

Figure 5.5- Nickel $2p_{3/2}$ versus silicon 2p signal attenuation due to UV/DCS/F_2 processing in the DCS rich regime. Points below and to the right of the "diagonal" constructed from $\lambda_{Si}/\lambda_{Ni}$ ratios represent nickel removal. A point in the lower right corner of the plot would represent complete nickel removal with no overlayer formation. The significance of the $\lambda_{Si}/\lambda_{Ni}$ ratios is explained in the text.

Figure 5.5 represents all of the nickel removal experiments in a nickel removal versus attenuation due to deposition framework. The figure shows nickel signal attenuation versus silicon signal attenuation. The "diagonal" lines represent the signal attenuation which would be expected solely from the presence of an overlayer:

$$I/Io=\exp(-d/\lambda\sin\theta) \qquad (1)$$

where d is the overlayer thickness, θ is the spectrometer take-off angle (90° for these experiments) and λ is the photoelectron mean free path through the overlayer for the respective element. The diagonal is obtained by choosing values λ for Si and Ni then plotting $(I/Io)_{Ni}$ vs $(I/Io)_{Si}$ for a series of overlayer thickness' "d". The diagonal will shift with the ratio of λ. The solid diagonal is a best fit through the points that appear to lie on a line, yielding a $\lambda_{Si}/\lambda_{Ni}$ ratio of 1.25. The dotted diagonal arises from a $\lambda_{Si}/\lambda_{Ni}$ ratio based on the relation:

$$\lambda \propto \text{KineticEnergy}^{1/2} \qquad (2)$$

which gives a ratio of 1.6. Any point lying below and to the right of the "diagonal" represents nickel signal attenuation which can not be accounted for by the presence of an overlayer, i.e. nickel removal. The extent of nickel removal can be roughly estimated by constructing a vertical "tie-line" between the diagonal and the x-axis, intersecting the point of interest. The ratio of the length of the portion of the tie line between the diagonal and the experimental point, and the entire length between the diagonal and the x-axis, will give the amount of

nickel removed. Any point lying on the x-axis would represent complete nickel removal. A point in the lower right corner of the plot (y=0, x=1) would represent complete nickel removal with no overlayer deposition. Any point on the left y-axis would represent fractional removal with no deposition. Inherent in this model are a few assumptions. First is that all of the silicon signal attenuation is due to the presence of a $SiCl_X$ overlayer. Second is that the as deposited nickel remains at the substrate-overlayer interface. If the first assumption is valid, then the second assumption is reasonable since the process is performed at room temperature. The first assumption breaks down when fluorine incorporation becomes significant, and Si-F bonding contributes to substrate signal attenuation. All of the runs which show silicon signal attenuation in figure 5.5 represent fluorine partial pressures on the order of 50 mTorr, where fluorine incorporation is not significant (see figure 5.6). Therefore, both assumptions are reasonable in the DCS rich regime.

From Figure 5.5, it is obvious that the most attractive process conditions are at DCS/F_2 ratios of 10/1 and 1/5. The 1/5 ratio is consistent with the results of Chang *et al.*, and if not for the initial problem with fluorine incorporation in the F_2 rich regime (see the sequence of experiments in Table 1), we would probably have explored the F_2 rich regime in much more detail. At 500 mTorr and a 1/5 ratio, we observed minimal fluorine incorporation, and no overlayer deposition (note that the 1/5 point falls on the y axis) as shown by the lack of attenuation of the silicon 2p peak and the reduced intensity of the fluorine 1s peak at 500 mTorr reactive gas pressure, as illustrated in Figure 5.6. Although the extent of nickel removal is only on the order of 30%, it is the most intriguing result obtained here and indicates the most attractive parameter space for further study. The 10/1 results are somewhat confusing. We do not have a good explanation for why we should observe substantial

removal at a ratio of 10/1 while the two ratios bracketing it, 20/1 and 5/1 show no removal. It is possible that this system could exhibit multiple maxima in terms of removal efficiency as a function of gas composition ratio.

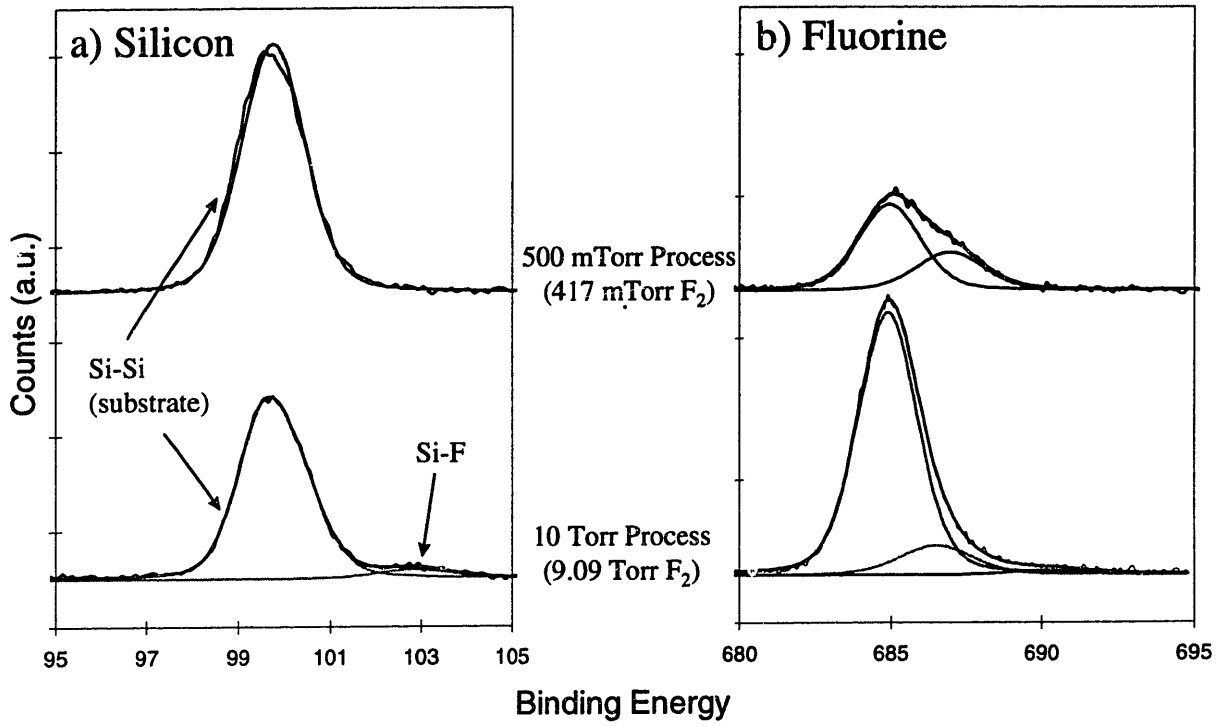

Figure 5.6-Silicon 2s and fluorine 1s photoelectron emission spectra after UV/DCS/F_2 processing in the fluorine rich regime. A process with 500 mTorr reactive gas results in significantly less fluorine incorporation into the substrate as compared to a 10 Torr process. This is evident by; 1) the reduced fluorine 1s photoemission intensity, 2) the lack of attenuation of the silicon substrate peak, and 3) the lack of significant Si-F bonding in the 500 mTorr spectra.

C. Mechanism of Metal Removal in UV/DCS/Halogen Processing

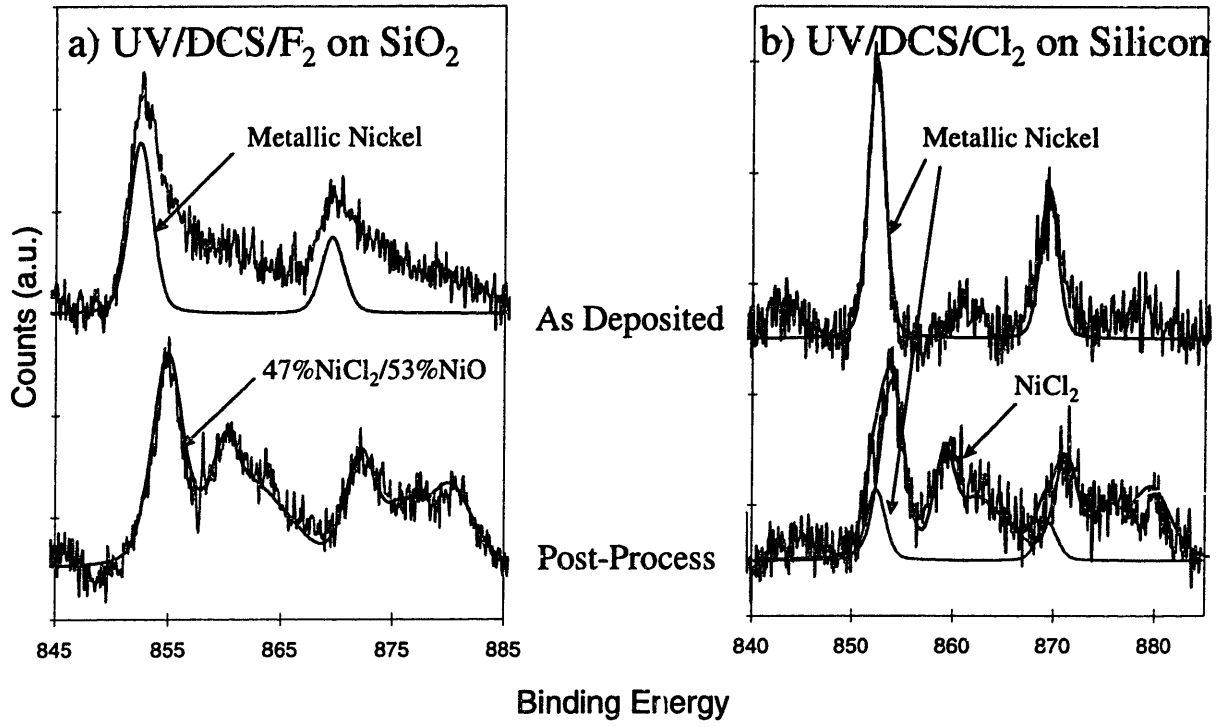

Figure 5.7-Nickel 2p photoelectron emission spectra illustrating the formation of $NiCl_2$ in UV/DCS/Halogen processing. In a), an initially mixed $NiO/Ni^{(0)}$ is converted to a mixed $NiO/NiCl_2$ after exposure to UV/DCS/F_2 at room temperature. In b), metallic nickel is converted to $NiCl_2$ in a UV/DCS/Cl_2 process at room temperature. In a UV/Cl_2 process, $NiCl_2$ does not form below ~100°C.

The spectra illustrated in figure 5.7 shed some light into the possible mechanism by which trace metals are removed in the UV/DCS/Halogen process. It is significant that $NiCl_2$ is formed at room temperature in the presence of dichlorosilane. In a UV/Cl_2 process, $NiCl_2$ does not form on a silicon surface below ~100°C (the lower limit of $NiCl_2$ formation on an oxide surface has not been determined, but the chlorination behavior illustrated in figure 5.7 a is similar to that observed at >100°C in UV/Cl_2). As was mentioned in Chapter 4, the chlorination reaction is a crucial step in the metals removal process. If volatile metal chlorides (or other metal bearing species) are not formed, trace metals are not removed from the wafer

surface. The UV/DCS/Halogen process appears to be more aggressive chemically than UV/Cl_2, allowing for the formation, and hence the subsequent removal, of metal chloride products at lower temperature. This tendency is not observed in the reaction of $UV/DCS/Cl_2$ with iron since iron also reacts readily with UV/Cl_2.

Sugino *et al.*[2,3] have postulated similar behavior in the $UV/SiCl_4/Cl_2$ system. They hypothesize that $SiCl_X$ species (produced from the reaction of Cl with silicon or from UV activated $SiCl_4$) either; 1) act as a catylyst for the reaction of chlorine with or, 2) react directly with, sodium, iron, and especially iron oxide to from volatile NaCl or $FeCl_X$ reaction products.

5.4 Conclusions

We have demonstrated iron removal to the detection limit of XPS and partial nickel removal with a UV activated dichlorosilane/fluorine process ($UV/DCS/F_2$) with the sample held at room temperature. Metal removal was achieved in a downstream process where there was no direct UV fluence to the wafer surface. Some problems associated with this process are the tendency towards fluorine incorporation (in the fluorine rich regime) and overlayer deposition (in the DCS rich regime). We have identified an attractive parameter space for further study, which shows potential for a short process which exhibits minimal fluorine incorporation and no overlayer deposition. Based on our work with the same chemistry in a thermal beam system, we expect copper to be readily removed with this process. We found no evidence that a $UV/DCS/Cl_2$ was superior to a UV/Cl_2 process, although the parameter space studied was admittedly limited. When compared to the UV/Cl_2 process, the UV/DCS/Halogen

system provides a more aggressive chemical pathway to the formation of chlorinated metal reaction products.

5.5 References

[1] J.P-C. Chang, Z. Zhang, H. Xu, H.H. Sawin, and J.W. Butterbaugh, submitted to J. Vac. Sci. Technol.

[2] R. Sugino, Y. Okui, M. Shigeno, S. Okubo, K. Takasaki, and T. Ito, Proceedings of the 1995 Symposium on Semiconductor Manufacturing, 262-265 (1995).

[3] R. Sugino, M. Okuno, and Y. Sato, in U.S. Patent # 5,578,133, (Fujitsu Limited, Kawasaki, Japan, Nov. 26, 1996).

Chapter 6

Integrated Dry Cleaning after Reactive Ion Etching of SiO_2 in Fluorocarbon Gases

The removal of fluorocarbon polymer and oxide residue formed by reactive ion etching (RIE) and oxygen plasma ashing on blanket wafers has been demonstrated with an integrated, all dry process. *In situ* X-ray Photoelectron Spectroscopy (XPS) was used to analyze the initial contamination and to monitor the contamination removal. The dry cleaning sequence consisted of: 1) an ultraviolet excited chlorine (UV/Cl_2) process to remove carbonaceous polymer contamination, 2) a reduced pressure vapor phase HF process to remove oxide contamination, and 3) an additional UV/Cl_2 process to remove polymer residue that was embedded in the oxide film. These dry processes were performed sequentially with vacuum transfer between each processing chamber and the XPS analysis chamber. The dry cleaning results compare favorably with a typical wet cleaning sequence.

6.1 Introduction

Plasma or reactive ion etching (RIE) of SiO_2 in fluorocarbon gas mixtures is widely used to anisotropically etch contact holes and vias in semiconductor device fabrication. Directional etching profiles and selectivity are achieved by including polymer forming gases in the etching recipe. These gases create an etch inhibiting film on the sidewalls of the patterned photoresist and oxide. A film is also deposited on the underlying silicon to which a contact is to be made. Besides the fluorocarbon, the polymer film often contains etching

products and contaminants such as metals, silicon, and oxides[1,2,3]. Additional background on the contamination and damage due to RIE processes is given in Chapter 1. The bulk of the photoresist and some of the polymer residue are removed in a subsequent ashing step using an oxygen-based plasma. If not removed, the polymer increases the contact resistance. Ashing is ineffective in eliminating metal contaminates which can adversely affect device yield and reliability[3] and results in the growth of a thin oxide layer on the silicon surface.

Removing polymer and photoresist residues, metals, and oxides after RIE and ashing is currently done using wet chemical solutions, but this technique is becoming less cost effective. Vacuum incompatibility, inadequate contaminant removal, and the environmental impact of the cleaning chemicals are some of the concerns associated with wet cleaning. Wafers must be transported out of the vacuum environment where etching and ashing are done to a wet bench. Liquid solutions may not effectively clean small, high aspect ratio contact holes, unless surfactants are used. Moreover, the volume of chemicals and water used in wet cleaning processes has come under increasing pressure because of safety and disposal costs. These concerns are the driving forces behind the development of dry cleaning processes to replace wet cleaning of contact holes.

Downstream plasma and neutral sources are dry processes that can potentially replace the wet process regime now used for post-RIE cleaning. Dry processing equipment lowers chemical consumption and has a smaller footprint than wet cleaning benches which should offset the greater equipment cost for dry processing[4]. Moreover, dry processing is done in the gas phase, making it vacuum compatible. In chemical downstream etching the wafer is physically separated from the plasma region to minimize the radiative flux (ions and photons) to the wafer. Neutral sources use heat or light to provide the activation energy needed to form

reactive species. Numerous dry and wet/dry cleaning processes applied to RIE residue removal have been reported in the literature[5,6,7,8,9,10]. While these processes have shown promise, they all involve plasma excitation of the reactive gas, and could potentially result in damage to the wafer.

Ultraviolet excited chlorine is effective in removing trace metal contaminants from wafer surfaces[11,12,13,14,15]. UV/Cl_2 is a process that readily etches silicon but does not etch SiO_2 significantly at our conditions. The UV/Cl_2 process acts to remove metallic contaminants through a combination of gas phase dissociation of molecular chlorine to create reactive atomic chlorine and surface photolysis. In Chapter 4 we demonstrated that UV/Cl_2 effectively removed copper from both silicon dioxide and silicon surfaces at 50°C by forming a volatile copper chloride species. Chlorine radicals are thermodynamically favored to spontaneously etch carbon and carbon rich fluorocarbon polymers producing volatile CF_XCl_Y compounds[16]. The thermodynamics of product formation as well as the observation that UV/Cl_2 removed adventitious carbon from wafer surfaces encouraged us to apply the process to the removal of RIE residue. The feasibility of etching polymer residue formed during RIE in CF_4/H_2 and CHF_3[17,18] with UV/Cl_2 has been previously demonstrated in the literature. Ikawa *et al.* reported etching RIE residue in 200 mTorr UV/Cl_2, although the temperature at which this was accomplished was not explicitly stated[18].

Anhydrous HF mixed with either water[19,20] or alcohol vapor[21,22,23,24] is an effective means of etching silicon oxide. Both atmospheric[24,25] and reduced pressure[19] commercial tools are available for this process. The etching reaction is thought to occur in a condensed liquid-like film on the wafer surface, but recent work has shown that both monolayer[22,23] and

multilayer etching regimes are possible. A *reduced pressure* process is more compatible with a vacuum environment and introduces a measure of control.

We demonstrate in this work that an integrated dry cleaning sequence is capable of removing blanket polymer and oxide films that were produced by RIE and RIE/ashing processes. In our integrated sequence, the majority of the polymer contamination was first removed with UV/Cl_2 exposure. The thin silicon oxide film exposed by removing the polymer was then stripped using an HF/vapor mixture. Finally, a second UV/Cl_2 process was used to remove embedded carbon which could not be removed before stripping the oxide film. Transfer of the samples between processing modules was done under vacuum at a base pressure of 10^{-7} Torr. The integrated UV/Cl_2 and HF/vapor processes removed post-RIE residue even when the samples were not ashed. The dry cleaning sequence showed results comparable to a typical post-RIE wet cleaning sequence consisting of an H_2SO_4/H_2O_2 (Piranha) clean followed by an SC1 clean and an aqueous HF dip.

6.3 Experimental

The experimental apparatus in which these experiments were performed is schematically illustrated in Figure 2.1. The system consists of a load lock, a UV reactor, an HF/vapor reactor, and an analytical chamber where we have the capability to perform XPS *in situ*. The samples are transported via magnetically coupled transfer rods between reaction and analytical chambers without air exposure. The UV reactor used in these experiments is described in Chapter 2.1.1. The HF/vapor reactor used in these experiments is described in Chapter 2.1.2. XPS analysis was performed in the chamber described in Chapter 2.1.3. The analyzer was set for a pass energy of 20 eV. Data was collected for less than 30 minutes for

any particular elemental spectrum to minimize x-ray exposure effects on the condition of the sample surface.

Surface roughness measurements were performed with a Topometrix TMX 2000 Atomic Force Microscope (AFM). Measurements were made in "tapping mode", *i.e.* a function generator was used to drive the tip with a low amplitude modulation so as to "blur" the effects of adsorbed films on the sample surface. We have found this operating mode to be advantageous when analyzing silicon surfaces. Topometrix Supertips, consisting of a high aspect ratio carbon filament grown on the end of a standard Si_3N_4 pyramidal tip, were used for the analysis, allowing for high lateral resolution and minimizing image convolution from the shape of the tip.

The samples were plasma etched and ashed in the Materials Technology Laboratory at MIT. Wafers containing stacked blanket films of 5000 Å thermal oxide/5000 Å polysilicon/100 Å thermal oxide on Si(100) were processed in a Lam 590 auto etch as follows: 1) "descum" consisting of 100 sccm O_2, 200 sccm He at a total pressure of 3 Torr; plasma power was 100 watts for 10 seconds; 2) plasma etch consisting of 30 sccm N_2, 5 sccm O_2, 125 sccm He, 30 sccm CHF_3 and 130 sccm CF_4 at a total pressure of 3 Torr; plasma power was 900 watts for 90 seconds; 3) (selected wafers) an ash in a barrel reactor at 400 millitorr O_2 and 900 watts for 30 minutes. After processing, each wafer was cleaved into 1 x 1 cm square samples which were mounted on holders made of alumina for insertion into the load lock and processing. Each wafer was wiped with isopropyl alcohol and blown dry with nitrogen immediately before insertion into the vacuum chamber. The IPA wipe did not effect the contaminating film resulting from processing, but was instead intended to remove gross surface contamination due to ambient exposure.

A wet cleaning sequence consisting of first, hot 3:1 H_2SO_4/H_2O_2 for 15 minutes (Piranha), second, 5:1:1 $H_2O/H_2O_2/NH_4OH$ for 15 minutes (SC1), and third, 100:1 H_2O/HF for 1 minute (HF Dip) was applied to samples which had been etched and ashed as described above. The samples were rinsed with fresh DI water after each wet cleaning step. All of the cleaning chemicals used were Mallinckrodt analytical reagent grade. The cleaning sequence was applied to three samples simultaneously, and one sample was removed after each wet cleaning step and inserted into the vacuum chamber. The transfer into the vacuum environment was accomplished as quickly as possible to avoid ambient contamination effects. Samples were exposed to air for not more than two minutes after the water rinse. A bare silicon sample ("control") was subjected to a Piranha clean and HF dip in order to establish the baseline level of carbonaceous contamination. Samples subjected to wet cleaning were not mounted on the alumina holders in order to avoid cross contamination from the mounting compound. Instead these samples were fastened to a stainless steel sample holder for insertion.

6.4 Results and Discussion

A. Analysis of Polymer Residue and Silicon Dioxide Films after RIE and Ashing

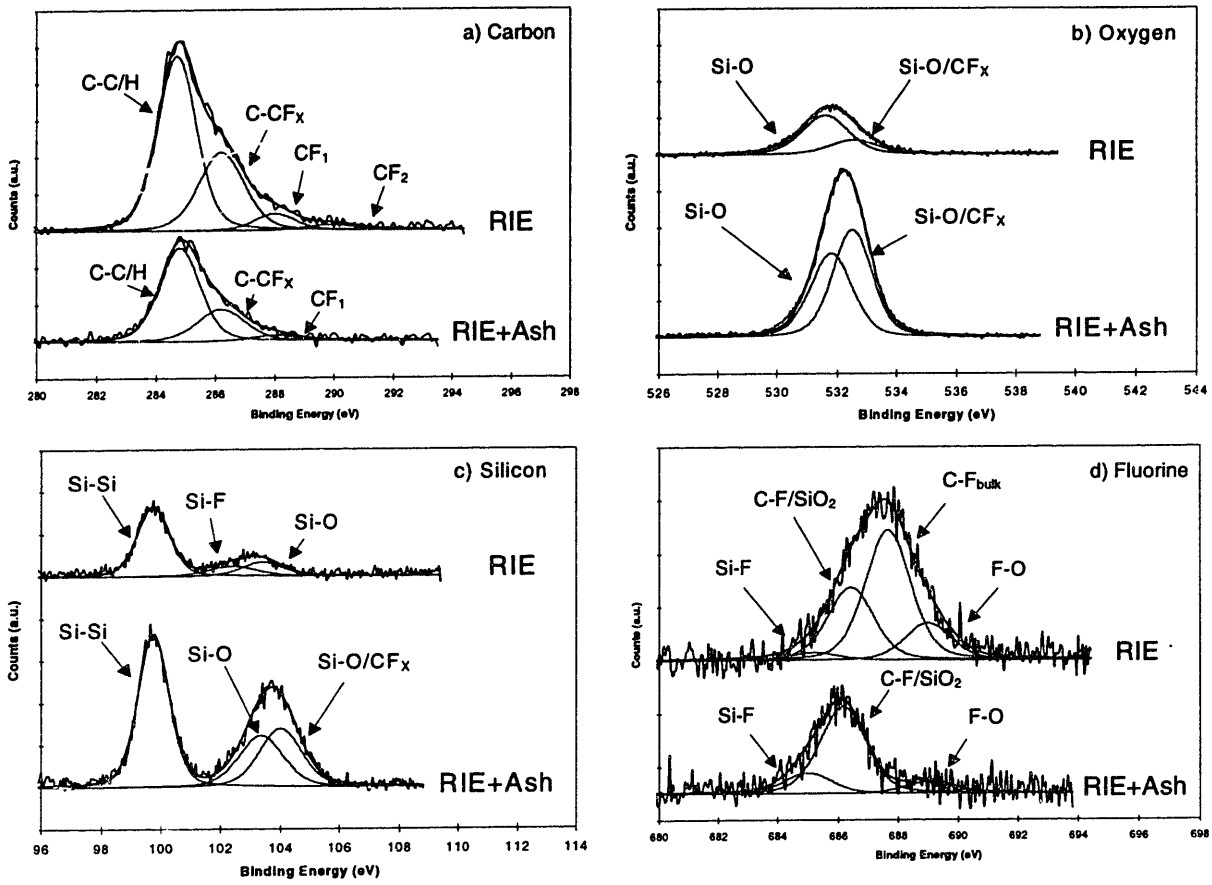

Figure 6.1- XPS spectra for a) carbon, b) oxygen, c) silicon, and d) fluorine after RIE and RIE + oxygen ashing. The oxygen ashing reduces the fluorocarbon polymer content of the contamination layer. The ashing process also results in oxide growth within the contaminating film.

XPS spectra of the polysilicon wafers after the etching process and after the etching and ashing processes are shown in Figure 6.1. The chemistry of these films has been investigated extensively and our XPS results agree qualitatively with what has been reported in the literature. The peak assignments shown in Figure 6.1 are adapted from a variety sources[5,6,26-30], including the database of XPS spectra from our own laboratory. Differences in spectrometer calibration from lab to lab make it difficult to extract absolute peak energies

from the literature, although relative peak energies are generally comparable. To compensate for sample charging effects, we have normalized all spectra to the silicon metal peak (Si-Si bonding), which is assigned a binding energy of 99.75 eV[5,9], and arises from the polysilicon substrate film. This component of the Si 2p spectrum is evident at all stages of this investigation, and is readily identifiable, making it an ideal reference. Whenever possible, a single chemical state was used as a reference in the peak fitting procedure. For example, to distinguish the Si-O state from the Si-O/CF_X state (defined below), a thermal oxide sample was used as a standard for the Si-O state, and all peak fits on the etched spectra utilized the peak energy and peak width from the thermal oxide standard. Table 6.1 summarizes the peak energies and corresponding chemical state assignments used in this work.

Before ashing, the carbon spectra of the films was richer in carbon than what has been reported for RIE in pure CF_4 or CF_4/H_2 mixtures. The films exhibited predominately C-C/H bonding, with a strong contribution from C-CF_x bonds but only a slight contribution from C-F_1 and very slight evidence of carbon bound to multiple fluorine atoms. Although not typical of pure CF_4 etching, this surface chemistry is typical of CHF_3 and C_xF_y/CHF_3 mixtures. The spectrum we obtained is very similar to that reported by Potter *et al.*[26] for pure CHF_3, and also consistent with the trend toward more C-C bonding relative to C-F bonding with increasing C_2F_6/CHF_3 ratio as reported by Yun *et al.*[27]. It should also be noted that these films were processed at a relatively high power of 900 W. This is consistent with the observations of Oehrlein *et al.*[28] which show a pronounced reduction of the F/C ratio in RIE etched films for increasing power from 275 to 1000 W. The silicon 2p line exhibits Si-Si bonding arising from the polysilicon substrate, and Si-O bonding with a slight contribution due to Si-F from the contaminating film. The fluorine spectrum shows two states of C-F bonding, which are

Element (line)	Chemical State	Binding Energy (eV)
Silicon (2p)	Si-Si	99.75 (reference)
	Si-F	102.4
	Si-O	103.4
	Si-O/CF_X	104
Chlorine (2p)	Si-Cl	199
	Cl-Si-F	200.4
	Cl-O	202.1
Carbon (1s)	C-C/H	284.7
	C-CF_X	286.2
	C-F_1	288
	C-F_2	289.9
Oxygen (1s)	Si-O	531.6
	Si-O/CF_X	532.4
Fluorine (1s)	Si-F	684.9
	C-F/SiO_2, C-F	686.2
	F-Si-Cl	687
	C-F_{BULK}	687.7
	F-O	689

Table 6.1-Summary of the binding energies and chemical state assignments used in this work.

attributable to bulk C-F and C-F bonds in a mixed oxide/fluorocarbon polymer environment denoted by C-F/SiO_2. These states are similar to the bulk and interfacial states reported by Cardinaud *et al.*[29]. Minor contributions attributable to both F-O and Si-F bonding can also be resolved in the fluorine spectrum prior to ashing. The oxygen spectrum shows primarily Si-O bonding with a slight contribution from Si-O in a mixed oxide/polymer environment denoted by Si-O/CF_X and corresponding to the C-F/SiO_2 peak in the fluorine line. The Si-O/CF_X component is characterized by an upward shift in binding energy of $\approx$ 0.6 eV from the Si-O peak. This observation is consistent with that of Robey and Oehrlein[30] who observed a similar shift in fluorinated SiO_2 layers.

Ellipsometric measurements were attempted to measure film thickness after RIE. The polysilicon films did not yield meaningful results, probably due to the inherent roughness of the polysilicon surface (see Figure 6.9). However, XPS analysis of single crystal substrates indicated that the composition and thickness of the contaminating films were similar to the polysilicon substrates, such that ellipsometric measurements of the single crystal wafers are valid for the polysilicon wafers. Measurements on single crystal substrates yielded a total contamination film thickness for the RIE samples of $\approx$ 50 Å. We were not able to fit the ellipsometric data with a multiple film model. Instead, the XPS data was used to estimate the relative thickness of the various layers in the contaminating film. The 50 Å total film thickness obtained from ellipsometry also correlates well with the XPS data.

Ashing altered the chemical makeup of the contamination layer, reducing the carbon and fluorine present and augmenting the oxygen. The intensity of the carbon spectrum was reduced by approximately one half, indicating a reduction in the fluorocarbon film thickness and the removal of the majority of the bulk fluorocarbon film. A slight shift of $\approx$ 0.3 eV was

observed in the carbon spectrum, although the relative energies of the fitted peaks are identical. This slight upward shift in binding energy can be attributed to the fact that the majority of the fluorocarbon is now present in a mixed polymer/oxide environment. The F/C ratio also decreased although contributions from C-CF_x and CF_1 were resolved. This observation is consistent with those of Park[5] and Oehrlein *et al.*[6] who report decreasing F/C ratios with oxygen plasma exposure. Correspondingly, an increase in the intensity of the substrate peak in the silicon spectrum was observed as the fluorocarbon film thickness was reduced. The Si-O signal grew relative to the Si-Si signal, indicating oxide growth. A significant proportion of the Si-O bonding arising from the ash was in a mixed fluorocarbon/oxide environment, denoted by Si-O/CF_X and characterized by an upward shift of $\approx$ 0.7 eV from the Si-O contribution. Less C-F bonding was evident in the fluorine line after the ash which indicates a reduction in the fluorocarbon content and corresponds with the reduction in intensity of the carbon line. Only C-F/SiO_2 bonding was resolved, again indicating that the majority of the bulk polymer film was removed and the remaining fluorocarbon was in a mixed polymer/oxide environment. Slight contributions from Si-F and F-O are also evident. The oxygen spectrum exhibited Si-O and Si-O/CF_X bonding, corresponding to the Si-O and Si-O/CF_X peaks in the silicon spectrum as discussed above. The intensity of the oxygen signal increased more than is accounted for by removal of the polymer overlayer, again indicating oxide growth within the contaminating film.

Based on our analysis, a representative cross-section of the contaminating films is given in Figure 6.2. After RIE, the contaminating film consisted of a layer of bulk fluorocarbon polymer approaching 40 Å in thickness, atop a layer of relatively "clean" SiO_2 approximately 10 Å thick. At the interface between the polymer and oxide was a transition

region of mixed composition, 5-10 Å in thickness. Ashing removed virtually all of the bulk fluorocarbon film, such that most of the remaining polymer was in a mixed fluorocarbon polymer/oxide environment. Ashing also reduced the total contaminating film thickness to about 30 Å although the amount of oxide in the layer increased, indicating that some of the polysilicon substrate was consumed by the ashing process.

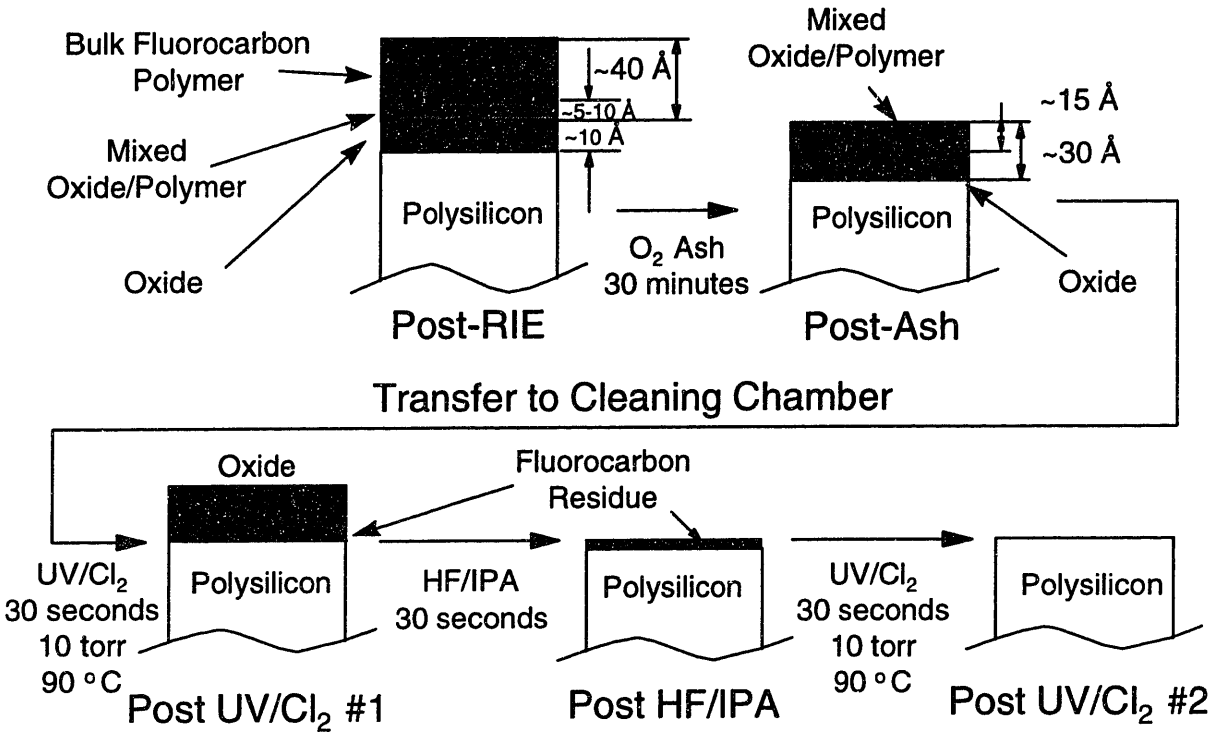

Figure 6.2- Schematic diagram of the contaminating films and the removal sequence. Samples emerge from RIE with a thin oxide and fluorocarbon overlayer. A 30 minute oxygen ash reduces the fluorocarbon content while increasing the oxide content. The samples are then transferred to the cleaning apparatus. A UV/Cl_2 process removes the fluorocarbon contamination but has little effect on the contamination layer thickness. An HF/IPA process removes the oxide layer, but reveals additional fluorocarbon contamination that was inaccessible to the first UV/Cl_2 process. A second UV/Cl_2 process removes this carbonaceous residue.

B. Removal of the Contaminating Films

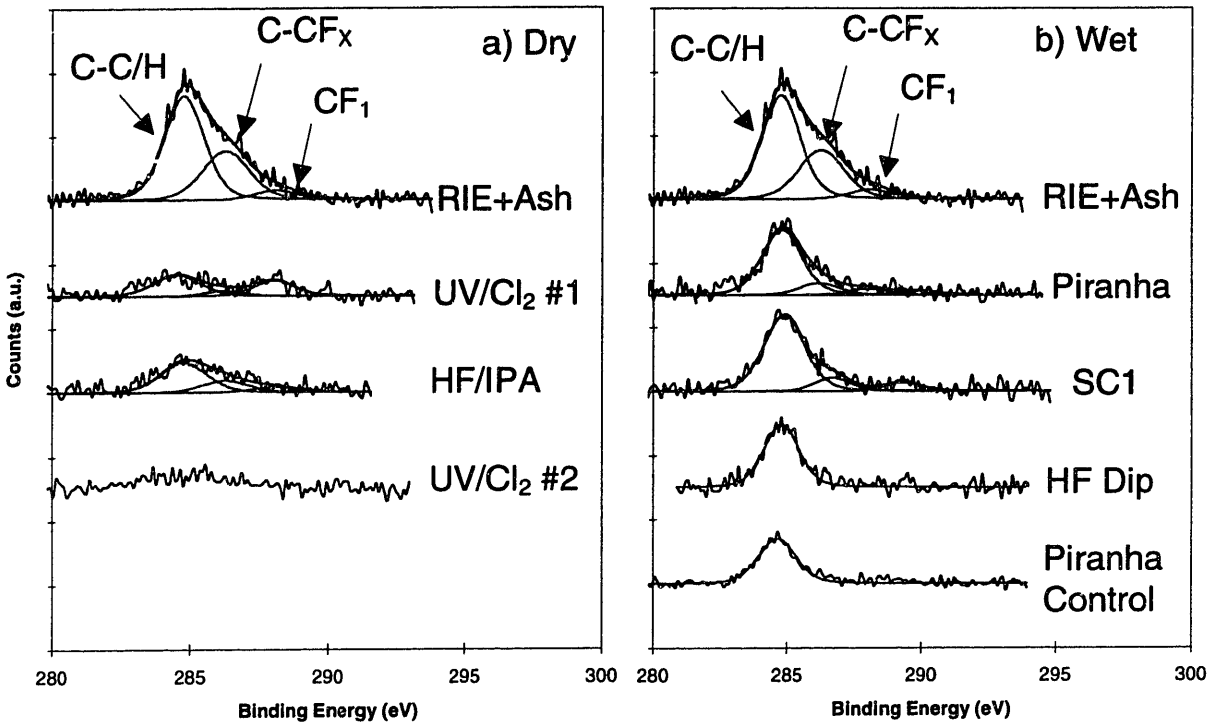

Figure 6.3- Comparison of carbon 1s photoelectron emission spectra from, a) a dry and, b) a wet cleaning sequence. Peak intensities for a) and b) are directly comparable. In the dry sequence, the first UV/Cl_2 process removes most of the fluorocarbon polymer character from the contaminating film. The HF/IPA process results in an apparent increase in the carbon intensity, due to the exposure of residual fluorocarbon which was obscured by the oxide layer. This carbon is chemically similar to the initial contamination. A second UV/Cl_2 process removes the residual fluorocarbon, resulting in a surface with minimal carbon contamination. The absence of ambient re-contamination in the dry sequence points out the inherent advantages of a clustered all dry approach to wafer cleaning. If the carbon level from a control wafer subjected to a Piranha clean is considered (Figure 6.3b, bottom spectrum), the resulting level of carbon contamination after both sequences is comparable.

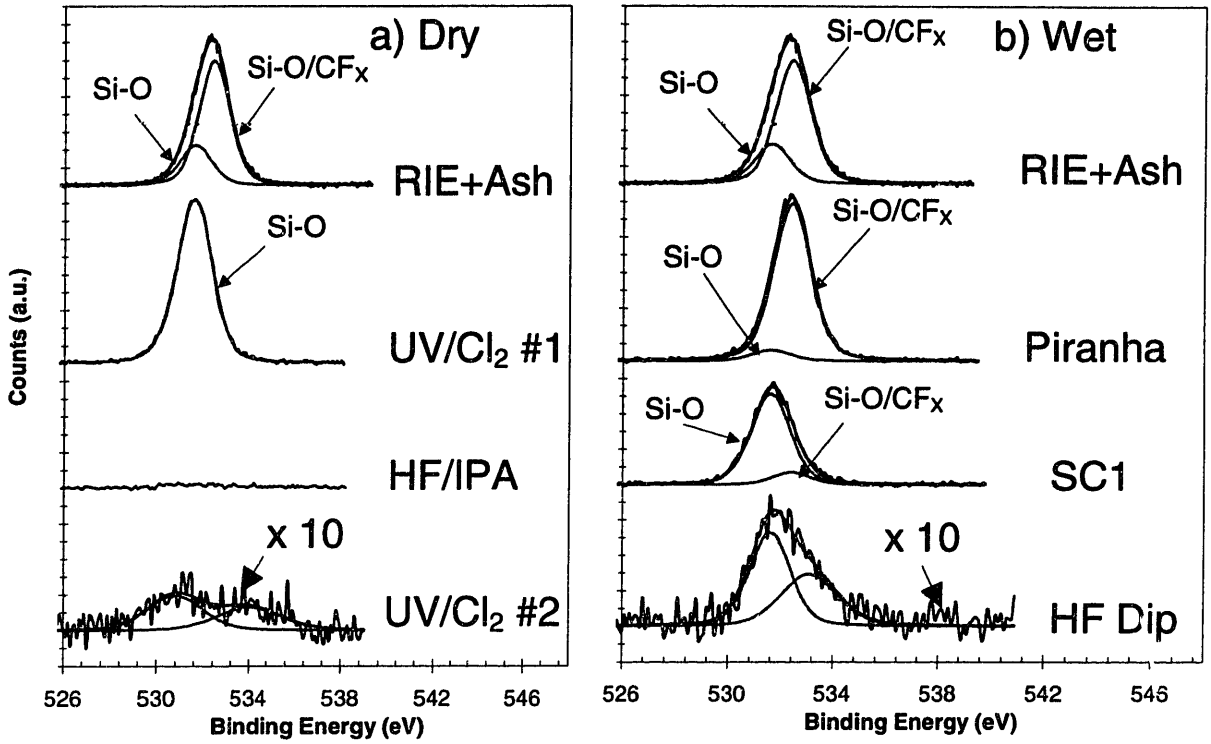

Figure 6.4- Comparison of oxygen 1s photoelectron emission spectra from, a) a dry and, b) a wet cleaning sequence. Peak intensities for a) and b) are directly comparable. In the dry sequence, the initial UV/Cl_2 process removes the fluorocarbon character from the mixed polymer/oxide layer, while not affecting the total amount of Si-O bonding. The HF/IPA process removes virtually all of the oxide. We have estimated the oxygen coverage after the second UV/Cl_2 process as ~1/3 monolayer. The SC1 step results in the removal of most of the $Si\text{-}O/CF_X$ bonding from the oxide. The SC1 step also results in partial removal of the oxide film, evidenced by the overall attenuation of the oxygen signal intensity. The wet sequence results in a higher final oxygen coverage, pointing out the advantage of avoiding oxide contamination from ambient moisture or rinsing with a dry cleaning sequence.

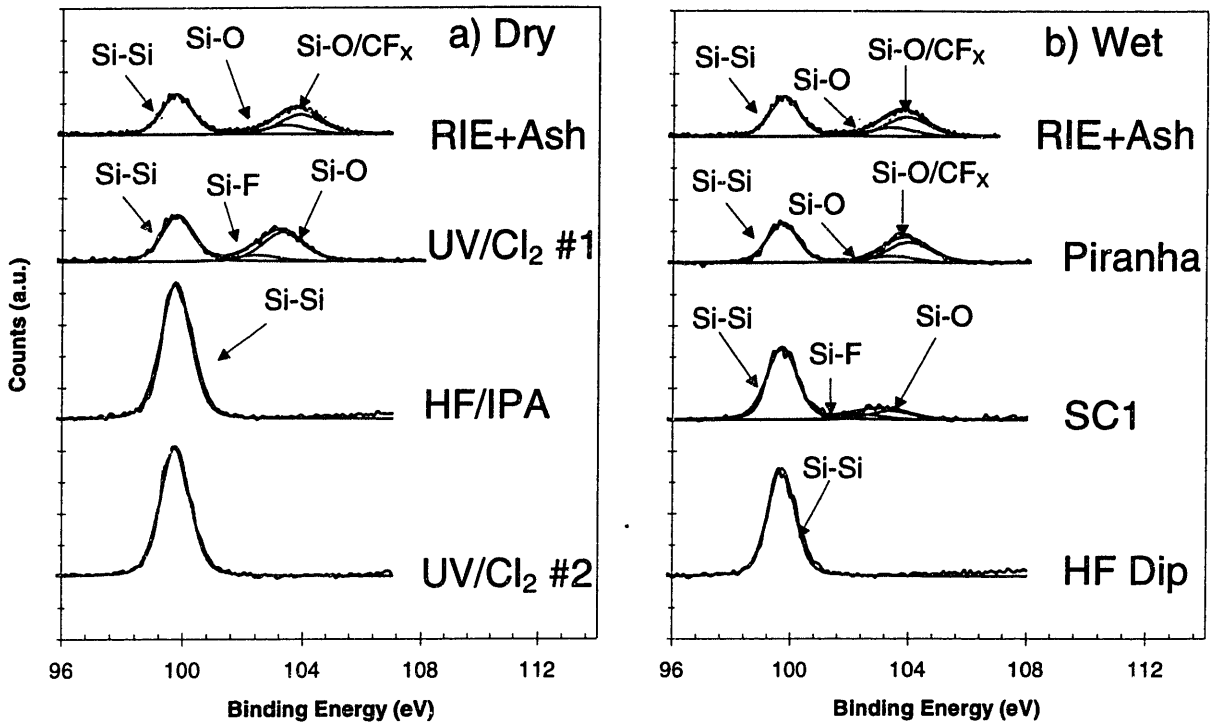

Figure 6.5- Comparison of silicon 2p photoelectron emission spectra from, a) a dry and, b) a wet cleaning sequence. Peak intensities for a) and b) are directly comparable. In the dry sequence, the UV/Cl_2 process removes the fluorocarbon character from the contaminating film, while not greatly affecting the overall amount of Si-O bonding. The HF/IPA step removes virtually all of the Si-O bonding. In the wet sequence, the SC1 step results in the removal of the $Si\text{-}O/CF_X$ bonding from the oxide, similar to the UV/Cl_2 step as discussed in the text. The SC1 step also results in partial removal of the oxide film, evidenced by the attenuation of the Si-O (103.4 eV) component and the growth of the Si metal (99.75 eV) peak. The intensity of the Si metal peak is attenuated in the final step of the wet process relative to the dry process because of increased carbon and oxygen coverage.

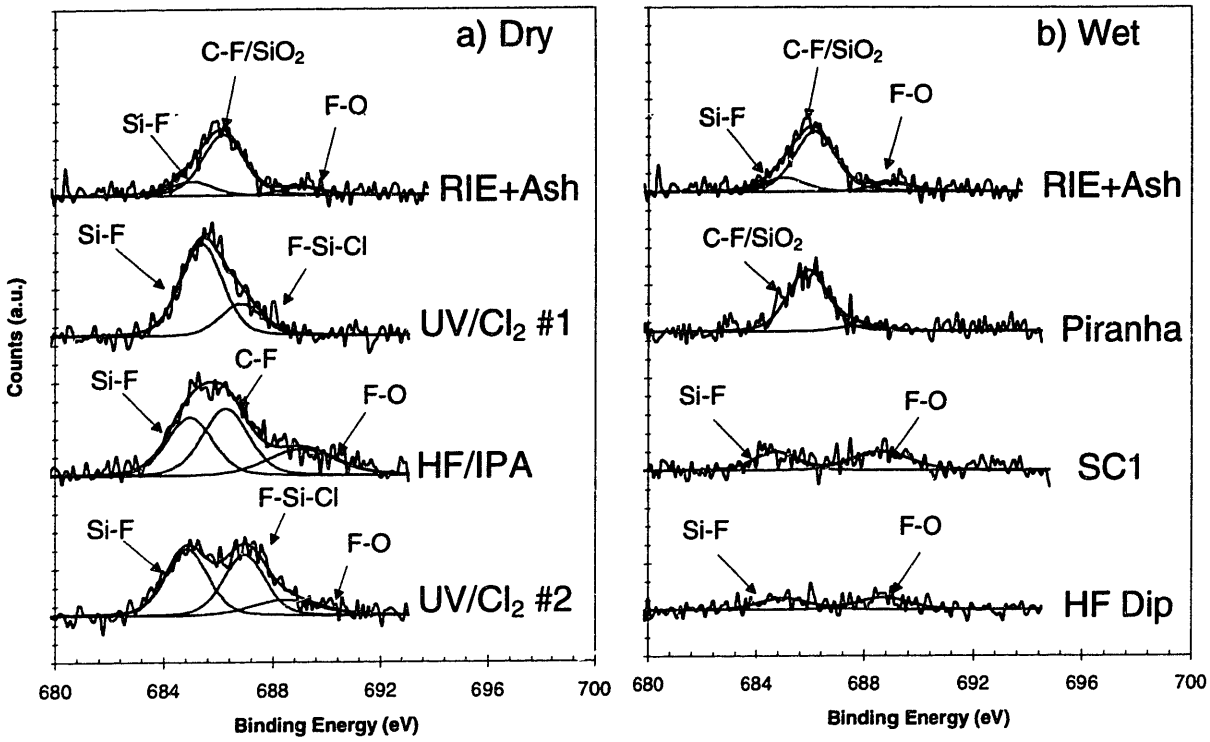

Figure 6.6- Comparison of fluorine 1s photoelectron emission spectra from, a) a dry and, b) a wet cleaning sequence. Peak intensities for a) and b) are directly comparable. In the dry sequence, the initial UV/Cl_2 process removes the fluorocarbon character from the film. The fluorocarbon bonding reappears after oxide removal with HF/IPA. The fluorine coverage after the second UV/Cl_2 process has been estimated as ~2/3 monolayer. In the wet sequence, the significant $C\text{-}F/SiO_2$ peak after the Piranha clean indicates that the fluorocarbon polymer is not removed from the contamination layer at this point. The wet sequence exhibits significantly less fluorine termination.

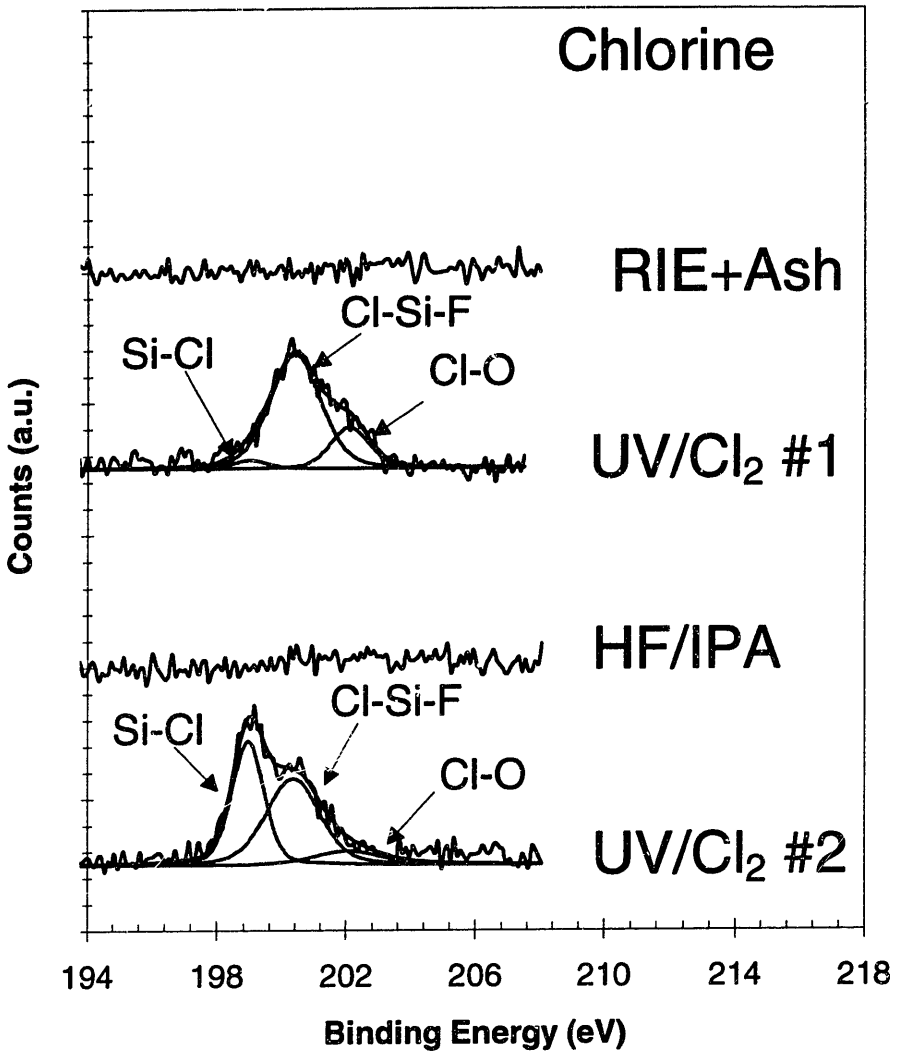

Figure 6.7- Chlorine 2p photoelectron emission spectra from an integrated dry cleaning sequence. The HF/IPA oxide strip removes virtually all of the residual chlorine from the wafer surface. The surface coverage of chlorine after the second UV/Cl_2 process has been estimated as ~1 monolayer. No chlorine was added to the surface by the wet sequence.

RIE + O_2 ashed samples were subjected to an integrated cleaning process as illustrated in Figure 6.2. XPS spectra for the integrated cleaning process are given in Figures 6.3-6.7. UV/Cl_2 was used to remove the fluorocarbon polymer from the contaminating film. Figure 6.3a shows that most of the carbon was removed by the initial UV/Cl_2 process. There was a measurable amount of carbon remaining that could not be removed by UV/Cl_2 at this stage, even with a drastically longer process duration. Correspondingly, the oxygen and silicon

spectra in Figures 6.4a and 6.5a respectively, both show that the fluorocarbon character of the mixed fluorocarbon polymer/oxide layer was removed by the UV/Cl_2 process. This is apparent by the shift from mostly Si-O/CF_X bonding to exclusively Si-O bonding in both spectra. The total amount of Si-O + Si-O/CF_X bonding appears to be unchanged by the UV/Cl_2 process. The intensity of the substrate p ak (Si-Si) was also unchanged by the UV/Cl_2 process. This indicates that the overall thickness of the contamination layer was not greatly affected by the UV/Cl_2 process, but the shift in the Si-O bonding in both the silicon and oxygen lines indicates that the fluorocarbon character was removed from the film. C-F/SiO_2 bonding was no longer resolved in the fluorine line shown in Figure 6.6a, corresponding to the reduction in intensity of the carbon signal and the removal of most of the fluorocarbon character from the contaminating film. Figure 6.7 shows that chlorine was added by the UV/Cl_2 process, and is present primarily as Cl-Si-F and Cl-O on the surface.

A vapor-phase HF/IPA process was used to remove the oxide film. Figure 6.3a shows that the intensity of the carbon line increased after HF/vapor processing. This phenomenon has also been observed to the same extent with a vapor phase HF/H_2O process, indicating that the increase of the carbon intensity is not due to IPA exposure (it should be mentioned that although only the HF/IPA results are presented here, we have obtained qualitatively similar residue removal with the UV/Cl_2-HF/H_2O system). The chemical state of the carbon revealed after the HF/IPA oxide strip is very similar to the initial RIE polymer contamination. This residual fluorocarbon either lies underneath the oxide and so was inaccessible to the initial UV/Cl_2 process, or was incorporated in the oxide film and concentrated on the surface as the oxide is etched away. The residual fluorocarbon was not removed by the vapor phase HF process as the oxide film was etched. This observation is consistent with other experiments in

our laboratory that have shown that adventitious carbon is not removed with vapor phase HF processing. Indeed, acceleration of oxide etching in vapor phase HF has been attributed to surface carbon[31]. Figures 6.4a and 6.5a show that the oxide film is almost completely removed after vapor-phase HF processing. Comparison of the signal intensity of the oxygen peak with a bulk oxide sample, using values for the mean free path ($\lambda_{103.4eV}$=27 Å, $\lambda \alpha E^{0.5}$) from Yano *et al.*[32] and monolayer oxide thickness (1ml = 2.48 Å) from Mathieu *et al.*[33], and assuming all of the detectable oxygen is on the surface yields an oxygen coverage of ≈ 1/3 monolayer. Coverages for other elements discussed below where scaled from the oxygen standard using the relative intensities and photoionization cross sections from Scofield[34]. The Si-O component of the silicon spectrum is no longer observed, and the Si-Si component has correspondingly grown. Figure 6.6a shows that although the absolute amount of fluorine is not greatly affected by the HF process, the distribution of chemical states is. The C-F component reappears due to the exposure of the polymeric contamination which was obscured by the oxide film. There is also a small contribution due to F-O bonding, arising from fluorine bonded to residual surface oxygen. Virtually all of the chlorine was removed during HF/vapor processing as shown in Figure 6.7.

A second UV/Cl_2 process removed most of the remaining carbon from the silicon surface, as shown in Figure 6.3a. The intensity of the carbon after the second UV/Cl_2 process is consistent with the background level of carbon contamination normally observed in our vacuum system. We have estimated the carbon coverage after the second UV/Cl_2 exposure as ≈ 1/2 monolayer. The oxygen and silicon spectra given in Figures 6.4a and 6.5a were unchanged. From Figure 6.6a, the interfacial F-C component of the fluorine spectrum has been removed, consistent with the removal of the polymer contamination.. We have estimated

the fluorine coverage as ≈ 2/3 monolayer. Chlorine was added to the surface by the second UV/Cl_2 process (Figure 6.7), and a strong Si-Cl component is present.. The chlorine coverage is estimated as ≈ 1 monolayer. Such a chlorine coverage can be easily removed by low energy Ar ion bombardment as is typically used as an *in situ* pre clean prior to metal deposition. An additional HF/vapor exposure may also serve to reduce the chlorine coverage after the second UV/Cl_2 process, although this was not attempted here.

C. Mechanism of Fluorocarbon Polymer Removal in UV/Cl_2

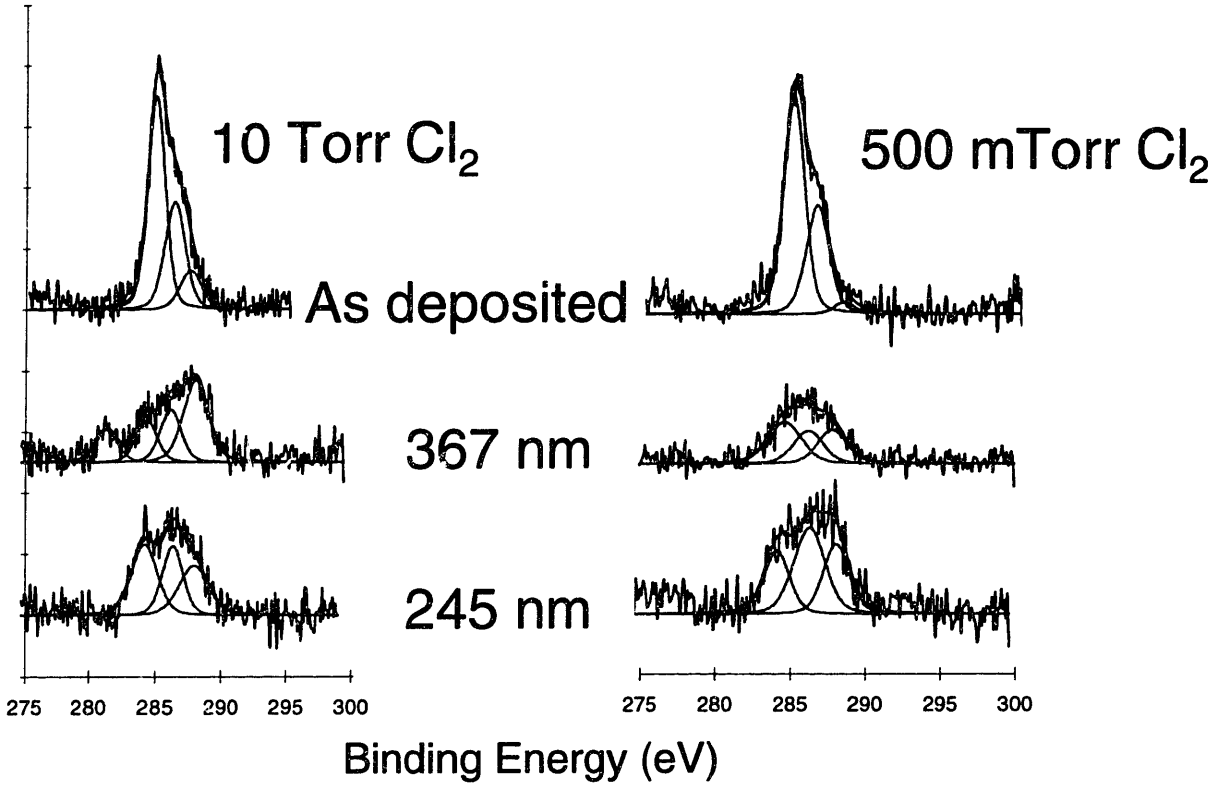

Figure 6.8- Carbon 1s photoelectron emission spectra illustrating the results monochromatic UV/Cl_2 etching experiments at a), 10 torr and b), 500 mTorr. All of the samples were exposed to UV/Cl_2 for 10 minutes at nominally 100°C. Significant polymer etching is observed with both Cl_2 dissociating (367 nm) and non-Cl_2 dissociating (245 nm) radiation, and at both high (10 Torr) and low (500 mTorr) pressure with both wavelengths. These results indicate that fluorocarbon polymer etching is influenced by both gas-phase and surface photolytic processes.

We have evidence that bulk fluorocarbon polymer etching is enhanced by both gas phase (chlorine radical production) and surface photolytic processes. Illuminating a chlorine gas phase but not the sample surface (i.e. downstream processing, as discussed with the UV/DCS/Halogen process in Chapter 5) with broad band UV light etched approximately 20 Å of post-RIE residue in 10 minutes at a nominal chlorine pressure of 20 Torr. The sample surface was placed 1 cm downstream from the illuminated gas volume. This result suggests that chlorine radicals produced in the gas phase etch bulk fluorocarbon polymer. Illuminating both the gas phase and the sample surface directly with monochromatic UV light produced etching of a bulk polymer film. Figure 6.8 illustrates the results of these experiments. In order to distinguish between the gas phase and surface etching channels, both a UV wavelength that dissociates chlorine (367 nm) and one that does not (245 nm) were chosen, and both produced polymer removal at 10 Torr and at 500 mTorr. The spectra obtained after etching with 245 nm radiation appear similar for a pressure of both 10 Torr and 500 mTorr, indicating that Cl_2 pressure does not significantly effect the etching chemistry of the surface process in the absence of Cl radicals. At 367 nm, the chemistry of the polymer film looks significantly different at 10 Torr and 500 mTorr, with the higher pressure film shifted toward more highly chlorinated (higher binding energy) products. Possibly, as in the case of the UV/Cl_2-copper system discussed in Chapter 4, surface photolytic processes are also active at 367 nm in the polymer etching process. These processes are only discernable at low chlorine pressure, since at higher pressure they are overwhelmed by predominance of the gas-phase (radical-driven) reaction channel due to the high concentration of Cl radicals.

In the system represented here, the mechanism may be quite different since the polymer residue after the oxygen plasma ash is not in a bulk state, but is incorporated in the

oxide layer. This is apparent by; 1) the shifted Si-O/CF_X bonding and the disappearance of the bulk F-C bonding after the ash when the polymer is incorporated, and 2) the shift back to Si-O bonding without an increase in intensity of the substrate or oxide peaks after the initial UV/Cl_2 process when the polymer is removed. The chemical shift indicates a chemical modification of the oxide layer, while the lack of intensity increase indicates that no overlayer was removed from the wafer surface. The removal of incorporated polymer is conceptually similar to the through-oxide etching mechanism proposed by Sugino *et al.*[13,14,15] where metals can be removed through a thin oxide.

D. Comparison Between "Wet " and "Dry" Cleaning Sequences

Figures 6.2-6.6 illustrate the comparison between the wet and dry cleaning sequences. Generally, the results from the dry cleaning sequence compared favorably with the wet cleaning sequence, and in some respects appeared superior due to the inherent advantages of avoiding ambient exposure during processing. In terms of process time, the wet and dry cleaning sequences were also comparable, to a first approximation. Although it is difficult to unambiguously assign a cleaning process time per wafer, since the wet processes are inherently batch and the dry processes are inherently single-wafer, a total cleaning process time of 90 seconds for a single wafer (dry) versus on the order of 60 minutes (including rinse time) for a batch of 25 wafers (wet) compares favorably.

From the carbon 1s spectra in Figure 6.3, it is apparent that the dry cleaning sequence is at least as effective as the wet sequence in removing polymeric and carbonaceous contamination. Even if the background carbon contamination level (*i.e.* the level of carbon observed on the control sample in the bottom spectrum of Figure 6.3b) is subtracted from the

raw spectra shown in the figure, the final carbon contamination level would still be comparable to that observed in the dry sequence as illustrated in figure 6.3a. This background subtraction may not be valid (especially for the early stages of the wet cleaning sequence as discussed below) since it is difficult to determine whether the levels of contamination observed in the spectra of Figure 6.3b are due to the purity of the cleaning chemicals, ambient re-contamination during transfer into the vacuum chamber, or incomplete removal of the etch contamination. We present evidence below that suggests that the Piranha clean is ineffective in removing the polymeric contamination, so at least at that stage of the process, most of the carbon present is not due to extraneous sources. In any event, the *absence* of re-contamination in the dry sequence illustrated in Figure 6.3a points out one of the inherent advantages of a clustered processing regimen.

Figures 6.4 and 6.5 show the oxygen 1s and silicon 2p spectra respectively from the wet and dry cleaning sequences. These two figures will be discussed simultaneously since they contain complimentary information. The Piranha clean did not significantly change the fluorocarbon character of the mixed polymer/oxide layer as can be seen by the prominent Si-O/CF_X component in both the silicon and oxygen lines, indicating that Piranha is ineffective in removing the polymeric contamination. The SC1 clean removed most of the fluorocarbon in the mixed layer, evidenced by the shift to mostly Si-O bonding in both the silicon and oxygen lines. The SC1 clean also resulted in slight etching of the oxide film. This was apparent from a reduction in intensity of the Si-O component of both the silicon and oxygen lines. The silicon metal component after the SC1 clean in Figure 6.5b has correspondingly grown relative to the Piranha clean, again indicating partial removal of the oxide overlayer. The oxide etching component of the SC1 step could explain why it was more efficient at removing

the oxide incorporated fluorocarbon. Removal of oxide could potentially expose residual fluorocarbon that was not attacked by the Piranha clean, which is known to cause native oxide growth. The final oxygen coverage was significantly lower for the dry process as compared to the wet sequence. The bottom spectra in Figures 6.4a and b have been exaggerated in scale so that this effect can be more clearly seen. Chemical state assignments have not been made to the low oxygen coverage peaks. The reduced intensity of the silicon metal peak after the wet process relative to the dry process (bottom spectra, Figure 6.5a and b) is partially due to the increased oxygen coverage and partially attributable to the higher carbon coverage after the wet process.

Figure 6.6 shows the fluorine 1s spectra from the wet and dry cleaning sequences. The large C-F/SiO_2 component in the fluorine line after the Piranha cleaning step would indicate that a substantial fraction of the carbon observed in the corresponding carbon spectrum (Figure 6.3b) is due to incomplete removal of the polymer film and not due to ambient or chemical contamination. The apparent absence of any C-F bonding after the SC1 clean would indicate that any remaining fluorocarbon contamination is removed by the SC1 cleaning step. The final level of fluorine coverage was much lower in the wet sequence than in the dry sequence. Fluorine was not appreciably added to the surface by the HF dip, which is consistent with the literature.

Figure 6.9 shows the surface morphology of a) an as etched and ashed (control) sample that was not subjected to any post etch processing, b) a sample subjected to the full wet cleaning sequence and c) a sample subjected to the full dry cleaning sequence. The surface roughness of samples a) b) and c) was measured as 68.5, 69.3, and 51.3 Å Rms respectively. The dry cleaned sample was slightly smoother than the other two. This may be attributable to

slight etching of the polysilicon with the UV/Cl_2 process, or possibly to variation in polysilicon morphology across the wafer surface. It should be noted that the UV/Cl_2 process is highly controllable in terms of the silicon etch rate. By adjusting the process conditions, etch rates from 10 to 1000's of Å/minute can be reproducibly obtained[12], as discussed in Chapter 3. This is highly beneficial in terms of substrate damage removal in the final UV/Cl_2 step of this dry cleaning sequence[35]. We have made no attempt here to optimize the amount of silicon removed in this final step.

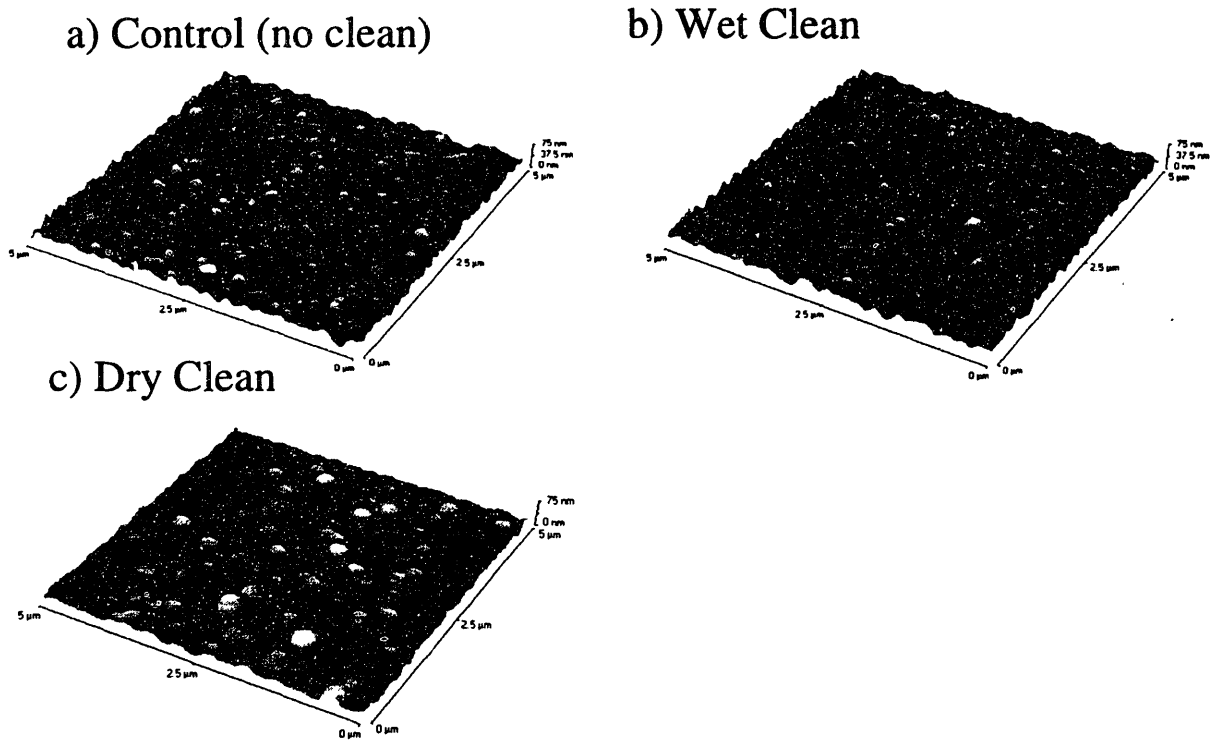

Figure 6.9- Comparison of surface morphology of a) a control sample, b) a sample subjected to the wet cleaning sequence and c) a sample subjected to the dry cleaning sequence. The surface roughness of all of the samples is comparable. Our AFM measurements yielded values of 68.5, 69.3 and 51.3 Å Rms for samples a), b), and c) respectively.

6.5 Conclusions

We have demonstrated an all-dry integrated cleaning sequence that is capable of removing blanket fluorocarbon and oxide films from poly- and single-crystal silicon substrates

that result after RIE etching + O_2 ashing. A UV/Cl_2 process was used to remove fluorocarbon polymer and residual carbon contamination. A reduced pressure vapor-phase HF/IPA process removed silicon oxide contamination. The cleaning sequence outlined here produces a silicon surface with negligible carbon and oxygen contamination. Small amounts of chlorine and fluorine are present on the surface after the cleaning sequence. The dry cleaning sequence compares favorably with an analogous wet cleaning sequence. Although we have not performed an electrical evaluation of our cleaning sequence, we have confidence that the lack of significant surface contamination and the ability to remove substrate damage by controlled silicon etching would yield acceptable and possibly even superior device characteristics. In a recent study, Richter *et al.*[10] conclude that "the electrical measurement data are consistent with the picture of chemical/structural evaluation" with regard to the correlation between auger electron spectroscopy surface analysis data and electrical tests after a cleaning procedure for similar post oxide etch contamination. We intend to support our cleaning results with electrical testing performed on full, patterned wafers in a future study.

6.6 References

[1] G.S. Oehrlein, Mat. Sci. Eng., B4 (1989) 441.

[2] P. Verdonck, C.M. Hasenack, and R.D. Mansano, J. Vac. Sci. Technol. B, 14(1) (1996) 538.

[3] J.P. Gambino, M.D. Monkowski, J.F. Shepard, and C.C. Parks, J. Electrochem. Soc., 137 (3) (1990) 976.

[4] R.A. Bowling, S.C. O'Brien, L.M.Loewenstein, M.H. Bennett, and B.K. Bohannon, Solid State Technology, 37 (1) (1994) 61.

[5] H-H Park, K-H Kwon, J-L Lee, K-Y Suh, O-J Kwon, K-I Cho and S-C Park, J. Appl. Phys., 76 (8) (1994) 4596.

[6] G.S. Oehrlein, J.G. Clabes, and P. Spirito, J. Electrochem. Soc., 133 (5) (1986) 1002.

[7] J.P. Simko, G.S. Oehrlein, and T.M. Mayer, J. Electrochem Soc., 138 (1) (1991) 277.

[8] T. Yasuda and G. Lucovsky, J. Vac. Sci. Technol. A, 11 (5) (1993) 2496.

[9] G.S. Oehrlein, G.J. Scilla, and S-J Jeng, Appl. Phys. Lett., 52 (11) (1988) 907.

[10] H.H. Richter, A. Wolff, K. Blum, K. Hoeppner, D. Kruger and R. Sorge, Vacuum, 47 (5) (1996) 437.

[11] J. W. Butterbaugh, D. C. Gray, C. F. Hiatt, H. H. Sawin, and A.S. Lawing, Proceedings of the Second International Symposium on Ultra Clean Processing of Silicon Surfaces, M. Heyns, M. Meuris, and P. Mertens eds., p. 229, Acco, Leuven, Belgium (1994).

[12] A.S. Lawing, A.J. Muscat, H.H. Sawin and J.W. Butterbaugh, Proceedings of the Fourth International Symposium on Cleaning Technology in Semiconductor Device Manufacturing, PV 95-20, J. Ruzyllo and R.E. Novak eds., p. 150, The Electrochemical Society, Pennington, N.J. (1996).

[13] R. Sugino, Y. Nara, T. Yamazaki, S. Watanabe, and T. Ito, Extended Abstracts of the 19th Conference on Solid State Devices and Materials, p. 207-210 Tokyo (1987).

[14] R. Sugino, Y. Okui, M. Okuno, M. Shigeno, Y. Sato, A. Oshawa, and T. Ito, IEICE Trans. Electron, Vol. E75-C, No. 7, p. 829-833 (1992).

[15] R. Sugino, Y. Nara, H. Horie, T. Ito, J. Appl. Phys., 76 (9) (1994) 5498

[16] Handbook of Chemistry and Physics, CRC Press, 61st Edition, (1979).

[17] E. Ikawa, S. Sugito, and Y. Kurogi, Surface Science, 183 (1987) 276.

[18] E. Ikawa, S. Sugito, N. Aoto, and Y. Kurogi, Proceddings of the 1987 Symposium on VLSI Technology, p. 27-28, Karuizawa, Japan, May 19-21 (1987).

[19] A. Izumi, *et al.*, in US Patent # 5,022,961 (Dainippon Screen Mfg. Co., Ltd., USA, 1991).

[20] C.R. Helms and B.E. Deal, J. Vac. Sci. Technol. A, 10 (4) (1992) 806.

[21] K. Torek, J. Ruzyllo, R. Grant, and R. Novak, J. Electrochem. Soc., 142 (4) (1995) 1322.

[22] A.J. Muscat, A.S. Lawing, H.H. Sawin, J.W. Butterbaugh, D. Syverson and C.F. Hiatt, Proceedings of the Fourth International Symposium on Cleaning Technology in

Semiconductor Device Manufacturing, PV 95-20, J. Ruzyllo and R.E. Novak eds., p. 371, The Electrochemical Society, Pennington, N.J. (1996).

[23] C.S. Lee, J.T. Baek, H.J. Yoo and S.I. Woo, J. Electrochem. Soc., 143 (3) (1996) 1099.

[24] D.J. Syverson and G.T. Duranko, Solid State Technology, 31 (10) (1988) 101.

[25] P. Burggraaf, Semiconductor International, 13 (11) (1990) 52.

[26] G.E. Potter, G.H. Morrison, P.K. Charvat, and A.L. Ruoff, J. Vac. Sci. Technol. B, 10(6) (1992) 2398-2406.

[27] S.J. Yun, S-J. Park, M-C Paek, and J.Y. Lee, J. Electrochem. Soc., 137 (8) (1990) 2634-2639.

[28] G.S. Oehrlein, A.A. Bright and S.W. Robey, J. Vac. Sci. Technol. A, 6 (3) (1987) 1989-1993.

[29] Ch. Cardinaud, G. Turban, B. Grolleau, J.P. Grandchamp, C. Lejeune, P. Scheiblin and E. Collard, Applied Surface Science, 36 (1989) 322-331.

[30] S.W. Robey and G.S. Oehrlein, Surface Science, 210 (1989) 429-448.

[31] T.K. Whidden, J. Allgair, J.M. Ryan, M.N. Kozicki and D.K. Ferry, J. Electrochem. Soc., 142 (4) (1995) 1199-1205.

[32] F. Yano, A. Hiraoka, T. Itoga, H. Kojima, K, Kanehori, and Y. Mitsui, J. Vac. Sci. Technol. A, 13 (6) (1995) 2671-2675.

[33] H.J. Mathieu, M. Datta, and D. Landolt, J. Vac. Sci. Technol. A, 3 (2) (1985) 331-335.

[34] J.H. Scofield, J. Electron. Spectrosc., 8 (1976) 129.

[35] D.K. Hwang, K. Torek, and J. Ruzyllo, Proceedings of the 1st International Symposium on Plasma Process Induced Damage, 137-140, AVS-IEEE/Electron Devices Society (1996).

Chapter 7

Integrated Processing of Blanket and Patterned Oxide Wafers

A totally integrated: oxide etch in an Inductively Coupled Plasma (ICP) reactor, oxygen plasma Post Etch Treatment (PET), and dry cleaning sequence has been demonstrated on blanket and patterned 4" oxide wafers. This process sequence was performed in a clustered system in our laboratory. In this apparatus, samples can be transferred between processing chambers and surface analysis can be performed while maintaining a base pressure in the low 10^{-8} Torr range. In this manner, we can mimic a clustered process, avoid ambient contamination, and obtain an accurate picture of the evolution of the wafer surface throughout the process sequence. We support our cleaning results with quasi *in situ* angle resolved X-ray Photoelectron Spectroscopy (XPS).

Our results on blanket wafers indicate that in most cases, an *in situ* high density oxygen plasma PET is effective in removing fluorocarbon contamination. A vapor phase HF process removes the oxide film resulting in a fairly clean surface. This is contrary to what we observed in the RIE/barrel ash system described in Chapter 6, where it was necessary to attack the polymer contamination before complete oxide removal was observed after HF processing. On patterned oxide wafers, the chemistry becomes more complex. Two types of contamination have been observed. The first, type 1, is analogous to the incorporated polymer observed in the RIE system and causes a similar upward binding energy shift in the SiO_2 binding energy in both the silicon and oxygen spectra. The second, type 2, is chemically bound to the oxide and causes a positive binding energy shift in silicon and a negative shift in

oxygen relative to SiO_2. The origin and significance of this type of contamination is still in question.

7.1 Background

In recent years, high density plasma etching has been investigated for semiconductor processing[1]. In a high density plasma etcher the plasma is generated remotely from the wafer, and a separate power supply is used to control the energy with which ions bombard the wafer surface. In this configuration, somewhat separate control is maintained between the plasma density and the ion energy. This differentiates high density etchers from conventional parallel plate designs, where the plasma density and ion bombardment energy are intimately coupled. Various types of sources can be used to excite the plasma above the wafer and these include; inductively (or transformer) coupled plasma sources (ICP or TCP), electron cyclotron resonance sources (ECR) and helicon wave sources. Generally, a capacitively coupled RF bias is used to control the energy with which ions bombard the wafer.

High density etchers offer the advantage of more reactive gas phase chemistry (since the plasma densities, and hence the "activation" of the gas phase etchants, are typically on the order of 1-2 orders of magnitude higher than capacitively coupled etchers) while maintaining relatively low ion bombardment energies and hence limiting the amount of ion induced damage to the wafer. In addition, high density sources operate efficiently at low pressures (typically 5-20 mTorr) such that a higher degree of directionality of ion bombardment can be maintained, allowing for the delineation of the narrow, high aspect ratio features required in current, and especially future, generations of devices. In a parallel plate configuration, operation at low pressure would require large inputs of power (due to the inefficiency of

operation of a capacitively coupled source in the low pressure regime) and result in prohibitively high ion bombardment energies[2].

These advantages do not come without a price. The reactive gas phase chemistry can create problems. For instance, in oxide etching the selectivity of oxide to photoresist is typically 2-3 times lower in a high density reactor due to the generation of large amounts of fluorine radicals in the plasma[1]. Polymer deposition on chamber surfaces is severe in high density oxide etchers, necessitating frequent chamber cleaning, typically with an oxygen plasma, to avoid particle generation due to de-lamination of the thick polymer buildup[1]. Charging, which leads to the breakdown of thin gate oxides, can also be a problem in high density reactors. Nevertheless, high density reactors are finding applications in "critical" processes such as high aspect ratio contact and via etch[1], and will undoubtedly find broader applications as process demands increase and the technology becomes better understood.

Although the basic mechanism of the selective etching of SiO_2 over silicon is the same in high density etchers as in parallel plate reactors (i.e. the deposition of a passivating polymer film on the silicon surface), the specifics can be quite different. Because of the high plasma density, the passivating polymer films are generally much thicker in a high density reactor, not only because more polymer precursors are generated in the higher density plasma, but because the higher concentration of reactive fluorine demands that a thicker polymer film be deposited to prevent excessive silicon etching.

The application of our dry cleaning methodology to the high density oxide etching system is a natural extension of the RIE system discussed in Chapter 6, and the systems are different enough that it remains a challenging problem. In this work, blanket and patterned oxide films were etched in an ICP etcher in pure C_2F_6 and mixtures of C_2F_6 and CHF_3. An *in*

situ oxygen plasma post-etch treatment (PET) was used to remove the bulk of the polymer contamination. A range of dry cleaning strategies were employed to attack the remainder of the contamination, and the processes used included combinations of vapor phase HF, UV/Cl_2 and UV/O_2.

High density oxide etching has been studied and the chemistry of the etch induced contamination has been reported in the literature[3,4,5,6,7,8,9]. The chemical composition of the post etch contamination is variable and depends on numerous process parameters including; gas composition, reactor power settings, wafer and reactor wall temperature, high density source type and reactor design. Generally, the F/C ratio of a deposited polymer film will decrease as the RF bias to the wafer, or "bottom power" (i.e. ion bombardment energy), is increased for a given gas composition[4]. The F/C ratio of a deposited polymer film will also decrease with the hydrogen content of the gas (either by addition or as part of the parent gas) for a given power setting[4,5,6]. Saturated hydrogen bearing gases such as CHF_3 and CH_2F_2 generally yield higher selectivity to silicon, higher polymer deposition rates and lower oxide etch rates than saturated fluorocarbon gases such as CF_4 and C_2F_6[3,5,10]. Additional background on high density oxide etching is given in Chapter 1.

7.2 Experimental

The experimental apparatus in which these experiments were performed is described in Chapter 2.2. In addition to the high density oxide etching process, the ability to perform the entire process sequence under high vacuum conditions (in the integrated processing apparatus illustrated in figure 2.7.) differentiates this work from the work described in Chapter 6. The ability to avoid ambient contamination effects, and specifically the growth of native oxide

films on the processed wafer surface, allows us to obtain a much more accurate picture of the evolution of the wafer surface chemistry through the process sequence.

The wafers used in this work were 5500 Å thermally grown oxide films on 4" p-type <100> silicon wafers. Both blanket oxide films and patterned wafers were used in these experiments. The masks used for patterning were designed in our laboratory using AutoCad, and printed via e-beam lithography by Diamon Images (120 Albright Way, Los Gatos, CA). The masks are schematically illustrated in Figure 7.1. The masks were originally designed to be used in a 5x I-line stepper, but unfortunately this piece of equipment did not come "on line" in time to be used. Instead, the same masks were used in a 1x stepper, such that the features obtained were 5 times bigger than originally intended (the feature sizes referred to in the remainder of this discussion reflect the actual wafer dimensions when the wafers were printed at 1x). Two different masks were utilized. The first contained a 5 cm x 5 cm grating pattern of 2.5 μm lines and 3.5 μm spaces. This pattern was used for angle resolved XPS analysis of the process sequence. The second pattern consisted of a series of arrays of different sized contact holes, ranging from 1.25 to 5 μm. This pattern was beneficial in process development because of the larger open area around the periphery of the patterned area (the "scribe line"), allowing for more efficient visual determination of oxide etch endpoint. This contact mask also gave us valuable information about critical dimension control in a more realistic feature geometry. A third mask was designed to define metal bond pads on the contact array. Although it was not utilized in this work, this mask will allow resistance measurements to be made on pairs of contacts in future cleaning evaluation studies.

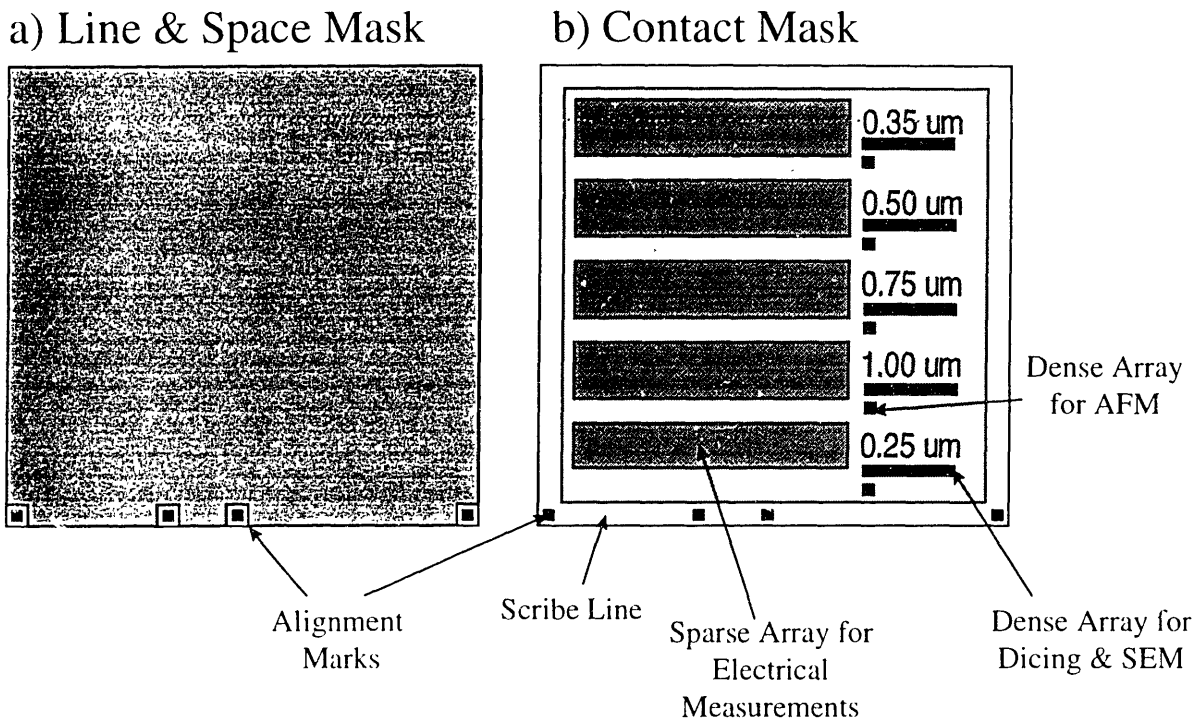

Figure 7.1-Schematic Diagram of the Masks used in this work. Note that the scribe line in the line & space mask is mostly filled with the pattern. In the contact mask, the "sparse arrays" consist of widely spaced contacts on a square grid for electrical measurements, while the "dense arrays" consist of closely packed contacts for critical dimension evaluation. Note that the dimensions on the mask illustrate the design dimensions, while the actual wafer dimensions in this work are 5 times larger.

In all of the experiments reported here the "top power" supplied to excite the plasma was 300 Watts supplied at 13.56 MHz. The bottom power used for oxide etching was variable and is noted in the following section where appropriate. The wafer electrode, or "bottom power" was driven at either 10 Mhz (for all of the blanket oxide experiments) or 11 Mhz although we do not believe this to be a significant factor in our results. The 11 Mhz power supply used in all of the patterned wafer results presented here tended to be more stable. Generally, etching in pure C_2F_6 was performed at 20 mTorr and etching in 1:1 C_2F_6:CHF_3 was done at 5 mTorr unless otherwise noted. The oxygen plasma PET was performed in the high density etcher. All PET's were perfomed at 50 mTorr with no power supplied to the wafer

electrode, except for the results illustrated in Figure 7.3, where the bottom power was 25 Watts at 10 Mhz.

Vapor-phase HF processing was performed in the chamber discussed in Section 2.2.5. In past experiments, and including the blanket oxide experiments discussed in this chapter, we needn't be concerned with the etch rate regime in which the HF/Vapor process was performed. However, with patterned wafers, the HF process must be performed in a parameter space where oxide etching is minimized. It is impossible to attack the native oxide aggressively, since because of the purely chemical and therefore isotropic nature of the vapor-phase HF etch we would etch the side walls at the same rate. Therefore, we had to have an accurate understanding of the thickness of the native oxide on the wafer surface, and also be able to design an HF process which would only etch this thickness with minimal over etch. The recent work of Y.P. Han in our laboratory has provided us with the information which was required to make these experiments successful. Figure 7.2 illustrates the two regimes of vapor phase HF etching. By operating well into the non-condensing regime, a purely surface etching reaction takes place. This surface reaction is typified by etch rates on the order of 10's of Å/min, whereas the condensed etching regime is typified by etch rates on the order of 1000's of Å/min. We were therefore able to design a process to etch on the order of 100 Å of oxide, and maintain the integrity of the side walls while completely stripping the ~50 Å PET grown oxide.

Quasi- *in situ* angle resolved XPS analysis was performed in the analytical chamber described in Section 2.2. Analyses on blanket films were performed at a pass energy of 20 eV in order to establish the chemical state binding energies for spectrum de-convolution. The pertinent binding energies used in this work are given in Table 1. In the interest of time, the

analyses on patterned wafers were performed at a pass energy of 50 eV, and in fact, the resolution does not appear that much worse, even though the count rate (especially at low take-off angle) is significantly increased. Spectra were taken at take-off angles of 90° and 30° on blanket films, and 90° and 20° on patterned wafers. Figure 7.3 illustrates the "line of sight" on a patterned wafer at the two angles, and the resulting analyzed area.

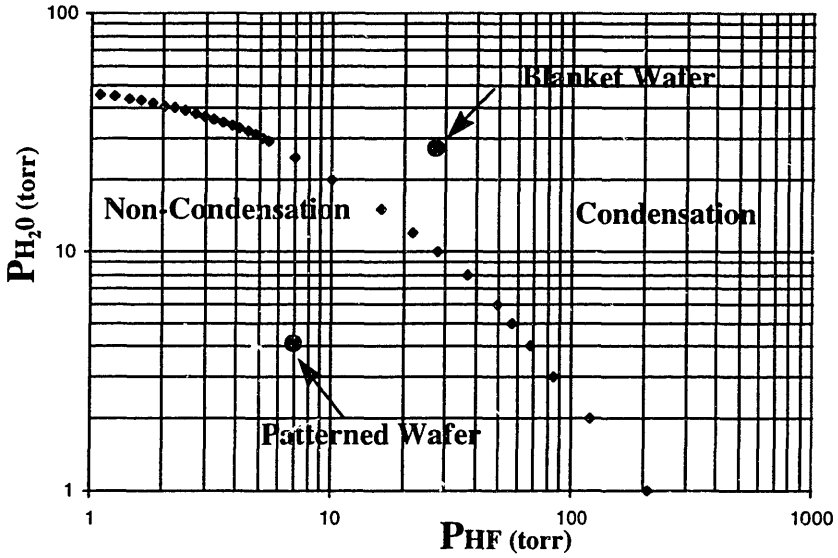

Figure 7.2-Condensation and non-condensation regimes in vapor-phase HF etching. The conditions for the blanket and patterned wafers are indicated.

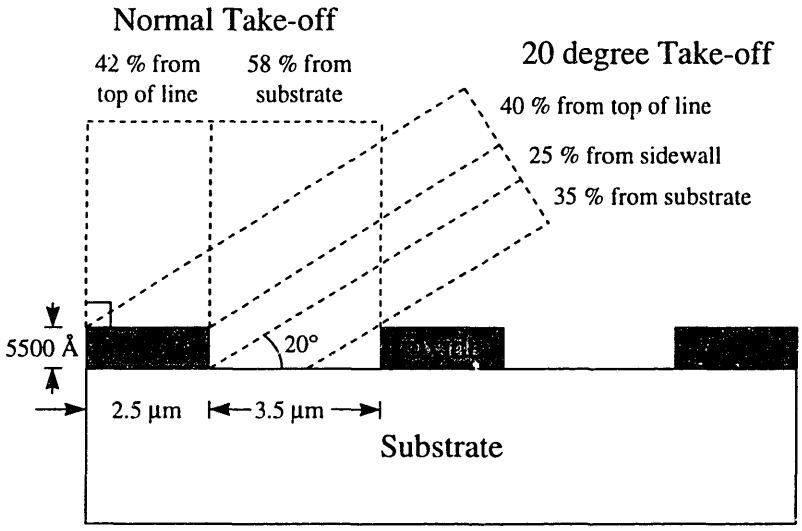

Figure 7.3-Schematic Diagram illustrating the "Lines of Sight" at 90° and 20° take-off angles on an idealized patterned wafer, and the resulting analyzed area.

Element (line)	Chemical State	Binding Energy (eV)
Silicon (2p)	Si-Si	99.75 (reference)
	SiO_2	105.0-105.8
	$Si\text{-}O_{Polymer}$	107.5-108.6
Carbon (1s)	C-Si	283
	C-C/H	284.3
	$C\text{-}CF_X$	286.4
	$C\text{-}F_1$	288.6
	$C\text{-}F_2$	290.4
	$C\text{-}F_3$	292.5
Oxygen (1s)	$Si\text{-}O_{Polymer}$	531.1-531.9
	SiO_2	533.4-533.9

Table 7.1-Summary of the pertinent binding energies and chemical state assignments used in this work.

7.3 Results and Discussion

A. Blanket Oxide Films

Figure 7.4 illustrates our initial integrated cleaning result on a blanket oxide. The initial approach was to apply the cleaning sequence from the RIE/barrel ash system (Chapter 6) to these samples.

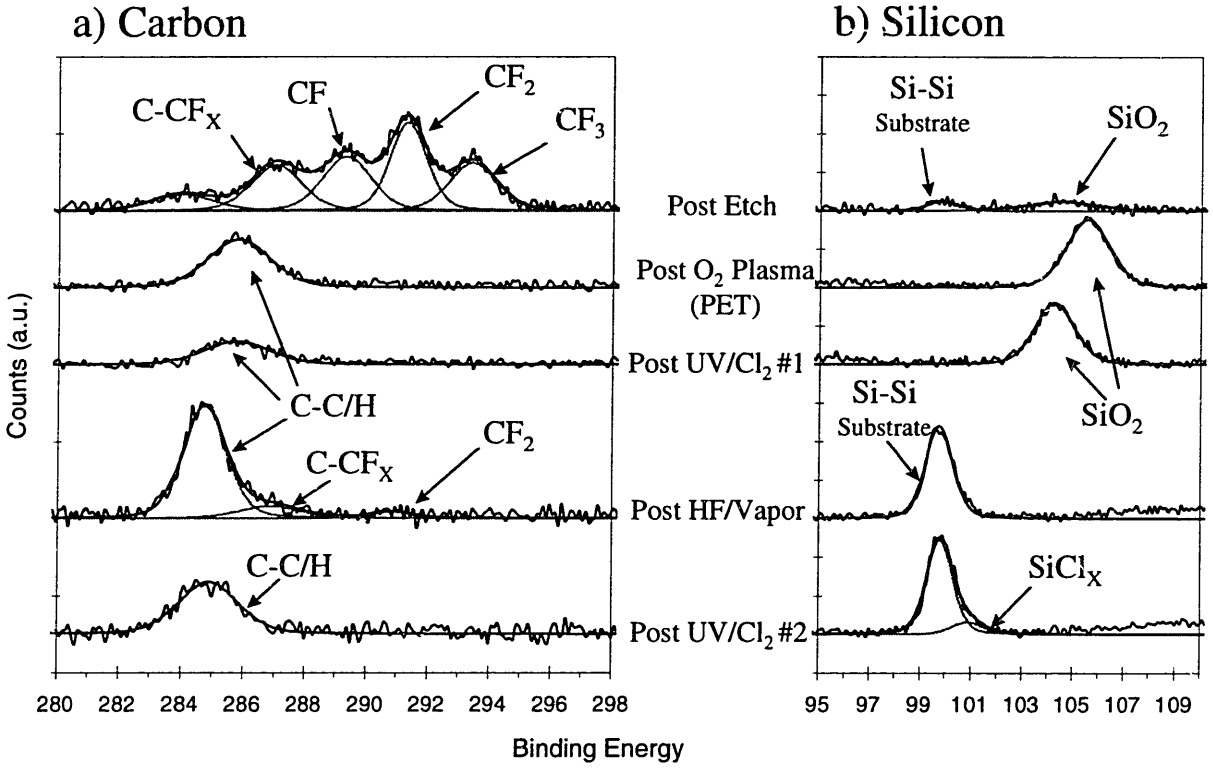

Figure 7.4-Carbon 1s and silicon 2p photoelectron emission spectra at normal take-off illustrating the RIE/barrel ash cleaning sequence applied to a blanket oxide film etched at 300 W top/25 W bottom in pure C_2F_6 at 45 mTorr and ashed in the high density reactor. The process sequence is represented by reading the spectra from top to bottom.

The post-etch level of polymeric contamination on the sample illustrated by figure 7.4 is a ~50 Å thick film with an average F/C ratio of 1.35. The F/C ratio is quite a bit higher than what we observed in the RIE system, but not atypical of what is generally seen after a high density etch. The resolution between the various C-F bonding states allows for more accurate determination of the binding energies than was possible in the RIE system. The PET

performed with 25 watts of bottom power removes the bulk of the fluorocarbon contamination and results in the growth of a >> 50 Å oxide. Note that the substrate peak is no longer resolved in the silicon spectrum, so the oxide thickness cannot be determined based on the XPS peak intensity. An initial UV/Cl_2 process, performed at 5 Torr Cl_2 for 1 minute, results in a reduction of the carbon intensity, but no apparent change in the chemical state of the carbon. The silicon spectrum shows a downward shift in the SiO_2 bonding, analogous to the shift which was observed in the RIE system. A HF/vapor process, results in the removal of the oxide film and reveals a large amount of mostly graphitic carbon. A second 5 Torr, 1 minute UV/Cl_2 process reduces the carbon signal to near the background level. $SiCl_X$ bonding is resolved in the silicon spectrum after the second UV/Cl_2 process.

Figure 7.5 illustrates an "HF first" process. Because of the efficiency of the oxygen plasma PET, we found it unnecessary to perform the UV/Cl_2 polymer removal step prior to stripping the oxide with an HF/vapor process. In the RIE system, complete oxide removal was not observed unless the organic contamination was attacked before the oxide strip. The *in situ* PET is more efficient at polymer removal because of the higher density of reactive oxygen species as compared to a conventional barrel asher. This PET was performed without the use of bottom power (as were the PET's in all of the subsequent figures which will be presented), and the ~ 50 Å oxide grown in the process is thinner than that represented in figure 7.4. Note that the substrate peak is still visible in figure 7.5, and is more pronounced at normal take-off angle. In this case, a UV/O_2/Cl_2 process was used to attack the residual carbon contamination. It is beneficial to combine or follow a UV/Cl_2 process with UV/O_2 exposure, because the residual chlorine becomes incorporated in the thin oxide film which grows upon exposure of a silicon surface to UV/O_2. The oxide-bound chlorine is then removed with a second HF/Vapor

process. Note the absence of $SiCl_X$ bonding in the silicon spectrum after the second HF process. It is unclear whether the carbon intensity after the second HF process is a result of the initial polymer contamination or whether it is cross-contamination from a processing chamber or the vacuum system. Most of this carbon is concentrated at the surface, where etch induced contamination would most likely be incorporated deeper in the substrate, as the corresponding normal incidence spectrum shows only a background level of carbon.

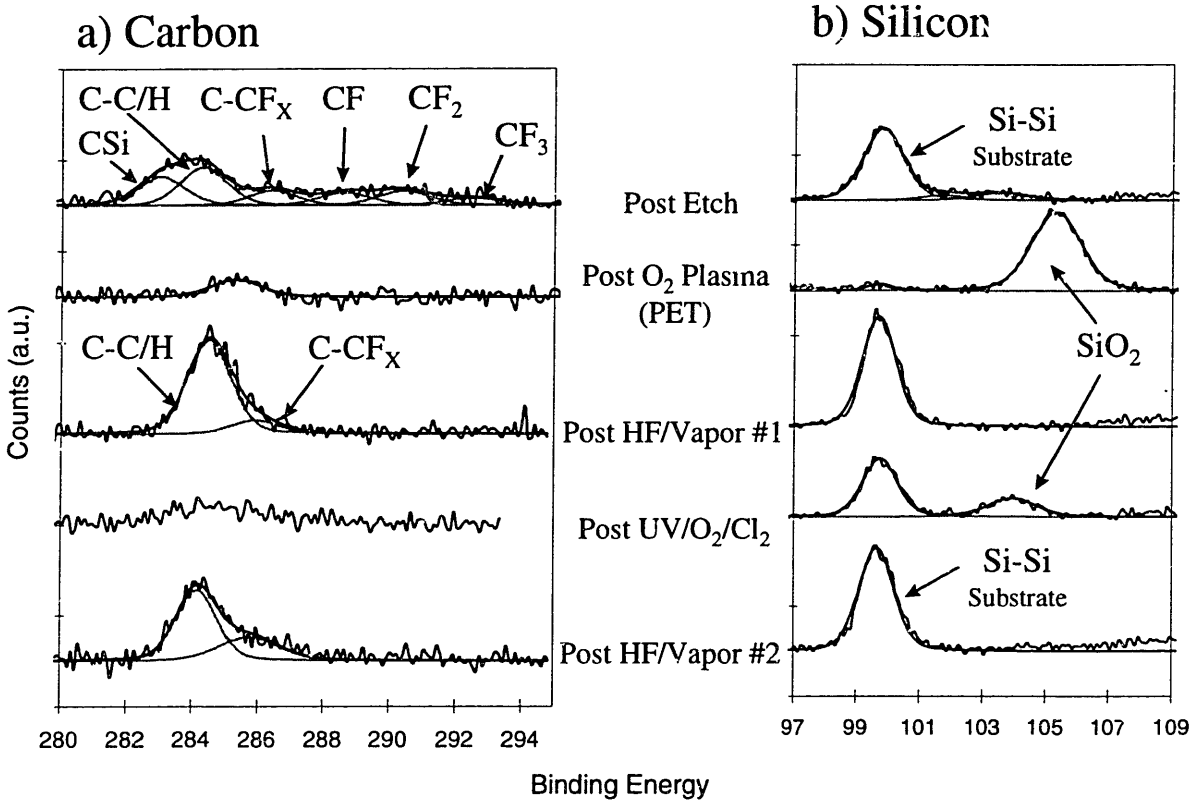

Figure 7.5-Carbon 1s and Silicon 2p photoelectron emission spectra at 30° take-off illustrating an "HF first" cleaning sequence applied to a blanket oxide film etched at 300 W top/50 W bottom in 4:1 C_2F_6:CHF_3 at 20 mTorr. The post-etch polymer is ~5 Å thick with an F/C ratio of ~0.5. The process sequence is represented by reading the spectra from top to bottom.

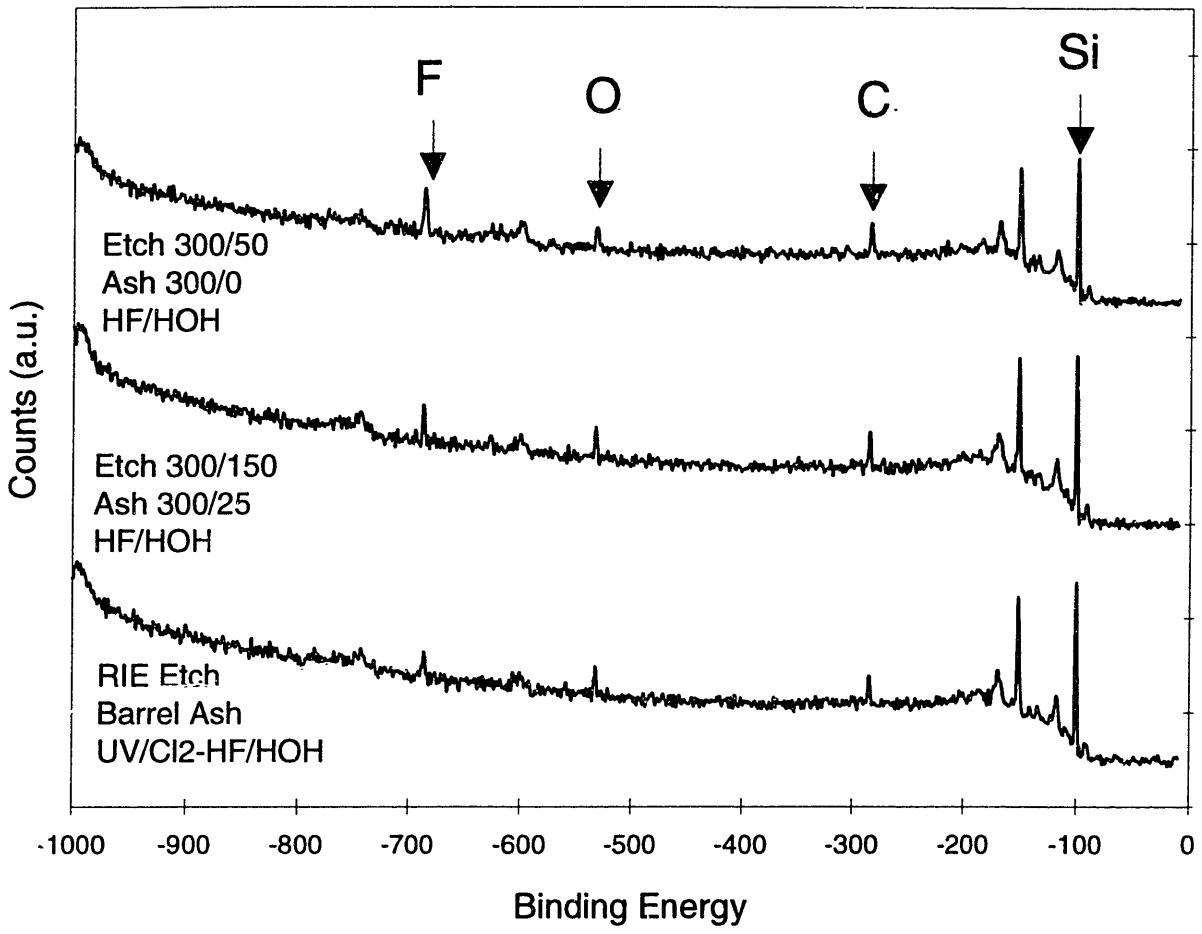

Figure 7.6-Survey spectra illustrating HF/Vapor only cleaning sequences on ICP etched and PET processed wafers compared to a UV/Cl_2-HF/Vapor cleaning sequence on an RIE etched barrel ashed wafer. Both of the post ICP etch polymers were ~ 5 Å thick with F/C ratios >1. The top/bottom power settings are given for the ICP etch and PET processes. The location of the major photoelectron emission peaks for silicon, fluorine, oxygen and carbon are indicated. The contamination level and surface chemistry are similar in all cases.

Figure 7.6 shows survey spectra after an ICP etch in 4:1 C_2F_6:CHF_3, PET, and HF/Vapor clean compared to a survey spectra after a UV/Cl_2 and HF/Vapor clean on RIE etched and barrel ashed blanket oxide films. All of the surfaces appear similar chemically and are characterized by monolayer levels of fluorine, oxygen and carbon contamination. An organic clean prior to the HF/Vapor process is not required to achieve complete oxide removal in the high density system.

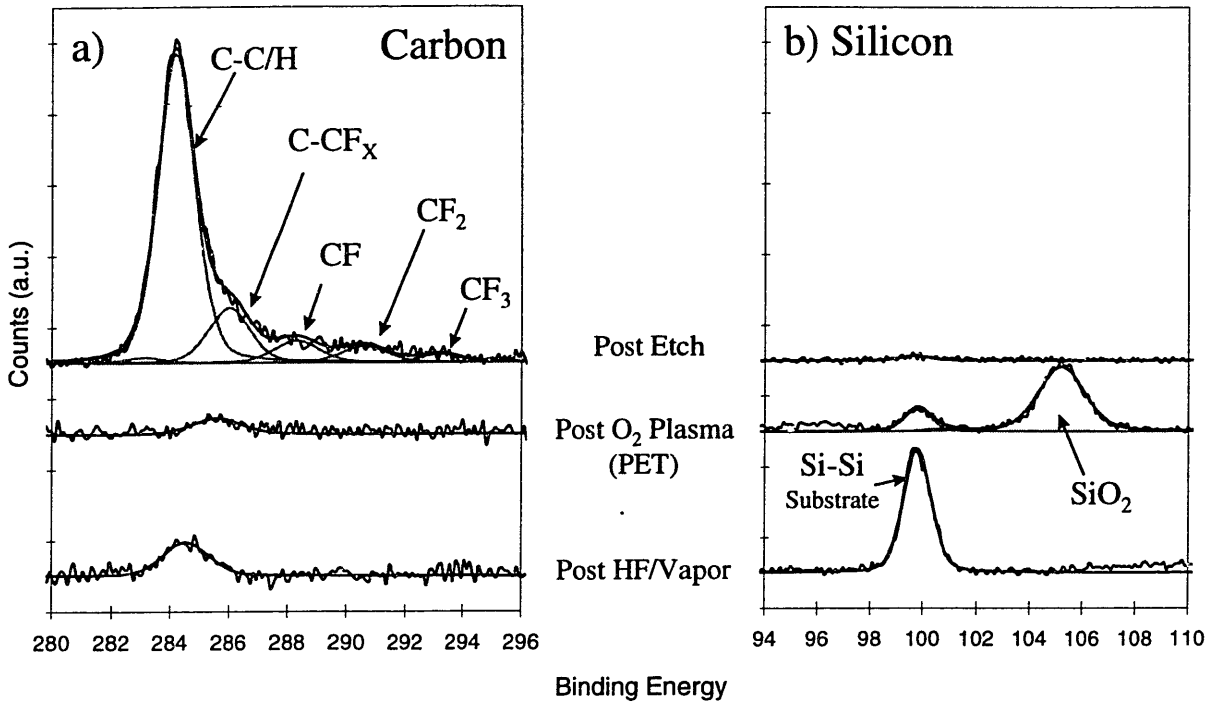

Figure 7.7- Carbon 1s and Silicon 2p photoelectron emission spectra illustrating an HF only clean applied to a blanket oxide film etched at 300 W top/150 W bottom in 1:1 C_2F_6:CHF_3 at 10 mTorr. The post-etch polymer is ~90 Å thick with an F/C ratio of ~0.2. The process sequence is represented by reading the spectra from top to bottom.

Figure 7.7 illustrates an HF/Vapor only cleaning sequence applied to a thick graphitic polymer layer. Note that the substrate peak is barely resolved in the post-etch spectrum. Even in this extreme case, the level of carbon after the oxide strip is relatively low. However, as shown in Figure 7.8, the level of fluorine on the wafer surface is significantly higher after this process than with a similar clean applied to a thinner polymer layer such as that illustrated in Figure 7.5. The difference in the final level of cleanliness of these initially drastically different surfaces illustrate that the etch conditions have an effect on the efficacy of the cleaning process.

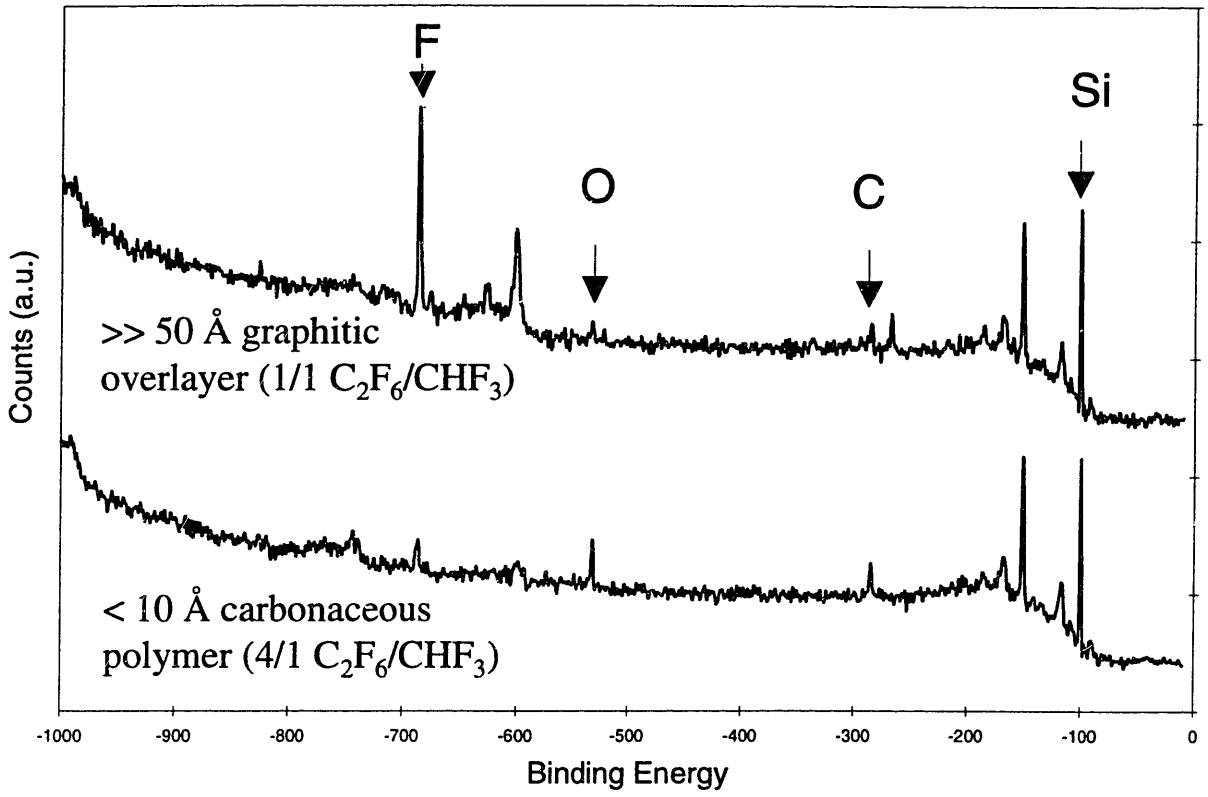

Figure 7.8-Survey spectra illustrating HF/Vapor only cleaning sequences on ICP etched and PET processed wafers. The location of the major photoelectron emission peaks for silicon, fluorine, oxygen and carbon are indicated. Although the oxide has been efficiently removed, the initially thicker contamination layer exhibits a much higher degree of fluorine contamination after the HF process.

B. Patterned Oxide Films

The processing of patterned oxide films was somewhat more problematic than the processing of blanket oxides. We endeavored to develop a process in which the integrity of the oxide lines was maintained, i.e. to mimic an industrial process as closely as possible in order to obtain contamination chemistry which was realistic and relevant to the current state of the art. This proved to be far from straight forward. The major problem in this system is the extremely poor resist to oxide selectivity in the ICP oxide etcher. We typically observed selectivity on the order of 0.5, where the typical selectivity obtained in an industrial etcher is 2-6[1,4], and on only one occasion was the oxide "cleared" without substantial roughening of the oxide surface beneath the resist. In the results presented here the oxide integrity was maintained over at least a substantial fraction of the oxide surface (see Figures 7.15 & 7.16).

Coupled with this is the difficulty in determining etch endpoint due to the lack of diagnostics in the ICP etcher, such that runs were typically made in a start-stop fashion with periodic visual inspection of the wafer surface to avoid significant over etching. The amount of over-etch was typically on the order of 10%. Oxide was etched at rates of 2000-3500 Å/min depending on the processing conditions.

Figure 7.9 illustrates the carbon spectra from an integrated cleaning process on a patterned surface. Qualitatively, the surface chemistry appears similar to what was observed on the blanket oxide samples. The most significant difference is the chemical state of the carbon contamination after the HF oxide strip, and especially after the UV/Cl_2 process. On patterned wafers, the residual carbon after the HF process is more fluorinated. And especially after the UV/Cl_2 process, where the carbon observed on the blanket wafers after a similar sequence was typically exclusively graphitic, a high degree of halogenation is observed (although these spectra were fit with the CF_X binding energies as listed in Table 1, it is likely that at this point in the process most of the carbon shifting is due to chlorination).

Figure 7.10 illustrates the effect of UV/Cl_2 processing on the residual carbon contamination left on a patterned wafer surface after an ICP etch, PET and HF/Vapor process. The initial level of contamination is reduced after 3 minutes of exposure, and is heavily halogenated, halogenation increasing with time from 0-3 minutes, with a chemical state distribution similar to what is shown in Figure 7.9. A further 3 minutes of processing has no effect on either the level of carbon or the chemical state.

The chemistry of carbon removal is obviously different on a patterned wafer surface. The most likely interpretation of these results is that the carbon which remains on the patterned wafers after UV/Cl_2 exposure is not associated with the exposed silicon surface but is incorporated in the oxide lines. We have already established that the UV/Cl_2 process is effective at removing polymer residue from an exposed silicon surface. Even incorporated carbon should be removed, since the etch rate of silicon in UV/Cl_2 is ~ 50 Å/min at 2 Torr and 100°C, because ~ 300 Å of substrate should have been removed in the process illustrated in Figure 7.10. This etching depth would be more than enough to remove any carbon which would have been incorporated into the substrate due to processing at the conditions used, especially if the ~50 Å of substrate consumed in the PET is considered. The efficacy of slight

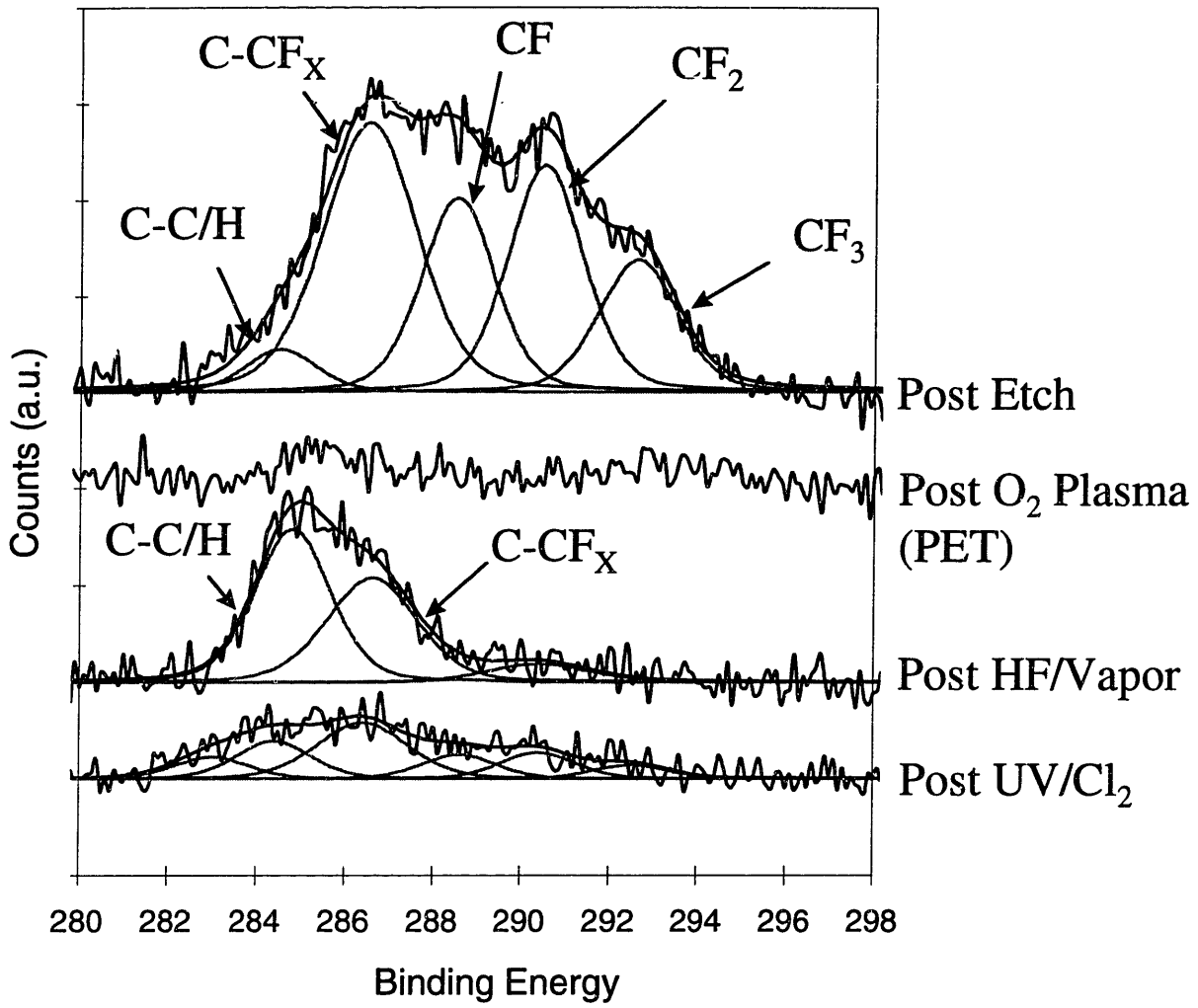

Figure 7.9- Carbon 1s photoelectron emission spectra illustrating an integrated cleaning sequence applied to a patterned oxide wafer (line & space) etched at 300 W top/45 W bottom in 1:1 C_2F_6:CHF_3 at 5 mTorr. The post-etch polymer was ~25 Å thick with an F/C ratio of ~1.14. The PET resulted in the growth of a ~50 Å thick oxide. The UV/Cl_2 process conditions were 3 minutes at 2 Torr and 100°C. The process sequence is represented by reading the spectra from top to bottom.

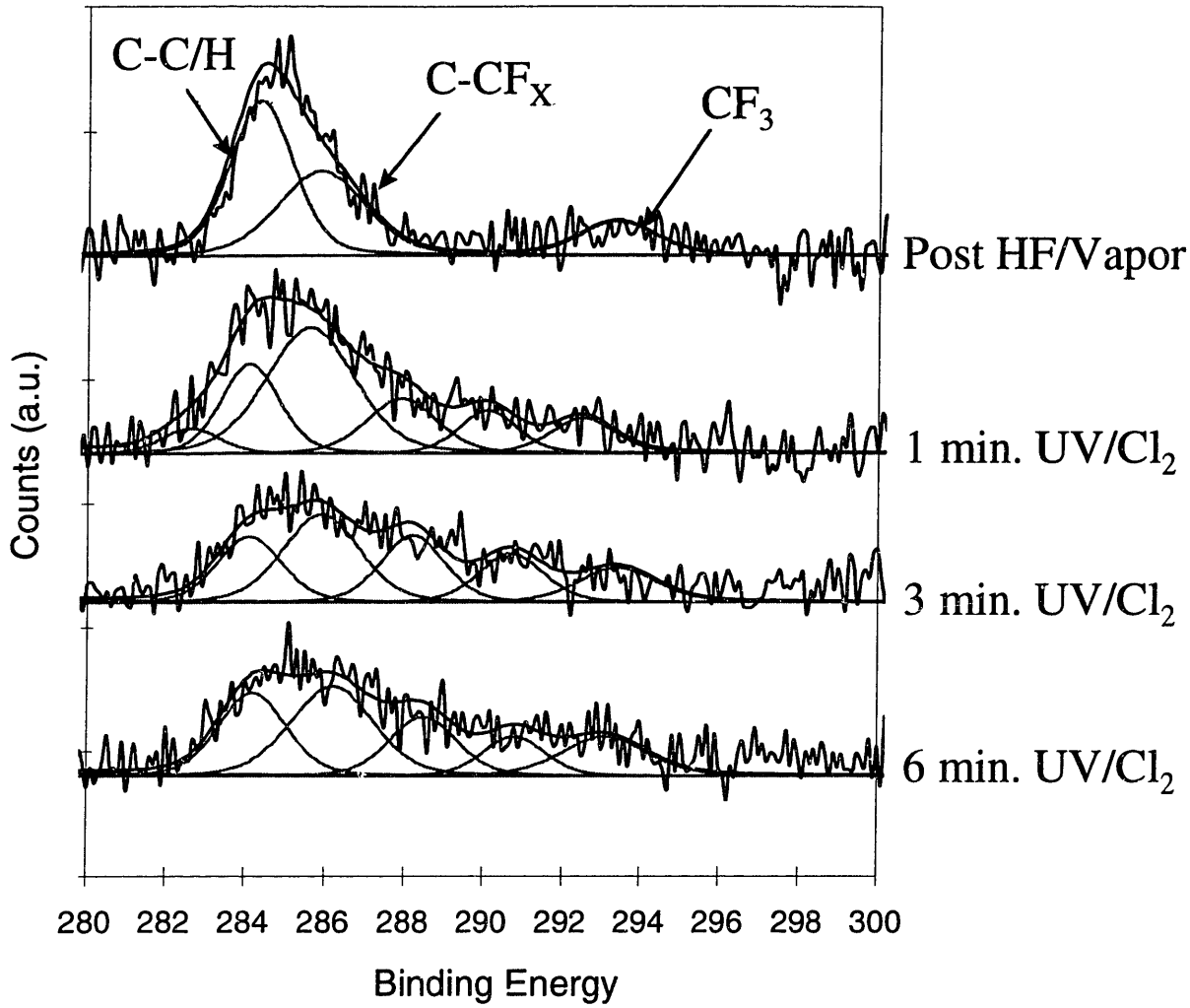

Figure 7.10- Carbon 1s photoelectron emission spectra illustrating the effect of UV/Cl_2 processing on a patterned oxide wafer (line & space) etched at 300 W top/37 W bottom in C_2F_6 at 15 mTorr. The post-etch polymer (not shown) was ~10 Å thick with an F/C ratio of ~1. The PET resulted in the growth of a ~50 Å thick oxide. The UV/Cl_2 process was performed at 2 Torr and 100°C. The process sequence is represented by reading the spectra from top to bottom. Times indicated at right represent the cumulative UV/Cl_2 processing time.

substrate etching (on the order of 100 Å) with UV/Cl_2 for the recovery of electrical properties after RIE has been established[11], and the degree of ion induced substrate damage and contamination incorporation is significantly less for the lower ion bombardment energies used in high density processing[12].

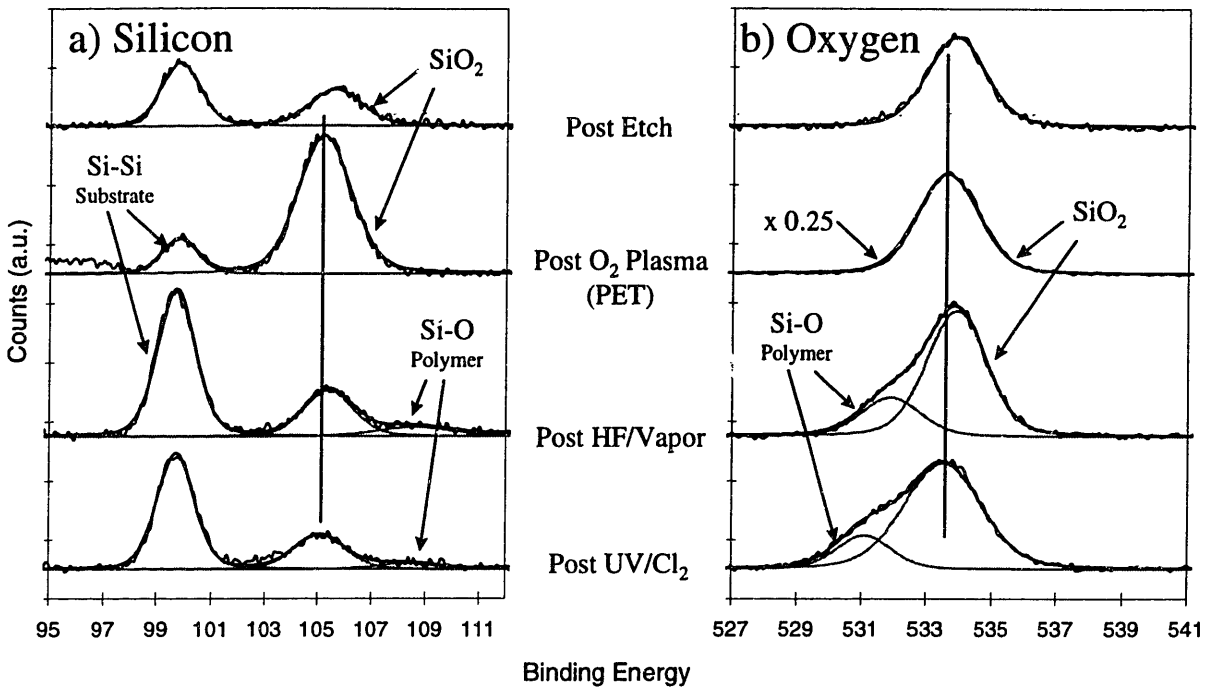

Figure 7.11- Silicon 2p and oxygen 1s photoelectron emission spectra corresponding to the carbon spectra illustrated in Figure 7.9. The vertical lines corresponding to the binding energy of "clean" SiO_2 are included to aid in visualizing chemical shifts. The process sequence is represented by reading the spectra from top to bottom.

The silicon and oxygen spectra illustrated in Figure 7.11 show evidence of carbon incorporated into the oxide lines on patterned wafers. Two distinct types of contamination are suggested by the spectra. The first ("type 1") is analogous to the polymer incorporated in the barrel ash grown oxide which was discussed in Chapter 6. This contamination is typified by a positive binding energy shift in the SiO_2 bonding in both the silicon and oxygen shift. Type 1 contamination is evident in the post etch and post HF/Vapor spectra illustrated in Figure 7.11. Since both the silicon and oxygen shifts are in the same direction, we believe that this type of contamination is not chemically bonded to the oxide. The shift in binding energy most likely arises from the buildup of excess positive charge in the oxide due to the presence of incorporated carbon contamination. Baer *et al.*[13] have attributed a similar shift in a self-

assembled monolayer SiO_2/Si system to the generation of trapped charge at the SiO_2/Si interface due to electron beam damage, while Kodama *et al.*[14] have noted that incorporated carbon causes positive charge build-up in a COB-DRAM device. Baer is careful to point out that this shift is not due to charging from the X-ray gun, but is an intrinsic property of the sample. Note that the SiO_2 binding energy shifts back after the PET and UV/Cl_2 processes corresponding to the removal of the type 1 contamination (to the analysis depth of XPS) by these processes. The second type of incorporated contamination ("type 2") is not well understood. This contamination is typified by a peak at ~108.5 eV in the silicon 2p photoemission, and a peak at ~531.5 eV in the oxygen 1s photoemission (although the exact binding energies appear to be somewhat variable and tend to shift with the SiO_2 shift due to type 1 contamination), and we have assigned it the designation $Si\text{-}O_{Polymer}$. Type 2 contamination is chemically bonded to the oxide and results in a positive binding energy shift for silicon and a negative binding energy shift for oxygen.

Figures 7.12 and 7.13 illustrate the effect of UV/Cl_2 on the contamination with angle resolved XPS. In the wafer represented in Figure 7.12, type 1 contamination is removed to the analysis depth of XPS by the UV/Cl_2 process. Note that in both the normal and 20 degree post UV/Cl_2 spectra, the shift due to type 1 contamination has been fully recovered. In the wafer illustrated in Figure 7.13, with a 33 % shorter UV/Cl_2 exposure time, the type 1 contamination is not fully removed. Note that the SiO_2 shift is more fully recovered in the 20 degree spectra than the normal spectra. The analysis depth of XPS goes as the sin of the take-off angle (see Chapter 1), and the generally accepted sampling depth of XPS is ~3 mean free paths[9], or ~90Å for silicon with Mg Kα radiation assuming λ=27Å[15]. Therefore, we can surmise that in the

sample represented by Figure 7.13, type 1 contamination was removed to a depth of approximately 30 Å, but is still incorporated in the oxide at a depth of 30-90 Å.

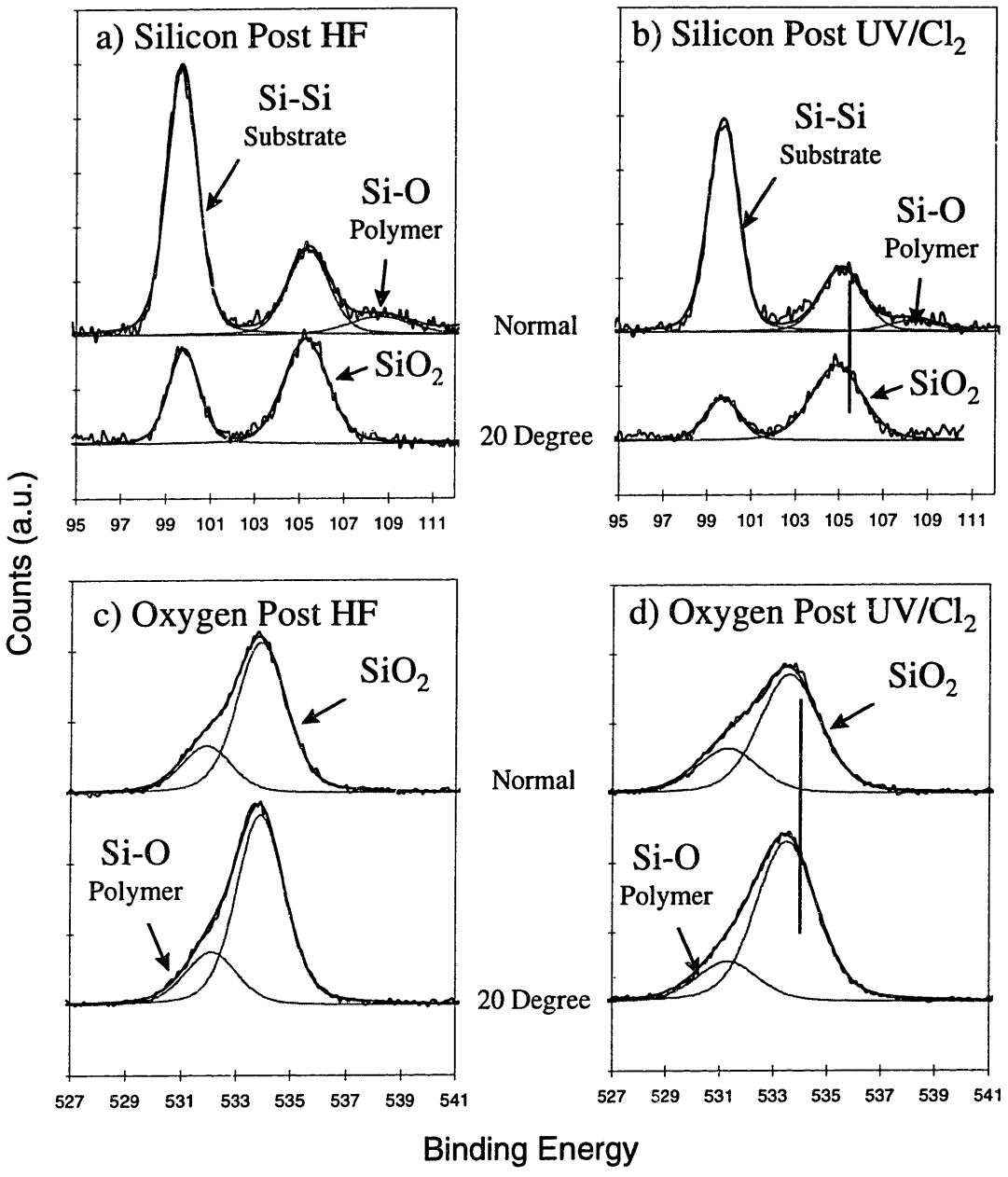

Figure 7.12- Normal take-off angle Silicon 2p and oxygen 1s photoelectron emission spectra from figure 7.11 compared to the 20 degree take-off angle spectra taken at the same point in the process sequence. The vertical lines corresponding to the binding energy of SiO_2 in the post/HF spectra are superimposed on the post UV/Cl_2 spectra to aid in visualizing chemical shifts.

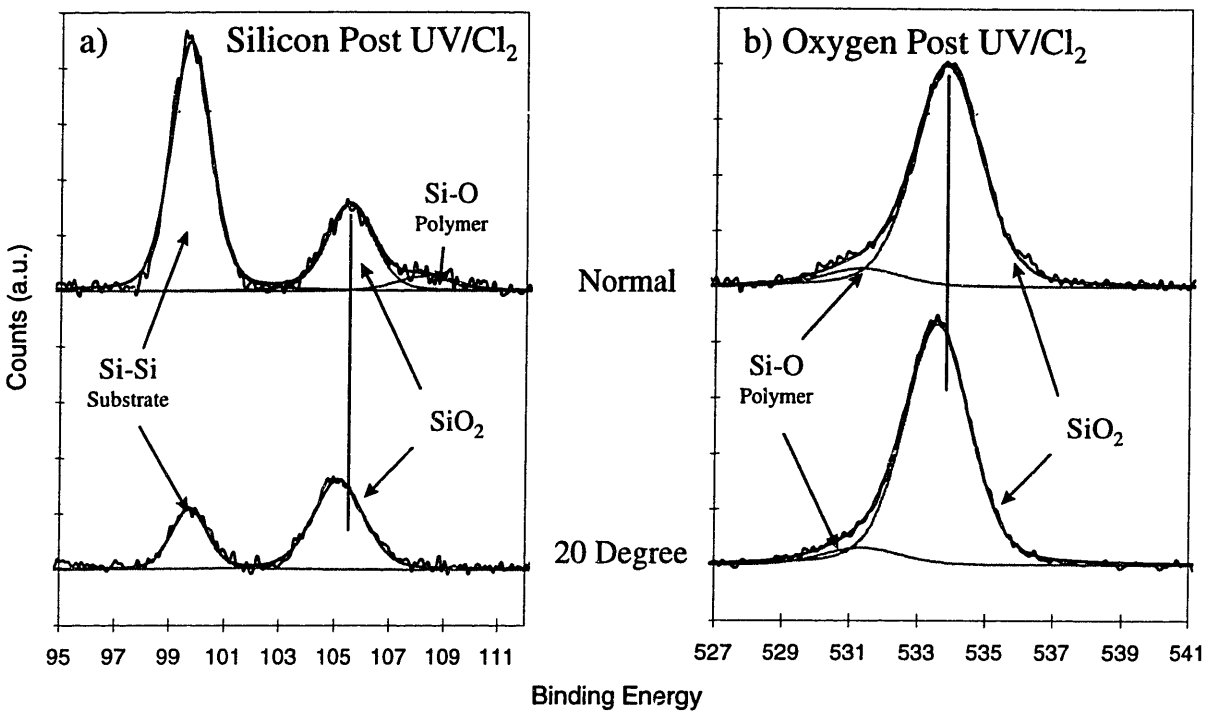

Figure 7.13- Normal take-off angle Silicon 2p and oxygen 1s photoelectron emission spectra from a patterned oxide wafer (line & space) etched at 300 W top/37 W bottom in C_2F_6 at 15 mTorr compared to the 20 degree take-off angle spectra taken after an etch, PET, HF/Vapor, and 2 minute, 2 torr, 100°C UV/Cl_2 process sequence. The vertical lines are superimposed to aid in visualizing chemical shifts.

Type 2 contamination is also evident in the samples illustrated in Figures 7.12 and 7.13. In both samples, the chemical state typical of type 2 contamination is not resolved in the silicon spectra at 20 degrees. It also comprises a lower percentage of the oxygen signal at 20 degrees. This indicates that type 2 contamination is not present at higher concentration on the oxide sidewalls. In addition, it is obvious that UV/Cl_2 processing is not very effective in removing type 2 contamination. This is not surprising, since type 2 contamination seems to be associated with SiO_2, and UV/Cl_2 does not etch oxide.

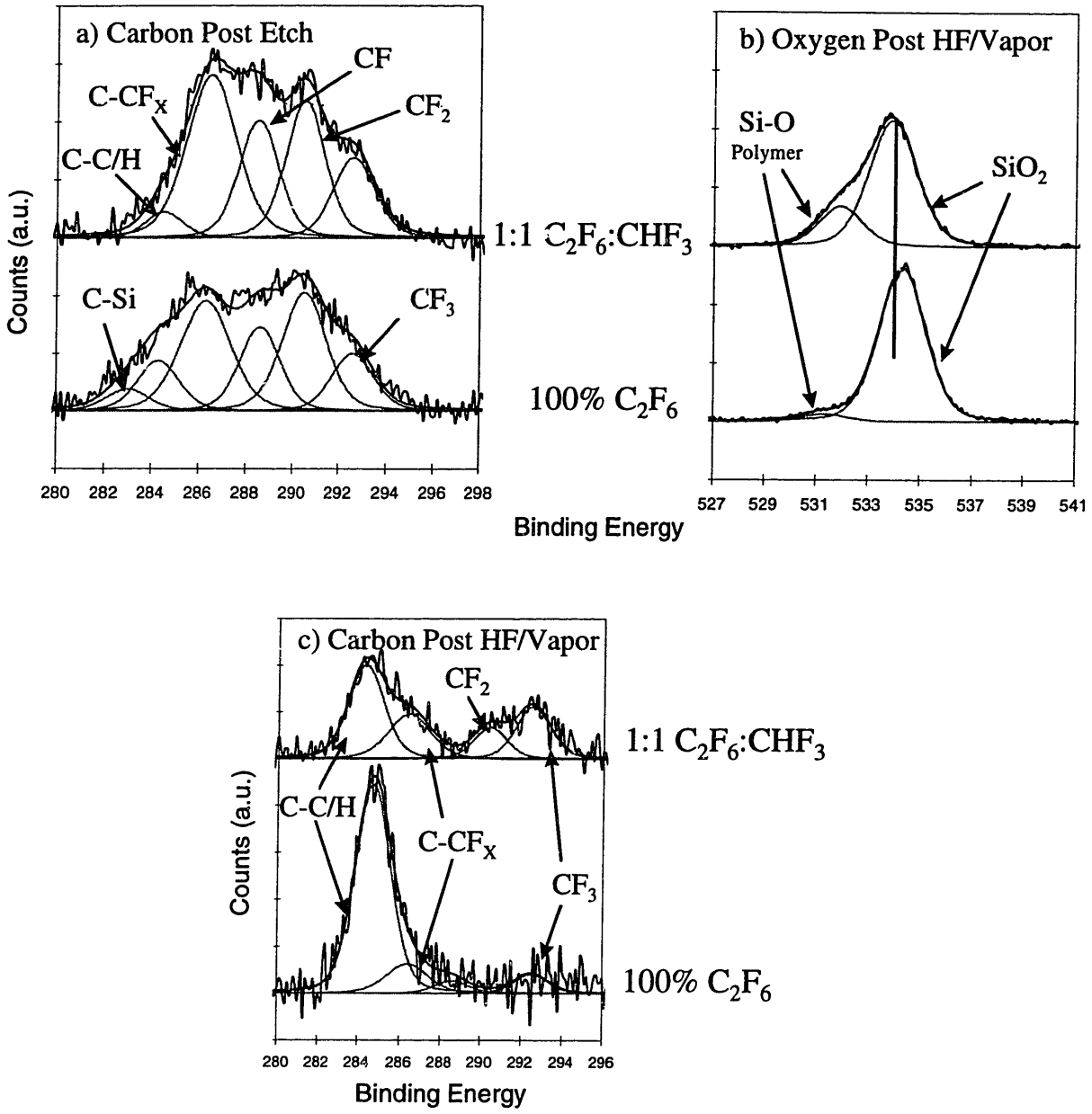

Figure 7.14-Carbon 1s and silicon 2p spectra illustrating some differences between line & space wafers etched in 1:1 C_2F_6:CHF_3 (5 mTorr) and 100% C_2F_6 (15 mTorr) chemistries at the same power settings. The polymer thickness' were 25 and 15 Å, and the F/C ratios were 1.14 and 1.22 for the 1:1 and 100% chemistries respectively. Both samples were given a PET that resulted in the growth of a 50 Å oxide.

Figure 7.14 illustrates some differences in the surface chemistry between samples etched in 1:1 C_2F_6:CHF_3 and 100% C_2F_6 chemistries. The most striking difference is the

disparity in the amount of type 2 contamination as evidenced by the oxygen spectra in Figure 7.14c. Figures 7.15 and 7.16 illustrate Atomic Force Microscopy (AFM) data from the same two samples.

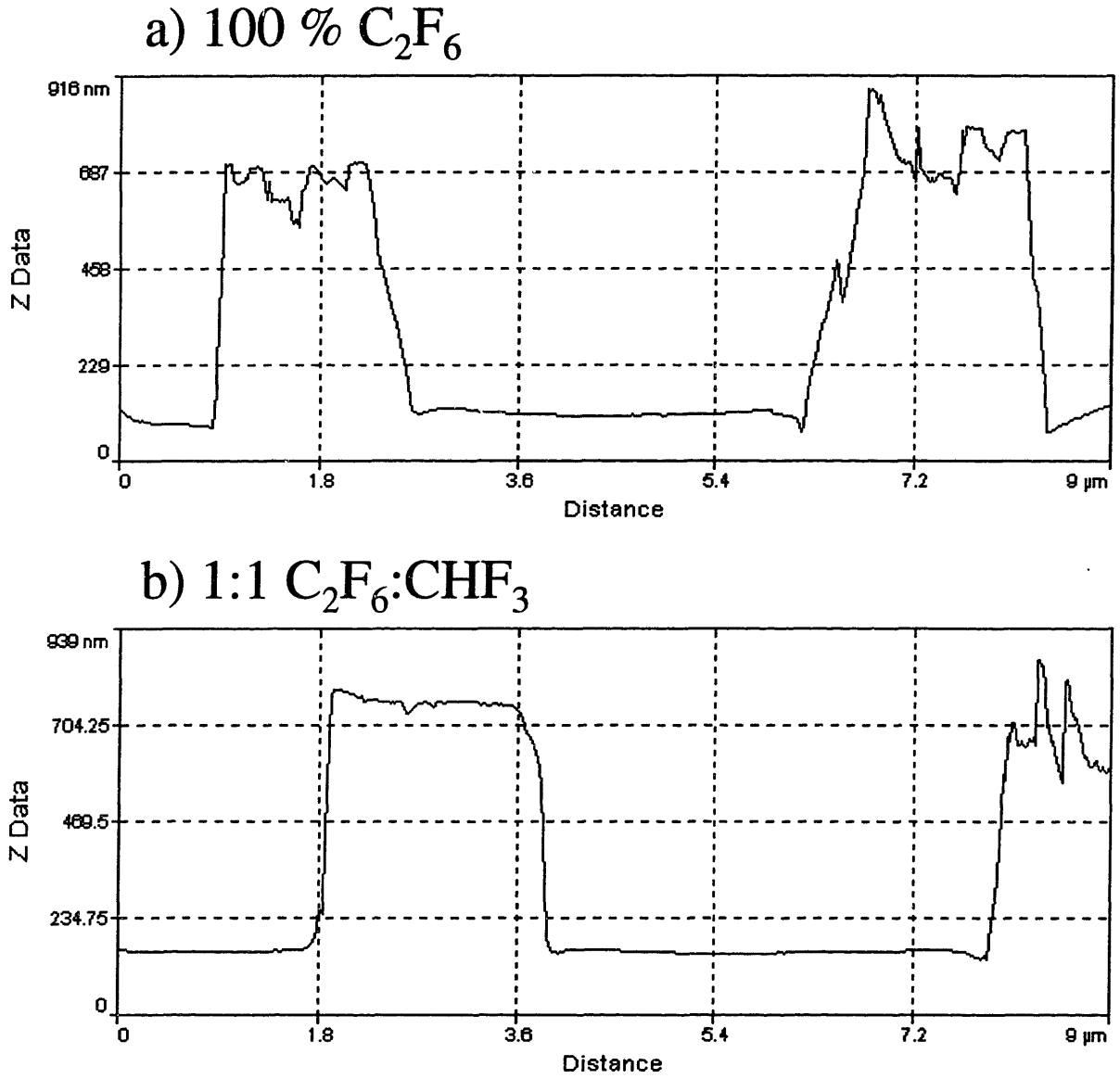

Figure 7.15- AFM line scans from the samples whose surface chemistry is represented by Figure 7.14.

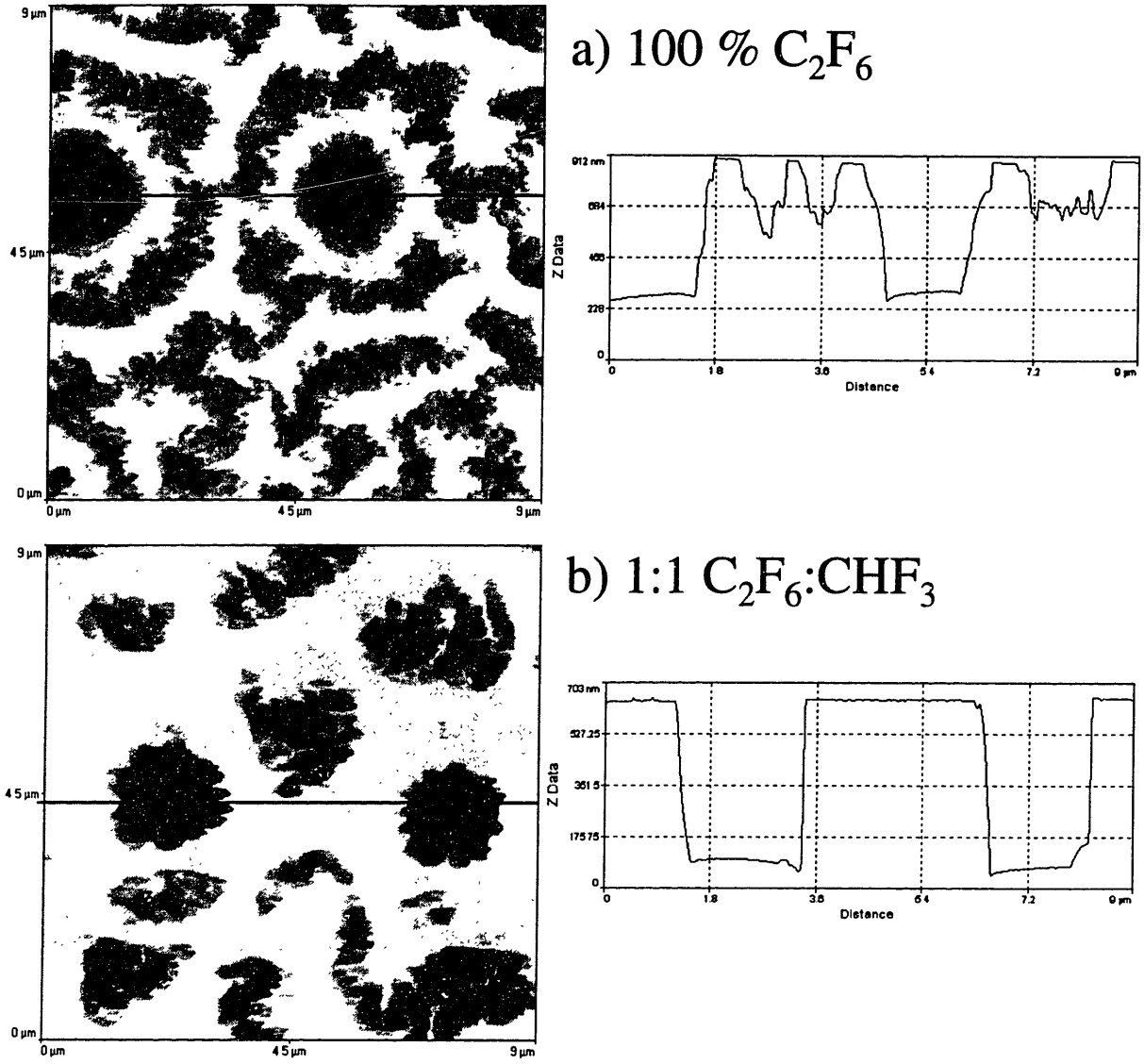

Figure 7.16- AFM images and corresponding line scans from contact mask samples which were etched at conditions identical to the line & space mask samples whose AFM scans are represented in Figure 7.15.

It is interesting, and perhaps significant, that the samples etched at a condition that yields more type 2 contamination (i.e. 1:1 C_2F_6:CHF_3) exhibit better critical dimension control. Note that the sidewalls are much more vertical on the features etched in the 1:1 chemistry on both the line & space and contact pattern. In the samples etched in pure C_2F_6, where type 2 contamination was not as pronounced, the sidewalls appear bowed, and the

dimension at the top of the feature is larger than that at the bottom. Especially note the "arena" effect around the periphery of the contacts illustrated in Figure 7.16a. This raises the possibility that type 2 contamination is associated with effective pattern transfer. Other pieces of evidence support this. The type 2 contamination chemical state has thus far not been observed on a contact pattern wafer with XPS, even one etched at conditions which exhibit type 2 contamination on a line & space pattern. With the contact pattern, the analyzed surface is effectively blanket resist-over-oxide, since the areal density of contacts in the analyzed area is >0.01%. This would suggest that type 2 contamination is associated with features on the wafer, since it is not observed unless a significant fraction of the surface is being etched. Also, notice that although resist "breakthrough" was observed over ~50% of the oxide surface on the sample represented by Figure 7.16a (note the alternating pattern of rough and smooth surface), there was always a "halo" of smooth oxide around the contacts. The same effect has been observed at the edges of oxide lines, even when the center of the line was roughened significantly (see Figure 7.15a). This would suggest that there is a passivation mechanism which depends on the presence of oxide etch products which is active in the region immediately adjacent to a feature being etched. Possibly, this passivation mechanism is coupled with the formation of type 2 contamination in the oxide adjacent to a feature being etched.

7.4 Conclusions

Preliminary experiments on integrated processing have been performed with an eye towards developing a totally integrated ICP etch, oxygen plasma PET, and dry cleaning sequence. Both blanket and patterned oxide films have been studied. Our results indicate that in this system, an "HF only" cleaning sequence yields a surface with a low level of surface

contamination. The reason for this is that the high density oxygen plasma PET is very efficient in removing surface polymeric contamination.

Two types of contamination were observed on patterned oxide wafers. Type 1 contamination is due to the presence of incorporated, but not chemically bonded, contamination and is analogous to the incorporated polymer discussed in Chapter 6. Type 1 contamination is typified by a positive binding energy shift in both the silicon and oxygen SiO_2 photoemission and is removed by UV/Cl_2 processing. Type 2 contamination is due to chemically bonded contamination in the oxide layer. Type 2 contamination is typified by a positive binding energy shift relative to SiO_2 in the silicon and a negative shift relative to SiO_2 in the oxygen photoemission and is not significantly affected by UV/Cl_2 processing. The nature of type 2 contamination is in question, but it may be related to critical dimension control.

7.5 References

[1] P. Singer, Semiconductor International, Vol. 20, No. 6, 109-114 (1997).

[2] M. Lieberman and R. Gottscho, "Design of High Density Plasma Sources for Materials Processing", Phys. of Thin Films: Advances in Res. and Dev., vol. 17, J. Vossen ed., Academic Press, Orlando, Florida (1993).

[3] G.S. Oehrlein, Y. Zhang, D. Vender, and M. Haverlag, J.Vac. Sci. Technol. A, vol. 12, no. 2, 323-332 (1994).

[4] G.S. Oehrlein, Y. Zhang, D. Vender, and O. Joubert, J. Vac. Sci. Technol. A, vol. 12, no 2, 333-344 (1994).

[5] T. Akimoto, E. Ikawa, T. Sango, K. Komachi, K. Katayama, and T. Ebata, Jpn. J. Appl. Phys., Vol. 33, No 12B, 7037-7041 (1994).

[6] T. Fukasawa, K. Kubota, H. Shindo, and Y. Horiike, Jpn. J. Appl. Phys., Vol. 33, No 12B, 7042-7046 (1994).

[7] Y. Miyakawa, K. Fujita, N. Hirashita, N. Ikegami, J. Hashimoto, T. Matsui, and J. Kanamori, Jpn. J. Appl. Phys., Vol. 33, No 12B, 7047-7052 (1994).

[8] J.H. Park, S.W. Chung, J.J. Kim, and W.S. Kim, J. Vac. Sci. Technol. B, Vol. 14, No. 1, 478-482 (1996).

[9] O. Joubert, P. Czuprynski, F.H. Bell, P. Berruyer, and R. Blanc, J. Vac. Sci. Technol. B, Vol. 15, No. 3, 629-639 (1997).

[10] O. Joubert, G.S. Oehrlein, and Y. Zhang, J. Vac. Sci. Technol. A, Vol. 12, No. 3, 658-664 (1994).

[11] D.K. Hwang, K. Torek, and J. Ruzyllo, Proceedings of the 1st International Symposium on Plasma Process Induced Damage, 137-140, AVS-IEEE/Electron Devices Society (1996).

[12] G.S. Oehrlein, J. Vac. Sci. Technol. A, vol. 11, no 1, 34-46 (1993).

[13] D.R. Baer, M.H. Engelhard, D.W. Schulte, D.E. Guenthier, Li-Qiong Wang, and P.C. Rieke, J. Vac. Sci. Technol. A, Vol. 12, No. 4, 2478-2490 (1994).

[14] N. Kodama, H. Mori, S. Saito, and K. Koyama, Nuc. Inst. & Met. Phys. Res. B, Vol. 118, No. 1-4, 505-508 (1996).

[15] F. Yano, A. Hiraoka, T. Itoga, H. Kojima, K, Kanehori, and Y. Mitsui, J. Vac. Sci. Technol. A, 13 (6) (1995) 2671-2675.

Appendix A

Mechanical Drawings

1. Second UV Reactor

Reactor Assembly Drawing

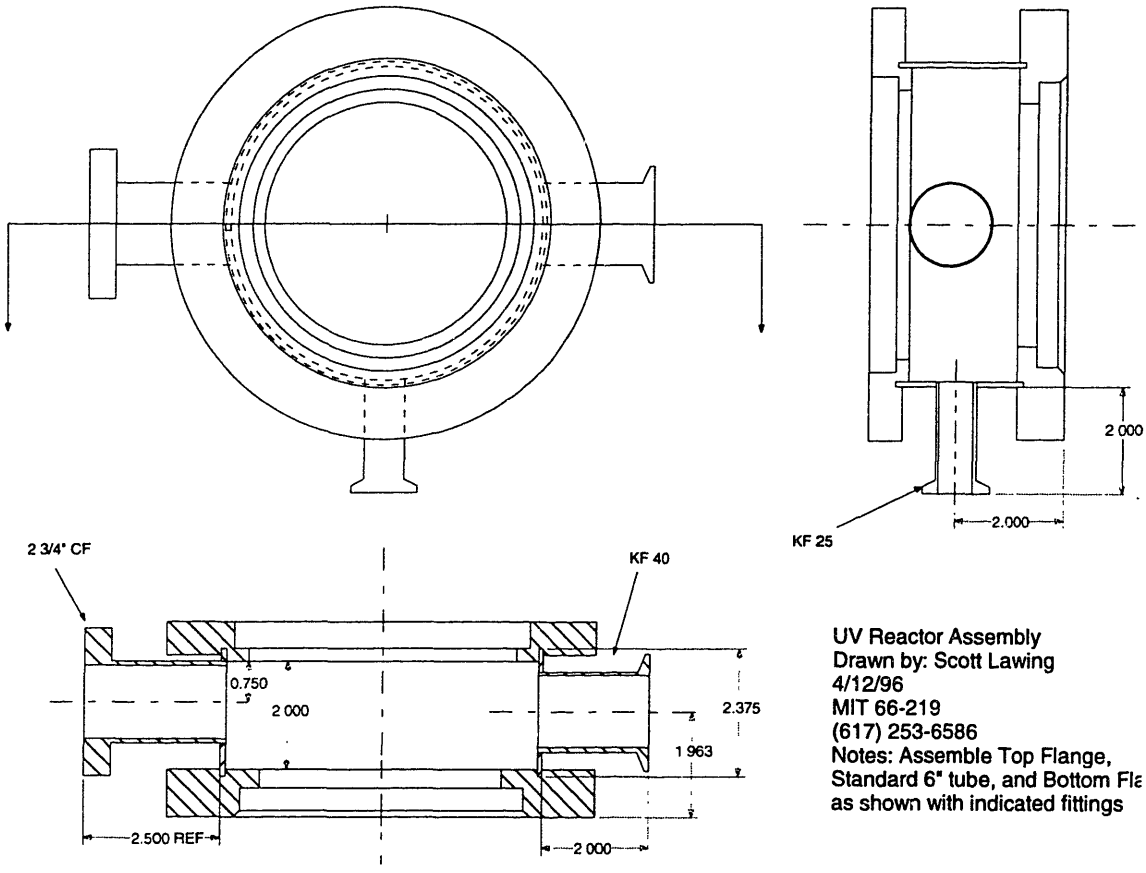

UV Reactor Assembly
Drawn by: Scott Lawing
4/12/96
MIT 66-219
(617) 253-6586
Notes: Assemble Top Flange, Standard 6" tube, and Bottom Fla as shown with indicated fittings

Top Flange

Top Flange
Drawn by: Scott Lawing
MIT 66-219 (617)-253-6586
4/12/96

Note:
O-ring seat dimensions shown left and bottom.
Overall dimensions shown right and top.

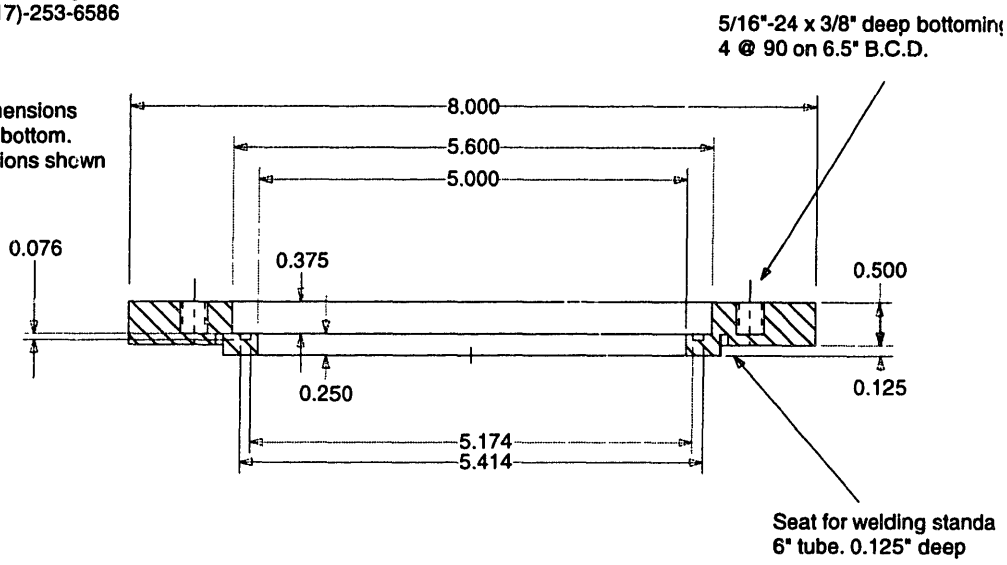

Gas Inlet Flange

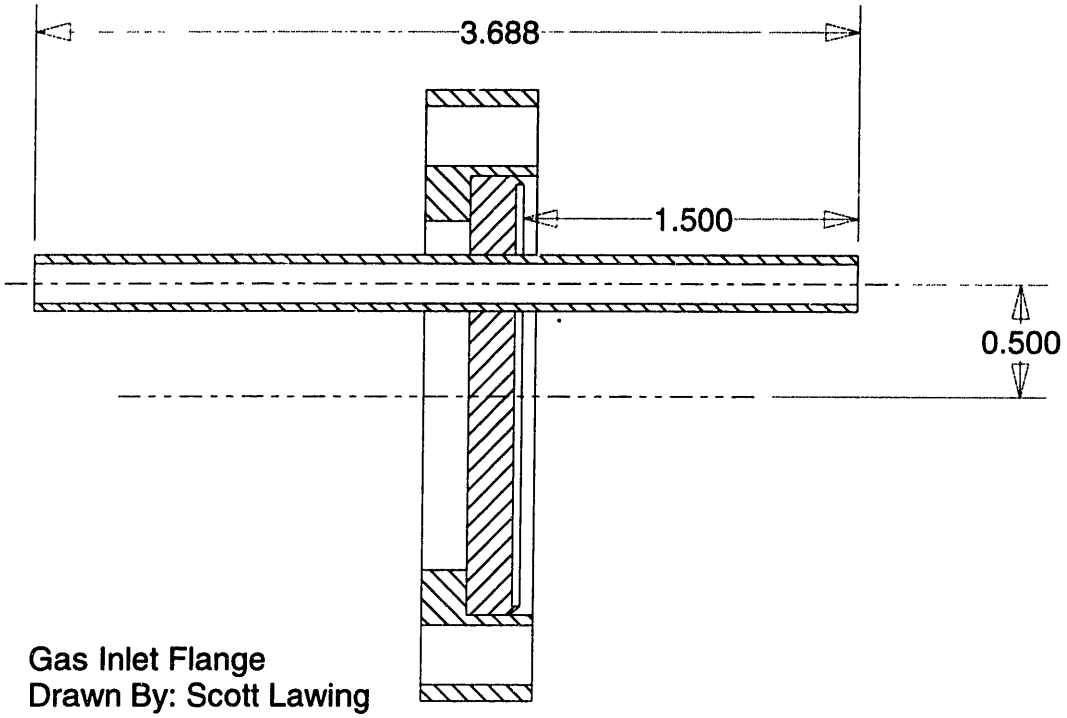

Gas Inlet Flange
Drawn By: Scott Lawing
MIT 66-219
(617) 253-6586

Notes: Machine from 2 3/4" Rotatable Conflat Blank. Weld 1/4" 0.035" wall ss tube as shown

Feed-Through Flange Assembly Drawing

Feed-Through Flange
Assembly Drawing
Drawn by: Scott Lawing
MIT 66-219
(617) 253-6586

Notes:
AssembleFeed-through flange
and differential seals 1 & 2
as shown

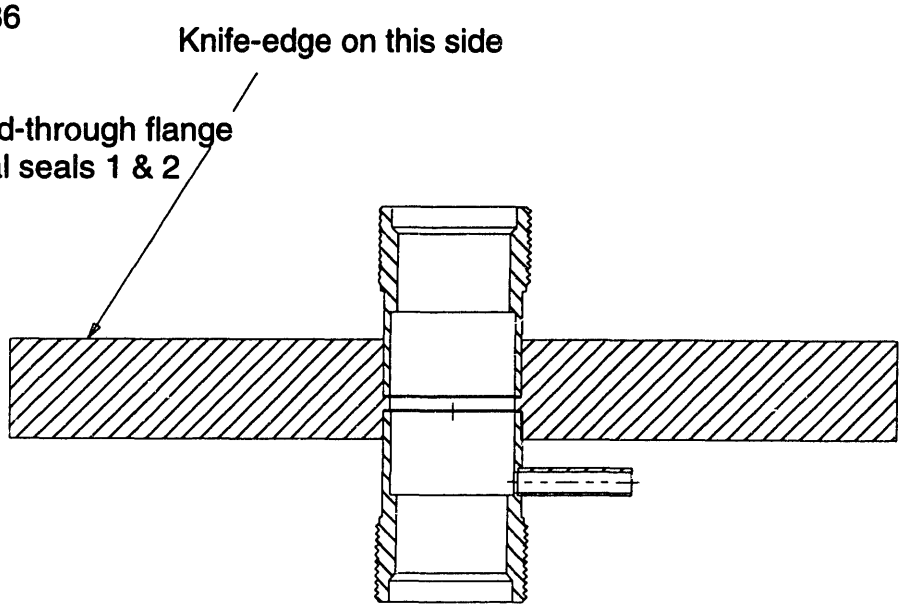

Feed-Through Flange

Feed-Through Flange
Drawn by: Scott Lawing
MIT 66-219
(617) 253-6586

Notes:
Machine from 8"
Conflat blank

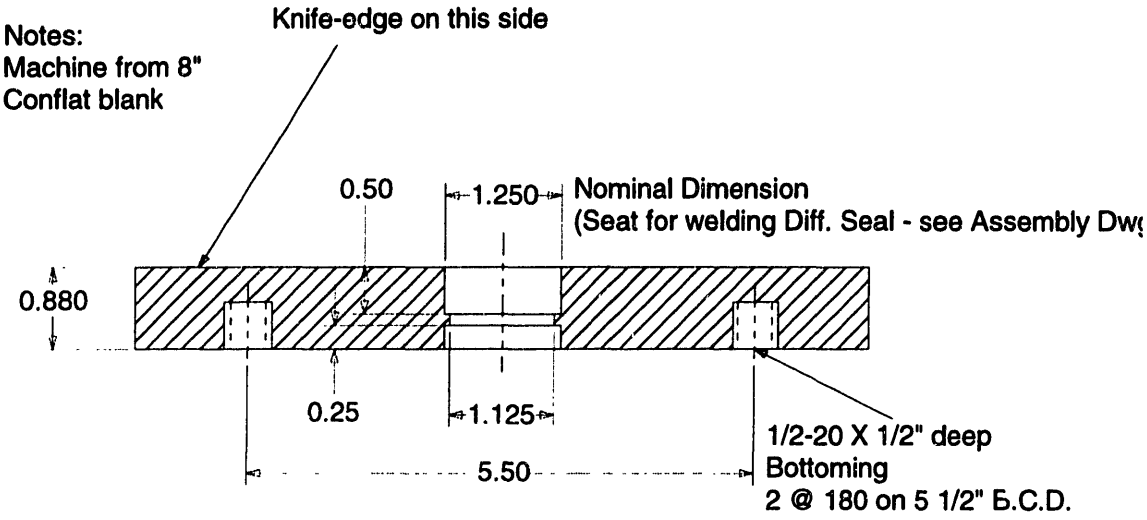

Differential Seal #1 (Feed Through Flange)

Differential Seal #1
Drawn by: Scott Lawing
MIT 66-219
(617)253-6586
Notes:Machine From
Cajon SS-16-UT-A-20

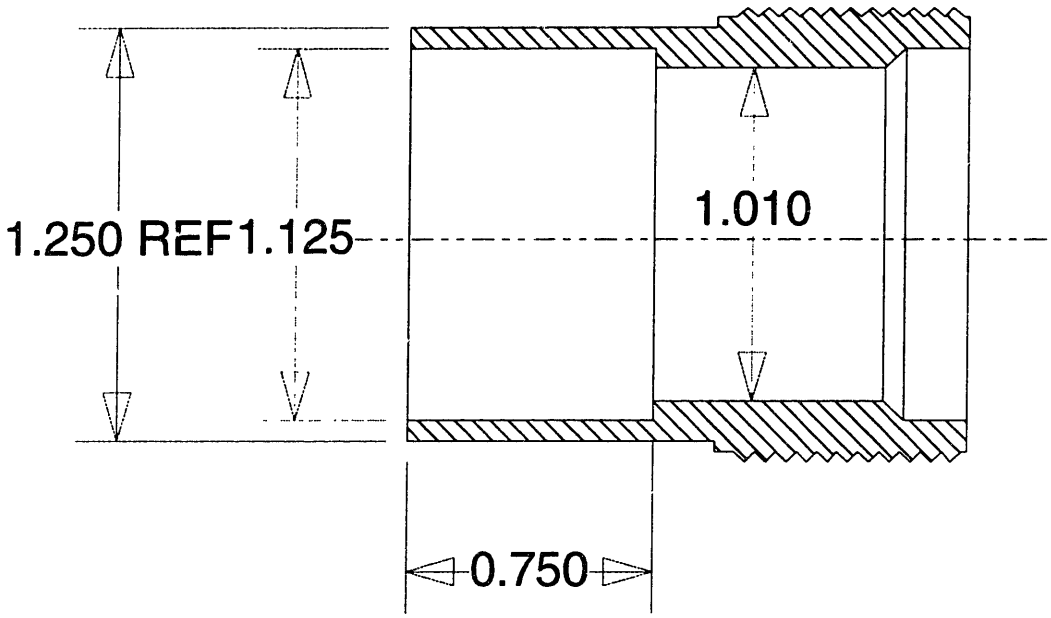

Differential Seal #2 (Feed Through Flange)

Differential Seal #2
Drawn by: Scott Lawing
MIT 66-219
(617)253-6586
Notes:Machine From
Cajon SS-16-UT-A-20

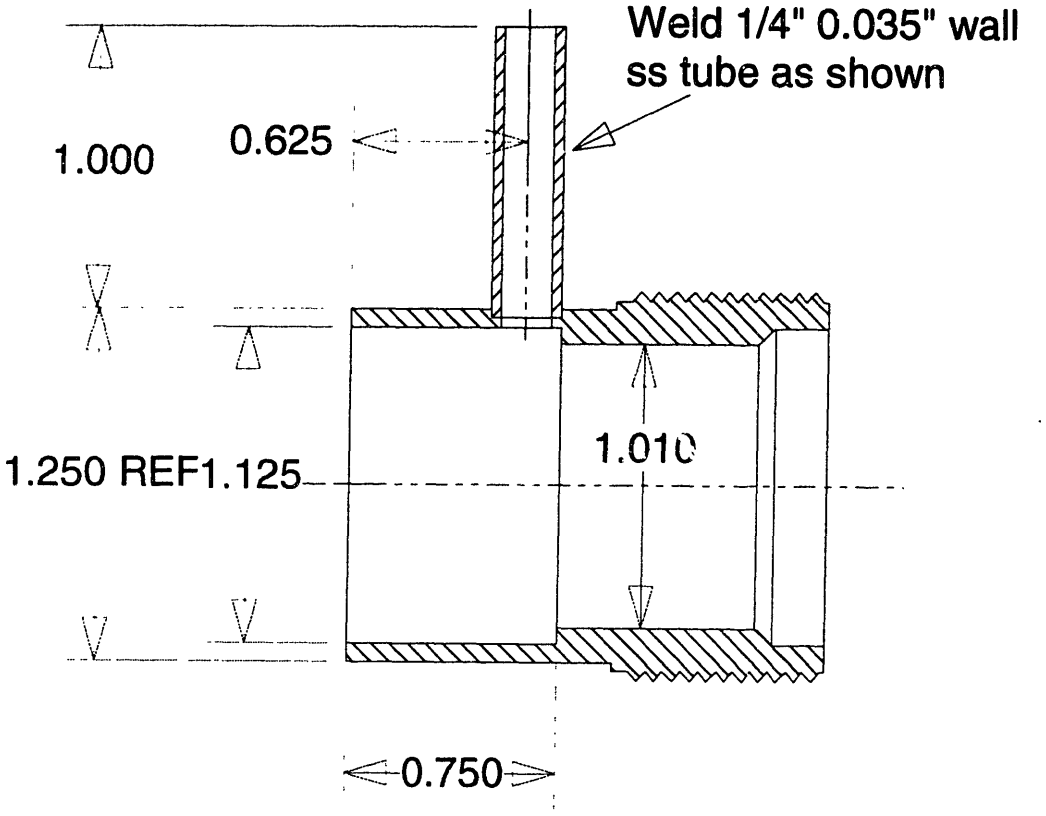

Wafer Platen Sleeve

Wafer Platen Sleeve
Drawn by: Scott Lawing
MIT 66-219
(617) 253-6586

Notes: Fabricate from
105 x 110 mm quartz tube.
UV absorbing quartz, i.e.
GE grade 254 or equivalent

DIMENSIONS IN MM

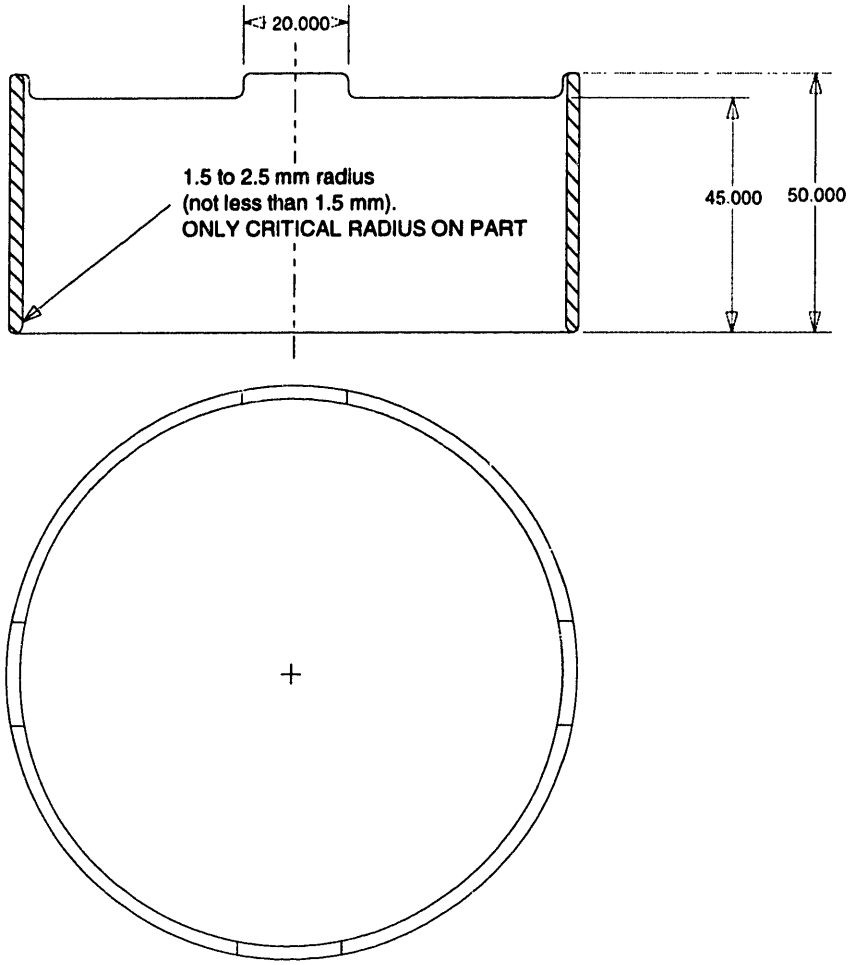

Chamber Sleeve

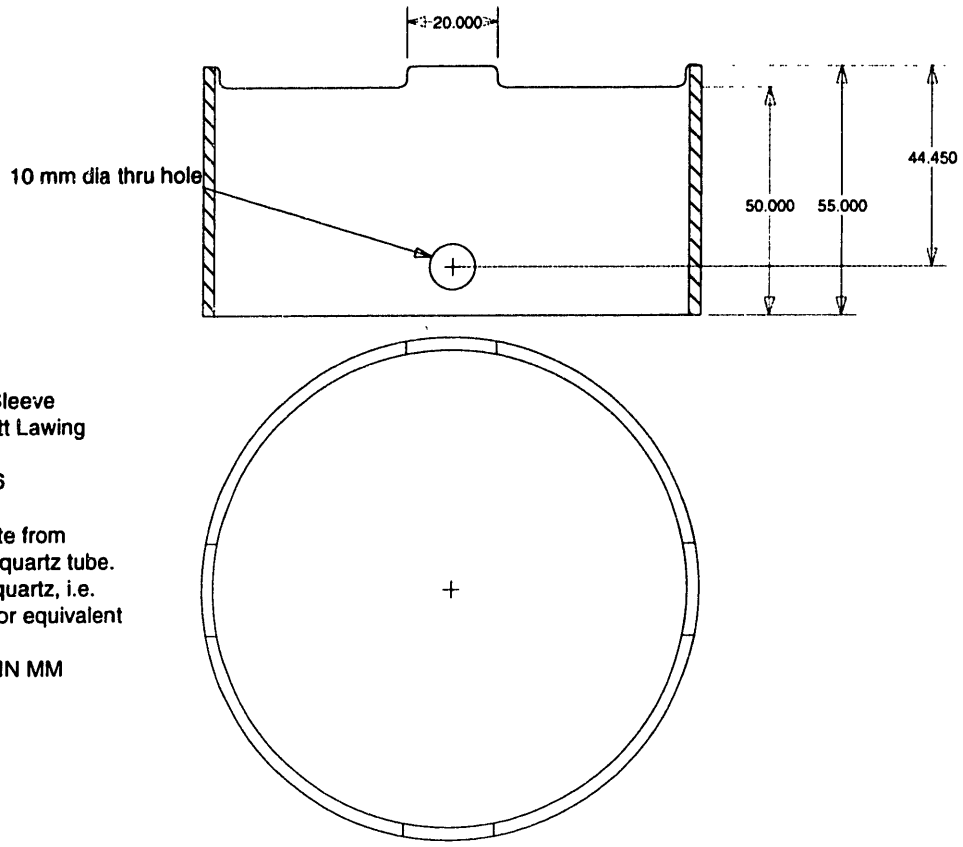

UV Chamber Sleeve
Drawn by: Scott Lawing
MIT 66-219
(617) 253-6586

Notes: Fabricate from
120 x 125 mm quartz tube.
UV absorbing quartz, i.e.
GE grade 254 or equivalent

DIMENSIONS IN MM

Wafer Platen Assembly Drawing

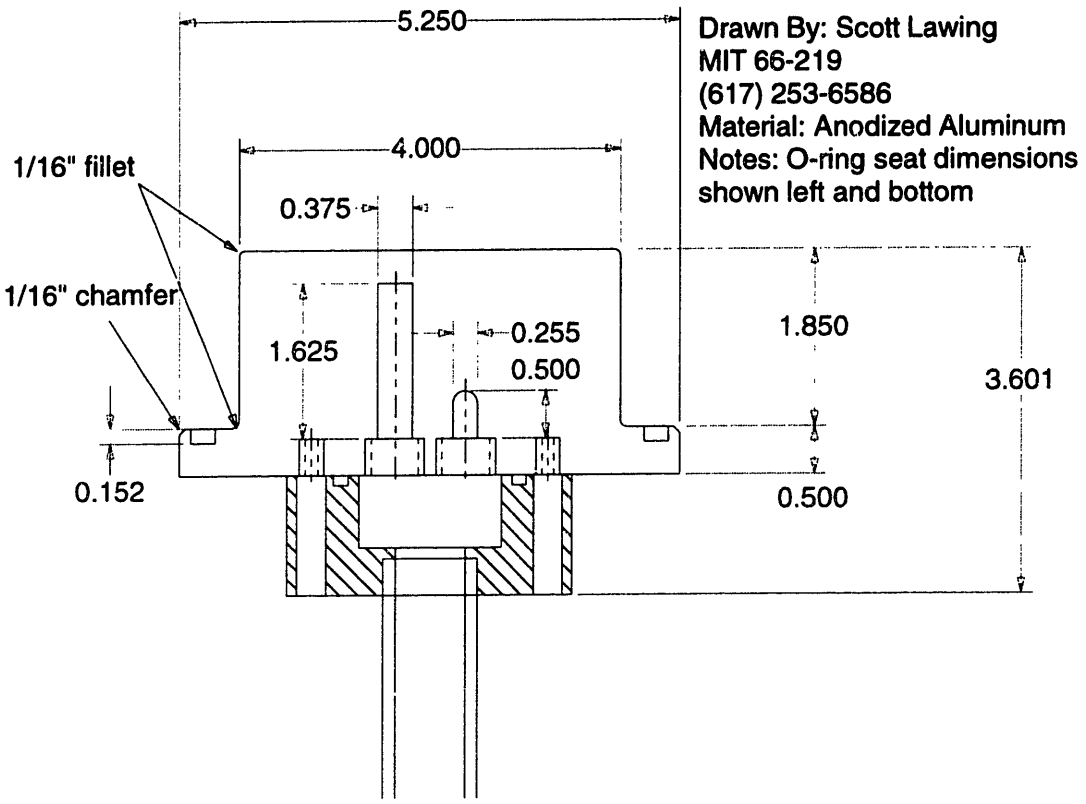

Wafer Platen

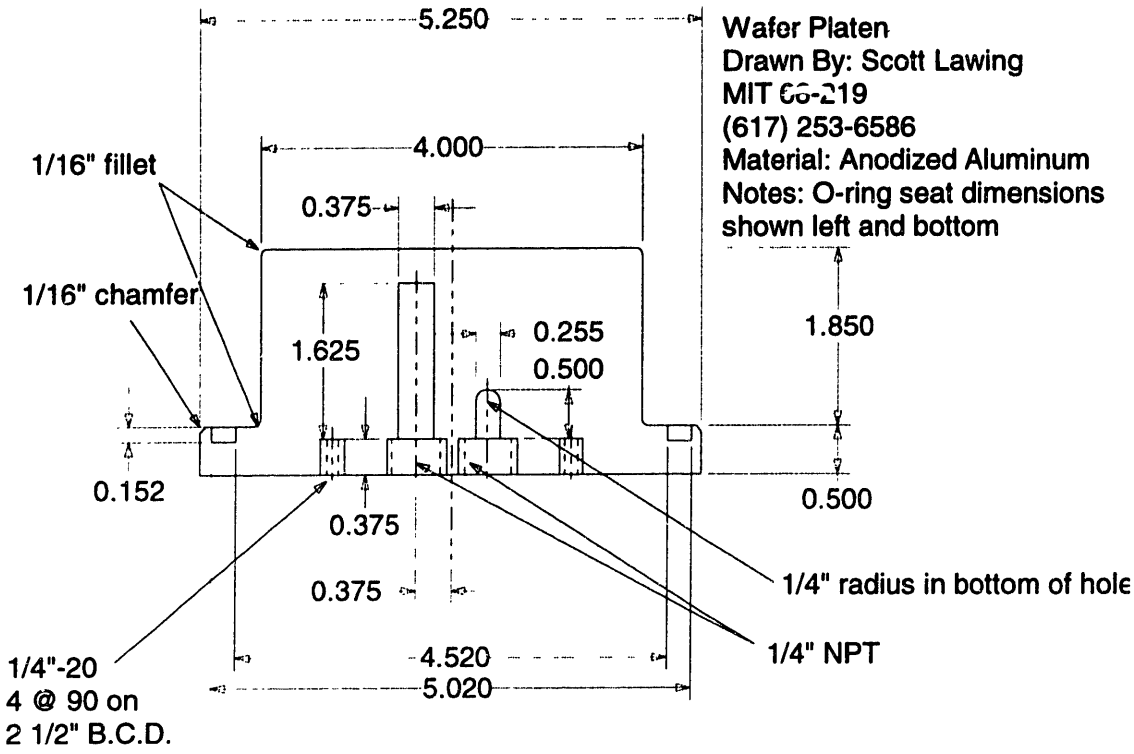

Transfer Rod Assembly Drawing

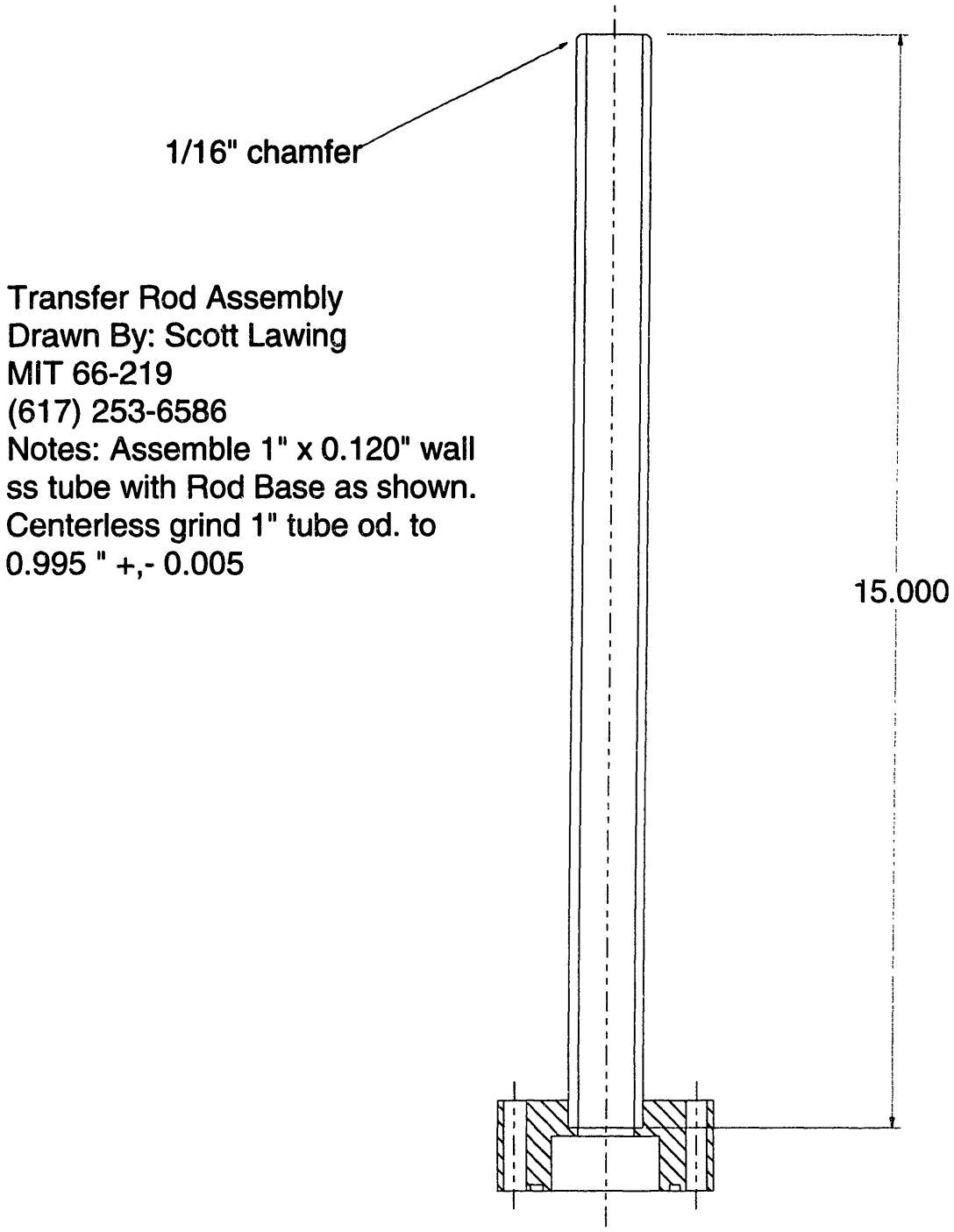

Transfer Rod Assembly
Drawn By: Scott Lawing
MIT 66-219
(617) 253-6586
Notes: Assemble 1" x 0.120" wall ss tube with Rod Base as shown. Centerless grind 1" tube od. to 0.995 " +,- 0.005

Transfer Rod Base

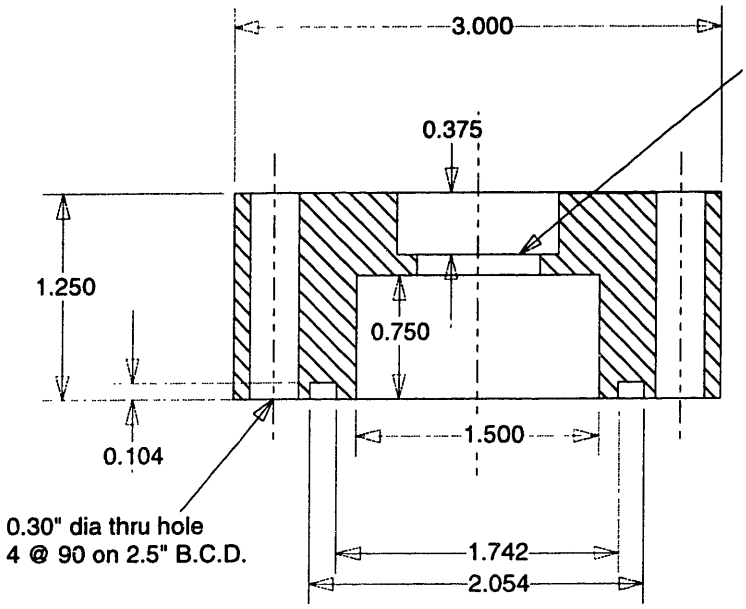

Nominal 1" dia. seat for welding 1" tube. See Transfer rod assembly drawing.

Transfer Rod Base
Drawn by: Scott Lawing
MIT 66-219
(617) 253-6586
Notes:Weld 1" tube as shown i
Transfer rod assembly

Transfer Rod Collar

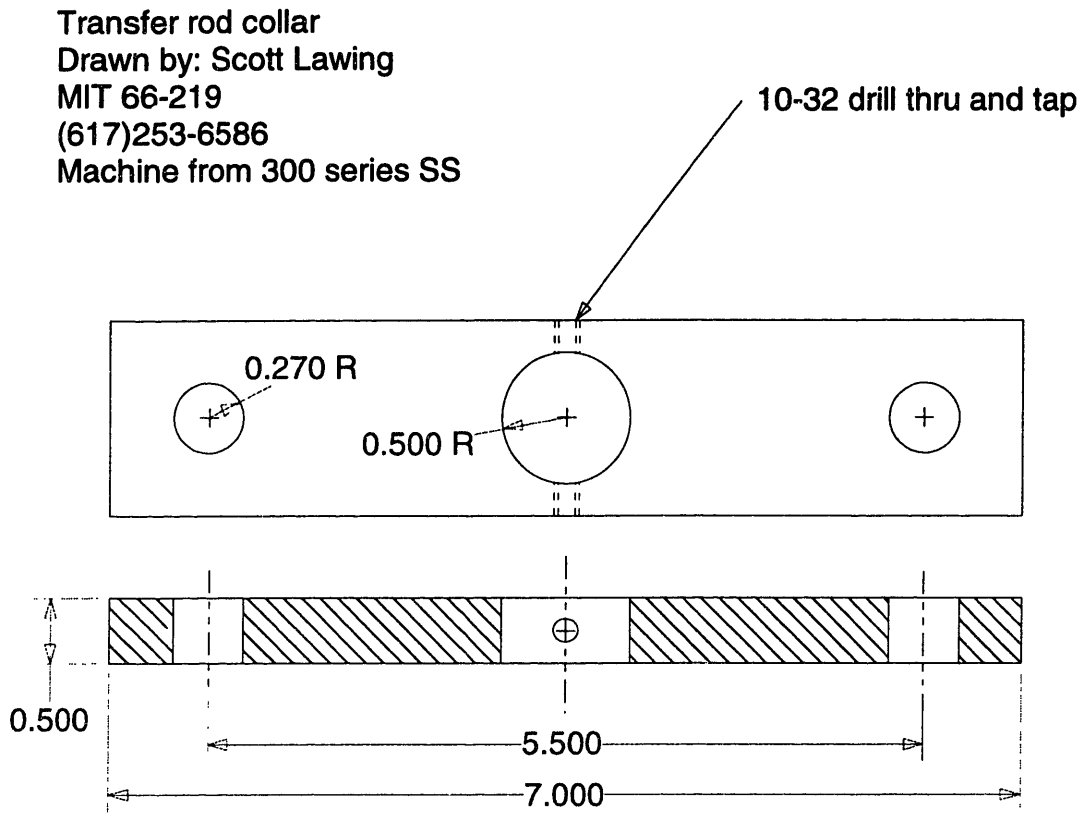

UV Window

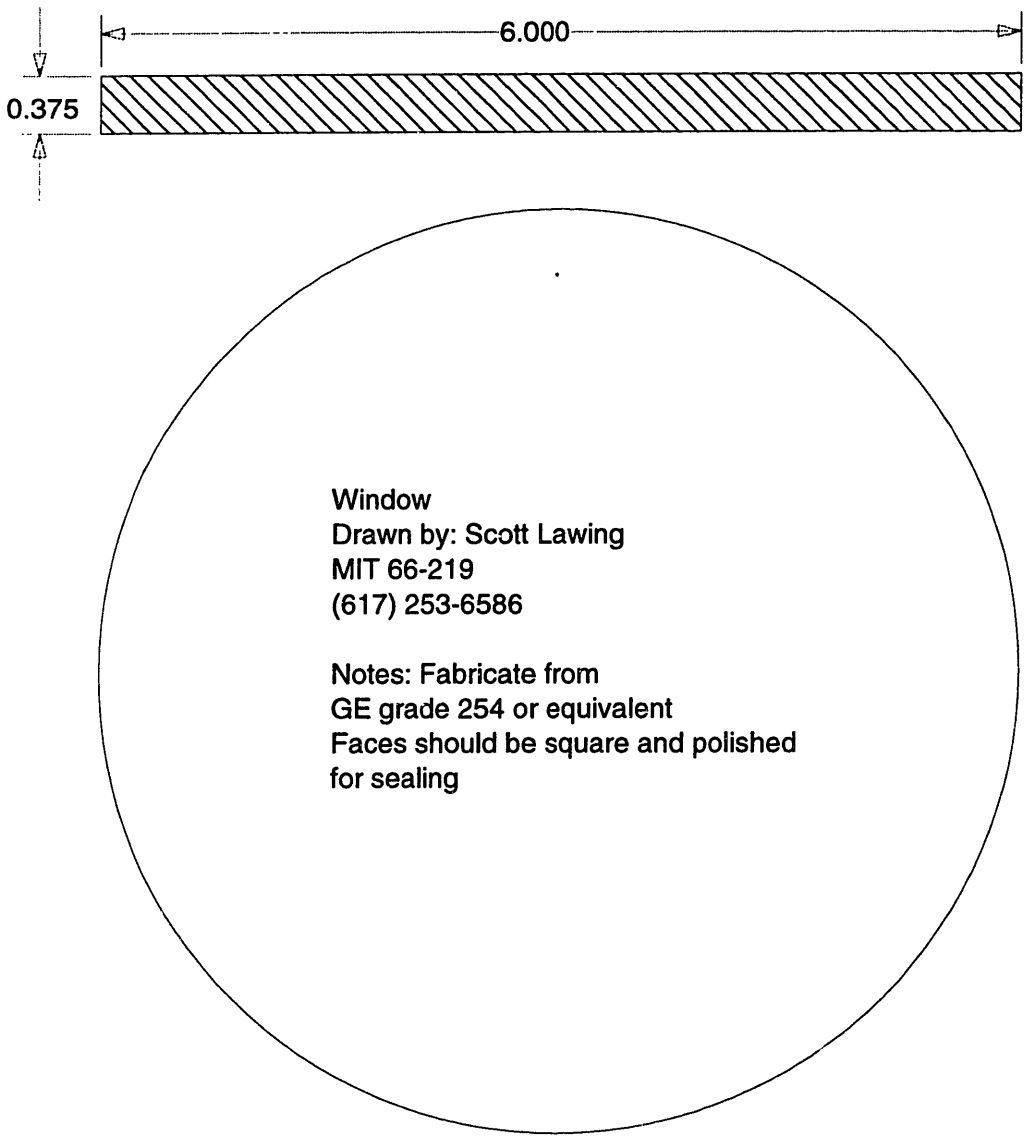
6.000
0.375
Window
Drawn by: Scott Lawing
MIT 66-219
(617) 253-6586
Notes: Fabricate from
GE grade 254 or equivalent
Faces should be square and polished
for sealing

2. First UV Reactor

Transfer Chamber

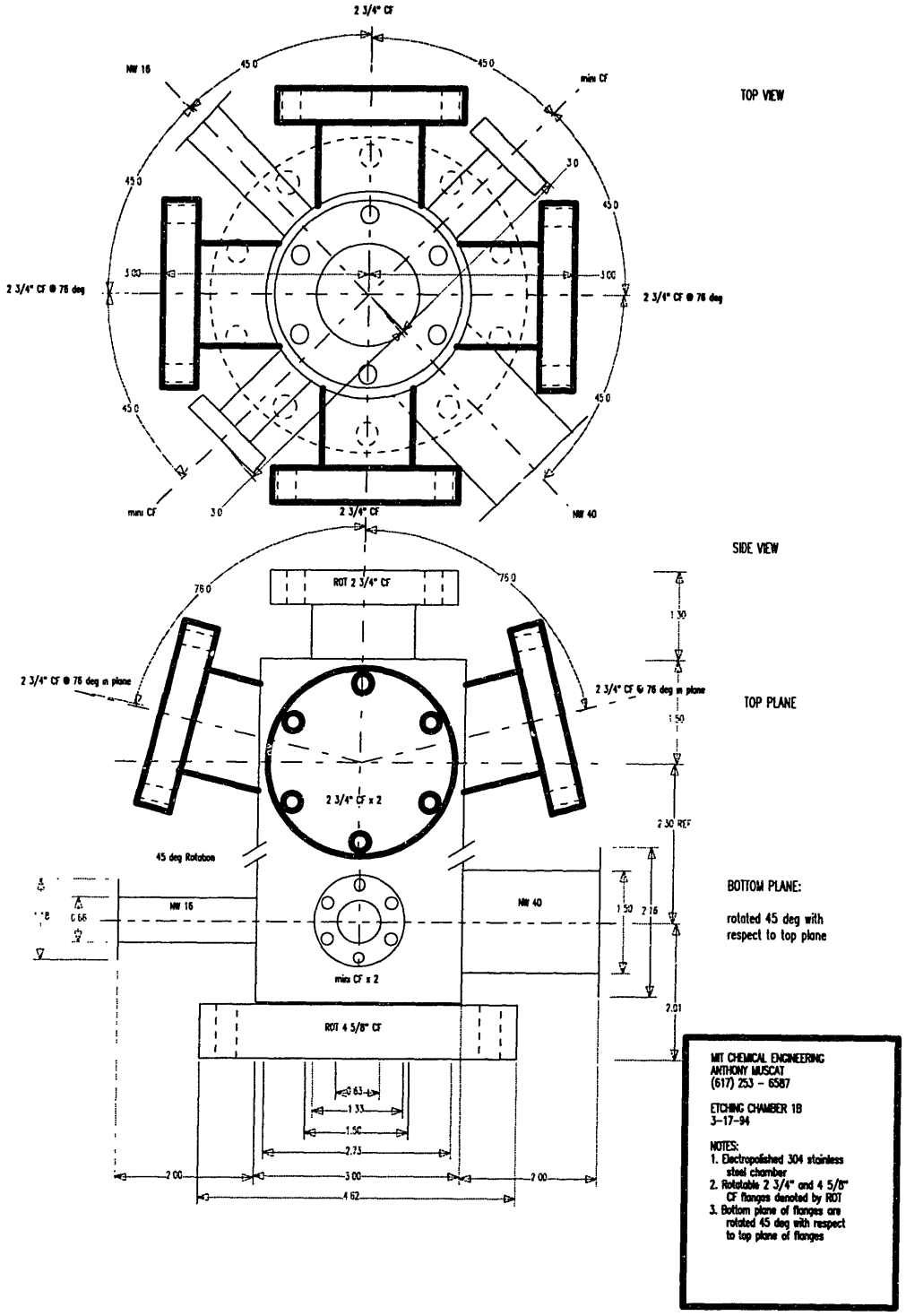

Macor Fork

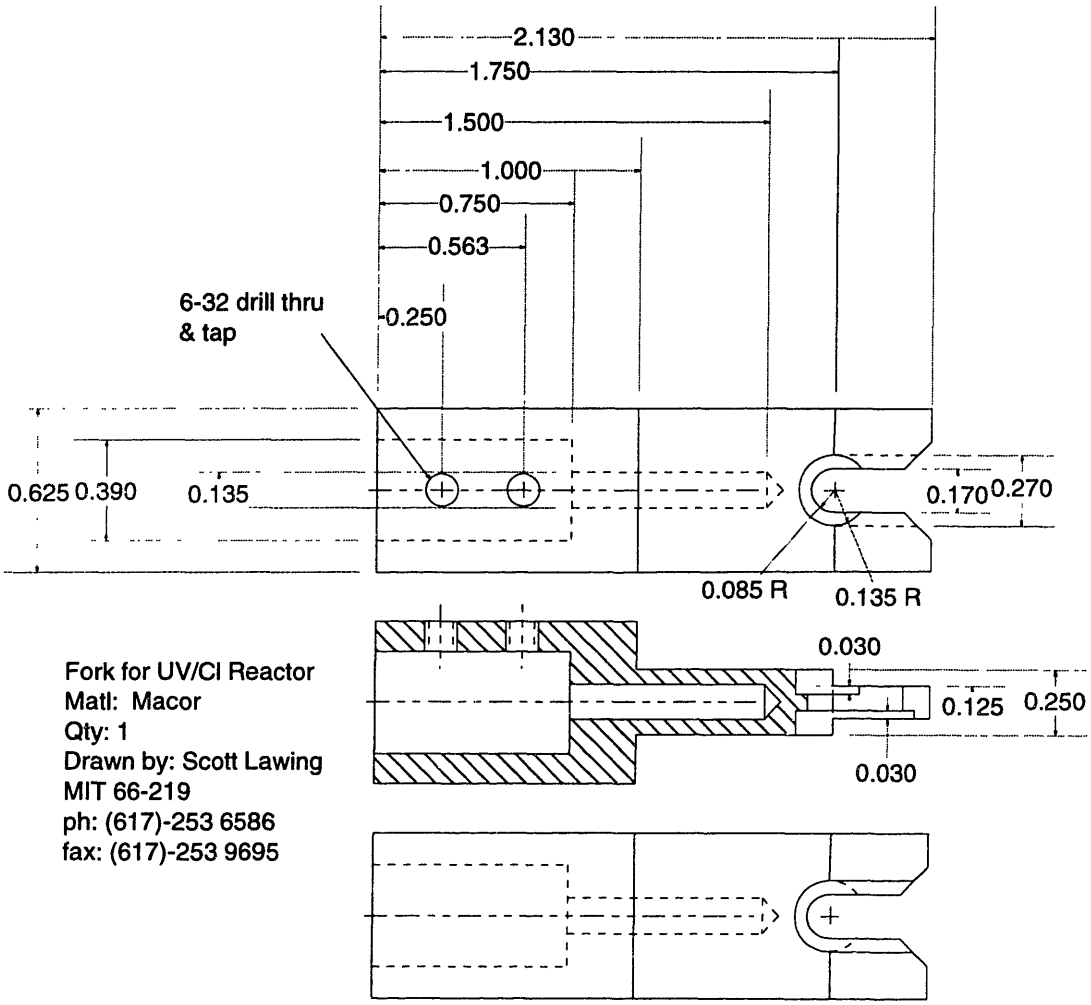

Fork for UV/Cl Reactor
Matl: Macor
Qty: 1
Drawn by: Scott Lawing
MIT 66-219
ph: (617)-253 6586
fax: (617)-253 9695

Transfer Rod Assembly Drawing and Detail

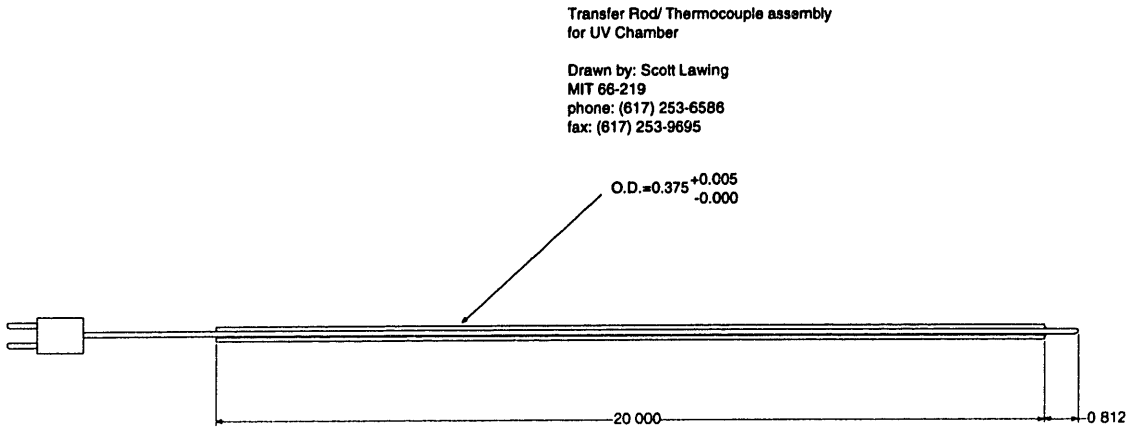

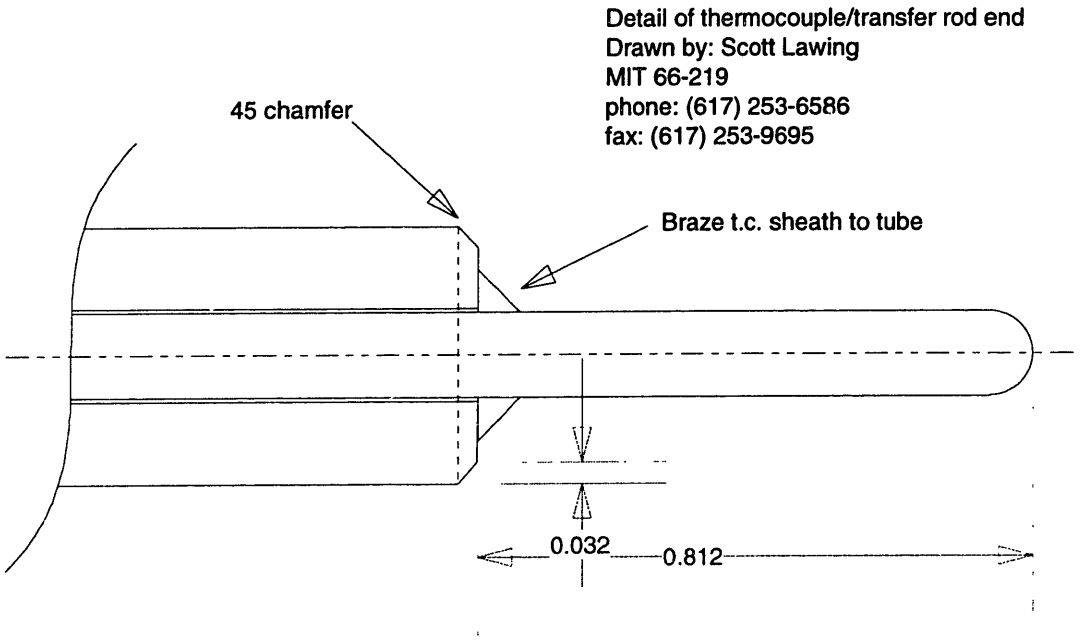

Macor Sample Holder #1

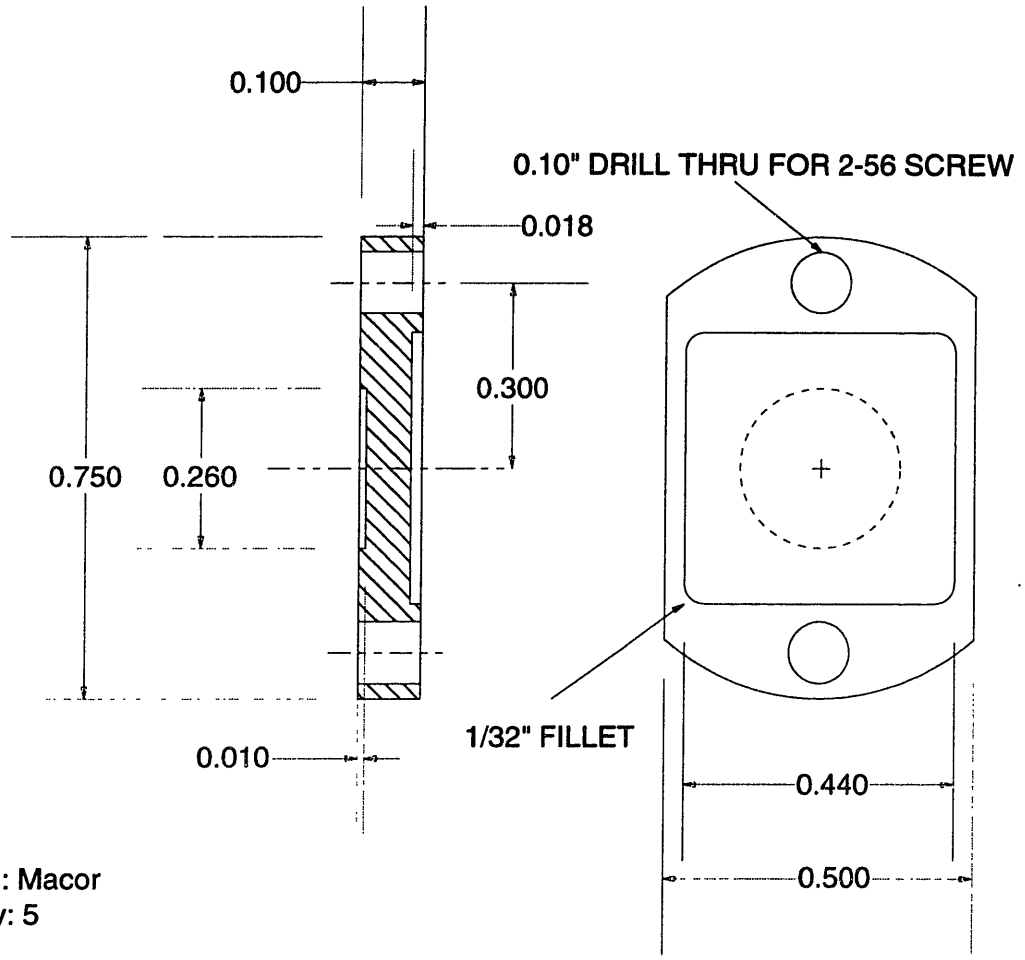

Material: Macor
Quantity: 5

Macor Sample Holder #2

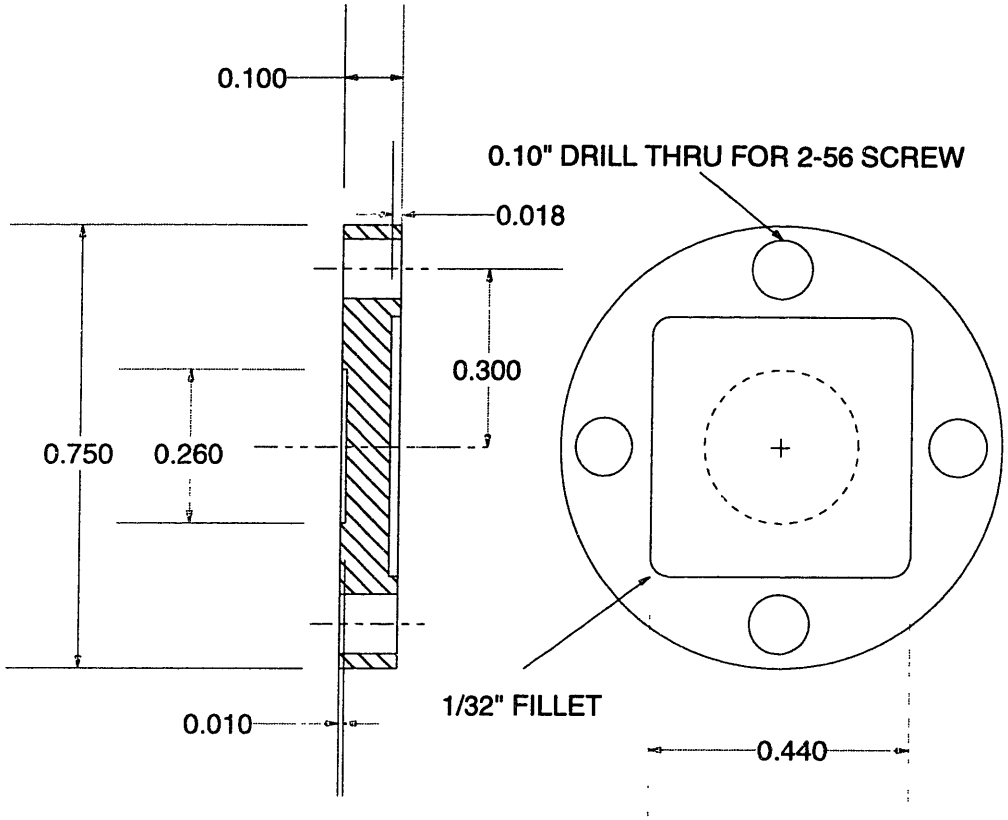

Material: Macor
Quantity: 5

3. X-Ray Gun

Water Fitting

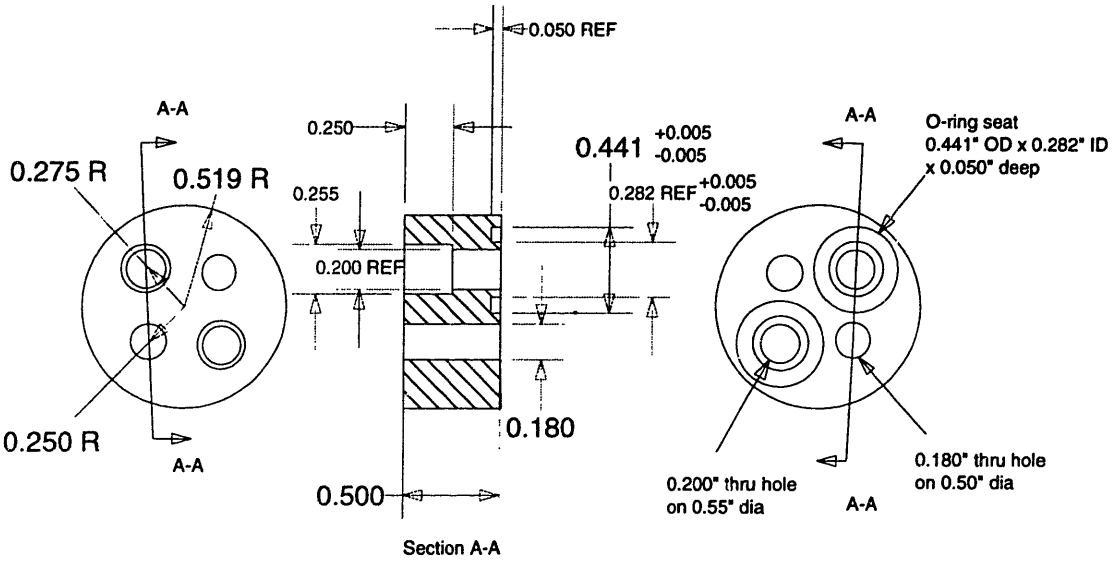

Drawn By Scott Lawing
MIT 66-219 (617)253-6586
Material: 300 series SS
Quantity: One
Requires 2 each -011 O-ring

Appendix B

List of Experimental Series and File Naming System

I have included this appendix in case anyone ever has to go back and dig out any of my old scans. I hope you can make sense of it!

Generally, file names begin with the letter representing the experimental series (see accompanying table) and the number of the experiment. For instance, for experiment #1 in the AJ series, dealing with wavelength dependent copper removal, files are named with aj01*.*. The metal or element pertinent to the file is sometimes included in the file name, i.e. aj01_cu*.*. For the most part, three types of files are contained in the database. These are; raw XPS data files (output from the VG100AX software), Matlab files (fitted XPS data output from the ESCA Tools software), and Microsoft Excel files (presentation domain). Excel files generally contain multiple sheets which represent the data contained in the ESCA Tools fits. The raw data files can be cross-referenced to the pertinent lab notebook. Raw data files also contain a header which lists information regarding the scan conditions; number of scans, dwell time, etc. that are required to scale the intensity of the scans relative to each other, as well as the conditions of the experiment. Be advised that the experimental conditions may not apply, i.e. if I forgot to enter them before I saved the file they may represent the information from the previous scan. *The lab notebook is more reliable for the experimental conditions!* Raw data files generally contain multiple survey and elemental scans (except for the earliest fits with the ESCA Tools software). For instance, the raw data file named aj01.1 contains a survey scan (10-1000 eV), an oxygen scan (525-545 eV), a silicon scan (90-120 eV), and a copper scan (925-975 eV). The raw data file named aj01_n.1 contains the same scan information normalized for charging, such that the silicon metal peak is set at 99.75 eV, i.e. the charged silicon peak falls at 102.5 eV, and 3.5 eV is subtracted from the binding energy of each scan in the normalized file on the header line. The ESCA Tools fit file named aj01_cu1.m contains the fitted data of the copper scan contained in aj01.1. The Excel file named aj01_cu.xls contains all of the copper fits from the aj01 experiments, i.e. the two sheets

in aj01_cu.xls, contain the data from aj01_cu1.m and aj01_cu2.m respectively. *.txt files generally contain information from the "composition" screen in ESCA Tools.

Note that if the raw data files are not in the directory listed in the accompanying table, they are most likely in "Crater Lake"\Big_Blue\Scottdata\Scottspm\new_xps. If they are not there, they are probably gone forever!

Of course, there are some deviations from this system here and there. For instance, some fit files may be named *.mb, in the case where a second fit of the raw data was performed (different background subtraction-things like that). But, with this information, I think you can make sense out of most of it. If not, give me a call If you can find me!

Series	Description of Experiments	Lab Notebook and Page #'s	File Locations	Dates Performed
A	Response surface on p-type <100> 5-20Ω cm UV/Cl_2 etching (in Dave Gray's Reactor)	1, 36-63	G:/Scott/Excel	9/1-27/93
B	Response surface on n+ <100> UV/Cl_2 etching (in Dave Gray's Reactor)	1, 64-85	"	9/27-10/7/93
K	Response surface on p-type <100> 5-20Ω cm UV/Cl_2 etching (in Dave Gray's Reactor)	2, 9-22	"	12/3-14/93
	All below in quartz tube reactor			
R	UV/Cl_2 etching runs with ceramic sample holder and oxide mask	2, 45	G:/Scott/FSI (Grapher)	9/12/94
S	"	2, 46-50	"	9/22-10/3/94
T	"	2, 51-55	"	10/12-13/94
U	parallel vs. normal incidence UV/Cl_2 etching	2, 56,58	"	11/1/94
V	" including angle resolved etching	2, 57,59-61	"	11/17/94
X	UV/ClF_3 silicon etching w/sapphire tube	2, 62-68	"	1/19-1/24/95
Y	UV/Cl_2 copper removal (old analyzer)	2, 69-96	G:/Scott/FSI	1/31-3/18/95
Z	parallel vs. normal incidence BPSG and nitride UV/ClF_3 etching w/sapphire tube	2, 97-100	"	4/9-10/95
AA	RIE clean (old analyzer)	3, 2-24	"	5/1-6/9/95
AB	UV/Cl_2 copper removal (old analyzer)	3, 25-29 3, 38-46	"	6/14-7/24/95
AC	UV/ClF_3 nitride etching w/sapphire tube	3, 30-31	"	6/28-30/95
AD	ClF_3 nitride etching w/sapphire tube	3, 47-50	"	7/25-28/95
	All below with VG100AX energy analyzer			
AE	UV/Cl_2 copper removal, includes sputter system calibration (AE06) Note, these fits are NOT with matlab software! Files are *.wk1.	3, 54-90	G:/Scott/ Cop_XPS	8/14-29/95
AF	", includes wet deposition (AF12)	3, 91-100 4, 1-7	"	8/31-9/19/95

n.a.	Witnessed description of copper removal mechanism	4, 13-15	"	10/24/95
RIE*	XPS analysis of etched and ashed wafers (MTL)	4, 22-25	G:/Scott/Thesis G:/Scott/ New_RIE	11/29/95
AH	RIE cleaning	4, 26-35	G:/Scott/Thesis G:/Scott/ New_RIE	
AI	UV/DCS/Halogen	4, 36-81	G:/Scott/FSI G:/Scott/ Ch5_XPS	12/11/95-2/26/96
AJ	Wavelength Dependent Metals Removal, includes improved processes	4, 82-100 5, 1- 41	G:/Scott/ Cop_XPS G:/Scott/ Ch4_XPS	3/1-6/4/96
Wet*	Pirhana-SC1-HF dip wet sequence on wafers from RIE* and AH series	5, 43-45	G:/Scott/Thesis G:/Scott/ New_RIE	6/20/96
AM	Wavelength Dependent RIE residue removal	5, 46-50	G:/Scott/Thesis G:/Scott/ New_RIE	6/25-7/1/96
AN	Pressure dependence of copper removal w/245 nm light	5, 51-56	G:/Scott/ Cop_XPS	8/1/96
	All Below in Clustered System			
AR	Integrated ICP etch, ash clean on blanket oxides	5, 68-88	G:/Scott/ AR_Runs	3/7-4/6/97
AT	Influence of Oxide surface on UV/Cl_2 metals removal	5, 89-98	G:/Scott/ Cop_XPS G:/Scott/ Ch4_XPS	5/1-5/27/97
AU	Integrated ICP etch, ash clean on patterned oxides	5, 99 + attached loose sheets	G:/Scott/ AU_Runs	6/1-7/9/97